

Copyright

by

Lionel Hervé Noël Ribeiro

2013

The Dissertation Committee for Lionel Hervé Noël Ribeiro Certifies that this is the approved version of the following dissertation:

Development of a Three-Dimensional Compositional Hydraulic Fracturing Simulator for Energized Fluids

Committee:

Mukul M. Sharma, Supervisor

Loukas F. Kallivokas

Tadeusz W. Patzek

Maša Prodanović

Kamy Sepehrnoori

**Development of a Three-Dimensional Compositional Hydraulic
Fracturing Simulator for Energized Fluids**

by

Lionel Hervé Noël Ribeiro, Ingénieur, M.S.E.

Dissertation

Presented to the Faculty of the Graduate School of

The University of Texas at Austin

in Partial Fulfillment

of the Requirements

for the Degree of

Doctor of Philosophy

The University of Texas at Austin

August 2013

Dedication

I dedicate this dissertation to my parents, Constantin and Jacqueline Ribeiro. This work would not have been possible without their endless love, constant support, and sacrifices.

Acknowledgements

I would like to express my sincere gratitude to my advisor, Dr. Mukul Sharma, for his guidance and support throughout the duration of this work. He has been a great source of inspiration and a true mentor for me; and I intend to carry his teaching with me throughout my career. I am particularly thankful for the collaborative atmosphere and for the numerous opportunities he gave me to present my work to industry partners.

I would like to thank the members of my dissertation committee, Drs. Loukas Kallivokas, Tadeusz Patzek, Maša Prodanović, and Kamy Sepehrnoori for their sound advice and contributions to my work. I would like to acknowledge the effort of all the professors at the University with whom I have had the opportunity to work and study. The lessons learned in the classroom have helped me in performing my research work, and they will be of great help for years to come. My great appreciation also goes out to the entire UT staff, who greatly facilitated the many challenges of graduate school. In particular, I cannot thank Jin Lee enough; her dedication to the success of students is remarkable.

This study has been influenced by many contributors. In particular, I would like to acknowledge the great work performed by Dr. Kyle Frieauf, who set up the stage for energized fracturing research at UT Austin. Also, I would like to acknowledge the work performed by Drs. Gu, Yew, Carey, and Ouyang in the 90s, as their work has been instrumental in the pursuit of my study. I owe many thanks to the Department of Energy and RPSEA (Research Partnership to Secure Energy for America) for their financial

support, as well as the numerous companies sponsoring the Joint Industry Project on *Hydraulic Fracturing and Sand Control* at UT Austin.

I am indebted to many of my friends and colleagues at UT Austin who shaped my research in so many ways. In particular, I would like to thank Somnath Mondal, Divya Ramaswamy, Nicolas Roussel, Sahil Malhotra, Mac Pedlow, Taner Sensoy, David Torres, Corey McCulley, Ripudaman Manchanda, Mandy Sutton, and Saptaswa Basu for making our graduate school journey so enjoyable.

My time in Austin has been an incredible experience, influenced by many friends and more, most notably Kelley Kalchthaler, Adnan Khaleel, and Karun Vijayraghavan (along with numerous soccer teammates and friends that I have not specifically named here). Finally, I would like to thank my family, notably Jacqueline Ribeiro, Constantin Ribeiro, Danielle Duport and Hervé Duport. Their love and support have helped me in the pursuit of my goals, and this work is dedicated to them.

Development of a Three-Dimensional Compositional Hydraulic Fracturing Simulator for Energized Fluids

Lionel Hervé Noël Ribeiro, Ph.D.

The University of Texas at Austin, 2013

Supervisor: Mukul M. Sharma

Current practices in energized treatments, using gases and foams, remain rudimentary in comparison to other fracturing fluid technologies. None of the available 3D fracturing models for incompressible water-based fluids have been able to capture the thermal and compositional effects that are important when using energized fluids, as their constitutive equations assume single-phase, single-component, incompressible fluid flow. These models introduce a bias in fluid selection because they do not accurately capture the unique behavior of energized fluids. The lack of modeling tools specifically suited for these fluids has hindered their design and field implementation.

This work uses a fully compositional 3D fracturing model to answer some of the questions surrounding the design of energized treatments. The new model is capable of handling any multi-component mixture of fluids and chemicals. Changes in fluid density, composition, and temperature are predicted using an energy balance equation and an equation of state. A wellbore model, which relates the surface and bottomhole conditions,

determines the pumping requirements. Fracture performance is assessed by a fractured well productivity model that accounts for damage in the invaded zone and finite fracture conductivity.

The combination of the fracture, productivity, and wellbore models forms a standalone simulator that is suitable for designing and optimizing energized treatments. The simulator offers a wide range of capabilities, making it suitable for many different applications ranging from hydraulic fracturing to long-term injections for enhanced oil recovery, well clean-up, or carbon sequestration purposes. The model is applicable to any well configuration: vertical, deviated, or horizontal. The resolution of the full 3D elasticity problem enables us to propagate the fracture across multiple layers, where height growth is controlled by the vertical distribution of the minimum horizontal stress.

We conducted several sensitivity studies to compare the fracture propagation, productivity, and pumping requirements of various fluid candidates in different reservoirs. The results show that good proppant placement and high fracture conductivities can be achieved with foams and gelled fluid formulations. Foams provide a wide range of viscosities without using excessive amounts of gelling agents. They also provide superior fluid-loss control, as the filter-cake is supplemented by the presence of gas bubbles that reduce liquid-flow into the porous medium. CO₂, LPG, and N₂ expand significantly (by 15% or more) as the reservoir heats the fluid inside the fracture. These fluids show virtually no damage in the invaded zone, which is a significant improvement upon water-based fluids in reservoirs that are prone to water blocking. These results, however, are contingent on an accurate fluid characterization supported by experimental data; therefore, our work advocates for complementary experimental studies on fluid rheology, proppant transport, and fluid leak-off.

A comprehensive sensitivity study over a wide range of reservoir conditions identified five key reservoir parameters for fluid selection: relative permeability curve, initial gas saturation, reservoir pressure, changes to rock mechanical properties, and water-sensitivity. Because energized fluids provide similar rheology and leak-off behaviors as water-based fluids, the primary design question is to evaluate the extent of the damaged zone against costs, fluid availability, and/or safety hazards. If the fluid-induced damage is acceptable, water-based fluids constitute a simple and attractive solution; otherwise, energized fluids are recommended. Notably, energized fluids are well-suited for reservoirs that are depleted, under-saturated, and/or water-sensitive. These fluids are also favorable in areas with a limited water supply. As water resources become constrained in many areas, reducing the water footprint and the environmental impact is of paramount concern, thereby making the use of energized treatments particularly attractive to replace or subsidize water in the fracturing process.

Table of Contents

List of Tables	xvii
List of Figures	xix
Chapter 1: Introduction	1
1.1 Context of the Study	1
1.1.1 Unconventional Oil and Gas Resources	1
1.1.2 A Wide Range of Fracturing Fluids.....	4
1.1.3 Limitations of Water-Based Fracturing Fluids	5
1.1.4 Historical Use of Energized Fluids	8
1.1.5 Main Advantages of Energized Fluids.....	9
1.2 Use of Energized Fluids in the Field (2011-2012).....	10
1.3 Objectives and Proposed Methodology	14
1.4 Structure of the Dissertation	15
References	21
Chapter 2: Review of Existing Fracture Models.....	24
2.1 Challenges in Fracture Modeling.....	24
2.2 Review of Classical 2D Fracture Models	25
2.2.1 Sneddon’s Model Formulation	25
2.2.2 PKN and KGD Models	26
2.3 Review of the First 2D Compositional Fracture Model.....	28
2.4 Review of Pseudo 3D Fracture Models	29
2.5 Review of 3D Planar Fracture Models.....	31
2.6 Review of General 3D (Non-Planar) Models	33
2.7 Limitations of Existing Models for Energized Fracturing.....	36
Nomenclature	44
References	45
Chapter 3: Formulation of the 3D Compositional Fracture Model.....	48
3.1 Problem Statement.....	49

3.1.1 Fracture Geometry	49
3.1.2 Main Variables for Fluid and Proppant	49
3.1.3 Material Balances.....	51
3.1.4 Main Variables for Fluid Composition	52
3.2 Flow Equations	52
3.2.1 Slurry Flow	53
3.2.2 Proppant Flow	55
3.2.3 Fluid Flow	57
3.2.4 Comments on Foam Stability and Rheology	57
3.3 Pressure Equation (Overall Mass Balance).....	58
3.4 Proppant Transport Equation	61
3.5 Component Transport Equation(s).....	63
3.5.1 Component Mass Fraction Formulation	64
3.5.2 Overall Component Mass Fraction Formulation	65
3.5.3 Saturation Formulation	66
3.6 Energy Balance Equation.....	68
3.6.1 Energy Balance Assumptions	68
3.6.2 Combined Energy Fluxes.....	69
3.6.3 Heat Lost due to Leak-off	70
3.6.4 Heat Gained from the Reservoir	71
3.6.5 Energy Balance Equation.....	72
3.7 Phase Behavior.....	73
3.7.1 Phase Density.....	74
3.7.2 Component Split between Phases (Solubility).....	75
3.7.3 Phase Behavior of most Common Fracturing Fluids.....	76
3.7.4 Comments on the Modeling of Foams.....	77
3.8 Fracture Mechanics.....	78
3.8.1 Fracture Opening Equation	79
3.8.2 Criterion for Fracture Propagation.....	79
3.9 Overview of the Mathematical Problem	81

3.9.1 Completeness of the Mathematical Problem	81
3.9.2 Complexity of the Mathematical Problem	82
3.9.2.1 Different Classes of PDEs	83
3.9.2.2 Strong Coupling between the PDEs.....	83
3.9.2.3 Non-Linearity.....	84
3.9.2.4 Moving-Boundary Problem	84
3.9.2.5 Singularities	85
3.10 Comparison with Existing Models.....	85
3.10.1 Comparison with 3D Planar Fracture Models	86
3.10.2 Comparison with a 2D Compositional Model (Friehauf and Sharma 2009).....	86
3.10.2.1 Fracture Mechanics	86
3.10.2.2 Flow Equations	87
3.10.2.3 General Features	87
Nomenclature.....	92
References.....	94
Chapter 4: Finite-Element Formulation and Main Algorithm.....	96
4.1 Solution of the Pressure Equation.....	97
4.2 Solution of the Compatibility Condition.....	102
4.3 Solution of the Convection-Dominated Equations	103
4.4 Solution of the Fracture Opening Equation	107
4.5 Main Algorithm	108
4.5.1 Overview of the Main Algorithm	108
4.5.2 Fracture Propagation.....	109
4.5.3 Adaptive Fracture Front Displacement.....	110
4.5.4 Time-Decoupling Scheme	111
4.5.5 Relaxation Process.....	112
4.5.6 Linear Solvers	113
4.6 Main Features of the Dynamic Unstructured Mesh.....	114
4.6.1 Past Developments.....	114

4.6.2 Mesh Structure	114
4.6.3 Elements and Shape Functions	115
4.6.4 Boundary Node Generation	117
4.6.5 Interior Node Generation	118
4.7 Main Differences with <i>UTFRAC-3D</i>	119
Nomenclature	128
References	130

Chapter 5: Wellbore and Fracture Productivity Models.....131

5.1 Temperature Variation in the Wellbore	132
5.1.1 Definition and Formulation of Heat Exchanges	132
5.1.2 Energy Balance Equation along the Wellbore	135
5.2 Pressure Variation in the Wellbore	135
5.2.1 Pressure Equation.....	136
5.2.2 Frictional Loss	136
5.3 Near-Wellbore Frictional Loss	138
5.3.1 Perforation Frictional Loss	139
5.3.2 Tortuosity Effects.....	140
5.4 Interpolation Scheme between the Fracture and the Reservoir	142
5.4.1 Algorithm for Interpolation.....	142
5.4.2 Barycentric Method	143
5.4.3 Interpolation Examples	144
5.5 Productivity Model for Fractured Well.....	145
5.5.1 Formulation of the Productivity Model	146
5.5.2 Properties of the Virgin Zone, Invaded Zone, and Fracture	149
5.5.3 Determination of the Invaded Zone Length.....	151
5.5.4 Comments Regarding Foams.....	153
5.6 Conclusions.....	154
Nomenclature.....	163
References.....	165

Chapter 6: Preliminary Results and Model Capabilities	167
6.1 Inputs and Outputs	167
6.1.1 Main Inputs	167
6.1.2 Main Outputs	169
6.2 Model Validation	170
6.2.1 Radial Example	170
6.2.2 PKN Example – No fluid leak-off	171
6.2.3 PKN Example – Fluid Leak-off	172
6.2.4 Comparison with a Planar 3D Fracturing Simulator	172
6.2.5 Comparison with Field Data	173
6.3 Model Capabilities: Energized Fluid Examples	174
6.3.1 Gelled LPG Fracturing Treatment	174
6.3.1.1 Compositional Case	175
6.3.1.2 Incompressible Case	175
6.3.2 Long-Term CO ₂ Injection	177
6.3.3 CO ₂ Foam Fracturing Treatment	178
6.3.4 Example of Wellbore Flow Calculations	180
6.4 Conclusions	182
References	196
Chapter 7: Phase Behavior, Rheology, and Leak-off of Energized Fluids ...	197
7.1 Phase Density	198
7.1.1 Model Formulation	198
7.1.2 Phase Density of Common Fracturing Fluids	200
7.2 Component Solubility	201
7.2.1 Model Formulation	201
7.2.2 Component Solubility of Common Fracturing Fluids	202
7.3 Rheology	203
7.3.1 Base-Fluid Rheology	203
7.3.2 Foam Stability	204
7.3.3 Stable Foam Rheology	205

7.3.3.1 Literature Review.....	205
7.3.3.2 In-House Experimental Work.....	208
7.3.3.3 Influence of Proppant Concentration.....	209
7.4 Challenges in Measuring Multi-Phase Leak-off Coefficients	210
7.4.1 Field Determination	211
7.4.2 Experimental Determination.....	212
7.5 Multi-Phase Leak-off Coefficients	214
7.5.1 In-House Experimental Results	215
7.5.2 Comparison with Published Data.....	216
7.6 Conclusions.....	217
Nomenclature.....	229
References.....	230

Chapter 8: Impact of Fluid and Reservoir Properties on Fracture Productivity: Identification of Key Parameters.....	232
8.1 Case Study: Results for 0.3-Quality N ₂ Foam	233
8.1.1 Reservoir Properties and Pumping Schedule.....	233
8.1.2 Pumping Requirements.....	235
8.1.3 Fracture Propagation.....	236
8.1.4 Fluid Invasion	237
8.1.5 Invaded Zone Properties	237
8.1.6 Fracture Productivity	238
8.2 Case Study: Comparison between Several Fluid Candidates	239
8.2.1 Pumping Requirements.....	239
8.2.2 Fracture Propagation.....	241
8.2.3 Invaded Zone Properties	241
8.2.4 Fracture Productivity	243
8.2.5 Limitations of the Case Study.....	244
8.3 Reservoir Sensitivity Study.....	245
8.3.1 Scope of the Study	245
8.3.2 Impact of Invaded Zone Permeability.....	246

8.3.3 Impact of Invaded Zone Length.....	248
8.3.4 Impact of Fracture Length and Height.....	249
8.3.5 Impact of Fracture Conductivity.....	250
8.4 Key Fracturing Fluid Properties.....	251
8.4.1 Density.....	251
8.4.2 Rheology.....	252
8.4.3 Leak-off.....	252
8.4.4 Shut-in Strategy.....	253
8.4.5 Safety Considerations.....	254
8.4.6 Cost and Availability.....	255
8.5 Key Reservoir Properties For Fluid Selection.....	256
8.6 Conclusions.....	258
Nomenclature.....	276
References.....	277
Chapter 9: Conclusions and Recommendations	278
9.1 Summary.....	278
9.2 Conclusions.....	279
9.2.1 Capabilities of the Fracturing Simulator.....	279
9.2.2 Design Recommendations.....	280
9.2.3 Unique Properties of Energized Fluids.....	282
9.3 Recommendations for Future Work.....	284
9.3.1 Usability of the Simulator.....	284
9.3.2 Key Areas of Improvement.....	286
9.3.3 Fluid Characterization.....	288
References.....	290
References.....	292
Vita.....	301

List of Tables

Table 1.1:	Estimated shale gas technically recoverable from selected basins in several countries, compared to proved reserves reported in 2009 (adapted from E.I.A. 2011).	17
Table 2.1:	Comparison of hydraulic fracture models.....	38
Table 3.1:	Main properties defining slurry, proppant, and fluid phases.	89
Table 3.2:	List of independent variables and equations. The problem is well-posed, as the number of independent equations equals the number of independent variables.	89
Table 4.1:	Comparison of the proppant transport, component transport, and temperature equations.	121
Table 4.2:	Choice of coefficients to obtain the proppant transport, component transport, and temperature equations from the generic problem given in Eq. 4.24.....	121
Table 4.3:	Matrix coefficients in Eq. 4.33 to solve the proppant transport, component transport, and temperature equations.	122
Table 6.1:	Main input parameters for the validation examples (radial and PKN geometries).....	183
Table 6.2:	Main input parameters for the gelled LPG and CO ₂ examples.....	183
Table 6.3:	Main input parameters for the 0.7-quality CO ₂ foam example.....	184
Table 7.1:	Rheology correlation values for N ₂ foams (from Reidenbach <i>et al.</i> 1986).	219
Table 7.2:	Comparison of foam leak-off data.	219
Table 8.1:	Main reservoir properties.	261

Table 8.2:	Pumping schedule for all the treatments used in the case study.	261
Table 8.3:	Fluid properties evaluated at 6200 psi and 150 °F.....	262
Table 8.4:	Fracture productivity (immediate flowback).	262
Table 8.5:	Fracture productivity (extended shut-in).	262

List of Figures

Figure 1.1: Map of 48 major shale gas basins located in 32 countries (from E.I.A. 2011).	18
Figure 1.2: Pyramid of oil and gas resources. Today, energized treatments are mostly used in tight gas and coal bed methane reservoirs, and their use is becoming more frequent in shale gas reservoirs (adapted from Sonnenberg 2010).	18
Figure 1.3: Fracturing operations in the U.S. in 2011-2012: (a) number of records per U.S. basin and (b) types of fracturing fluid (based on public data available on www.fracfocus.org).	19
Figure 1.4: Energized fracturing operations in the U.S. in 2011-2012: (a) number of records per U.S. basin and (b) number of records per operator (based on public data available on www.fracfocus.org).	19
Figure 1.5: Type of fluids used per operator in a selected area of the DJ Basin (based on public data available on www.fracfocus.org).	20
Figure 1.6: Fluid composition (on a mass basis) for each energized treatment design implemented in a selected region of the DJ Basin (based on public data available on www.fracfocus.org).	20
Figure 2.1: Representation of a radial or Penny-shaped fracture subject to a constant fluid pressure (from Adachi <i>et al.</i> 2007). R is a fracture radius; p is the constant fluid pressure; Q_0 is the injection rate; and w is the local width.	39

Figure 2.2: Representation of a PKN fracture (from Economides and Nolte 2000). The parameters L , h_f , and w are fracture length, height, and width, respectively.	39
Figure 2.3: Representation of a KGD fracture (from Economides and Nolte 2000). The parameters L , h_f , and w are fracture length, height, and width, respectively.	40
Figure 2.4: Representation of a pseudo 3D fracture (from Weng 1992).	40
Figure 2.5: Representation of a pseudo 3D fracture using the lumped elliptical approach (from Adachi <i>et al.</i> 2007).	41
Figure 2.6: Representation of a pseudo 3D fracture using the cell-based approach (from Adachi <i>et al.</i> 2007).	41
Figure 2.7: Comparison of fracture shapes predicted by pseudo 3D and fully 3D (planar) models (from Weng 1992).	42
Figure 2.8: Representation of the approximate 2D fluid flow introduced by Weng (1992) in his pseudo 3D model. At the element of interest, the outer flow field is approximated as local radial flow (from Weng 1992).	42
Figure 2.9: Representation of a 3D planar fracture using a dynamic unstructured mesh.	43
Figure 2.10: Representation of a 3D non-planar fracture. The fracture is allowed to move freely in all dimensions (from Rungamornrat <i>et al.</i> 2005). S is the fracture surface which is composed of the surfaces S^+ and S^- ; ∂S is the contour of the surface S ; w is the fracture width enclosed between S^+ and S^- ; and l, m, n, q are normal vectors used for the spatial integration of Eq. 2.5.	43

Figure 3.1: Representation of the fracture domain (Ω). The boundary of the domain ($\partial\Omega$) consists of the fracture front ($\partial\Omega_f$), the perforated interval along the wellbore ($\partial\Omega_p$), and the non-perforated section of the wellbore ($\partial\Omega_c$).	90
Figure 3.2: Representation of the main variables characterizing a two-phase slurry mixture. These variables are defined in the nomenclature.	90
Figure 3.3: Example of compositional calculations for 0.7-quality CO ₂ foam. ...	91
Figure 3.4: Pseudo 1D transient heat transfer between the fracture and the reservoir (top view).	91
Figure 4.1: Simplified version of the main algorithm. The green color indicates equations that are used in conventional fracturing simulators; blue indicates equations that are modified to account for multi-phase compressible fluid flow; and red indicates equations that are not present in traditional fracturing models.	123
Figure 4.2: General structure of the algorithm implemented in <i>EFRAC-3D</i> . The left side shows the iterative process used to compute pressure and width for a calculated time step Δt^n . The right side shows the time-forward loop used to compute proppant concentration, fluid temperature, and fluid composition.	124
Figure 4.3: Fracture propagation scheme. The node with the maximum stress intensity factor ($K_{I_{max}}$) advances by a distance equal to the maximum front displacement (Δd_{max}). The motion of the other boundary nodes is governed by Eq. 4.37. The old fracture is indicated in red, and the new fracture is indicated in blue.	125

Figure 4.4: Movement of the boundary nodes between times t^n and t^{n+1} . Each node advances along its outward normal direction (adapted from Gu 1987).	125
Figure 4.5: Example illustrating the evolution of the time step calculated from the compatibility condition (for the validation case presented in Section 6.2.3).	126
Figure 4.6: Time decoupling scheme. First, we compute fracture width and pressure using a relaxation iterative procedure. Then, we solve the transport equations using a time-forward loop and individual iterative schemes.	126
Figure 4.7: Master elements for the regular triangular (Ω_t), regular quadrilateral (Ω_q), and singular quadrilateral (Ω_s) elements.	127
Figure 4.8: Node arrangement at the fracture tip. By construction, each pair of triangle and quadrilateral shares a side (from Gu 1987).	127
Figure 5.1: Wellbore configuration and heat flow through a series of resistances (from Hasan and Kabir 2012).	155
Figure 5.2: Well made of segments of variable inclination and pipe diameter (from Hasan and Kabir 2012).	155
Figure 5.3: Evolution of the discharge coefficient due to sand erosion (from Crump and Conway 1988).	156
Figure 5.4: Tortuosity effect: the fracture twists and turns to align itself with the preferred direction of propagation (from Economides and Nolte 2000).	156

Figure 5.5: Interpolation scheme that relates the unstructured fracture grid to the Cartesian reservoir grid. Only the nodes indicated in blue are interpolated for this element.	157
Figure 5.6: Algorithm used for the interpolation scheme.....	157
Figure 5.7: Fracture width calculated from the fracture mechanics equation in the unstructured fracture mesh.....	158
Figure 5.8: Fracture width mapped in the reservoir mesh using the interpolation scheme.....	158
Figure 5.9: Mass of water per unit area placed into the reservoir at the end of pumping.	159
Figure 5.10: Mass of water per unit area placed into the reservoir after shut-in.	159
Figure 5.11: Length of the invaded zone at the end of pumping.....	160
Figure 5.12: Length of the invaded zone after shut-in.	160
Figure 5.13: Association of flow resistances forming the productivity model (from Friehauf, Suri, and Sharma 2010). Because of the symmetry, only a quarter of the fractured well system is shown. R_{out} is the resistance in the outer ellipse; $R_{el,i}$ is a resistance in the virgin zone; $R_{d,i}$ is a resistance in the invaded zone; and $R_{f,i}$ is to a resistance along the fracture. The outer ellipse is delimited by a_2 and b_2 ; and the inner ellipse is delimited by a_1 and b_1	161
Figure 5.14: Inner ellipse minor axis versus a_{prats} conductivity (from Friehauf, Suri, and Sharma 2010).	162

Figure 5.15: Illustration of the water blocking effect. The water that is not recovered creates a high-water saturation zone that impedes the flow of oil and gas. The use of energized fluids improves clean-up in and around the fracture.	162
Figure 6.1: Vertical distribution of the <i>in-situ</i> minimum horizontal stress for the validation examples (radial and PKN geometries).	185
Figure 6.2: Vertical distribution of the <i>in-situ</i> minimum horizontal stress for the energized examples (LPG, CO ₂ , and CO ₂ foam).	185
Figure 6.3: Final width profile (radial example, no leak-off).....	186
Figure 6.4: Comparison between fracturing models (radial example, no leak-off): (a) fracture radius over time and (b) average width over time.	186
Figure 6.5: Final width profile (PKN example, no leak-off).....	187
Figure 6.6: Comparison between fracturing models (PKN example, no leak-off): (a) fracture half-length over time and (b) maximum width over time.	187
Figure 6.7: Final width profile (PKN example, with leak-off).....	188
Figure 6.8: Comparison between fracturing models (PKN example, with leak-off): (a) half-length over time and (b) maximum width over time.	188
Figure 6.9: Final width profile for gelled LPG injection (<i>Stress A</i> distribution) using the compositional simulator. Fluid expansion is taken into account.	189
Figure 6.10: Final width profile for gelled LPG injection (<i>Stress A</i> distribution) assuming the fracturing fluid remains incompressible.	189

Figure 6.11: Impact of fluid expansion on fracture geometry (LPG example, <i>Stress A</i> distribution): (a) height over time and (b) maximum width over time.	190
Figure 6.12: Impact of fluid expansion on pumping requirements (LPG example, <i>Stress A</i> distribution): (a) net pressure over time and (b) pressure drop along the wellbore over time.....	190
Figure 6.13: Width profile after 10 days of CO ₂ injection (<i>Stress B</i> distribution)....	191
Figure 6.14: Width profile after 200 days of CO ₂ injection (<i>Stress B</i> distribution)..	191
Figure 6.15: Evolution of fracture geometry for long-term CO ₂ injection: (a) half-length and height over time and (b) maximum width over time. The time step increases over time, as indicated by the increasing gaps between markers.....	192
Figure 6.16: Fracture width for 0.7-quality CO ₂ foam (<i>Stress C</i> distribution)....	192
Figure 6.17: Fluid temperature for 0.7-quality CO ₂ foam (<i>Stress C</i> distribution).	193
Figure 6.18: Gas phase density for 0.7-quality CO ₂ foam (<i>Stress C</i> distribution).	193
Figure 6.19: Proppant concentration (volume fraction) for 0.7-quality CO ₂ foam (<i>Stress C</i> distribution).	194
Figure 6.20: Horizontal well profile: (a) position of the survey stations in the vertical-lateral depth referential and (b) 3D isometric representation in our interface (not to scale).....	194

Figure 6.21: Pumping requirements: (a) fluid pressure over time and (b) gas saturation over time. Foam quality is higher at the surface than the designed quality at the perforations because of gas compressibility.	195
Figure 6.22: Density of the liquid phase, gas phase, and slurry mixture along the wellbore: (a) after 5 minutes of pumping and (b) after 18 minutes of pumping. The markers indicate the position of the survey stations.	195
Figure 7.1: Density of pure water phase: comparison between our model and the experimental data compiled in Sandler (2007).	220
Figure 7.2: Density of pure N ₂ phase: comparison between our model and the experimental data provided by Saddington and Krase (1934).	220
Figure 7.3: Density of pure CO ₂ phase: comparison between our model and the data obtained with <i>PVTsim</i>	221
Figure 7.4: Density of a LPG mixture of 90% of C ₃ and 10% of n-C ₄ per volume: comparison between our model and the data obtained with <i>PVTsim</i>	221
Figure 7.5: Solubility of N ₂ in water: comparison between our model and the experimental data provided by Goodman and Krase (1931).	222
Figure 7.6: Solubility of CO ₂ in water: comparison between our model and the experimental data provided by Rumpf <i>et al.</i> (1994).	222
Figure 7.7: Solubility of CO ₂ in an equimolar mixture of water and methanol: comparison between our model and the experimental data provided by Xia <i>et al.</i> (2004).	223
Figure 7.8: Water saturation for stable 0.7-quality CO ₂ foam after 5 min.	223

Figure 7.9: Water saturation for unstable 0.7-quality CO ₂ foam after 5 min.	224
Figure 7.10: Illustration of the three flow regimes: commingled, foam, and mist. The transition between the regimes can be vague, and the scarcity of rheology data does not allow a proper characterization of the fluid behavior over a large spectrum. Often, multiple interpretations are possible because of the limited number of data points (indicated by the blue markers).	224
Figure 7.11: Simplified schematic of the foam-loop system, with relevant measurements shown in red.	225
Figure 7.12: N ₂ foam apparent viscosity versus shear rate for multiple foam qualities.	225
Figure 7.13: Comparison of N ₂ foam apparent viscosity measurements for multiple qualities (at a shear rate of 100 s ⁻¹).	226
Figure 7.14: Drawing of the fluid-loss cell (courtesy of TEMCO). The thick arrows indicate the direction of flow imposed in the circulating loop, and the thin arrows indicate the direction of fluid leak-off.	226
Figure 7.15: External filter-cakes observed after leak-off tests on Berea (left side) and Nugget (right side) sandstone samples. The ability of the fluid to form a rapid polymer-rich filter-cake is critical in reducing fluid-loss.	227
Figure 7.16: Effect of foam quality on liquid leak-off under various testing conditions. A significant decrease in liquid leak-off limits the fluid-induced damage.	227
Figure 7.17: Effect of foam quality on gas leak-off under various testing conditions. The behavior at high qualities is poorly understood.	228

Figure 7.18: Outlet composition enriched in the liquid phase as the result of filtration.	228
Figure 8.1: <i>In-situ</i> stress distribution and mechanical properties of each layer.	263
Figure 8.2: Evolution of pressure at different locations along the well.	263
Figure 8.3: Fracture propagation for the 0.3-quality N ₂ foam example: (a) position of the fracture front over time, (b) final fracture width, (c) final temperature distribution, and (d) final volumetric proppant concentration.....	264
Figure 8.4: Mass per unit area of each component that has invaded the reservoir for the 0.3-quality N ₂ foam example: (a) water invasion at the end of pumping, (b) N ₂ invasion at the end of pumping, (c) water invasion after an extended shut-in, and (d) N ₂ invasion after an extended shut-in.	265
Figure 8.5: Properties of the invaded zone for the 0.3-quality N ₂ foam example: (a) invaded zone length at the end of pumping, (b) water saturation in the invaded zone at the end of pumping, (c) invaded zone length after an extended shut-in, and (d) water saturation in the invaded zone after an extended shut-in. The initial water saturation in the reservoir is 0.35..	266
Figure 8.6: Evolution of the surface pressure for the different fluids considered in the case study.	267
Figure 8.7: Final fracture geometry using: (a) cross-linked water-based gel, (b) gelled LPG, (c) 0.3-quality CO ₂ foam, and (d) 0.65-quality CO ₂ foam.	268

Figure 8.8: Invaded zone length at the end of pumping using: (a) cross-linked water-based gel, (b) gelled LPG, (c) 0.3-quality CO ₂ foam, and (d) 0.65-quality CO ₂ foam.	269
Figure 8.9: Water saturation at the end of pumping using: (a) cross-linked water-based gel, (b) gelled LPG, (c) 0.3-quality CO ₂ foam, and (d) 0.65-quality CO ₂ foam.	270
Figure 8.10: Fracture productivity of the various fluid candidates for the immediate flowback and extended shut-in cases.	271
Figure 8.11: Relative permeability curves that are representative of (1) dry gas reservoir, (2) intermediate reservoir, and (3) strongly water-wet reservoir.	271
Figure 8.12: Impact of invaded zone permeability on productivity ($L_f/L_{drained}=1$ and $F_{cd}=0.6$).	272
Figure 8.13: Impact of invaded zone length on productivity ($L_f/L_{drained}=1$ and $F_{cd}=0.6$).	272
Figure 8.14: Impact of fracture length on productivity ($k_d/k=0.01$ and $h_{leak}/w=20$).	273
Figure 8.15: Impact of fracture conductivity on productivity for different fracture lengths ($k_d/k=0.005$ and $h_{leak}/w=20$).	273
Figure 8.16: Impact of fracture conductivity on productivity for different permeabilities in an undamaged reservoir ($L_f/L_{drained}=0.8$ and $h_{leak}/w=50$).	274
Figure 8.17: Impact of fracture conductivity on productivity for different permeabilities in a damaged reservoir ($L_f/L_{drained}=0.8$, $h_{leak}/w=50$, $k_s/k=0.001$, and $r_s/r_w=3$).	274

Figure 8.18: Impact of fluid density on fracture propagation. Lighter fluids are more prone to vertical migration because of the increasing contrast between the stress gradient (0.65 psi/ft here) and the fluid gradient (0.433, 0.354, 0.222, and 0.125 psi/ft for water, CO₂, LPG and N₂, respectively) in a given layer.....275

Chapter 1: Introduction

Although energized fracturing treatments have been used since the early seventies in reservoirs that are depleted, under-saturated, or water-sensitive, the unconventional energy boom in North America has dramatically revived the industry interest in “engineered” fluid formulations, such as foams¹ and pure gases. Present practices in energized² fracturing treatments remain nonetheless rudimentary in comparison to other fracturing fluid technologies, because of the limited understanding of multi-phase fluid-loss and phase behavior that occurs in these complex fluids. Additionally, the lack of modeling tools specifically suited for these fluids has hindered the design and the field implementation of energized treatments. This work intends to answer some of the questions surrounding the design of energized treatments. The main goal is to assess the benefits introduced by energizing the fracturing fluid, using a new three-dimensional (3D) compositional fracturing model.

1.1 CONTEXT OF THE STUDY

1.1.1 Unconventional Oil and Gas Resources

The development of shale oil and gas is one of the biggest energy stories of the past thirty years. Technological advances in hydraulic fracturing and horizontal drilling have unlocked large reservoirs that were considered inaccessible 30 years ago. The new accessibility to vast quantities of domestic gas trapped in shales has dramatically changed the status of natural gas. Similarly, large quantities of associated oil have been found in

¹ In this dissertation, we use the term *foam* to refer to a two-phase fluid mixture, irrespective of the flow regime (comingled, foam, or mist). Although a misnomer, this terminology is commonly used in practice.

² We define energized fluids as fluids that include at least one compressible phase.

many liquid-rich shales, such as the Bakken, Eagle Ford, and Niobrara formations. Unconventional oil and gas are now seen as the most likely energy sources capable of bridging the gap between dirty coal, rare conventional oil and gas, and renewable energies that would be efficient enough to take over the world energy burden.

In the United States, shale gas production has increased from 0.39 trillion cubic feet (TCF) in 2000 to 4.87 TCF in 2010. Shale gas production represented 23% of the total natural gas production in 2010. By 2035, the U.S. Energy Information Administration (E.I.A.) predicts that shale gas may account for half of the U.S. natural gas production (Annual Energy Outlook 2013 Early Release, 2013). Over the past couple of years, low gas prices have incited the industry to focus on liquid-rich shales over dry gas shales. In 2012, approximately 1 million barrels of oil per day were produced from shales and ultra-low permeability dolomites. According to estimates made by the E.I.A., the production of oil and gas from domestic shales has saved the U.S economy nearly 500 billion. This energy boom impacted job creation, economic growth, and energy security.

Even though the shale business is essentially concentrated in North America, unconventional oil and gas resources are far from being confined to the U.S. In the 2011 Annual Energy Outlook, the E.I.A. investigated 48 shales gas basins in 32 countries shown in **Fig. 1.1**. The E.I.A. assessed that 6,622 TCF of technically recoverable resources are confined in shales worldwide. **Table 1.1** shows the distribution of shale gas resources in the countries with the largest technically recoverable resources among the 32 countries considered in the study. These estimates are most likely very conservative because of the limited amount of data and the rudimentary understanding of trapping mechanisms in shales. Qualitatively, the data indicate that the shale business is expected to grow internationally.

In addition to these shale oil and gas resources, vast quantities of gas have been produced in tight gas reservoirs over the past 40 years. These reservoirs are typically defined as gas reservoirs that can only be produced at economic flow rates by stimulating the well by hydraulic fracture treatments or by the use of horizontal or multilateral wellbores. This implies that the vast majority of gas wells in tight gas fields need to be stimulated using a fracturing treatment. Although no standard definition exists, tight-gas reservoirs are usually defined as reservoirs with permeability ranging from 1 μ D to 0.1 mD; whereas shale reservoirs typically exhibit permeabilities ranging from 1 nD to 1 μ D.

The production from tight-gas reservoirs has stabilized over the past 10 years, and the E.I.A. predicted that the gas production from tight sands would remain stable over the next 40 years (Annual Energy Outlook 2011). In 2009, 6.6 TCF of gas were produced from tight gas reservoirs in the U.S., accounting for more than 30% of the domestic natural gas production. Historically, tight gas reservoirs have been the primary target for energized fracturing treatments, with numerous foam treatments implemented in the field in the 1980s (King 1985). Today, foam treatments are still routinely used in numerous legacy wells.

Fig. 1.2 displays the different categories of oil and gas resources as a pyramid of energy sources. At the top of the pyramid, conventional oil and gas resources are easily accessible but their volumes become scarcer. As we move toward the base of the pyramid, the volume of resources in place becomes significantly larger, but their production requires improved technologies at an increasing cost. As indicated in Fig. 1.2, energized treatments are primarily used in tight gas and coal bed methane reservoirs, but they are also becoming more frequent in shale gas reservoirs.

1.1.2 A Wide Range of Fracturing Fluids

Despite the predominance of slickwater and water-based gels, many fluid formulations exist and have been implemented in the field for several decades. The range of fracturing fluids includes slickwater, water-based polymer fluids, surfactant fluids, energized fluids, and non-aqueous fluids. The non-aqueous fluids refer primarily to methanol-containing fluids and liquefied-petroleum based fluids. In this dissertation, *water-based fluids* refer to any single-phase, incompressible, water-based fluids (such as slick-water, linear gels, and cross-linked gels), and *energized fluids* refer to any fluids containing at least one compressible, sometimes soluble, gas phase. Energized fluids can be either single-phase, such as CO₂, N₂, and liquefied petroleum gas (LPG), or multi-phase, such as foams. For foams, the continuous external phase can be a water-based, an oil-based, or a visco-elastic surfactant formulation, and the discontinuous internal phase is typically CO₂ or N₂. The reader may refer to Dantas *et al.* (2005) for a thorough review of conventional fracturing fluids, and to the summary compiled by Gupta (2011) for a more exhaustive list of unconventional fracturing fluid candidates. The main motivation behind having a wide range of fracturing fluids is to cope with different rock formations, reservoir fluids, pumping schedules, and horsepower requirements.

The speed at which unconventional resources have been developing has led some fracturing designers to use a copy and paste approach, namely using slickwater or hybrid fractures (slickwater pad followed by a gelled fluid) in a systematic manner, irrespective of the reservoir properties. However, shales vary widely in mineralogy, total organic content, and stress state even within a small aerial extent. Two shales are not alike, and the same applies to tight gas sands. Therefore, a single completion strategy is not expected to be optimum for all wells. The estimated ultimate recovery in these plays

varies from 15-35% (King, 2010) depending on the operator. Optimization of completion techniques can yield significantly higher returns on investment, and more efficient use of the natural resources. Careful analysis is required to replace a one-size-fits-all approach and achieve the next level of performance enhancement.

1.1.3 Limitations of Water-Based Fracturing Fluids

In many unconventional reservoirs, gas wells do not perform to their potential when using water-based fracturing treatments. The sub-optimal fracture productivity can be attributed to many factors, such as (1) low reservoir pressure, (2) limited fracture length, (3) poor proppant placement, and (4) low proppant conductivity. Numerous mechanisms have been identified as detrimental to fracture conductivity: (1) water blocking, (2) gel damage, (3) proppant settling, (4) proppant embedment, (5) fines migration, and (6) clay swelling. The extent of these mechanisms depends on the nature of the interactions between the reservoir rock and the injected fracturing fluid. In some reservoirs, the invasion of water severely damages the reservoir rock and alters fluid saturation, thereby impeding hydrocarbon production. In these reservoirs, operators may use energized or non-aqueous fracturing fluids to bolster gas production.

In addition to the issues identified above, operators may also consider alternatives to water treatments when access to the necessary water supply is unworkable. Massive slick-water fracturing campaigns require large quantities of water. In 2012, Chesapeake Energy claimed that the “hydraulic fracturing of a typical Chesapeake horizontal deep shale natural gas or oil well requires an average of 4.5 million gallons per well” (Chesapeake 2012). To put things in perspective, all shale gas wells drilled and completed in the United States in 2011 consumed on the order of 130 billion gallons of

water, which is equivalent to about 0.3 percent of the total U.S. freshwater consumption. In Texas, the amount of fresh water used in 2011 for drilling and fracturing amounted to almost 1 percent of all water withdrawals in the state (Nicot and Scanlon 2012). These large quantities of water may not be readily available either because the water supply is limited, or because the water quality is not compatible with the desired chemistry of the fracturing fluid additives (friction reducers, emulsifiers, gelling agent, etc.)

Additionally, a multitude of regulations at the federal, state, or local levels may limit water usage in certain areas. Under the current regulatory scheme, the legislative burden related to hydraulic fracturing in the U.S. is largely left to the individual states. In states with long oil and gas histories such as Texas and Louisiana, the ongoing legislation and oil field practices have generally been effective at enforcing environmental protection efforts. However, in states that are new to oil and gas exploration and production, such as Pennsylvania, New York, and West Virginia, numerous incidents have revealed the limits of the current regulations. At the federal level, governments can impose technical requirements on companies or request specific work programs and environmental impact assessments. At the local level, several cities decided in 2011 to unilaterally ban hydraulic fracturing or drilling activities in their jurisdiction, in response to recent public protests against shale gas operations in the Marcellus. This was the case in the cities of Buffalo, Philadelphia, New York City, and Pittsburgh. These bans have been regarded as largely symbolic, as they violate the state's right to regulate oil and gas operations. They nonetheless illustrate public concerns regarding water use in fracturing operations. They also resulted in a *de facto* suspension of fracturing activities in those municipalities, as the courts' decisions are still pending.

The opposition to hydraulic fracturing is even more pronounced outside the U.S. Several countries, such as France and Germany, recently mandated a moratorium suspending fracturing operations. The ongoing legislation is not specific regarding the type of fluid that is prohibited. Thus, it remains unclear if this opposition is primarily against the large water usage associated with hydraulic fracturing, or against the hydraulic fracturing process itself.

Finally, financial constraints have also prompted operators to consider using energized or non-aqueous fluids for fracturing. From a financial standpoint, the true cost of water management may be particularly expensive in some areas. To fully appreciate the life cycle costs of fluids used for hydraulic fracturing, one needs to examine the total costs of fluid acquisition, management and disposal (Watts 2013). The cost to acquire, transport, store, use, treat, recover, recycle and reuse, or dispose water represents a significant investment for energy producers and service companies. The cost of water disposal is strongly site-specific. In states like Texas and Oklahoma, flowback and produced water are typically re-injected in deep injection wells located near the oil field. This solution is usually regarded as very economical. This is not the case in states like Pennsylvania, where water injection in nearby aquifers is prohibited. The transport and disposal in storage facilities becomes very expensive.

Ultimately, the key factors influencing the decision of using energized fluids are: (1) possible productivity enhancement, (2) limited water supply, (3) restrictions on water use, and (4) financial incentives. These reasons have prompted the industry to consider waterless and foam fracturing treatments as viable alternatives to water-based fluids.

1.1.4 Historical Use of Energized Fluids

The use of energized fracturing fluids in the field goes back to the 70s, with a preference for CO₂ and N₂ foams. The vast majority of these treatments have been performed in North America, primarily in reservoirs that were depleted, under-saturated, and/or water-sensitive. Foam treatments were used first in the early 70s, before gaining some significant popularity in the 80s. The reader may refer to the work of Bleakley (1980), Wendorff and Ainley (1981), Grundman (1983), King (1985), Gabris and Taylor (1986), Ward (1986), and Harris (1992) for more details on the field implementation of foams.

Petroleum-based fluids have been used as fracturing fluids since the 70s (Hurst 1972; Smith 1973), sometimes with the addition of CO₂ (Hurst 1972). More recently, Taylor *et al.* (2006) and Tudor *et al.* (2009) described the properties of gelled LPG for fracturing applications. The first attempt to use liquid CO₂ as a sole fracturing fluid goes back to 1981 (Lillies and King 1982). Since then, liquid CO₂ has been primarily used in Canada (Sinal 1987; Tudor *et al.* 1994; Gupta and Bobier 1998; and Mazza 2001). Pure N₂ (with and without proppant) have been used mainly in shallow formations since the late 70s (Abel 1981; Freeman *et al.* 1983; and Gottschling *et al.* 1985). These references show that energized fluids have been used successfully in various reservoirs for the past forty years. More recent studies on the implementation of energized fluids in the field include the work of Burke *et al.* (2011) in the Montney shale in Canada, and the work of Granado *et al.* (2013) in the Pugliese basin in Italy.

1.1.5 Main Advantages of Energized Fluids

From a productivity standpoint, the primary advantages of energized fluids are: (1) limiting the amount of liquid placed in the rock matrix (thereby improving the fluid recovery), and (2) minimizing the contact between water and water-sensitive clays and fines. In under-saturated gas formations, the invasion (imbibition) of water from the fracturing fluid can be very detrimental to gas productivity, as any additional water remains trapped due to capillary retention. The increase in water saturation significantly reduces the relative permeability to gas, sometimes by orders of magnitude (Parekh and Sharma 2004; Mahadevan and Sharma 2005). This adverse phenomenon is referred to as water blocking or water trapping. When energized fluids are used, the presence of free gas and soluble gas, which comes out of solution as the pressure decreases, enhances flowback.

The base lithology – i.e. the mineral composition – of a given rock formation impacts the recovery process of water, gas, and oil. For example, oil-based fluids, LPG, CO₂, and high-quality foams are recommended in water-sensitive formations to prevent excessive fines migration and clay swelling. In many shales and clay-rich sands, proppant conductivity drops considerably in the presence of water because the rock-fluid interactions soften the rock and promote proppant embedment. It has been recognized for over 50 years by the drilling side of the industry that shales are sensitive to water exposure, but this fact is often ignored when designing fracturing treatments.

In addition to the potential productivity enhancement, using energized fluids aids in the reduction in water use by several means. The first is through the sheer substitution of water by CO₂, N₂, or any other non-aqueous fluids. For instance, a 70-quality foam contains only 30% of water on a volume basis; while non-aqueous fluids completely

eliminate the need for water. The second is through the reduction of the total volume of fluid needed to perform the same hydraulic fracturing job. In foams, an increase in the volume fraction of the energized component (foam quality) reduces the leak-off of the liquid phase. This leak-off reduction can be quite significant (Harris 1985; Harris 1987; Ribeiro and Sharma 2012). Consequently, this reduces the total volume of fluid required to generate a given fracture volume. The required volume of fluid to be pumped at the surface is further reduced because of fluid expansion down the wellbore and along the fracture. Energized fluids are compressible, and the volume expansion can be quite significant. For most practical applications, the injected volume of fluid can be reduced by 10 to 30% to generate the same volume of fluid downhole.

1.2 USE OF ENERGIZED FLUIDS IN THE FIELD (2011-2012)

This section provides a quick overview of the current use of energized fractures in North America³, using publicly available data. The objective is to identify the share of energized fluids used in fracturing operations, as well as the prime locations for these energized treatments. Since 2011, a large number of the fracturing treatments conducted in the U.S. have been reported on the FracFocus website (www.fracfocus.org), which is a joint project between the Ground Water Protection Council and the Interstate Oil and Gas Compact Commission. For each well, companies have been reporting basic well information (API well number, location, operator, depth, etc.) as well as the detailed fracturing fluid composition. In several states⁴, chemical disclosure legislations have made the reporting on FracFocus mandatory, whereas the reporting is voluntary in other

³ The authors would like to acknowledge PacWest Consulting Partners, and in particular Christopher Robart, for providing the database used in this section.

⁴ As of 2012, these states were Arizona, Arkansas, Colorado, Michigan, Montana, New Mexico, Pennsylvania, Texas, West Virginia, and Wyoming.

states. Using these publicly available data, PacWest Consulting Partners generated a comprehensive U.S. database and is developing a similar database for Canada. This U.S. database is used for the following analysis.

The U.S. database contains 32,175 well records since 2011. The database accounts for almost 70% of the fractures recorded in 2011, and 85% of the fractures recorded in 2012. As seen in **Fig. 1.3a**, a large share of the fracturing operations was performed in the Permian, Eagle Ford, DJ Basin, Marcellus, Barnett, and Bakken formations. The data tend to support the significant push toward liquid-rich shale formations made by many operating companies. As seen in **Fig. 1.3b**, slickwater, gelled, and hybrid fracturing fluids contribute to 97.1% of the total number of fracturing jobs. 609 energized fracturing treatments have been reported, which contributes to 2.4% of the U.S. fracturing treatments. Energized treatments were more than four times more common than acid treatments in the U.S. In Canada, energized fluids contribute to about 25 to 30% of the total number of fracturing jobs. The actual distribution is not included here because the database does not cover a sample size large enough to be significant. The indicated range is nonetheless consistent with estimates provided by several operating and service companies.

Fig. 1.4 shows the distribution of energized fracture records per U.S. plays. The predominant plays were the San Juan, Raton, Marcellus, DJ Basin, Cleveland, Piceance, Uinta, and Granite Wash basins. The remaining treatments were performed in the North Rockies (8), Wind River (6), Anadarko (5), Haynesville (5), Antrim (5), Big Horn (4), etc. The records indicate that energized treatments are still mostly performed in vertical legacy wells located in tight gas reservoirs. The San Juan basin witnessed 41% of the 609 energized treatments recorded in the U.S.; however, the main player in that basin,

ConocoPhillips, announced in March 2013 that the operations would slow down in that region. The database also indicates a significant increase of energized treatments in shales. In these reservoirs, energized treatments are used in multi-fractured horizontal wells. In particular, a few attempts were made in some of the major shale formations: Permian, Eagle Ford, Utica and Bakken shales. This trend is expected to grow in the years to come, especially in places like the Utica shale where the water supply is limited, and/or the cost of water handling and water disposal is prohibitive. This expected growth constitutes a major business opportunity for gas providers. Many of them (Air Liquide, Air Products, Linde, Praxair, etc.) are anticipating major investments in the oil and gas business in the next ten years.

Fig. 1.4b shows the distribution of energized fracture records per operator. In 2012, ConocoPhillips, XTO/ExxonMobil, Pioneer Energy Resources, Range Resources, Mewbourne, WPX, and Noble Energy were the dominant players in the U.S. energized fracturing business. The remaining operations were shared between numerous companies, including Kerr-McGee/Anadarko (17), Patara (13), Black Raven (10), Encana (10), Energen (10), BP (6), Devon (6), Marathon (6), Apache (4), Chevron (4), etc. Further analysis of the data shows that each operator had a preferential fluid formulation that was consistently used in a given reservoir. For instance, some companies systematically used linear gels while others systematically used cross-linked gels in the same basin. Similarly, some companies systematically preferred CO₂ while others preferred N₂ for the internal phase.

The motivations behind a particular choice of fracturing fluid are not transparent. Rather than a careful optimization of the energized fluid system, the decision often relies primarily on company policies. **Fig. 1.5** shows the type of fracturing fluids used by Noble

Energy, Kerr-McGee/Anadarko, and Black Raven in a similar region of the DJ Basin in 2011 and 2012. Both the percentage and the number of treatments performed in that region are reported. **Fig. 1.6** shows the fluid composition on a mass basis of the different energized fluids used by each operator. For each energized design, the fluid composition remained virtually unchanged from one well to another. Noble Energy used 36%-CO₂ (on a volume basis) cross-linked foam; Black Raven used slightly higher-quality CO₂ cross-linked foam; and Kerr McGee implemented two N₂ designs. Half of the energized jobs were performed using 60%-N₂ cross-linked foam, while the other jobs barely used any nitrogen. It should be noted that the fluid composition indicated in Fig. 1.6 is given on a mass basis, while foam qualities are typically expressed on a volume basis.

This field example supports the observation that operators rarely optimize the energized treatment design during the development stage. There are several reasons explaining this tendency. First, the capital expenditures and operational costs are higher when using energized fluids, so many operators may be reluctant to speculate on a potential productivity enhancement. Second, field implementation is more challenging for energized treatments as compared to routine water-based treatments. In particular, many fracturing crews are not very experienced with the methodologies and the proper safety requirements for the use of gases. Third, the well production depends on many factors that are independent from the choice of fracturing fluid, and these factors are not easily measurable. Therefore, the sample size is often not large enough to draw meaningful conclusions regarding fluid selection.

1.3 OBJECTIVES AND PROPOSED METHODOLOGY

The primary objective of this work is to improve the design of energized fracturing treatments. If the qualitative pros and cons of the different fracturing fluids are known, little is known regarding the quantitative benefits of energizing the fracturing fluid. This work uses a modeling approach to answer some of these questions. To achieve this objective, we have built the first 3D compositional model for hydraulic fracturing. The specific objectives of this research may be further broken down as follows:

- i. Formulate a well-posed mathematical problem that governs the propagation of a planar fracture initiated by an energized fluid. The model should allow fracture height growth based on stress intensity factor calculations.
- ii. Develop the first 3D, compositional, non-isothermal, fracturing simulator. The simulator intends to capture the thermal and compositional changes occurring in the fracturing fluid, in both vertical and horizontal wells.
- iii. Implement a well productivity model communicating with the fracturing model to assess well performance.
- iv. Identify through simulations the most critical parameters in the design of an energized fracturing treatment. Based on the subsequent sensitivity study, design recommendations will be provided for different types of reservoirs in lieu of a costly field trial-and-error approach.
- v. Identify reservoir parameters that are critical for fluid selection, and identify reservoirs that are prime candidates for using energized fluids.

1.4 STRUCTURE OF THE DISSERTATION

The research discussed here forms the basis for creating the first 3D compositional model for energized fracture treatments. The research is divided into the following chapters:

Chapter 2 reviews past fracture models. The theory and assumptions of each model are included. This chapter presents the main limitations of existing fracture models, and it places an emphasis on what can and cannot be included in the new model.

Chapter 3 presents the theories and equations behind the new fracture model. For the first time in a 3D fracturing model, the fundamental equations are derived for a multi-phase, compressible, non-isothermal, fluid system. The fracture mechanics aspect of the problem is based on the work of past authors.

Chapter 4 introduces the finite-element formulation of the fracture problem. The derivations show how to obtain a weak formulation of the problem starting from the strong formulation of the problem defined in Chapter 3. Chapter 4 also covers some of the computational aspects that are essential when developing the fracturing code.

Chapter 5 presents the wellbore and fracture productivity models that are communicating with the fracture model. The wellbore model follows the work of Hasan and Kabir (2002) for vertical, deviated, and horizontal wellbores. The two-phase fracture productivity model extends the model of Friehauf, Suri, and Sharma (2010) to the case of a reservoir with multiple vertical layers. This chapter reviews the assumptions, theory, and equations formulated by Friehauf, Suri, and Sharma (2010).

Chapter 6 is a compilation of example runs to show the main features of the simulator. Notably, this chapter describes the inputs and outputs of the simulator. The new model is also compared to prior models for validation purposes.

Chapter 7 reviews the phase behavior, rheology, and leak-off behavior of the energized fluids presented in this work. These fluid properties are critical inputs to the simulator. In particular, Chapter 7 addresses the issue of estimating multi-phase leak-off coefficients from laboratory experiments and field measurements.

Chapter 8 is a sensitivity study on fracturing parameters. This chapter starts with an example of fluid selection in a representative tight gas reservoir. Then, critical fluid properties for fluid selection are identified, and design recommendations are provided for different types of reservoirs. Finally, this chapter identifies the most critical reservoir properties influencing fluid selection.

Chapter 9 summarizes the conclusions stemming from the dissertation and outlines recommendations for future work.

Table 1.1: Estimated shale gas technically recoverable from selected basins in several countries, compared to proved reserves reported in 2009 (adapted from E.I.A. 2011).

Countries	Proved Natural Gas Reserves* (TCF)	Technically Recoverable Shale Gas Resources (TCF)
China	107	1275
United States	273	862
Argentina	13	774
Mexico	12	681
Australia	110	396
Canada	62	388
Libya	55	290
Algeria	159	187
Brazil	13	180
Total above areas	804	5043

**Proved gas reserves: Oil and Gas Journal, Dec. 6, 2010, p46-49.*

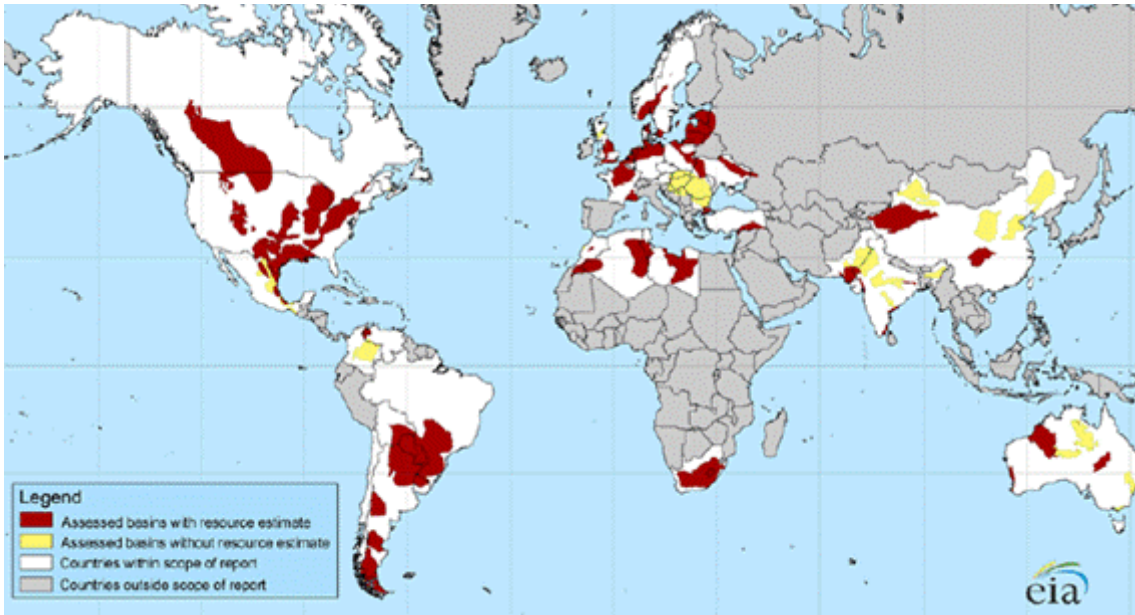


Figure 1.1: Map of 48 major shale gas basins located in 32 countries (from E.I.A. 2011).

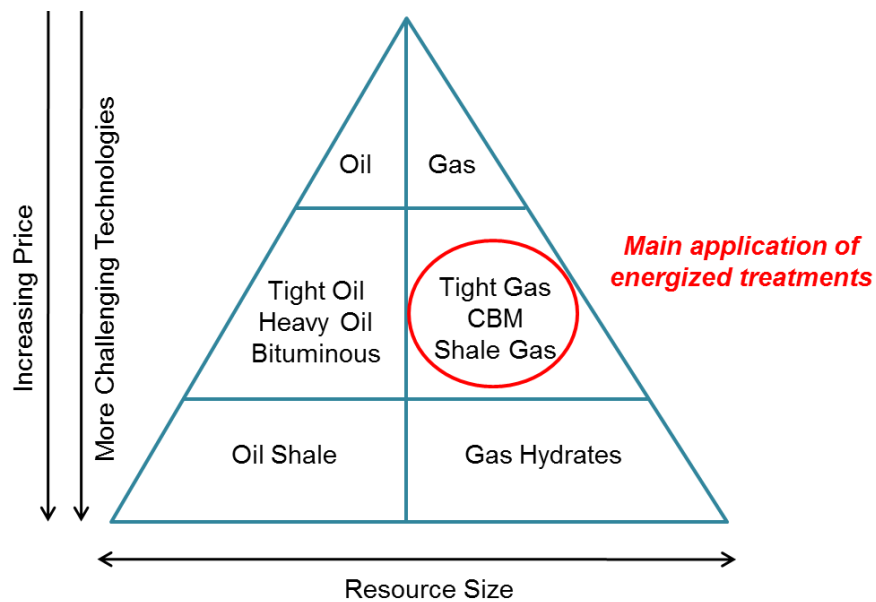


Figure 1.2: Pyramid of oil and gas resources. Today, energized treatments are mostly used in tight gas and coal bed methane reservoirs, and their use is becoming more frequent in shale gas reservoirs (adapted from Sonnenberg 2010).

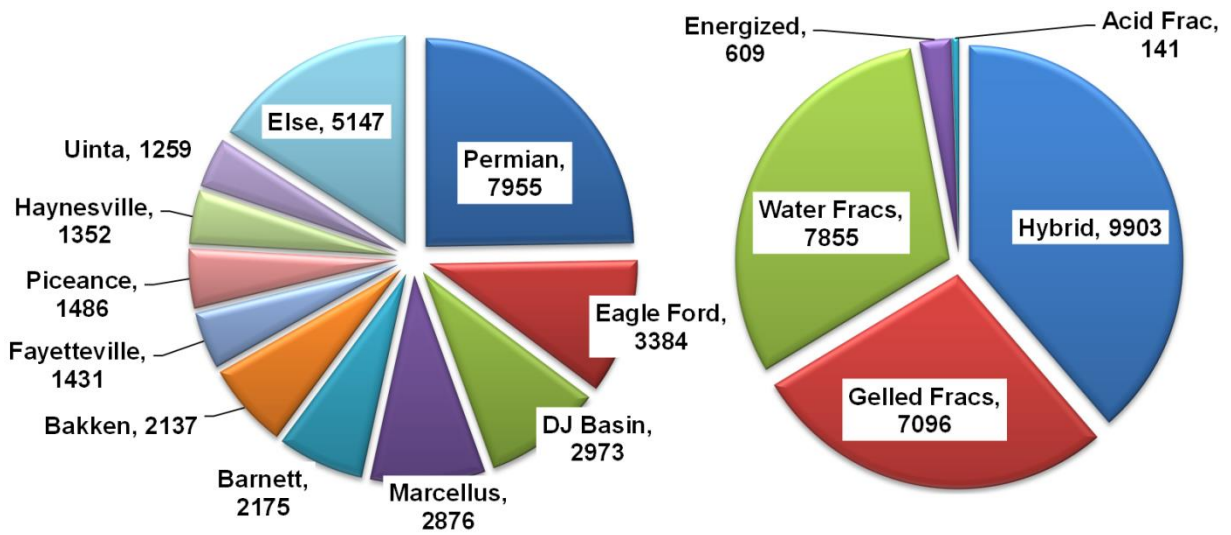


Figure 1.3: Fracturing operations in the U.S. in 2011-2012: (a) number of records per U.S. basin and (b) types of fracturing fluid (based on public data available on www.fracfocus.org).

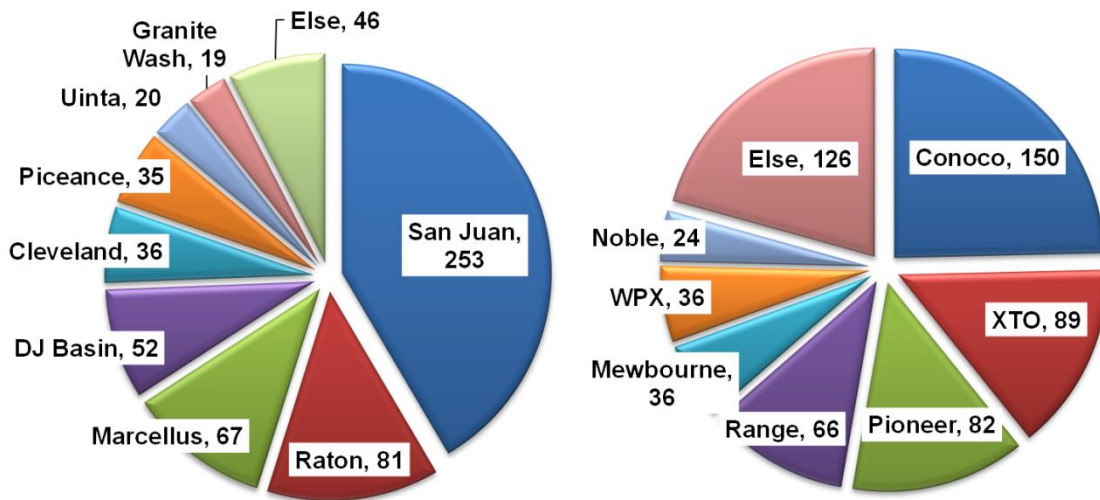


Figure 1.4: Energized fracturing operations in the U.S. in 2011-2012: (a) number of records per U.S. basin and (b) number of records per operator (based on public data available on www.fracfocus.org).

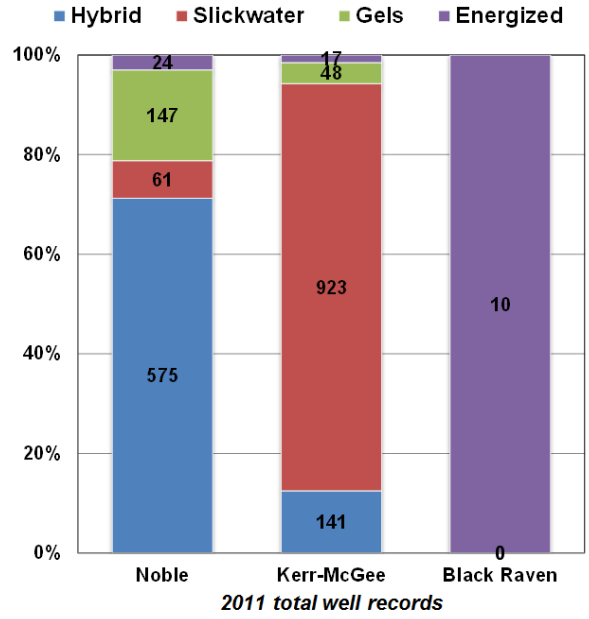


Figure 1.5: Type of fluids used per operator in a selected area of the DJ Basin (based on public data available on www.fracfocus.org).

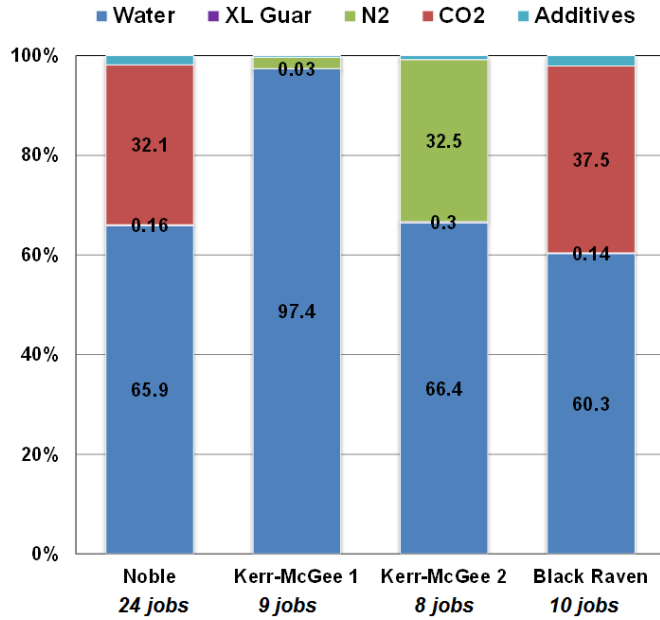


Figure 1.6: Fluid composition (on a mass basis) for each energized treatment design implemented in a selected region of the DJ Basin (based on public data available on www.fracfocus.org).

REFERENCES

- Abel, J.C. 1981. Application of Nitrogen Fracturing in the Ohio Shale. Paper SPE 10378 presented at the SPE Eastern Regional Meeting, Columbus, Ohio, 4-6 November.
- Bleakley, W.B. 1980. Mitchell Energy Foam Fracs Tight Gas Zones. *Pet. Eng. Intern.* December 1980: 24-28.
- Burke, L.H., Nevison, G.W., and Peters W.E. 2011. Improved Unconventional Gas Recovery With Energized Fracturing Fluids: Montney Example. Paper SPE 149344 presented at the SPE Eastern Regional Meeting, Columbus, Ohio, 17-19 August.
- Chesapeake, water usage website, 2012. Available at <http://www.hydraulicfracturing.com/Water-Usage/Pages/Information.aspx>.
- Dantas, T.N., Santanna, V.C., Neto, A.A. and Moura M.C. 2005. Hydraulic Gel Fracturing. *J. Dispersion Sci. Technol.* **26**: 1-4.
- Freeman, E.R., Abel, J.C., Kim, C.M., and Heinrich, C. 1983. A Stimulation Technique Using Only Nitrogen. *J. Pet Tech* **35**(12): 2165-2174. SPE 10129-PA.
- Friehauf, K.E., Suri, A., and Sharma, M.M. 2010. A Simple and Accurate Model for Well Productivity for Hydraulically Fractured Wells. *SPE Prod & Oper* **25**(4): 453-460. SPE 119264-PA.
- Gabris S. and Taylor J., 1986. The Utility of CO₂ as an Energizing Component for Fracturing Fluids. *SPE Prod Eng* **1**(5): 351-358. SPE 13794-PA.
- Gottschling, J.C., Royce, T.N., and Shuck, L.Z. 1985. Nitrogen Gas and Sand: A New Technique for Stimulation of Devonian Shale. *J. Pet Tech* **37**(5): 901-907. SPE 12313-PA.
- Granado, L.E., Garritano R., Lorefice, R., and Ceccarelli, R.L. 2013. Revitalizing Mature Gas Field Using Energized Fracturing Technology In South Italy. Paper SPE 164649 presented at the SPE North Africa Technical Conference and Exhibition, Cairo, Egypt, 15-17 April.
- Grundman, S.R. 1983. Foam Stimulation. *J. Pet Tech* **35**(3): 597-602. SPE 9754-PA.
- Gupta, D.V.S. and Bobier, D.M. 1998. The History and Success of Liquid CO₂ and CO₂/N₂ Fracturing System. Paper SPE 40016 presented at the SPE Gas Technology Symposium, Calgary, Canada, 15-18 March.
- Gupta, D.V.S. 2011. Unconventional Fracturing Fluids: What, Where and Why. Technical Workshops for the Hydraulic Fracturing Study, U.S. E.P.A., presented at Arlington, Virginia, February 2011.
- Harris, P.C. 1985. Dynamic Fluid-Loss Characteristics of Nitrogen Foam Fracturing Fluids. *J. Pet Tech* **37**(11): 1847-1852. SPE 11065-PA.

- Harris, P.C. 1987. Dynamic Fluid-Loss Characteristics of CO₂-Foam Fracturing Fluids. *SPE Prod Eng* **2**(2): 89-94. SPE 13180-PA.
- Harris, P.C. 1992. Application of Foam Fluids To Minimize Damage During Fracturing. Paper SPE 22394 presented at the International Meeting on Petroleum Engineering, Beijing, China, 24-27 March.
- Hurst, R.E. 1972. Use of Liquified Gases as Fracture Fluids for Dry Gas Reservoirs. Paper SPE 4116 presented at the Fall Meeting of the Society of Petroleum Engineers of AIME, San Antonio, Texas, 8-11 October.
- King, G.E. 1985. Foam and Nitrified Fluid Treatments-Stimulation Techniques and More. Paper SPE 14477 based on a speech presented as a Distinguished Lecture during the 1985-1986 season.
- King, G.E. 2010. Thirty Years of Gas Shale Fracturing: What Have We Learned? Paper SPE 133456 presented at the SPE Annual Technical Conference and Exhibition, Florence, Italy, 19-22 September.
- Lillies, A.T. and King S.R. 1982. Sand Fracturing with Liquid Carbon Dioxide. Paper SPE 11341 presented at the SPE Production Technology Symposium, Hobbs, New Mexico, 8-9 November.
- Mahadevan, J. and Sharma, M.M. 2005. Factors Affecting Cleanup of Water Blocks: A Laboratory Investigation. *SPE J.* **10**(3): 238-246. SPE 103229-PA.
- Mazza, R. 2001. Liquid-Free CO₂/Sand Stimulations: An Overlooked Technology – Production Update. Paper SPE 72383 presented at the SPE Eastern Regional Meeting, Canton, Ohio, 17-19 October.
- Nicot, J.P. and Scanlon, B.R. 2012. Water Use for Shale-Gas Production in Texas, U.S. *Environ. Sci. Technol.* **46**: 3580-3586.
- PacWest FracDB, Product Overview. Available at www.pacwestcp.com/research/fracdb
- Parekh, B. and Sharma, M.M. 2004. Cleanup of Water Blocks in Depleted Low-Permeability Reservoirs. Paper SPE 89837 presented at the SPE Annual Technical Conference and Exhibition, Houston, Texas, 26–29 September.
- Ribeiro, L.H. and Sharma, M.M.. 2012. Multi-Phase Fluid-Loss Properties and Return Permeability of Energized Fracturing Fluids. *SPE Prod & Oper* **27**(3): 265-277. SPE 139622-PA.
- Sinal, M.L. and Lancaster, G. 1987. Liquid CO₂ Fracturing: Advantages And Limitations. *J Cdn. Pet Tech* **26**(5): 26-30.
- Smith, C.F. 1973. Gas Well Fracturing Using Gelled Non-Aqueous Fluids. Paper SPE 4678 presented at the Fall Meeting of the Society of Petroleum Engineers of AIME, Las Vegas, Nevada, 1-3 October 1973.

- Sonnenberg, S.A. 2010. Core Analysis and Unconventional Reservoirs, available online at <http://www.tight-oil-shale-plays.com/media/downloads/inline/steve-sonnenberg-colorado-school-of-mines.1295453329.pdf>
- U.S. Energy Information Administration 2011. Annual Energy Outlook 2011 with projections to 2035. DOE/EIA-0383.
- U.S. Energy Information Administration 2013. Annual Energy Outlook, Early Release 2013. DOE/EIA-0383ER.
- Taylor, R.S., Lestz, R.S., Wilson, L., Funkhouser, G.P., Watkins, H., and Attaway, D. 2006. Liquid Petroleum Gas Fracturing Fluids for Unconventional Gas Reservoirs. Paper 2006-169 presented at the Canadian International Petroleum Conference, Calgary, Canada, June 13-15.
- Tudor, R., Vozniak, C., Peters, W., and Banks, M.-L. 1994. Technical Advances In Liquid CO₂ Fracturing. Paper 94-36 presented at the Annual Technical Meeting, Calgary, Canada, June 12-15.
- Tudor, E.H., Nevison, G.W., Allen, S., Pike, B. 2009. 100% Gelled LPG Fracturing Process: An Alternative to Conventional Water-Based Fracturing Techniques. Paper SPE 124495 presented at the SPE Eastern Regional Meeting, Charleston, West Virginia, 23-25 September.
- Ward, V.L. 1986. N₂ and CO₂ in the Oil Field: Stimulation and Completion Applications. *SPE Prod Eng* 1(4): 275-278. SPE 12594-PA.
- Watts, R. 2013. A Day in the Life of a Barrel of Water. Transcript of the presentation made at the 4th Annual AIPG Symposium, Canton, Ohio, 10-12 April.
- Wendorff, C.L. and Ainley, B.R., 1981. Massive Hydraulic Fracturing of High-Temperature Wells with Stable Frac Foams. Paper SPE 10257 presented at the Fall Technical Conference and Exhibition, San Antonio, Texas, 5-7 October.

The format used for references in this chapter and the subsequent ones is recommended by The Society of Petroleum Engineers (2013).

Chapter 2: Review of Existing Fracture Models

The objective of this chapter is to understand the main advantages and limitations of some of the most popular fracture models, by offering a review of past models¹. In particular, this chapter emphasizes the differences in the treatment of the fracture opening equation.

The work we propose is mostly influenced by the work of two research groups. The first group developed one of the first 3D planar fracturing codes in the early 1990s. This group included Drs. Yew, Gu, Carey, and Ouyang, who all worked in the Engineering Mechanics department at the University of Texas at Austin at that time. The second main contribution is the work done by Drs. Friehauf and Sharma at the University of Texas at Austin. For the first time, these authors incorporated compositional and thermal effects into a fracturing model.

The work of these two research groups has been instrumental in the pursuit of this study. The reader is encouraged to refer to some of their publications for more information (Gu 1987; Ouyang 1994; Yew 1997; Friehauf 2009; Friehauf and Sharma 2009). Many of the ideas expressed in this study were first discussed by these authors. The model we propose may be regarded as an extension of their work.

2.1 CHALLENGES IN FRACTURE MODELING

The modeling of a pressure-driven fracture propagating in a porous, elastic medium is a very complex physical process. Even in its most basic form, it consists of

¹ The reader may refer to Adachi *et al.* (2007) for a more exhaustive review of classical fracture models.

solving a system of non-linear, time-dependent, moving-boundary, partial differential equations. These coupled equations govern: the mechanical deformation of the rock, the conservation of mass, and the fluid flow within the fracture. A propagation criterion determines the shape of the fracture.

The hydraulic fracturing problem is further complicated by the presence of heterogeneities in the Earth, local variations in *in-situ* stresses, and poorly defined rock behavior and failure mechanisms. To make things more complex, model validation and calibration are hindered by the limited access to direct experimental measurements. In practice, very little is known regarding downhole fracture dimensions and pre-existing reservoir heterogeneities. Often, the only calibration tool is the surface pressure response. Micro-seismic data can now supplement well pressure data to estimate fracture dimensions. Consequently, major assumptions are required to model hydraulic fracturing. Many models have been derived, based on different assumptions that emphasize the relative importance of different aspects of the fracture propagation process.

2.2 REVIEW OF CLASSICAL 2D FRACTURE MODELS

2.2.1 Sneddon's Model Formulation

The first notable fracture model was proposed by Sneddon (1946) and Sneddon and Elliot (1946). Using linear elastic theory, they developed the first solutions for the stress field and pressure associated with static pressurized cracks. The basic assumptions are that the fracture has a circular shape and is subject to a constant fluid pressure (**Fig. 2.1**). Under these assumptions, the width at a given distance r_c for a uniformly pressurized crack of radius R is given by:

$$w(r_c, t) = \frac{8(1-\nu^2)R(t)}{\pi E} \Delta P_{net}(t) \sqrt{1 - \left(\frac{r_c}{R(t)}\right)^2} \quad (2.1)$$

In Eq. 2.1, ΔP_{net} is the net pressure defined as the fluid pressure P minus the external stress σ ; ν is Poisson's ratio; and E is Young's modulus. Although the pressure remains uniform across the crack, its value evolves over time as the fracture propagates. This value is obtained from the requirement that the energy needed to create a given surface area must equal the work done by the fluid pressure to open the corresponding additional width. Fluid pressure is thus a function of both the radius of the fracture and the specific surface energy.

2.2.2 PKN and KGD Models

A classic method in fracture modeling is the two-dimensional (2D), constant-height, PKN model, first derived by Perkins and Kern (1961) and then extended by Nordgren (1972), as well as the KGD model first proposed by Khristianovich and Zheltov (1955) and later extended by Geertsma and de Klerk (1969). Variations of the PKN and KGD models were used routinely for treatment designs as recently as the late 1990s. They are still used today for validation purposes and for providing valuable insight in the understanding of the fracture propagation process.

These 2D models differ primarily because they assume plane strain in the vertical and horizontal directions, respectively. In essence, the difference between the models is that Perkins and Kern (1961) focused on the fluid flow problem but used simplified assumptions for the treatment of the fracture mechanics problem; while Khristianovich and Zheltov (1955) focused on the fracture mechanics problem and made simplified assumptions regarding fluid flow.

Figs. 2.2 and **2.3** show the shape of a PKN fracture and of a KGD fracture, respectively. The difference in the fracture shape results from assumptions used to convert a 3D fracture mechanics problem to a 2D plane strain model. In the PKN formulation, each vertical cross section acts independently, which is equivalent to assuming that the pressure at any section is affected primarily by fracture height rather than fracture length. This behavior is a direct consequence of the vertical plane strain assumption. Alternatively, each horizontal cross section acts independently in the KGD formulation. The pressure at any section is primarily affected by fracture length rather than fracture height, and the tip region plays a more important role in the KGD formulation. This behavior is a direct consequence of the horizontal plane strain assumption. From a practical standpoint, the PKN formulation has generally been regarded as best-suited for long, well-constrained fractures, while the KGD formulation has generally been regarded as best-suited for cases where the fracture height exceeds the fracture length.

Several methods have been used to solve the PKN and the KGD fracture problems. Using simplified assumptions, these problems can be solved analytically. The analytical solutions provide a better understanding of different regimes of fracture propagation. Today, dynamic fracture propagation problems are typically solved numerically. As shown by Sneddon (1946) and Nordgren (1972), the width of a crack in an elastic body is directly proportional to the difference between the fluid pressure and the applied stress. If the strain is confined to the y - z plane, the width is given by:

$$w(x, y, t) = \frac{1-\nu}{G} \sqrt{h^2 - 4y^2} \Delta P_{net}(x, t) \quad \text{for } |y| < \frac{h}{2} \quad (2.2)$$

In Eq. 2.2, h is the constant fracture height; ν is Poisson's ratio; G is the shear modulus; x is the position along the fracture length; and y is the position along the fracture height. Eq. 2.2 provides an analytic expression that relates the local fracture width to the effective stress applied at that particular point. This equation has been used in most of the 2D, constant-height, fracturing models, and most notably in the PKN and KGD fracture models. This formulation is particularly useful from a numerical standpoint because it can be used independently at each nodal point.

The change in fluid pressure is then estimated from the continuity equation and the fluid flow equation. 2D models assume one-dimensional (1D) fluid flow along the fracture length. The 1D fluid flow assumption prohibits fluid flow in the vertical direction. As a result, the fluid pressure is only a function of fracture length (as seen in Eq. 2.2).

2.3 REVIEW OF THE FIRST 2D COMPOSITIONAL FRACTURE MODEL

Friehauf (2009) and Friehauf and Sharma (2009) have recently developed the first compositional 2D hydraulic fracturing simulator, originally named *EFRAC*. In this paper, their model is referred to as *EFRAC-2D* to distinguish it from our new model (*EFRAC-3D*). Their model incorporated, for the first time, thermal and compositional effects in addition to fracture mechanics and proppant transport in the fracture.

Their treatment of the mechanical model is very similar to the PKN model developed by Perkins and Kern (1961), and Nordgren (1972). The only difference in their fracture mechanics formulation is that the net pressure is a function of both fracture length and height (as seen in Eq. 2.3). This behavior is a direct consequence of the 2D fluid flow assumption they used.

$$w(x, y, t) = \frac{1-\nu}{G} \sqrt{h^2 - 4y^2} [\Delta P_{net}(x, t)]_y \quad \text{for } |y| < \frac{h}{2} \quad (2.3)$$

In Eq. 2.3, the net pressure is averaged vertically (y direction). The cross-section average confers a pseudo 1D shape on the pressure profile. This is the only difference with the fracture opening equation given in Eq. 2.2.

The main contribution of the work of Frieauf and Sharma (2009) concerns the treatment of the fluid flow problem. Their model was the first fracturing model to consider:

- Multi-phase, multi-component, compressible fluid flow,
- Changes in the fracturing fluid composition,
- Changes in fluid temperature along the fracture,
- An equation of state to evaluate phase behavior, and
- Phase-dependent leak-off into the rock matrix.

The framework proposed by these authors was instrumental in the development of the new model.

2.4 REVIEW OF PSEUDO 3D FRACTURE MODELS

Following the development of the constant-height PKN and KGD models, several pseudo 3D (P3D) and 3D fracturing models have been developed to account for fracture height growth. P3D models attempt to capture the physical behavior of a planar 3D fracture at minimal computational cost. A non-exhaustive list of P3D models includes the ones of Advani and Lee (1982), Palmer and Carroll (1983), Settari and Cleary (1984), and Weng (1992). These models have been regarded as extensions of the work of Simonson *et*

al. (1978), who developed the first solutions for fracture height growth in a three-layer reservoir.

Constant-height 2D models do not consider the influence of the bounding layers and fracture propagation is independent of the vertical stress profile, which is contradictory to field evidence. Height growth is allowed in P3D models, as seen in **Fig. 2.4**. P3D models ascertain a certain form of the fracture and do not solve the complete elasticity problem in a rigorous 3D manner. Using the rock mechanic assumptions used in the PKN or KGD model, many different authors have attempted to incorporate a more accurate 2D fluid flow representation.

There are two categories of P3D: lumped-based and cell-based models. In the lumped-based approach, the fracture geometry consists of two-half ellipses joined in their centers in the fracture length direction (**Fig. 2.5**). The fracture length, top half-ellipse, and bottom half-ellipse are calculated at each time step. In the cell-based approach, the fracture is sub-divided into a series of PKN-like cells that are perpendicular to the axis of fracture propagation (**Fig. 2.6**). The height of each cell is calculated individually. This method is consistent with the basic assumption used in the PKN model, namely that the fluid pressure at any section is affected primarily by fracture height rather than length. For each vertical cell, the reservoir elastic properties are averaged over all layers covering the cell. In these two approaches, the dominant direction of fracture propagation is prescribed. For instance, the fracture is not allowed to stop growing in the target layer while continuing to propagate in the upper layer where the *in-situ* stress is lower.

2D fracture models reduce the fluid flow problem to a 1D problem. Several models assume 1D fluid flow along the fracture length direction while others assume

curved 1D fluid flow along pre-determined streamlines. The streamlines extend from the perforated interval to the edges of the ellipse formed by the fracture. The oversimplification of the fluid flow problem may result in exaggerated fracture height growth and poor fracture containment. Several authors (Weng 1992; Economides and Nolte 2000) have identified discrepancies in predicted fracture geometry. **Fig. 2.7**, borrowed from Weng (1992), shows an example of exaggerated fracture height growth predicted by a P3D model, as compared to a 3D model. To remediate this problem, Weng (1992) introduced the effect of 2D fluid flow into a conventional P3D model by replacing the 1D vertical fluid flow with an approximate 2D fluid flow (**Fig. 2.8**). The basic assumption is that the approximate flow field depends on the height of the PKN-like cells.

2.5 REVIEW OF 3D PLANAR FRACTURE MODELS

Another family of models encompasses 3D planar models, which essentially solve the 3D elasticity problem with a planar fracture geometry. This assumption prohibits fracture propagation out of the prescribed plane. In this sense, the term “three-dimensional” does not refer to a full three-dimensional problem, in which the fracture can move freely in three dimensions. Although a misnomer, this terminology is commonly used in fracture modeling. The planar assumption is reasonable in most cases since the fracture propagates in the direction perpendicular to the minimum horizontal stress.

In essence, 3D fracture mechanics models are 3D elasticity problems with the restriction that the fracture propagates in a given plane. Assuming an isotropic, homogeneous, elastic medium, the Navier-Cauchy problem reduces to the tensile mode-I fracture opening equation. The fracture opening equation is a boundary integral equation

that relates the fracture width to the net pressure. A boundary integral formulation is required since a local stress applied at a given location deforms the entire surface of the elastic body. The boundary integral was derived independently by several authors, including Kossecka (1971), Bui (1977), and Weaver (1977):

$$-P(x, y) + \sigma_{h \min}(x, y) = \frac{G}{4\pi(1-\nu)} \int_{\Omega} \left[\frac{\partial}{\partial x} \left(\frac{1}{r} \right) \frac{\partial w(x, y)}{\partial x'} + \frac{\partial}{\partial y} \left(\frac{1}{r} \right) \frac{\partial w(x, y)}{\partial y'} \right] d\Omega \quad (2.4)$$

where $r = \sqrt{(x' - x)^2 + (y' - y)^2}$

Eq. 2.4 is singular and its resolution requires complex numerical methods. Several approaches have been used, and the reader is referred to the pioneering work of Clifton and Abou-Sayed (1981), Cleary *et al.* (1983), Abou-Sayed *et al.* (1984), and the work of Gu (1987), Ouyang (1994) and Yew (1997).

These models solve the fundamental 3D elasticity problem, thereby allowing fracture height growth and fracture propagation in multiple layers. Essentially, the boundary of the planar fracture moves outward as the fluid provides enough energy to open the crack locally. Different fracture propagation criteria exist, but the process is usually described using linear elastic theory. A popular fracture propagation criterion was derived by Mastrojannis *et al.* (1979). In their model, the movement of the fracture front in both the vertical and horizontal directions is based on stress intensity factor calculations.

Both the width and shape of the fracture vary with time and are highly dependent on the fluid pressure distribution, which is obtained from the pressure gradients caused by fluid flow inside the fracture. Fluid flow is assumed to be two-dimensional, which makes the fluid flow problem highly sensitive to fracture width and geometry. Thus, the fracture

mechanics and the fluid flow problems are tightly coupled. Chapter 4 provides an example of algorithm used to solve this convoluted problem. For more details regarding the coupling between fracture geometry and fluid flow problems, the reader may refer to Yew (1997), Economides and Nolte (2000), and Adachi *et al.* (2007).

The solution of the 3D fracture problem is firmly related to the nature of the meshing and interpolation techniques. Since the main direction of fracture propagation is not prescribed, a dynamic unstructured grid is typically used to represent the fracture face. **Fig. 2.9** shows an example of a dynamic unstructured mesh (generated in this work). The fracture is constituted of inner triangular and outer quadrilateral elements. The quadrilateral elements are used to perform the stress-intensity calculations and apply the propagation criterion. Hence, the failure criterion remains intrinsically grid-dependent (Economides and Nolte 2000).

2.6 REVIEW OF GENERAL 3D (NON-PLANAR) MODELS

For the sake of completeness, this section reviews 3D non-planar, also referred to as general 3D (G3D), fracture models. G3D models make no assumptions regarding the orientation and the shape of the fracture. Fractures may deviate from a planar geometry for various reasons. The deviation can appear locally near the perforations, as this is observed in horizontal wells when the well is not aligned with the direction of the minimum horizontal stress. It is also observed in deviated wells when the set of perforations forms an angle with the fracture plane. Non-planar fracture deviation can also appear on a larger scale. The deviation can be abrupt when the induced fracture reaches large reservoir heterogeneities such as faults, bedding planes, and natural fractures. Alternatively, a smooth deviation from the initial plane of propagation may

occur if there is a large *in-situ* stress reorientation. The fracture alignment is then governed by the local orientation of the *in-situ* stress field.

G3D models are the only models capable of investigating these complex fracture propagation patterns. G3D solve the full 3D elasticity problem without prescribing any propagation plane. Contrary to the planar formulation (Eq. 2.4), the non-planar equation is not symmetric along a prescribed plane (as seen in **Fig. 2.10**). The fracture opening equation is a boundary integral equation that relates the fracture width to the net pressure (Spence and Sharp 1985; Pierce and Siebrits 2001).

$$-P(x, y) + \sigma_{n\min}(x, y) = \int_S C(x, y; \xi, \eta) w(\xi, \eta) d\xi d\eta \quad (2.5)$$

In Eq. 2.5, S is the surface of the 3D fracture; C is the non-local kernel function that contains all the information regarding the layered elastic medium; x and y are the locations in a fixed referential; and ξ and η are the locations in the local (curved) referential. The new set of dummy variables (ξ, η) is required to account for local misalignment. Eq. 2.5 is a more general formulation of the 3D elastic problem that encompasses the planar case. With a planar fracture under mode-I loading, the kernel C reduces to the kernel of the integral equation shown in Eq. 2.4. The general expression of the kernel C is not of particular interest for this study.

The resolution of Eq. 2.5 is computationally intensive. The mathematicians Spence and Sharp (1985) proposed an alternative solution to the fracture mechanics problem based on a self-similarity assumption. Their work has constituted the layout of numerous numerical studies on fracturing propagation. A computational technique based

on a boundary element formulation of the elasticity problem has been proposed by Rungamornmat *et al.* (2004), and more recently by Alekseenko *et al.* (2013).

Despite the enhanced capabilities of G3D models, their practical use remains very limited. G3D models are particularly applicable in research environments, for which they are used to closely study fracture initiation and near-wellbore complexities. One example of such a study was recently published by Alekseenko *et al.* (2013). These models are computationally intensive and generally require a specialist to obtain and interpret the results; therefore, G3D models are not discussed further in this dissertation.

In addition, this dissertation does not intend to cover many other topics that are of particular interest in fracture modeling. These include:

1. Propagation of multiple fractures (Olson 2004; Dahi-Taleghani and Olson 2011);
2. Interactions with natural fractures (de Pater and Beugelsdijk 2005; Dahi-Taleghani and Olson 2011);
3. Layer debonding along interfaces (Warpinski and Teufel 1987; Barree and Winterfeld 1998);
4. Effect of plasticity (van Dam and de Pater 2001; van Dam *et al.* 2002);
5. Mode-II and mode-III fracture opening (Jones and Hirth 2001; Hossain *et al.* 2002);
6. Effect of fluid lag and dry tip zone on fracture propagation (Groenenboom *et al.* 2001); and
7. Modeling of heterogeneous reservoirs (Jonoud *et al.* 2013).

2.7 LIMITATIONS OF EXISTING MODELS FOR ENERGIZED FRACTURING

In the context of energized fracture modeling, the models presented in this chapter suffer several limitations. With the exception of the model developed by Frieauf and Sharma (2009), all the models presented in this chapter treat the fluid flow problem in a manner that is not representative of the behavior of energized fluids. Indeed, the fundamental equations assume single-phase, single-component, incompressible fluid flow. Typically, the fracturing fluid is assumed to be isothermal, with the fluid properties evaluated at the reservoir temperature. A volume balance is done on the fracturing fluid to track the amount of fluid leak-off and fluid injected, but both the density and the composition of the fluid remain constant. The leak-off rate is assumed to be the same for the entire fluid, which is inconsistent with experimental evidence that shows that gas leaks off slower than water. These assumptions are not compatible with the behavior of a two-phase, two-component, compressible CO₂ foam system for instance. In fact, none of the available 3D fracturing models for incompressible water-based fluids have been able to capture the thermal and compositional effects that are important when using energized fluids.

The only notable exception is the model developed by Frieauf and Sharma (2009). Their compositional 2D hydraulic fracturing model was the first model to incorporate thermal and compositional effects in addition to fracture mechanics and proppant transport in the fracture. The fundamental equations assume multi-phase, multi-component, compressible fluid flow. The main limitation of their model is the simplified treatment of the fracture mechanics problem. The fracture is constrained to the PKN geometry (Nordgren 1972). This formulation is not suitable for formations with low stress contrast, in which fractures tend to have lower aspect (length over height) ratios.

Also, the model cannot predict the propagation of a single fracture over multiple zones, as may be the case in more realistic *in-situ* stress distributions. Their model is also limited to fracture initiation in vertical wells.

The primary objective of this work is to propose a 3D planar fracturing model that is suitable for designing energized fracturing treatments. The model is intended to be similar to traditional planar 3D models from a fracture mechanics standpoint, and to be similar to the model developed by Frieauf and Sharma (2009) from a fluid flow standpoint. **Table 2.1** draws a comparison between a standard 3D hydraulic fracturing simulator, the 2D compositional simulator developed by Frieauf and Sharma (2009), and the new 3D compositional simulator. The table addresses some of the capabilities of the different models and their suitability for various design tasks. Current simulators offer a wide range of capabilities, and the list of properties described in Table 2.1 does not intend to be exhaustive. For instance, several new models are capable of propagating multi-stage horizontal fractures. The compositional model does not have such capabilities and, currently, it is limited to the propagation of a single fracture. The additional complexity of the new model is particularly suited for describing the performance of energized fluids. For incompressible single-phase fluids, the additional model complexity is not justified.

Table 2.1: Comparison of hydraulic fracture models.

Features	Current Simulators*	Friehauf and Sharma (2009)	3D Compositional Model
Fracture Shape	P3D or 3D planar (G3D is rare)	2D elliptical PKN	3D planar
Well Profile	Vertical, deviated, or horizontal	Vertical wells only	Vertical, deviated, or horizontal
Multiple Fractures	Multiple clusters available	Single cluster	Single cluster
Fracture Propagation	Stress intensity factors	Global mass balance	Stress intensity factors
Temperature	Isothermal	From energy balance Eq.	From energy balance Eq.
Fluid Density	Constant	Function of (P, T)	Function of (P, T)
Wellbore Hydraulics	Foam flow option	Multi-phase	Multi-phase
Proppant Settling	Numerous single-phase options	Homogenous	Phase-dependent
Leak-off	Single-phase	Phase-dependent	Phase-dependent

*Current simulators also offer numerous enhanced capabilities that are not listed here.

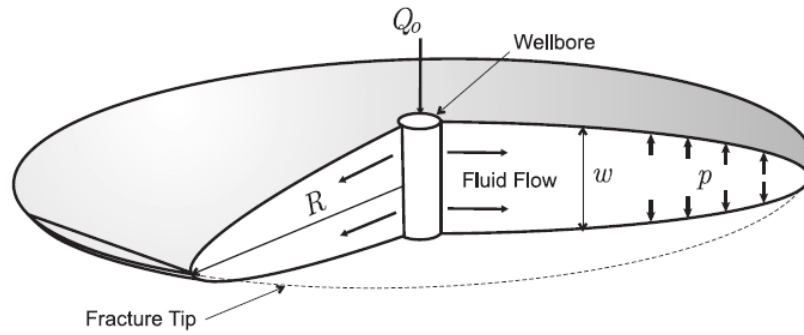


Figure 2.1: Representation of a radial or Penny-shaped fracture subject to a constant fluid pressure (from Adachi *et al.* 2007). R is a fracture radius; p is the constant fluid pressure; Q_0 is the injection rate; and w is the local width.

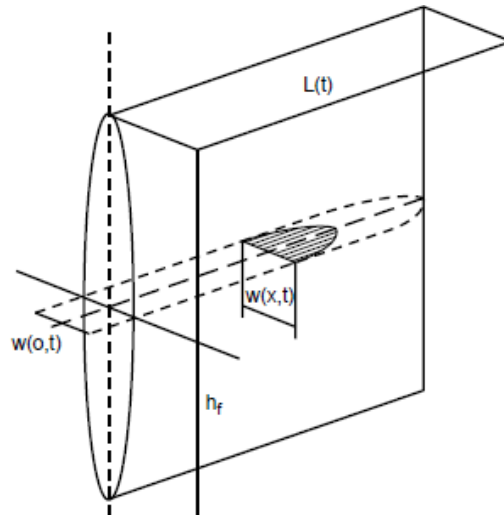


Figure 2.2: Representation of a PKN fracture (from Economides and Nolte 2000). The parameters L , h_f , and w are fracture length, height, and width, respectively.

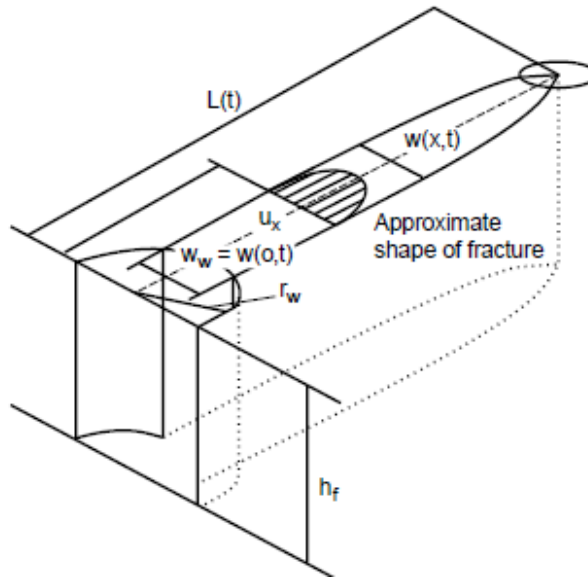


Figure 2.3: Representation of a KGD fracture (from Economides and Nolte 2000). The parameters L , h_f , and w are fracture length, height, and width, respectively.

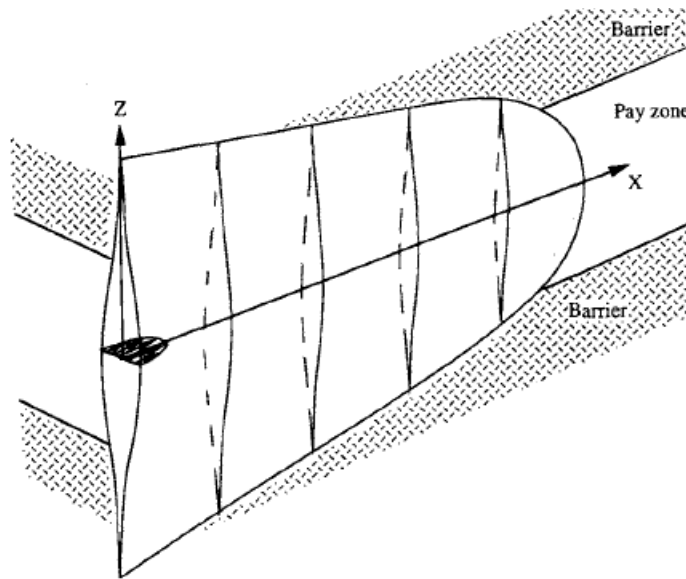


Figure 2.4: Representation of a pseudo 3D fracture (from Weng 1992).

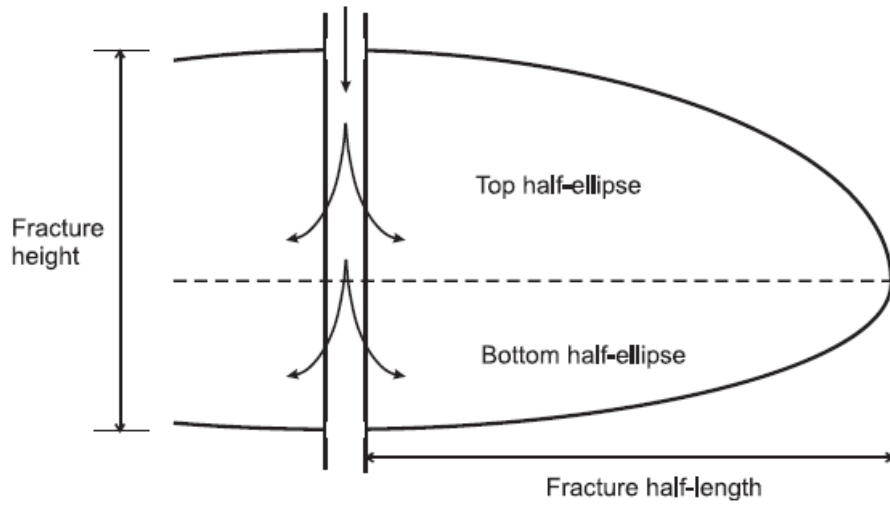


Figure 2.5: Representation of a pseudo 3D fracture using the lumped elliptical approach (from Adachi *et al.* 2007).

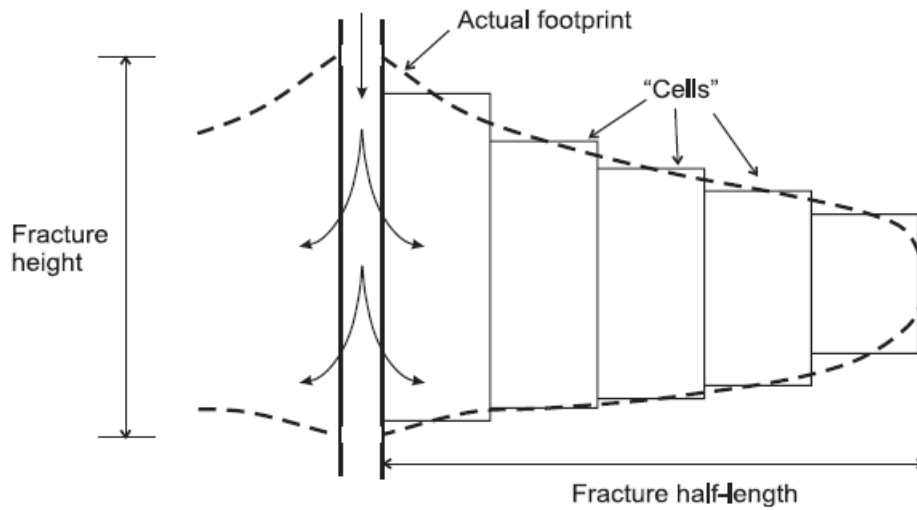


Figure 2.6: Representation of a pseudo 3D fracture using the cell-based approach (from Adachi *et al.* 2007).

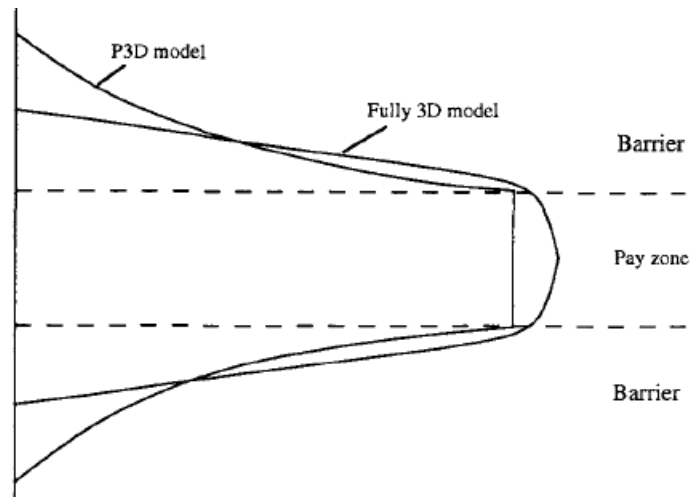


Figure 2.7: Comparison of fracture shapes predicted by pseudo 3D and fully 3D (planar) models (from Weng 1992).

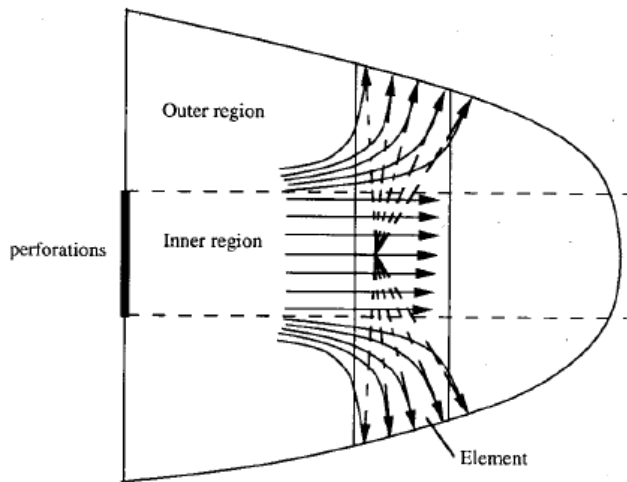


Figure 2.8: Representation of the approximate 2D fluid flow introduced by Weng (1992) in his pseudo 3D model. At the element of interest, the outer flow field is approximated as local radial flow (from Weng 1992).

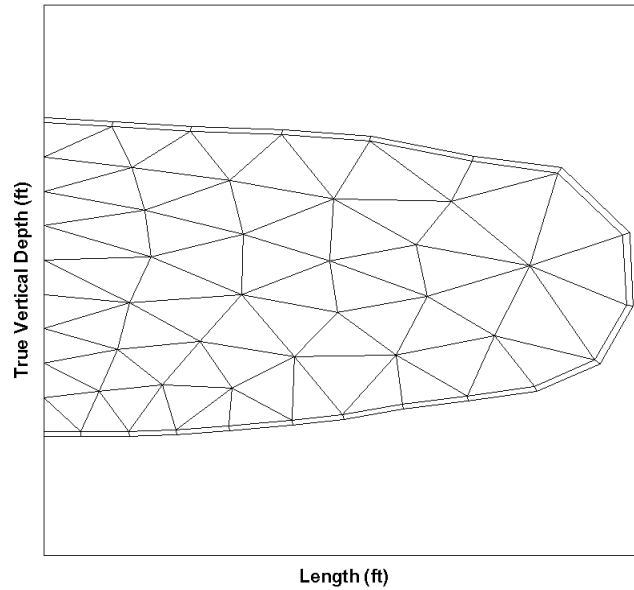


Figure 2.9: Representation of a 3D planar fracture using a dynamic unstructured mesh.

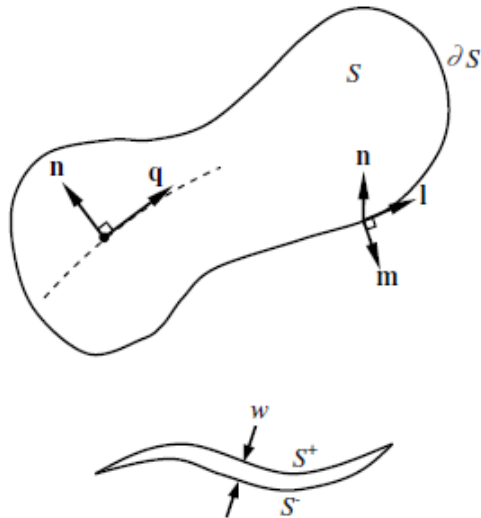


Figure 2.10: Representation of a 3D non-planar fracture. The fracture is allowed to move freely in all dimensions (from Rungamornrat *et al.* 2005). S is the fracture surface which is composed of the surfaces S^+ and S^- ; ∂S is the contour of the surface S ; w is the fracture width enclosed between S^+ and S^- ; and l, m, n, q are normal vectors used for the spatial integration of Eq. 2.5.

NOMENCLATURE

C	= non-local kernel function in Eq. 2.5
E	= Young's modulus, psi
G	= shear modulus, psi
h	= fracture height, ft
Q_0	= injection rate, bbl/min
l, m, n, q	= normal vectors shown in Fig. 2.10 for integration of Eq. 2.5
r	= distance defined in Eq. 2.4, ft
r_c	= radial distance from center, ft
R	= radial crack radius, ft
S	= fracture surface which is composed of S^+ and S^- , ft ²
t	= time, min
w	= fracture width, ft
x	= horizontal location, ft
y	= vertical location, ft

Greek Symbols

∂S	= line-contour of the fracture, ft
ΔP_{net}	= net pressure, psi
σ_{hmin}	= <i>in-situ</i> minimum horizontal stress, psi
ζ, η	= positions in the curved referential, ft
ν	= Poisson's ratio
Ω	= fracture domain

REFERENCES

- Abou-Sayed, A.S, Sinha, K.P., and Clifton, R.J 1984. Evaluation of the Influence of *In-Situ* Reservoir Conditions on the Geometry of Hydraulic Fractures Using a 3-D Simulator: Part 1–Technical Approach, Paper SPE/DOE/GRI 12877, Unconventional Gas Recovery Symposium, Pittsburg, Pennsylvania, 13-15 May.
- Adachi, J.I, Siebrits, E., Peirce, A., and Desroches, J. 2007. Computer Simulation of Hydraulic Fractures, *Int. J. of Rock Mech. and Min. Sci. & Geomech* **44**: 739-757.
- Advani, S. and Lee, J. 1982. Finite Element Model Simulations Associated with Hydraulic Fracturing. *SPE J.* **22**(2): 209-219. 8914-PA.
- Alekseenko, O.P., Potapenko, D.I., Cherny, S.G., Esipov, D.V., Kuranakov, D.S., and Lapin, V.N. 2013. 3D Modeling of Fracture Initiation From Perforated Non-cemented Wellbore. *SPE J.* (to be published). SPE 151585-PA.
- Barree, R.D. and Winterfeld, P.H. 1998. Effects of Shear Planes and Interfacial Slippage on Fracture Growth and Treating Pressures. Paper SPE 48926 presented at the SPE Annual Technical Conference and Exhibition, New Orleans, Louisiana, 27-30 September.
- Bui, H. 1977. An Integral Equations Method for Solving the Problem of a Plane Crack of Arbitrary Shape. *J. Mech. Phys. Solids* **25**: 29-39.
- Cleary, M.P., Kawadas, M., and Lam, K.Y. 1983. Development of a Fully Three-Dimensional Simulator for Analysis and Design of Hydraulic Fracturing. Paper SPE 11631 presented at the Symposium on Low-Permeability Gas Reservoirs, Denver, Colorado, 14-16 March.
- Clifton, R.J. and Abou-Sayed, A.S. 1981. A Variational Approach to the Prediction of the Three-Dimensional Geometry of Hydraulic Fractures. Paper SPE 9879 presented at the SPE/DOE Low Permeability Gas Reservoirs Symposium, Denver, Colorado, 27-29 May.
- Dahi-Taleghani, A. and Olson, J.E. 2011. Numerical Modeling of Multistranded-Hydraulic-Fracture Propagation: Accounting for the Interaction Between Induced and Natural Fractures. *SPE J.* **16**(3): 575-581. SPE 124884-PA.
- de Pater, C.J. and Beugelsdijk, L.J.L. 2005. Experiments and Numerical Simulation of Hydraulic Fracturing in Naturally Fractured Rock. Paper ARMA 05-780 presented at The 40th U.S. Symposium on Rock Mechanics (USRMS), Anchorage, Alaska, 25-29 June.
- Economides, M. and Nolte, K.G. 2000, *Reservoir Stimulation, Third Edition*, John Wiley and Sons, New York City, New York.
- Friehauf, K.E. 2009. Simulation and Design of Energized Hydraulic Fractures. Ph.D. Dissertation, The University of Texas at Austin, Austin, Texas (August 2009).
- Friehauf, K.E. and Sharma, M.M. 2009. A New Compositional Model for Hydraulic Fracturing With Energized Fluids. *SPE Prod & Opera* **24**(4): 562-572. SPE 115750-PA.

- Geertsma, J., and de Klerk, F. 1969. A Rapid Method of Predicting Width and Extent of Hydraulically Induced Fractures. *J. Pet Tech* **21**(12): 1571-1581. SPE 2458-PA.
- Groenenboom, J., van Dam, D.B. and de Pater, C.J 2001. Time-Lapse Ultrasonic Measurements of Laboratory Hydraulic-Fracture Growth: Tip Behavior and Width Profile. *SPE J.* **6**(1): 14-24. SPE 68882-PA.
- Gu, H. 1987. A Study of Propagation of Hydraulically Induced Fractures, Ph.D. Dissertation, The University of Texas at Austin, Austin, Texas (December 1987).
- Hossain M.M., Rahman M.K. and Rahman, S.S. 2002. A Shear Dilation Stimulation Model for Production Enhancement From Naturally Fractured Reservoirs. *SPE J.* **7**(2): 183-195. SPE 78355-PA.
- Jones, R.H. and Hirth, J.P. 2001. Effects on Mixed-Mode I/III Loading on Environment-Induced Cracking. *J. Corrosion* **57**(1).
- Jonoud, S., Wennberg, O.P. Casini, G., and Larsen, J.A. 2013. Capturing the Effect of Fracture Heterogeneity on Multiphase Flow During Fluid Injection. *SPE RE & E* **16**(2): 194-208. SPE 147834-PA.
- Kossecka, E. 1971. Defects as Surface Distribution of Double Forces. *Arch. Mech.* **23**: 481-494.
- Khristianovich, S.A. and Zheltov, Y.P 1955. Formation of Vertical Fractures by means of Highly Viscous Liquid. *Proc. SPE 4th World Pet congress 2*: 579-586. Rome, Italy. WPC 6132.
- Mastrojannis, E.N., Keer, L.M., and Mura, T. 1979. Stress Intensity Factor for a Plane Crack under Normal Pressure. *Int. Journ. Fracture* **15**: 247-258.
- Nordgren, R.P. 1972. Propagation of a Vertical Hydraulic Fracture. *SPE J.* **12**(4): 306-314. SPE 3009-PA.
- Olson, J.E. 2004. Predicting Fracture Swarms – the Influence of Subcritical Crack Growth and the Crack-Tip Process on Joint Spacing in Rocks. In The Initiation, Propagation, and Arrest of Joints and Other Fractures, Geol soc London Special publication **231**: 73-87.
- Ouyang, S. 1994. Propagation of Hydraulically Induced Fractures with Proppant Transport, Ph.D. Dissertation. The University of Texas at Austin, Austin, Texas (May 1994).
- Palmer, I.D. and Carroll, H.B. Jr 1983. Three-Dimensional Hydraulic Fracture Propagation in the Presence of Stress Variations. *SPE J.* **23**: 870-878. SPE 10849-PA.
- Perkins, T.K and Kern, L.R. 1961. Widths of Hydraulic Fractures, *J. Pet Tech* **13**(9): 937-949. SPE 89-PA.
- Pierce, A.P and Siebrits, E. 2001. The Scaled Flexibility Matrix Method for the Efficient Solution of Boundary Value Problems in 2D and 3D Layered Elastic Media. *Comp. Meth. Appl. Mech. Eng.* **190**(46): 5935-5956.

- Rungamornrat, J., Wheeler, M.F., and Mear M.E. 2005. Coupling of Fracture/Non-Newtonian Flow for Simulating Non-planar Evolution of Hydraulic Fractures. SPE Paper 96968 presented at the SPE Annual Technical Conference and Exhibition, Dallas, Texas, 9-12 October.
- Settari, A., and Cleary, M.P. 1984. Three-Dimensional Simulation of Hydraulic Fracturing. *J. Pet Tech* **36**(7): 1177-1190. SPE 10504-PA.
- Simonson, E.R., Abou-Sayed, A.S., and Clifton, R.J. 1978. Containment of Massive Hydraulic Fractures. *SPE J.* **18**(1): 27-32. SPE 6089-PA.
- Sneddon, I.N. 1946. The Distribution of Stress in the Neighbourhood of a Crack in an Elastic Solid. *P Roy Soc Lond, Series A* **187**: 229-260.
- Sneddon, I.N. and Elliott, H.A. 1946. The Opening of a Griffith Crack Under Internal Pressure. *Quart Appl. Math* **4**: 262-267.
- Spence, D.A. and Sharp, P.W. 1985. Self-Similar Solution for Elastohydrodynamic Cavity Flow. *P Roy Soc Lond, Series A* **400**: 289-313.
- Van Dam, D.B. and de Pater C.J. 2001. Roughness of Hydraulic Fractures: Importance of In-Situ Stress and Tip Processes. *SPE J.* **6**(1): 4-13. SPE 68775-PA.
- Van Dam, D.B., Papanastasiou, P., and de Pater C.J. 2002. Impact of Rock Plasticity on Hydraulic Fracture Propagation and Closure. *SPE Prod & Fac* **17**(3): 149-159. SPE 78812-PA.
- Warpinski, N.R. and Teufel, L.W. 1987. Influence of Geologic Discontinuities on Hydraulic Fracture Propagation, *J Pet. Tech.* **39**(2): 209-220. SPE 13224-PA.
- Weaver, J. 1977. Three-Dimensional Crack Analysis. *Int. J. Solids Structures* **13**: 321-330.
- Weng, X. 1992. Incorporation of 2D Fluid Flow Into a Pseudo-3D Hydraulic Fracturing Simulator. *SPE Prod Eng.*, **7**(4): 331-337. SPE 21849-PA.
- Yew, C.H. 1997, *Mechanics of Hydraulic Fracturing*, Gulf Publishing Company, Houston, Texas.
- Zhang, X., Jeffrey, R.G. and Thiercelin, M. 2007. Deflection and propagation of fluid-driven fractures at frictional bedding interfaces: A numerical investigation, *J. Structural Geol.* **29**: 396-410.

Chapter 3: Formulation of the 3D Compositional Fracture Model

This chapter¹ presents the theories and equations that form the basis of the first 3D compositional fracturing model. The model predicts changes in fluid temperature, density, and composition inside the fracture and along the wellbore. The objective of this chapter is to formulate a well-posed system of equations governing fracture propagation. This chapter does not intend to propose a specific algorithm to solve these equations, and the resolution of the mathematical problem is addressed in Chapter 4.

In this dissertation, the formulation of the problem intends to be as general as possible. The fracturing fluid consists of multiple components (NC), multiple phases (NP), and proppant distributed within the NP phases. There is no assumption regarding phase behavior and fluid rheology. Any *a priori* model may be implemented to model the fluid behavior since these properties are evaluated locally at each node.

To a large extent, our treatment of the fluid flow problem is similar to the model presented by Friehauf (2009) and Friehauf and Sharma (2009); and our treatment of the fracture mechanics problem is similar to the model presented by Gu (1987), Ouyang (1994) and Yew (1997). This chapter highlights the differences and similitudes between this model and past models. Specifically, we discuss the justifications for the assumptions we made, and we address the advantages and limitations of the new model.

¹ Many of the ideas expressed in this chapter were first written in SPE 159812 (Ribeiro and Sharma 2013).

3.1 PROBLEM STATEMENT

3.1.1 Fracture Geometry

The fracture is assumed to be planar, vertical, and symmetric with respect to the wellbore (bi-wing). There is no assumption regarding the shape of the fracture, which can grow both in length and in height. Fracture width (along the z -axis) is negligible compared to fracture height (along the y -axis) and length (along the x -axis). The 3D fracture geometry is contained in the x - y plane, as shown in **Fig. 3.1**. The fracture width, which is normal to the x - y plane, is an unknown that is calculated for each node located at a given x - and y -coordinates; therefore, the 3D planar fracture model is a 2D mathematical problem. Ω is the fracture surface that is delimited by the fracture contour $\partial\Omega$. This is the domain in which we are solving the constitutive equations. $\partial\Omega_f$ is the fracture front; $\partial\Omega_p$ is the perforated interval along the wellbore; and $\partial\Omega_c$ is the non-perforated section of the wellbore that is contained in the fracture propagation plane.

3.1.2 Main Variables for Fluid and Proppant

The fracturing fluid consists of NP fluid phases and NC components distributed among these NP phases. Energized fluids are either single-phase or two-phase mixtures, so NP is equal to 1 or 2. The fracturing fluid may transport proppant, and the mixture is referred to as slurry. **Fig. 3.2** shows the notation introduced for two-phase fluids carrying proppant. For fluid phases, the convention is that subscript 1 refers to the liquid phase and subscript 2 refers to the gas phase. For components, subscript 1 refers to the water component (if water is present) and the following subscripts refer to the energized components (CO_2 , N_2 , MeOH , etc.). As indicated in the nomenclature, the superscript ^{*} refers to a slurry property. For example, ρ_1^* refers to the density of slurry phase 1 (which

contains fluid phase 1 and the proppant carried by fluid phase 1), whereas ρ_1 refers to the density of fluid phase 1. To make the derivations as general as possible, we define the following volumes of fluid and proppant:

$$\left\{ \begin{array}{l} V_j = \text{Volume of fluid phase } j \\ V_{p,j} = \text{Volume of proppant included in slurry phase } j \\ V_j^* = V_j + V_{p,j} = \text{Volume of slurry phase } j \text{ (including proppant)} \\ V_{fluid} = \sum_{j=1}^{NP} V_j = \text{Total volume of fluid} \\ V_p = \sum_{j=1}^{NP} V_{p,j} = \text{Total volume of proppant} \\ V_T = \sum_{j=1}^{NP} V_j^* = V_{fluid} + V_p = \text{Total volume of fluid including proppant} \end{array} \right. \quad (3.1)$$

By definition, the saturations of the fluid and slurry phase j are given by:

$$S_j = \frac{V_j}{V_{fluid}} = \frac{V_j}{\sum_{j=1}^{NP} V_j} \quad \text{and} \quad S_j^* = \frac{V_j^*}{V_T} = \frac{V_j^*}{\sum_{j=1}^{NP} V_j^*} \quad (3.2)$$

In Eq. 3.2, S_j refers to the saturation of fluid phase j on a fluid volume basis, and S_j^* refers to the saturation of slurry phase j on a slurry volume basis (fluid + proppant). In addition, the fracturing fluid may transport proppant. The total volume concentration of proppant is denoted by c , which corresponds to:

$$c = \frac{V_p}{V_T} = \frac{\sum_{j=1}^{NP} V_{p,j}}{\sum_{j=1}^{NP} V_j^*} \quad (3.3)$$

We define γ_j as the proppant concentration (volume fraction) in slurry phase j . To remain as general as possible, we assume that the proppant does not have to be uniformly

distributed among the phases, and $K\gamma$ is defined as the ratio of the proppant concentration in the two phases:

$$\gamma_j = \frac{V_{p,j}}{V_j^*} \quad \text{and} \quad K\gamma = \frac{\gamma_2^*}{\gamma_1^*} \quad (3.4)$$

3.1.3 Material Balances

Using the definitions provided in Eqs. 3.1 to 3.4, several material balances yield useful relationships that are used in the derivations of the constitutive equations. By construction, the sum of the saturations on a fluid and slurry volume basis adds up to one:

$$\sum_{j=1}^{NP} S_j = 1 \quad \text{and} \quad \sum_{j=1}^{NP} S_j^* = 1 \quad (3.5)$$

The volume concentration of proppant c is related to the proppant concentration γ_j in each slurry phase j as follows:

$$c = \frac{V_p}{V_T} = \frac{1}{V_T} \sum_{j=1}^{NP} V_{p,j} = \sum_{j=1}^{NP} \frac{V_j^*}{V_T} \frac{V_{p,j}}{V_j^*} = \sum_{j=1}^{NP} S_j^* \gamma_j \quad (3.6)$$

The saturation S_j^* (defined on a slurry volume basis) is related to the saturation S_j (defined on a fluid volume basis) as follows:

$$\begin{aligned} S_j^* &= \frac{V_j^*}{V_T} = \frac{V_j + V_{p,j}}{V_T} = \frac{V_j}{V_{fluid}} \frac{V_{fluid}}{V_T} + \frac{V_j^*}{V_T} \frac{V_{p,j}}{V_j^*} = S_j(1-c) + S_j^* \gamma_j \\ \Rightarrow S_j^* &= S_j \left(\frac{1-c}{1-\gamma_j} \right) \end{aligned} \quad (3.7)$$

3.1.4 Main Variables for Fluid Composition

The fracturing fluid contains NC components that may partition in both phases, and the component split between phases is governed by local thermodynamic equilibrium. As seen in Fig. 3.2, we define ω_{ij} as the mass fraction of component i in phase j , and z_i as the overall mass fraction of component i . We also use the conventional notation for liquid-vapor equilibrium, in which x_i and y_i are the mass fractions of component i in the liquid and gas phases, respectively. For a two-phase fluid, the overall mass fraction of component i is given by:

$$z_i = \frac{\sum_{j=1}^{NP} \rho_j S_j \omega_{ij}}{\sum_{j=1}^{NP} \rho_j S_j} = \frac{x_i \rho_1 S_1 + y_i \rho_2 S_2}{\rho_1 S_1 + \rho_2 S_2} \quad (3.8)$$

Fig. 3.3 provides an example of compositional calculations for 0.7-quality CO₂ foam. By definition, the saturation of the gas phase is 0.7, and the saturation of the liquid phase is 0.3. The water component does not partition in the gas phase, so $y_1=0$; CO₂ is the only component in the gas phase, so $y_2=1$. Under the given conditions of pressure and temperature, the solubility of CO₂ in water is 6% by mass, so $x_1=0.94$ and $x_2=0.06$. Under these conditions, the density of the liquid and gas phases is 63 lbm/ft³ and 51 lbm/ft³, respectively. Using Eq. 3.8, the overall mass fraction of water is 0.325, and the overall mass fraction of CO₂ is 0.675.

3.2 FLOW EQUATIONS

The flow equations relate the flow of the fluid in the fracture to the fluid pressure gradients. The fracturing fluid is assumed to flow between essentially parallel porous walls. Fluid flow is idealized as that of a 2D, laminar, compressible, power-law fluid.

Each phase is assumed to behave locally as a power-law fluid with known power-law index and consistency. This assumption is not a significant limitation as different power-law parameters can be assigned at each node. These parameters are known functions of polymer loading, temperature, proppant concentration, pH, shear history, surfactant conditions, and other factors. Any *a priori* model that describes changes in n and K can easily be incorporated into the fracture model since we use the local values of n and K .

3.2.1 Slurry Flow

We first derive the velocity profile for a laminar, single-phase, compressible, power-law fluid subject to a given pressure distribution. The fluid is flowing in a pseudo steady-state manner. Because the fracture is much thinner along the z -axis (fracture width), the velocity gradients are negligible along the x and y -axis. The power-law fluid rheology is characterized by:

$$\mu = K \sqrt{\left(\frac{\partial v_x}{\partial z}\right)^2 + \left(\frac{\partial v_y}{\partial z}\right)^2}^{n-1} \quad (3.9)$$

We also assume that the flow is symmetric and that there is no slippage at the fracture wall. The Navier-Stokes equation governing fluid flow between two parallel plates is solved along the x and y -axis to obtain the flow rate per unit fracture height:

$$\begin{cases} q_x = -\frac{n}{2n+1} K^{-1/n} \left(\left(\frac{\partial P}{\partial x} \right)^2 + \left(\frac{\partial P}{\partial y} + \rho g \right)^2 \right)^{\frac{1-n}{2n}} \left(\frac{w^{\frac{2n+1}{n}}}{2^{\frac{n+1}{n}}} \right) \times \left(\frac{\partial P}{\partial x} \right) \\ q_y = -\frac{n}{2n+1} K^{-1/n} \left(\left(\frac{\partial P}{\partial x} \right)^2 + \left(\frac{\partial P}{\partial y} + \rho g \right)^2 \right)^{\frac{1-n}{2n}} \left(\frac{w^{\frac{2n+1}{n}}}{2^{\frac{n+1}{n}}} \right) \times \left(\frac{\partial P}{\partial y} + \rho g \right) \end{cases} \quad (3.10)$$

Eq. 3.10 expresses the flow rate per unit height of a compressible, single-phase, power-law fluid. For a single-phase Newtonian fluid, Eq. 3.10 reduces to the traditional equation for fluid flow in a slot of narrow width:

$$q_x = -\frac{w^3}{12\mu} \left(\frac{\partial P}{\partial x} \right) \quad ; \quad q_y = -\frac{w^3}{12\mu} \left(\frac{\partial P}{\partial y} + \rho g \right) \quad (3.11)$$

The presence of multiple phases alters the flow behavior because: (1) each phase may have a different rheology; (2) the no-slip boundary at the fracture wall is not valid at the interfaces between phases; (3) each phase does not occupy the full fracture volume; and (4) each phase may interfere with its neighbors. The rheology of each slurry phase depends on both the fluid rheology and the proppant concentration within that phase. We assume that the phases do not interfere, so each phase may be seen as a fluid flowing in a separate conduit, of which the diameter is proportional to the phase saturation. Also, we assume that the slippage that may occur at the interfaces between phases does not significantly alter fluid flow. Under these assumptions, the flow rate of the slurry phase j becomes:

$$\left\{ \begin{array}{l} q_{j,x}^* = -S_j^* \frac{n_j}{2n_j+1} K_j^{-1/n_j} \left(\left(\frac{\partial P}{\partial x} \right)^2 + \left(\frac{\partial P}{\partial y} + \rho_j^* g \right)^2 \right)^{\frac{1-n_j}{2n_j}} \left(\frac{w^{\frac{2n_j+1}{n_j}}}{2^{\frac{n_j+1}{n_j}}} \right) \times \left(\frac{\partial P}{\partial x} \right) \\ q_{j,y}^* = -S_j^* \frac{n_j}{2n_j+1} K_j^{-1/n_j} \left(\left(\frac{\partial P}{\partial x} \right)^2 + \left(\frac{\partial P}{\partial y} + \rho_j^* g \right)^2 \right)^{\frac{1-n_j}{2n_j}} \left(\frac{w^{\frac{2n_j+1}{n_j}}}{2^{\frac{n_j+1}{n_j}}} \right) \times \left(\frac{\partial P}{\partial y} + \rho_j^* g \right) \end{array} \right. \quad (3.12)$$

In Eq. 3.12, the rheology parameters n and K have subscripts j since each phase may have different values. The superscript $*$ denotes a quantity proper to a slurry phase, not just to a fluid phase. Eq. 3.12 may be written in a more compact form by using the

parameter A_j^* , which relates the flow rate per unit height of the phase j to the pressure gradient:

$$\begin{cases} A_j^* = -\frac{n_j}{2n_j+1} K_j^{-1} \left(\frac{w_j^{n_j+1}}{2^{n_j}} \right) \left[\left(\frac{\partial P}{\partial x} \right)^2 + \left(\frac{\partial P}{\partial y} + \rho_j^* g \right)^2 \right]^{\frac{1-n_j}{2n_j}} \\ q_{j,x}^* = A_j^* S_j^* \left(\frac{\partial P}{\partial x} \right) \quad ; \quad q_{j,y}^* = A_j^* S_j^* \left(\frac{\partial P}{\partial y} + \rho_j^* g \right) \end{cases} \quad (3.13)$$

The total flow rate of the mixture per unit height is the sum of the contributions of the NP phases, as seen in Eq. 3.14:

$$\begin{cases} q_x^* = \sum_{j=1}^{NP} q_{j,x}^* = \sum_{j=1}^{NP} A_j S_j^* \frac{\partial P}{\partial x} \\ q_y^* = \sum_{j=1}^{NP} q_{j,y}^* = \sum_{j=1}^{NP} A_j S_j^* \left(\frac{\partial P}{\partial y} + \rho_j g \right) \end{cases} \quad (3.14)$$

3.2.2 Proppant Flow

Because of proppant settling (in the y -direction) and proppant retardation (in the x -direction), the fluid and proppant contained in each slurry phase may travel at different velocities. We introduce retardation factors in the x and y -directions to describe the relative motion of the proppant with respect to the slurry ($\lambda_{j,x}$ and $\lambda_{j,y}$, respectively). These retardation factors are phase-dependent. They are introduced so that proppant fluxes can be expressed in terms of slurry fluxes, as shown in Eq. 3.15:

$$\begin{cases} q_{p,j,x} = \gamma_j \lambda_{j,x} q_{j,x}^* \\ q_{p,j,y} = \gamma_j \lambda_{j,y} q_{j,y}^* \end{cases} \quad \text{where} \quad \lambda_{j,x} = k_{ret,j} \quad \text{and} \quad \lambda_{j,y} = \left(1 - \frac{V_{set} w}{q_{j,y}^*} \right) \quad (3.15)$$

Here, k_{ret} refers to the proppant retardation effect and V_{set} refers to the settling velocity. The settling is due to the density contrast between the proppant and the carrying fluid. As a first approximation, the settling velocity is calculated with Stokes' law:

$$V_{Stokes} = \frac{(\rho_p - \rho_f)gd_p^2}{18\mu} \quad (3.16)$$

Stokes' law is valid for low Reynolds number flows in an unbounded wall. Additional corrections are needed to account for the effects of fracture walls, inertia, and proppant concentration (Gadde *et al.* 2004). We assume that these corrections are independent of each other, as seen in Eq. 3.17:

$$V_{set} = V_{Stokes} \times f(\text{Re})f(c)f(w) \begin{cases} f(\text{Re}) = \frac{0.3736\mu^{0.57}}{\rho_f^{0.29}(\rho_p - \rho_f)^{0.29}d_p^{0.86}} \\ f(c) = 1 - 4.8c + 8.8c^2 - 5.9c^3 \\ f(w) = 1 - 1.563\left(\frac{d_p}{w}\right) + 0.563\left(\frac{d_p}{w}\right)^2 \end{cases} \quad (3.17)$$

Additionally, the proppant may experience a velocity reduction in the x -direction. Gadde *et al.* (2004) and Liu (2006) proposed correlations accounting for the effect of fracture walls and proppant concentration on proppant retardation:

$$\begin{cases} \frac{1}{w_c^2} = 1.411\left(\frac{1}{d_p^2} - \frac{1}{w^2}\right)c^{0.8} \\ k_{ret} = 1 + \left(\frac{d_p}{w_c}\right) - 2.02\left(\frac{d_p}{w_c}\right)^2 \end{cases} \quad (3.18)$$

3.2.3 Fluid Flow

Because of proppant settling and retardation, the fluid phase has a different velocity than its slurry counterpart. The mass flux of slurry phase j is equal to the sum of the associated fluid and proppant mass fluxes:

$$\rho_j^* q_{j,x}^* = \rho_j q_{j,x} + \rho_p q_{p,j,x} \Rightarrow q_{j,x} = q_{j,x}^* \left(\frac{\rho_j^*}{\rho_j} - \frac{\rho_p}{\rho_j} \gamma_j \lambda_{j,x} \right) \quad (3.19)$$

Similar derivations may be performed in the y -direction to define the fluid fluxes in terms of slurry fluxes:

$$\begin{cases} q_{j,x} = q_{j,x}^* \left((1 - \gamma_j) + \frac{\rho_p}{\rho_j} \gamma_j (1 - \lambda_{j,x}) \right) \\ q_{j,y} = q_{j,y}^* \left((1 - \gamma_j) + \frac{\rho_p}{\rho_j} \gamma_j (1 - \lambda_{j,y}) \right) \end{cases} \quad (3.20)$$

The fluid flow properties of the slurry, proppant, and fluid phases have now been derived, and will be used in the subsequent derivations of the transport equations. **Table 3.1** shows how the different properties are related. Specifically, the proppant and fluid fluxes are expressed in terms of the slurry fluxes.

3.2.4 Comments on Foam Stability and Rheology

The derivations provided in this chapter intend to be as general as possible, so the resulting equations may appear overly complex in many cases. For single-phase incompressible fluids, the flow equations reduce to the common formulation found in most fracturing simulators (Clifton and Abou-Sayed 1981; Cleary *et al.* 1983; Settari and Cleary 1984; Yew 1997; Economides and Nolte 2000; Adachi *et al.* 2007).

For stable foams, the two phases travel at the same velocity, and there is no slippage. Consequently, the same power-law parameters are assigned to both phases. From a transport standpoint, stable foam is seen as a single “pseudo phase”. The reader may refer to Chapter 7 of this dissertation, as well as to the work of Reidenbach *et al.* (1986), Valkó and Economides (1997), and Khade and Shah (2004) for more details on foam rheology. The addition of proppant further complicates the slurry rheology.

Furthermore, interfacial forces prevent gravity segregation in stable foams. This effect is simply modeled by replacing the density of a given slurry phase (ρ_j^*) by the total slurry density (ρ_T^*) in the convective term in the y -direction of Eq. 3.13. For unstable foams, the interfacial forces are not capable of holding the gas bubbles inside the external liquid phase. As the gas bubbles coalesce, the gas pocket migrates upward because of gravity segregation. After a few minutes, the water and gas phases are completely separated, and the mixture loses its viscosity. Gravity segregation occurs because of the contrast between the liquid and the gas densities, as shown in Chapter 7.

3.3 PRESSURE EQUATION (OVERALL MASS BALANCE)

The pressure equation is an overall continuity equation that expresses the conservation of mass for compressible, multi-phase, slurry mixtures. The overall mass flux is the sum of the contributions of the NP slurry phases. Assuming that these contributions are linearly independent, the continuity equation is given by:

$$\frac{\partial}{\partial t}(w\bar{m}_T) + \nabla \cdot \left(\sum_{j=1}^{NP} \vec{q}_j^* \rho_j^* \right) + \sum_{j=1}^{NP} q_{L,j} \rho_j = 0 \quad (3.21)$$

In Eq. 3.21, the accumulation term includes the total slurry mass flowing through the fracture on a total volume basis, which is given by:

$$\bar{m}_T = \frac{m_T^*}{V_T} = \frac{m_p + m_f}{V_T} = \rho_p c + (1-c) \sum_{j=1}^{NP} \rho_j S_j \quad (3.22)$$

The total slurry mass flowing through the fracture on a total volume basis equals the density of the slurry mixture; hence, Eq. 3.22 may be expressed as:

$$\bar{m}_T = \rho_T^* = \sum_{j=1}^{NP} \rho_j^* S_j^* \quad (3.23)$$

In addition, we assume that the fluid-loss rate is phase-dependent and follows Carter's filtration model (Carter 1957). Inserting Eqs. 3.13 and 3.23 into Eq. 3.21, the pressure equation takes the form of a diffusivity equation:

$$\begin{aligned} & \frac{\partial}{\partial t} \left\{ w \left(\sum_{j=1}^{NP} \rho_j^* S_j^* \right) \right\} + \frac{\partial}{\partial x} \left\{ \left(\sum_{j=1}^{NP} \rho_j^* A_j^* S_j^* \right) \frac{\partial P}{\partial x} \right\} + \frac{\partial}{\partial y} \left\{ \left(\sum_{j=1}^{NP} \rho_j^* A_j^* S_j^* \right) \frac{\partial P}{\partial y} \right\} \\ & + \frac{\partial}{\partial y} \left\{ \left(\sum_{j=1}^{NP} \rho_j^{*2} A_j^* S_j^* \right) g \right\} + \sum_{j=1}^{NP} \frac{2C_{w,j} \rho_j}{\sqrt{t-\tau}} = 0 \end{aligned} \quad (3.24)$$

In Eq. 3.24, the first term is the accumulation term; the second is the convective flux along the x -direction; the third is the convective flux along the y -direction; the fourth is the gravity contribution; and the fifth is the fluid-loss rate to the rock formation. In our definition of the fluid-loss rate, the leak-off coefficient is phase-dependent ($C_{w,j}$). This coefficient is a function of the fluid saturation, but it does not have to be proportional to the fluid saturation. Because of this assumption, the fluid saturation does not appear in the fluid-loss term, contrary to the model proposed by Frieauf and Sharma (2009). Any *a priori* model that describes changes in $C_{w,j}$ can easily be incorporated into the fracture model since we use local values at each node.

Initial conditions (ICs) and boundary conditions (BCs) are required to solve this partial differential equation (PDE). Initially, the fluid pressure is equal to the fracture initiation pressure, which is slightly higher than the minimum horizontal stress. For the BCs, the pumping rate per unit height is specified along the perforated interval ($\partial\Omega_p$). No fluid flows out of the fracture front ($\partial\Omega_f$) or from the non-perforated section of the wellbore ($\partial\Omega_c$); thus, we use no-flow BCs along these intervals:

$$\underline{ICs}: P = \sigma_{h\min} + \Delta P_{\text{toughness}} \quad \text{over } \Omega \quad (3.25)$$

$$\underline{BCs}: \begin{cases} A^* \frac{\partial P}{\partial n} = A^* \frac{\partial P}{\partial x} = (q_x)_{inj} & \text{on } \partial\Omega_p \\ \frac{\partial P}{\partial n} = 0 & \text{on } \partial\Omega_f \text{ and } \partial\Omega_c \end{cases} \quad (3.26)$$

Because only natural (Neumann) BCs are specified and because the pressure equation only involves pressure gradients, the equation is singular and the solution is determined within a constant. In other words, a solution of Eq. 3.24 plus an arbitrary constant is also a solution of that equation. The arbitrary constant is determined from the requirement that the fracture propagates at each time step. The net pressure at the perforations is adjusted so that the fluid pressure, and therefore the stress intensity factor, is high enough to overcome a critical value (fracture toughness) somewhere along the fracture tip. This method is significantly different from 2D and pseudo 3D fracturing models, which essentially prescribe that the net pressure is zero at a pre-defined location along the tip.

The increase in fracture mass must equal the mass of fluid pumped minus the mass of fluid that leaked off. This overall conservation of mass is enforced by a so-called

compatibility equation. The time step (Δt^n) used for solving Eq. 3.24 is calculated from this condition. Eq. 3.27 is a necessary condition to the existence of a solution:

$$\Delta t^n = \frac{\Delta m_{fracture} + \Delta m_{leakoff}}{\dot{m}_{pumped}} \quad (3.27)$$

Δt^n denotes the time step increment; $\Delta m_{fracture}$ is the change in fracturing fluid mass during Δt^n ; $\Delta m_{leakoff}$ is the mass of fluid that leaked off during Δt^n ; and \dot{m}_{pumped} is the mass flow rate imposed at the perforations. A similar compatibility condition was derived for incompressible fluids by Gu (1987) and Yew (1997) to ensure that the overall volume conservation was satisfied. Because the fracturing fluid is now compressible, the new time step requirement is derived from the overall mass conservation.

3.4 PROPPANT TRANSPORT EQUATION

Similarly to the derivation of the pressure equation, the derivation of the proppant transport equation intends to be as general as possible. No assumption is made regarding the proppant distribution within the two phases. The proppant remains incompressible, but the fluid transporting the proppant is compressible. We also assume that the proppant does not leak-off into the rock formation because of size exclusion. The continuity equation with respect to proppant is given by:

$$\frac{\partial}{\partial t}(w\bar{m}_p) + \nabla \cdot \left(\sum_{j=1}^{NP} \rho_p \vec{q}_{p,j} \right) = 0 \quad (3.28)$$

In Eq. 3.28, the accumulation term includes the mass of proppant flowing through the fracture on a total volume basis, which is given by:

$$\bar{m}_p = \frac{m_p}{V_T} = \sum_{j=1}^{NP} S_j^* \bar{m}_{p,j} = \rho_p \left(\sum_{j=1}^{NP} S_j^* \gamma_j \right) = \rho_p c \quad (3.29)$$

Inserting Eqs. 3.15 and 3.29 into Eq. 3.28, the proppant transport equation takes the form of a convective-dominated equation:

$$\frac{\partial}{\partial t}(wc) + \frac{\partial}{\partial x} \left(\sum_{j=1}^{NP} \gamma_j \lambda_{j,x} A_j^* S_j^* \left(\frac{\partial P}{\partial x} \right) \right) + \frac{\partial}{\partial y} \left(\sum_{j=1}^{NP} \gamma_j \lambda_{j,y} A_j^* S_j^* \left(\frac{\partial P}{\partial y} + \rho_j^* g \right) \right) = 0 \quad (3.30)$$

Eq. 3.30 is not practical to solve for the proppant concentration c . A more useful formulation is obtained when expressing the convective terms as a function of the proppant concentration c . To do so, we assume that the proppant split K_γ is a known function, which is not limiting our model since we use the local value of K_γ at each node.

Eq. 3.30 can be re-arranged as:

$$\frac{\partial}{\partial t}(wc) + \frac{\partial}{\partial x} \left(c \left(\frac{\lambda_{1,x} q_{1,x}^* + K_\gamma \lambda_{2,x} q_{2,x}^*}{K_\gamma + S_1^* (1 - K_\gamma)} \right) \right) + \frac{\partial}{\partial y} \left(c \left(\frac{\lambda_{1,y} q_{1,y}^* + K_\gamma \lambda_{2,y} q_{2,y}^*}{K_\gamma + S_1^* (1 - K_\gamma)} \right) \right) = 0 \quad (3.31)$$

If the proppant is uniformly distributed within the two phases, Eq. 3.31 becomes:

$$\frac{\partial}{\partial t}(wc) + \frac{\partial}{\partial x} \left(c (\lambda_{1,x} q_{1,x}^* + \lambda_{2,x} q_{2,x}^*) \right) + \frac{\partial}{\partial y} \left(c (\lambda_{1,y} q_{1,y}^* + \lambda_{2,y} q_{2,y}^*) \right) = 0 \quad (3.32)$$

Initially, the proppant concentration is zero. For the BCs, we assume that the proppant concentration at the perforations is equal to the injected concentration (along $\partial\Omega_p$). No proppant flows out of the fracture front ($\partial\Omega_f$) or from the non-perforated section of the wellbore ($\partial\Omega_c$):

$$\underline{ICs}: c = 0 \quad \text{over } \Omega \quad (3.33)$$

$$\underline{BCs}: \begin{cases} c = c_{inj} & \text{on } \partial\Omega_p \\ \frac{\partial c}{\partial n} = 0 & \text{on } \partial\Omega_f \text{ and } \partial\Omega_c \end{cases} \quad (3.34)$$

In addition, we assume that the proppant is made of rigid spheres of equal diameter; therefore, the proppant concentration cannot exceed the maximum packing of spheres of equal diameter (0.52). This additional restriction is enforced numerically by locally spreading the excess proppant when the calculated concentration reaches the maximum value.

Although the derivations of the pressure and proppant transport equations both start from a continuity equation and share some similarities, the resulting equations differ fundamentally. The pressure equation is a diffusivity equation, which is an elliptic PDE, while the proppant transport equation is a convection-dominated equation, which combines parabolic and hyperbolic PDEs. The behavior, smoothness, and mathematical resolution of these equations are dramatically different. This is discussed in greater detail in Chapter 4.

3.5 COMPONENT TRANSPORT EQUATION(S)

For single-phase fluids, no additional PDE is required to track the changes in fluid composition. The leak-off rate is phase-dependent, rather than component-dependent; therefore, the composition of a single-phase mixture of components remains uniform, and the solution of the component transport equations is trivial. However, the density, viscosity, and leak-off coefficient of the fluid changes over time and location, due to changes in pressure and temperature.

For multi-phase mixtures, each component can be transported by fluid phases flowing at different velocities. The fluid phase itself has a different velocity than its slurry counterpart because of proppant settling and retardation. As the proppant is slowing down, the fluid is accelerating with respect to the slurry. Also, the rate of fluid-loss may be different for each component depending on the component split between the two phases. The resolution of the component transport equations is thus required when using two-phase fluids. Because there are NC components, there are NC mass component transport equations. These equations may be written in terms of the mass fraction of each component (ω_{ij}), the overall mass fraction of each component (z_i), or the fluid saturation (S_1). These fundamental formulations are derived in this section.

3.5.1 Component Mass Fraction Formulation

The derivation of the component transport equation is mathematically similar to the derivation of the proppant transport equation. In fact, the proppant may be seen as an additional component except the proppant is not subject to the thermodynamic equilibrium requirements. No assumption is made regarding the split of each component within the two phases. The split may be obtained from empirical data, known equilibrium values (also known as K -values), or from an equation of state. We assume that the leak-off coefficients are only phase-dependent, so each component is leaking off with its associated phase(s). Assuming that the fluxes are linearly independent, the continuity equation for component i is given by:

$$\frac{\partial}{\partial t}(w\bar{m}_i) + \nabla \cdot \left(\sum_{j=1}^{NP} \vec{q}_j \bar{m}_{i,j} \right) + \sum_{j=1}^{NP} q_{L,i} \bar{m}_{i,j} = 0 \quad (3.35)$$

In Eq. 3.35, the accumulation term includes the mass of component i flowing through the fracture on a total volume basis, which is given by:

$$\bar{m}_i = \sum_{j=1}^{NP} \bar{m}_{i,j} = \frac{1}{V_T} \sum_{j=1}^{NP} \omega_{ij} \rho_j V_j = \sum_{j=1}^{NP} \omega_{ij} \rho_j (1 - \gamma_j) S_j^* = (1 - c) \sum_{j=1}^{NP} \omega_{ij} \rho_j S_j \quad (3.36)$$

Inserting Eqs. 3.20 and 3.36 into Eq. 3.35, the component transport equation takes the form of a convection-dominated equation:

$$\begin{aligned} \frac{\partial}{\partial t} \left(w(1-c) \left(\sum_{j=1}^{NP} \omega_{ij} \rho_j S_j \right) \right) + \frac{\partial}{\partial x} \left(\sum_{j=1}^{NP} \omega_{ij} \rho_j q_{j,x} \right) + \frac{\partial}{\partial y} \left(\sum_{j=1}^{NP} \omega_{ij} \rho_j q_{j,y} \right) \\ + \frac{2}{\sqrt{t-\tau}} \sum_{j=1}^{NP} C_{w,j} \omega_{ij} \rho_j = 0 \end{aligned} \quad (3.37)$$

Initially, the mass fraction of each component is uniform inside the fracture. The composition is governed by the initial conditions of pressure and temperature. Dirichlet BCs are imposed at the perforations and no-flux Neumann BCs are imposed everywhere else:

$$\underline{ICs}: \omega_{ij} = \omega_{ij}(P(t=0), T(t=0)) \quad \text{over } \Omega \quad (3.38)$$

$$\underline{BCs}: \begin{cases} \omega_{ij} = \omega_{ij,inj} & \text{on } \partial\Omega_p \\ \frac{\partial \omega_{ij}}{\partial n} = 0 & \text{on } \partial\Omega_f \text{ and } \partial\Omega_c \end{cases} \quad (3.39)$$

3.5.2 Overall Component Mass Fraction Formulation

Using Eq. 3.37 to solve for the mass fraction ω_{ij} is not practical, as the summation over the multiple flux contributions prevents a direct time resolution of the equation. Moreover, flash calculations require knowledge of the overall mass fraction of each

component in order to estimate the split within each phase. A more useful formulation is obtained when expressing the accumulation term in terms of the overall mass fraction z_i :

$$\begin{aligned} & \frac{\partial}{\partial t} \left(w(1-c) \left(\sum_{j=1}^{NP} \rho_j S_j \right) z_i \right) + \frac{\partial}{\partial x} \left(\sum_{j=1}^{NP} \omega_{ij} \rho_j q_{j,x} \right) + \frac{\partial}{\partial y} \left(\sum_{j=1}^{NP} \omega_{ij} \rho_j q_{j,y} \right) \\ & + \frac{2}{\sqrt{t-\tau}} \sum_{j=1}^{NP} C_{w,j} \omega_{ij} \rho_j = 0 \end{aligned} \quad (3.40)$$

The ICs and BCs are similar to the ones introduced in the previous formulation:

$$\underline{ICs}: z_i = z_i(t=0) \quad \text{over } \Omega \quad (3.41)$$

$$\underline{BCs}: \begin{cases} z_{ij} = z_{i,inj} & \text{on } \partial\Omega_p \\ \frac{\partial z_i}{\partial n} = 0 & \text{on } \partial\Omega_f \text{ and } \partial\Omega_c \end{cases} \quad (3.42)$$

The formulation given in Eq. 3.40 is particularly useful when using a time-explicit scheme. In that case, the new overall mass fraction may be used to perform flash calculations at the new conditions of pressure and temperature in order to estimate the component split between phases.

3.5.3 Saturation Formulation

The overall mass fraction formulation remains impractical when a time-implicit scheme is used. As discussed in Chapter 4, a time-implicit scheme is preferred to solve transport equations, which are convection-diffusion PDEs. Eq. 3.40 may still be used with a time-implicit scheme, but a more stable formulation is obtained when solving for the fluid saturation. The convective fluxes are proportional to the fluid saturation, so solving for this variable tends to improve numerical stability. If there are more than two

components, the first transport equation is solved in terms of S_1 , and the subsequent transport equations are solved in terms of z_i or ω_{ij} .

Typically, foams are made of water and a second (energized) component, such as CO_2 and N_2 foams; and the water component does not partition in the gas phase. For N_2 foams, the liquid phase only contains water, and the gas phase only contains nitrogen. For CO_2 foams, the liquid phase contains water and some soluble CO_2 , and the gas phase only contains CO_2 . The amount of soluble CO_2 is predicted by the K -value K_2 , which is the mass fraction of CO_2 in the gas phase divided by the mass fraction of CO_2 in the liquid phase. For N_2 foams, $1/K_2$ is equal to 0. Only one equation is thus required to know the fluid composition. Eq. 3.40 may be written in terms of the saturation S_1 as follows:

$$\begin{aligned} & \frac{\partial}{\partial t} \left\{ S_1 w (1-c) \left(1 - \frac{1}{\bar{K}_2} \right) \rho_1 \right\} + \frac{\partial}{\partial x} \left\{ S_1 (1-c) \rho_1 A_1^* \alpha_{1,x} \left(1 - \frac{1}{\bar{K}_2} \right) \left(\frac{\partial P}{\partial x} \right) \right\} \\ & + \frac{\partial}{\partial y} \left\{ S_1 (1-c) \rho_1 A_1^* \alpha_{1,y} \left(1 - \frac{1}{\bar{K}_2} \right) \left(\frac{\partial P}{\partial y} + \rho_1^* g \right) \right\} + \frac{2}{\sqrt{t-\tau}} \left\{ \rho_1 C_{w,1} \left(1 - \frac{1}{\bar{K}_2} \right) \right\} = 0 \quad (3.43) \end{aligned}$$

where $\alpha_{j,x} = 1 + \frac{\rho_p}{\rho_j} \frac{\gamma_j}{1-\gamma_j} (1 - \lambda_{j,x})$

The associated ICs and BCs are given by:

$$\underline{ICs}: S_1 = S_1(t=0) \quad \text{over } \Omega \quad (3.44)$$

$$\underline{BCs}: \begin{cases} S_1 = S_{1,inj} & \text{on } \partial\Omega_p \\ \frac{\partial S_1}{\partial n} = 0 & \text{on } \partial\Omega_f \text{ and } \partial\Omega_c \end{cases} \quad (3.45)$$

The mathematical solution of the component transport equations is similar to the solution of the proppant transport equation.

3.6 ENERGY BALANCE EQUATION

An energy balance equation models the heat transfers occurring between the fracturing fluid and the reservoir. A rigorous treatment of heat transfers becomes important, as changes in temperature affect the fracturing fluid's composition, density, and rheology. The derivation of the energy balance equation requires additional assumptions, which are given below.

3.6.1 Energy Balance Assumptions

The additional assumptions required to derive the energy balance equation are:

- The fluid and proppant temperatures are the same.
- The injection temperature is known over time.
- The temperature does not vary along the fracture width (z -axis).
- The axial conduction in the fluid is negligible when compared to the forced convection in both the x and y directions.
- The kinetic and viscous effects are negligible as compared to forced convection.
- The enthalpy of a fluid phase is only temperature-dependent.
- The heat capacity of each phase is constant.
- The reservoir fluid(s) and the rock have the same temperature.
- The heat capacity of the reservoir is constant and refers to the heat capacity of the fluid-filled reservoir.

- Heat is transferred between the reservoir and the slurry by conduction at the fracture walls. The conduction is affected by fluid leak-off.
- Heat is lost by convection at the fracture walls due to fluid leak-off.
- The contributions of each fluid phase and proppant can be summed up linearly.

These assumptions are also mentioned later, as they are needed in the subsequent derivations.

3.6.2 Combined Energy Fluxes

The combined energy flux encompasses the convective energy flux, the molecular heat flux, and the viscous heat flux. Axial conduction is negligible compared to convection in the x - and y -directions. Also, the slurry flow rate is small enough that the heat dissipated by the viscous stresses and the kinetic energy is negligible; therefore, the combined energy flux of a given fluid becomes:

$$\vec{e} = \vec{q}_c + [\tilde{\tau} \cdot \vec{q}]_x + \left(\frac{1}{2} \rho v^2 + \rho H \right) \vec{q} = \rho H \vec{q} \quad (3.46)$$

We assume that the enthalpy of a given fluid is not pressure-dependent and only temperature-dependent. Assuming that the heat capacity of the fluid remains constant, the change in enthalpy is given by:

$$H - H^0 = \int_{T^0}^T C_p dT + \int_{T^0}^T \left[V - T \left(\frac{\partial V}{\partial T} \right)_P \right] dP = \int_{T^0}^T C_p dT = C_p (T - T^0) \quad (3.47)$$

Using an adequate enthalpy reference, the combined energy flux becomes:

$$\bar{e} = \rho C_p T \bar{q} \quad (3.48)$$

We now assume that the slurry is composed of NP phases containing proppant. The proppant and the fluid are assumed to be at the same temperature. They form a pseudo single phase, whose thermal properties depend on both the proppant and the fluid thermal properties. We define an equivalent heat capacity for each slurry phase ($C_{p,j}^*$) as the weighted average of the slurry properties:

$$C_{p,j}^* = \frac{(1-c)C_{p,j}\rho_j + cC_{p,p}\rho_p}{(1-c)\rho_j + c\rho_p} = \frac{(1-c)C_{p,j}\rho_j + cC_{p,p}\rho_p}{\rho_j^*} \quad (3.49)$$

The total energy flux is the sum of the contributions of the NP slurry phases. Assuming that these contributions are independent, the combined energy flux becomes:

$$\bar{e} = \sum_{j=1}^{NP} (\rho H \bar{q})_j = T \sum_{j=1}^{NP} (\rho_j^* C_{p,j}^* \bar{q}_j^*) \quad (3.50)$$

3.6.3 Heat Lost due to Leak-off

Heat is lost to the rock formation through the fracture walls as the fluid leaks off. We assume that the conduction, the viscous effects and the kinetic effects are negligible compared to the convective heat transfers. The combined energy flux for a single-phase fluid leaking-off is defined in the direction normal to the fracture face as:

$$e_l = q_{c,l} + [\tau \cdot q_l]_z + \left(\frac{1}{2} \rho v^2 + \rho H \right) q_l = \rho H q_l = \rho C_p T q_l \quad (3.51)$$

The fluid-loss rate follows Carter's model (1957). The total energy flux is the sum of the contributions of the NP slurry phases. Assuming that these contributions are independent, the energy flux for a multi-phase fluid leaking-off is given by:

$$e_l = \frac{2}{\sqrt{t-\tau}} T \left(\sum_{j=1}^{NP} \rho_j C_{p,j} C_j \right) \quad (3.52)$$

3.6.4 Heat Gained from the Reservoir

The reservoir formation heats the fluid by conduction. Conversely, the reservoir placed in contact with the fracture cools down over time. In some cases, this is precisely the objective of the stimulation treatment. As the reservoir cools down, the rock shrinks and becomes more brittle. This effect, referred to as *thermally-induced fracturing*, promotes fracture propagation.

Since the fracture is very narrow, we assume that the surface heat transfers only occur along the z -axis, which is normal to the fracture face. We also assume that there is no heat transfer occurring along the y -axis. This reduces the transient heat transfer problem to a pseudo 1D transient problem for each horizontal slice of the reservoir. The undisturbed reservoir temperature is a known function of depth, so the heat conduction flux remains dependent on depth. **Fig. 3.4** shows a simplified schematic of the pseudo 1D problem. The undisturbed reservoir temperature is the temperature of the reservoir far away from the fracture. Mathematically, it is the temperature for z going to infinity.

If we neglect the convective effect of the fluid loss into the formation, the energy balance reduces to the transient 1D heat equation along the z -axis. This well-known problem has been solved analytically by many authors, including Carslaw and Jaeger (1959), and Hasan and Kabir (2002). The conductive heat flux is proportional to the temperature difference between the undisturbed reservoir temperature and the temperature of the rock directly in contact with the fracture. The conductive heat flux per unit height is given by:

$$Q_{cond}(x, y, t) = 2\sqrt{\frac{K_R \rho_R C_{pR}}{\pi t}} (T_f(x, y, t) - T_R(y)) \quad (3.53)$$

Eq. 3.53 is valid for a purely conductive problem. This is not the case here because some of the fracturing fluid leaks off into the rock formation. Additional correction factors have been identified to model the reduction of heat conduction associated with leak-off (Meyer 1989). This correction, referred to as heat blockage, encompasses both the cooling of the reservoir due to fluid leak-off and the additional thermal resistance offered by the fluid that has invaded the formation:

$$Q_{cond}(x, y, t) = 2\sqrt{\frac{K_R \rho_R C_{pR}}{\pi t}} (T_f(x, y, t) - T_R(y)) \psi(C) \Phi(C) \quad (3.54)$$

The two correction terms are time-dependent. They have been identified by Meyer (1989) as:

$$\begin{cases} \psi(C) = \exp(-\lambda^2) - \sqrt{\pi} \lambda \operatorname{erfc}(\lambda) \\ \Phi(C) = \sqrt{\pi} \beta \exp(\beta^2) \operatorname{erfc}(\beta) \end{cases} \quad \text{where} \quad \begin{cases} \lambda = \frac{C}{2\sqrt{\alpha_R}} \frac{(\rho C p)_{fL} \rho_f}{(\rho C p)_R \rho_{fL}} \\ \beta = \frac{\beta_o \sqrt{1-t/\tau}}{w / w_{\max}} \\ \beta_o = \frac{Nuk_f \sqrt{\alpha_R t}}{wk_R \Psi(\lambda)} \end{cases} \quad (3.55)$$

3.6.5 Energy Balance Equation

The general expression of the unsteady energy balance equation is given by:

$$\frac{\partial}{\partial t} (w(\rho H)_T) + \nabla \cdot (\vec{e}) + e_i - Q_{cond} = 0 \quad (3.56)$$

For a multi-phase slurry mixture, the accumulation term is defined as a linear combination of enthalpy terms:

$$w(\rho H)_T = Tw \left(\sum_{j=1}^{NP} S_j^* \rho_j^* C_{p,j}^* \right) \quad (3.57)$$

Inserting Eqs. 3.50, 3.52, 3.54, and 3.57 into Eq. 3.56, the unsteady energy balance equation takes the form of a convective-dominated equation:

$$\begin{aligned} & \frac{\partial}{\partial t} \left\{ Tw \left(\sum_{j=1}^{NP} S_j^* \rho_j^* C_{p,j}^* \right) \right\} + \frac{\partial}{\partial x} \left\{ T \left(\sum_{j=1}^{NP} q_{j,x}^* \rho_j^* C_{p,j}^* \right) \right\} + \frac{\partial}{\partial y} \left\{ T \left(\sum_{j=1}^{NP} q_{j,y}^* \rho_j^* C_{p,j}^* \right) \right\} \\ & + \frac{2}{\sqrt{t-\tau}} \left\{ T \left(\sum_{j=1}^{NP} \rho_j C_{p,j} C_{w,j} \right) \right\} + \frac{2}{\sqrt{t-\tau}} \sqrt{\frac{K_R \rho_R C_{p,R}}{\pi}} \psi(C) \Phi(C) (T - T_R) = 0 \end{aligned} \quad (3.58)$$

Initially, the temperature equals the temperature of the fluid injected at the perforations. As for the proppant transport equation, Dirichlet BCs are imposed at the perforations and no-flux Neumann BCs are imposed everywhere else:

$$\underline{ICS}: T = T_{inj} (t = 0) \quad \text{over } \Omega \quad (3.59)$$

$$\underline{BCS}: \begin{cases} T = T_{inj} & \text{on } \partial\Omega_p \\ \frac{\partial T}{\partial n} = 0 & \text{on } \partial\Omega_f \text{ and } \partial\Omega_c \end{cases} \quad (3.60)$$

3.7 PHASE BEHAVIOR

Thus far, we have derived five different PDEs governing the pressure, proppant distribution, component mass fraction, temperature, and fracture width. Additional equations are required to enforce the local thermodynamic equilibrium, which postulate

that all phases are in phase equilibrium at all times. These classical thermodynamic equations are local expressions that are valid at each nodal location.

There is no assumption regarding the phase behavior of the fluid. Any *a priori* model that describes changes in phase behavior of the fluid as a function of temperature, pressure, and composition can easily be incorporated into the fracture model since we use local values at each node. The thermodynamic equations consist of: (1) NP equations governing the density of each fluid phase, (2) $NC*(NP-1)$ fugacity equations ensuring thermodynamic equilibrium for each component, and (3) NP continuity equations ensuring that the sum of the mass fractions in a given phase equals one. Although these equations will be discussed in greater detail in Chapter 7, they are mentioned here in the interest of completeness.

3.7.1 Phase Density

The density of a given phase is a function of pressure, temperature, and fluid composition. Any equation of state (EoS) may be used to predict phase density. This is the most general approach, as the same ES is able to predict the phase density of different fluids. Friehauf and Sharma (2009) followed this approach and used the Peng-Robinson EoS. However, a given EoS may not be particularly suited to a certain fluid type. For instance, the Peng-Robinson EoS is not well-suited for polar fluids like water. Since water is the most common component used in fracturing, this choice may not be judicious. Also, the use of an EoS significantly slows down the computations.

An alternative approach is to use empirical correlations for estimating phase density. For liquid-like fluids, thermal expansion (α_T) and isothermal compressibility (β_P) are taken into account. For gas-like fluids, phase density may be calculated from the real

gas EoS, for which the compressibility factor is obtained from a mathematical fit of the experimental work of Standing and Katz (1942). In fact, any *a priori* correlation may be implemented into the code. These correlations provide a simple yet effective way to estimate the density of a given fluid phase:

$$\rho(P,T) = \rho_0(P_0, T_0) \times e^{[-\alpha_T(T-T_0)]} \times e^{[\beta_P(P-P_0)]} \quad (3.61)$$

$$\rho(P,T) = \frac{M_w P}{Z(P, T_r) RT} \quad (3.62)$$

The main advantages of this approach are its simplicity, rapidity, and flexibility. However, this approach is not general, so an additional correlation may be required when a new fluid type is prescribed.

3.7.2 Component Split between Phases (Solubility)

Similarly, the component split between phases may be obtained from an EoS, Friehauf and Sharma (2009) used the Peng-Robinson EoS for that purpose. However, this method is computationally demanding, particularly for a 3D code. Instead, the solubility of two phase multi-component systems may be estimated from K -values that are function of pressure and temperature. The K -values capture the physics expressed by Henry's Law, which states that the solubility of a gas in a liquid is directly proportional to the partial pressure of the gas above the liquid. This is the preferred approach in this work.

$$K_{eq,i} = \frac{y_i}{x_i} = \frac{\omega_{i2}}{\omega_{i1}} = f(P, T) \quad (3.63)$$

The K -values result from the more general requirement that the fugacity of each component remains equal in all phases:

$$f_i^{(1)} = f_i^{(2)} = \dots = f_i^{(NP)} \quad (3.64)$$

Eq. 3.64 is valid for each component, so the number of fugacity equations is equal to $NC*(NP-1)$. The last requirement is imposed by the continuity equation in each phase. The sum of the mass fractions of all the components contained in a given phase equals one:

$$\sum_{i=1}^{NC} \omega_j = 1 \quad (3.65)$$

3.7.3 Phase Behavior of most Common Fracturing Fluids

A very general formulation of the problem may appear impractical in some cases. The following list of fracturing fluids covers more than 99.9% of the field treatments: water, visco-elastic surfactant, pure CO₂, LPG, pure N₂, CO₂ foam, N₂ foam, binary CO₂-N₂ foam, and methanol-CO₂ foam. These fluid formulations may or may not contain a gelling agent. We assume that the gelling agent does not alter phase behavior, but only fluid rheology. Similarly, we assume that the presence of proppant does not alter phase behavior. For these fluids, simple empirical correlations can be used to characterize their phase behavior. These correlations may be tailored to accurately model fluid density and component solubility. For more exotic fluids, general equations can still be used to predict their density and solubility.

For single-phase fluids, fluid composition remains constant, irrespective of the number of components in that phase. There is no need to solve the component mass fraction equations, and the fugacity equations are not required. The remaining task is to estimate the phase density as a function of pressure and temperature for a given mixture

of components. For instance, the density of LPG mixtures is affected by the presence of heavy components.

For two-phase fluids, the number of fugacity equations equals NC . In our formulation, the NC fugacity equations (3.60) are replaced by the NC K -values equations (3.59). In most cases, one of the components (water) does not partition into the gas phase, so the saturation formulation presented in section 3.5 is preferred over the component mass fraction formulation. The last task is to estimate the phase density of each phase as a function of pressure, temperature, and composition. The only difference with the single-phase case is that the composition of a given phase is no longer constant.

3.7.4 Comments on the Modeling of Foams

The modeling of (stable) foams² is based on several critical assumptions that are summarized in this section. As discussed in Section 3.2.4, foam is regarded as a single “pseudo phase” from a transport standpoint, as the two phases travel at the same velocity. Alternatively, as mentioned in Section 3.7.3, foam is regarded as two separate phases from a thermodynamic standpoint, as each individual phase has its own density and composition. The two approaches coexist with the following assumptions:

1. *Viscosity*: Foam is regarded as a single pseudo phase: the same power-law parameters are assigned to both phases; therefore, the two phases travel at the same velocity and there is no slippage.
2. *Interfacial forces*: Interfacial forces prevent gravity segregation. The surfactant limits the coalescence of gas bubbles, which enables them to coexist with the external liquid phase.

² Unless stated otherwise, “foams” always imply “stable foams” in this dissertation.

3. *Phase density*: Each phase has its own density, which is a function of pressure, temperature, and composition. The variations in phase density explain the variations in foam quality along the wellbore.
4. *Leak-off*: Each phase has its own individual leak-off coefficient. The preferential leak-off of the liquid phase contributes to variations in foam quality inside the fracture.
5. *Composition*: The composition of each phase is governed by the local thermodynamic equilibrium. The solubility of each component is a function of pressure and temperature.
6. *Proppant*: The addition of proppant modifies the rheology of the pseudo phase and the density of the mixture; however, it does not impact the phase behavior of the two phases.

In essence, foam is regarded as a single pseudo phase (items 1, 2, and 6), whose properties depend on foam quality and phase behavior of each phase (items 3, 4, and 5). Although there is no slippage due to viscosity variations and there is no gravity segregation, the foam quality varies because of differentiated leak-off, phase expansion, and solubility.

3.8 FRACTURE MECHANICS

As mentioned in Chapter 2, our treatment of the fracture mechanics problem is similar to the work proposed by Yew, Gu, Carey, and Ouyang, who developed one of the first 3D planar fracturing codes in the early 1990s. The equations presented in this section are given without their derivations because they are identical to the ones presented by

these authors. For more information regarding the mechanical formulation of the problem, the reader is encouraged to refer to Gu (1987), Ouyang (1994), and Yew (1997).

3.8.1 Fracture Opening Equation

Assuming an isotropic, homogeneous, elastic medium, the 3D elasticity problem is essentially the Navier-Cauchy problem relating strains to applied stresses. Under these assumptions, the problem reduces to the tensile mode-I fracture opening equation. For planar fractures, the fracture opening equation is a boundary integral equation that relates the pressure on the crack faces to the crack opening. A boundary integral formulation is required since a local stress applied at a given location deforms the entire surface of the elastic body. The integral equation was derived independently by Kossecka (1971), Bui (1977), and Weaver (1977):

$$-P(x, y) + \sigma_{h\min}(x, y) = \frac{G}{4\pi(1-\nu)} \int_{\Omega} \left[\frac{\partial}{\partial x} \left(\frac{1}{r} \right) \frac{\partial w(x, y)}{\partial x'} + \frac{\partial}{\partial y} \left(\frac{1}{r} \right) \frac{\partial w(x, y)}{\partial y'} \right] d\Omega \quad (3.66)$$

where $r = \sqrt{(x' - x)^2 + (y' - y)^2}$

Eq. 3.66 gives the width of the fracture for a known load distribution. The load is defined locally as the difference between the fluid pressure in the fracture and the minimum horizontal stress acting on the fracture face. Additionally, the fracture width is zero along the fracture front:

$$\underline{BC} : w = 0 \quad \text{on } \partial\Omega_f \quad (3.67)$$

3.8.2 Criterion for Fracture Propagation

The fracture propagation criterion follows the theory of linear elasticity for a brittle material subject to tensile (mode-I) opening. The theory involves the computation

of the mode-I stress intensity factor (K_I), which is used to predict the stress state (or “stress intensity”) near the tip of the crack caused by a remote load. The expression of the stress intensity factor depends on the mode of failure and the geometry of the problem. For mode-I opening of a 3D planar crack, K_I is given by:

$$K_I(x, y) = \frac{G}{4(1-\nu)} \sqrt{\frac{2\pi}{r_{tip}(x, y)}} w(x, y) \quad (3.68)$$

In Eq. 3.68, $r_{tip}(x, y)$ is the minimum distance between the node of interest located at (x, y) and the fracture front. A fracture propagation criterion controls the advance of the crack front, by relating the intensity of the stress state ahead of the crack to the critical intensity necessary for tensile opening of the rock. Front propagation is proportional to the difference between K_I and the rock toughness (K_{IC}), as established by Mastrojannis *et al.* (1979). The criterion for fracture propagation is applied locally as:

$$\Delta d = \max\left(\Delta d_{\max}\left(\frac{K_I - K_{IC}}{K_{IC}}\right); 0\right) \quad (3.69)$$

Eq. 3.69 ensures that a given location along the fracture boundary is not propagating artificially if the local stress intensity factor does not exceed the critical value. The direction of displacement is not prescribed in advance, and the fracture shape evolves freely in all the directions contained in the propagation plane. This 3D formulation significantly differs from 2D mechanical models, which require that the fracture boundary in the plane of propagation be specified in advance.

3.9 OVERVIEW OF THE MATHEMATICAL PROBLEM

The system of PDEs presented in this chapter constitutes the core of this research work. This section addresses the completeness of the mathematical problem and the main complexities associated with the resolution of the fundamental system of PDEs.

3.9.1 Completeness of the Mathematical Problem

Before attempting to solve the mathematical problem, it is critical to ensure that the problem is well-posed. This is (usually) the case when the number of independent variables equals the number of independent equations. At a given time, the fracture problem is fully solved if we can compute the fracture geometry, fluid composition, fluid temperature, fluid pressure, and proppant distribution. The fluid composition is characterized by the saturation, density, and component mass fraction(s) in each phase. As seen on the left side of **Table 3.2**, the number of independent variables equal $(4+3NP+NC*NP)$ for a fluid containing NC components distributed in NP phases. Additional variables are dependent variables that are directly defined from this set of independent unknowns. For example, the overall mass fraction of each component (z_i) is a dependent variable defined by Eq. 3.8.

Thus far, we have derived five different PDEs governing pressure, proppant distribution, component mass fraction, temperature, and fracture width. In addition, the local thermodynamic equations consist of: (1) NP equations of states governing the density of each fluid phase, (2) $NC*(NP-1)$ fugacity equations ensuring thermodynamic equilibrium for each component, and (3) NP continuity equations ensuring that the sum of the mass fractions in a given phase equals one. For some of these equations, we presented multiple formulations. For example, Section 3.5 presented equations that may

be solved for the mass fraction of each component in each phase (ω_{ij}), for the overall mass fraction of each component (z_i), or for the fluid saturation (S_1). In fact, there is infinity of dependent equations that could be derived from the above equations. For instance, the pressure equation is simply the sum of all the component mass fractions equations and the proppant transport equation.

As seen on the right side of **Table 3.2**, the degree of freedom of the equations equals $(4+3NP+NC*NP)$ for a fluid containing NC components distributed in NP phases. The set of equations presented here constitutes a complete set of independent equations, for which the number of independent equations equals the number of independent variables. The compositional fracture problem is well-posed and a numerical solution is possible.

3.9.2 Complexity of the Mathematical Problem

Solving this set of PDEs is a challenging task for five main reasons:

- The PDEs are of different classes (elliptic versus parabolic-hyperbolic);
- There is a strong coupling between the PDEs;
- Several of the PDEs are non-linear;
- This is a moving-boundary problem; and
- The fracture opening equation is singular.

These complexities have hindered the development of fracturing codes for many years, and they still represent a challenging task today.

3.9.2.1 Different Classes of PDEs

A PDE's class plays a fundamental role in the behavior of the solutions, particularly in determining the smoothness of the solutions. The nature of the appropriate initial and boundary conditions depend on the PDE's class. Typically, solutions of elliptic PDEs are as smooth as the coefficients allow. For example, solutions of Laplace's equation are analytic within the domain where they are defined, but solutions may assume boundary values that are not smooth. The pressure equation is an elliptic PDE. The dominant term is the spatial derivative of second order, which smoothes out the solution within the interior of the domain. The variable of interest (pressure) does not appear in the accumulation term, which is viewed as a source term.

Alternatively, the accumulation term plays a critical role in parabolic PDEs. Solutions of parabolic PDEs smooth out as the time variable increases. The absence of a dominant diffusion term promotes the formation of sharp fronts and discontinuities, which may cause the solution to oscillate. The proppant transport, component transport, and temperature equations are convection-dominated PDEs; therefore, they are more prone to oscillations. In general, spatial derivatives of even order (2nd order in our case) dampen oscillations while derivatives of odd order (1st order in our case) promote oscillations. The numerical treatment of these equations is significantly different.

3.9.2.2 Strong Coupling between the PDEs

The numerous inter-dependences between the PDEs further complicate the resolution of the set of PDEs. For instance, the pressure equation and the fracture opening equation are tightly coupled. The presence of the $1/w^3$ term in the pressure equation

makes the equation highly sensitive to changes in fracture width. As discussed in Chapter 4, a complex iterative scheme is required to solve these coupled equations.

3.9.2.3 Non-Linearity

Several of the constitutive PDEs are nonlinear. The convective term in the pressure equation involves the square of the pressure gradient, which introduces a non-linearity. Similarly, the convective flux in the proppant transport equation is also a function of the proppant concentration. The non-linearity is more subtle in the energy balance equation, as the density is itself a function of temperature. The use of iterative schemes reduces some of the numerical instabilities associated with the non-linearity of the PDEs.

3.9.2.4 Moving-Boundary Problem

Perhaps the most defining feature of the fracture propagation problem is that it is a moving-boundary problem. This characteristic is highly unusual in most engineering disciplines. In mathematics, a moving-boundary (or “free-boundary”) problem is a PDE to be solved for both an unknown function and an unknown domain Ω . The segment $\partial\Omega$ of the boundary of Ω which is not known at the outset of the problem is the free boundary.

The classic example is the melting of ice. Given a block of ice, we can solve the heat equation given appropriate initial and boundary conditions to determine its temperature. However, if in any region the temperature is greater than the melting point of ice, this domain will be occupied by liquid water instead. This problem is the classical Stefan problem, which aims to describe the temperature distribution in a homogeneous medium undergoing a phase change. This is accomplished by solving the heat equation

imposing the initial temperature distribution on the whole medium, and a particular boundary condition, the Stefan condition, on the evolving boundary between its two phases. The location of the ice/liquid interface is controlled dynamically by the solution of the PDE. This evolving boundary is an unknown surface that constitutes a fundamental part of the solution. Similarly, the fracture propagation problem is a moving-boundary problem, and the primary objective of the model is to track the evolution of the boundary (fracture shape) over time.

3.9.2.5 Singularities

Finally, the fracture opening equation becomes singular as r converges to zero, and thus $1/r$ diverges to infinity. As discussed by Yew (1997), this boundary integral equation is weakly singular, and it converges only in a Cauchy principal value sense. The singularity is overcome by using an appropriate coordinate transformation in the finite element formulation of the problem and by using specific elements along the fracture tip. However, the use of specific elements to perform the stress-intensity calculations makes the propagation criterion intrinsically grid-dependent (Economides and Nolte 2000). The methods used to overcome these singularities are addressed in Chapter 4.

3.10 COMPARISON WITH EXISTING MODELS

This section highlights the differences between the new model and past fracturing models. In particular, we emphasize the differences between this 3D compositional model and the 2D compositional model developed by Frieauf and Sharma (2009).

3.10.1 Comparison with 3D Planar Fracture Models

For traditional fluid formulations, this 3D compositional fracture model is designed to be similar to traditional 3D planar fracture models. Therefore, the treatment of the fracture mechanics problem is similar to the formulation used by many authors who modeled 3D planar fracture propagation: Clifton and Abou-Sayed (1981), Barree (1983), Cleary *et al.* (1983), Abou-Sayed *et al.* (1984), Settari and Cleary (1984), and Yew (1997). However, the treatment of the fluid flow problem differs. The main differences between this model and a traditional 3D planar model are comparable to the differences between a compositional reservoir model and a black oil reservoir model. The main differences include:

- Multi-phase, multi-component, compressible fluid flow;
- Changes in fluid temperature and composition inside the fracture;
- Changes in fluid composition inside the fracture; and
- Phase-dependent leak-off.

3.10.2 Comparison with a 2D Compositional Model (Friehauf and Sharma 2009)

The only other compositional fracturing model is the 2D model developed by Friehauf and Sharma (2009). In their model, the fracture geometry is limited to a constant-height, PKN-like fracture geometry, while our model allows for 3D planar fracture propagation. In addition, subtle differences exist regarding the derivations of the fluid flow equations. The additional capabilities of the new model are listed below:

3.10.2.1 Fracture Mechanics

- The fracture can propagate across multiple layers.

- The direction of fracture propagation is not prescribed.
- The vertical distribution of the minimum horizontal stress and the mechanical properties of the bounding layers impact fracture growth.
- The fracture toughness influences fracture length and height growth.
- The gravity effect impacts the shape of the fracture.
- The width profile is not necessarily symmetric, and the maximum fracture width is not necessarily at the wellbore.

3.10.2.2 Flow Equations

- The proppant concentration does not have to be uniform between phases.
- The density and solubility calculations are preferably performed using empirical correlations (instead of using an EoS).
- The fluid phase accelerates compared to its proppant counterpart.
- Proppant settling and retardation are phase-dependent.
- The leak-off rate is not necessarily proportional to the phase saturation.

3.10.2.3 General Features

- The wellbore may be vertical, deviated, or horizontal.
- The tubing, casing, and cement dimensions can vary along the wellbore.
- The frictional loss drop through the perforations is calculated.
- The productivity calculations may be done in multiple layers.
- This model does not allow the propagation of multiple fractures.

In the model developed by Friehauf and Sharma (2009), multiple fractures can be initiated from the same vertical wellbore. This is one of the recommended future developments for the new model. This feature would be particularly useful for simulating the propagation of multiple fractures from the same horizontal wellbore.

Table 3.1: Main properties defining slurry, proppant, and fluid phases.

Properties	Slurry Phase	Proppant Phase	Fluid Phase
Density	$\rho_j^* = \rho_p \gamma_j + \rho_j (1 - \gamma_j)$	ρ_p	ρ_j
Saturation	S_j^*	γ_j	$S_j = S_j^* \left(\frac{1 - \gamma_j}{1 - c} \right)$
Flux (x-axis)	$q_{j,x}^* = A_j S_j^* \left(\frac{\partial P}{\partial x} \right)$	$q_{p,j,x} = q_{j,x}^* \gamma_j \lambda_{j,x}$	$q_{j,x} = q_{j,x}^* \left((1 - \gamma_j) + \frac{\rho_p}{\rho_j} \gamma_j (1 - \lambda_{j,x}) \right)$
Flux (y-axis)	$q_{j,y}^* = A_j S_j^* \left(\frac{\partial P}{\partial y} + \rho_j^* g \right)$	$q_{p,j,y} = q_{j,y}^* \gamma_j \lambda_{j,y}$	$q_{j,y} = q_{j,y}^* \left((1 - \gamma_j) + \frac{\rho_p}{\rho_j} \gamma_j (1 - \lambda_{j,y}) \right)$

Table 3.2: List of independent variables and equations. The problem is well-posed, as the number of independent equations equals the number of independent variables.

Unknowns	Number of Independent Variables	Equations	Degree of Freedom
w	1	Fracture Mechanics	1
c	1	Proppant Transport	1
T	1	Energy Balance	1
F_j^*	NP	Flow Equations	NP
ρ_j	NP	Equation of State	NP
P	1	$\sum S_j = 1$	1
S_j	NP	$\sum x_{ij} = 1$	NP
ω_{ij}	$NC^* NP$	Fugacity Equations	$NC^*(NP-1)$
Total	$4+3NP+NC^*NP$	Total	$4+3NP+NC^*NP$

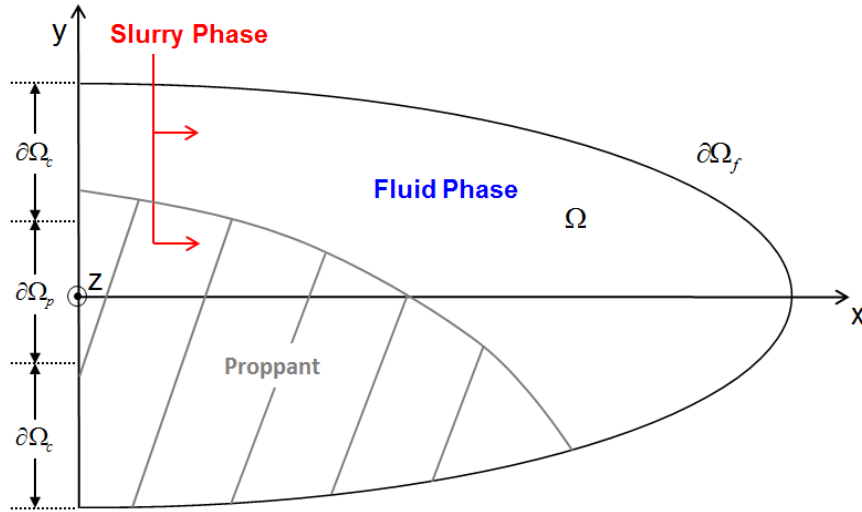


Figure 3.1: Representation of the fracture domain (Ω). The boundary of the domain ($\partial\Omega$) consists of the fracture front ($\partial\Omega_f$), the perforated interval along the wellbore ($\partial\Omega_p$), and the non-perforated section of the wellbore ($\partial\Omega_c$).

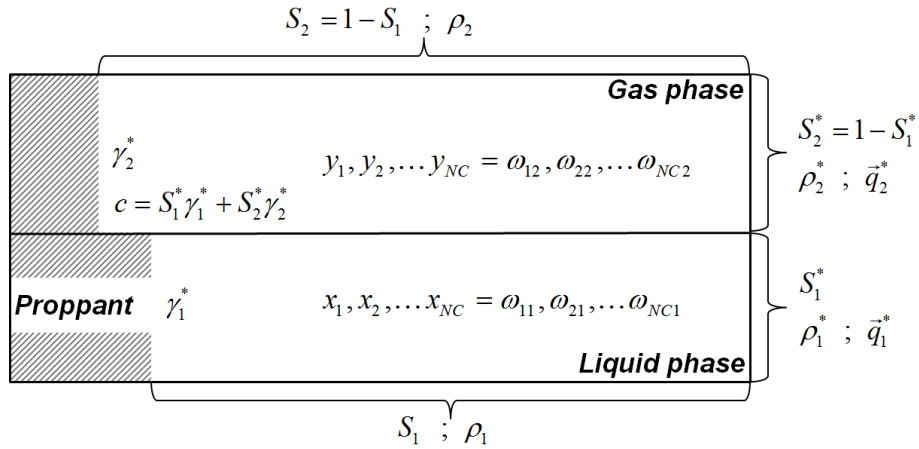


Figure 3.2: Representation of the main variables characterizing a two-phase slurry mixture. These variables are defined in the nomenclature.

Gas phase	$\left\{ \begin{aligned} z_1 &= \frac{0.94 \times 0.3 \times 63 + 0 \times 0.7 \times 51}{0.3 \times 63 + 0.7 \times 51} \approx 0.325 \\ z_2 &= \frac{0.06 \times 0.3 \times 63 + 1 \times 0.7 \times 51}{0.3 \times 63 + 0.7 \times 51} \approx 0.675 \end{aligned} \right.$
$\left\{ \begin{aligned} y_1 &= 0 \\ y_2 &= 1 \end{aligned} \right. ; S_2 = 0.7 ; \rho_2 = 51 \frac{lbm}{ft^3}$	
Liquid phase	
$\left\{ \begin{aligned} x_1 &= 0.94 \\ x_2 &= 0.06 \end{aligned} \right. ; S_1 = 0.3 ; \rho_1 = 63 \frac{lbm}{ft^3}$	

Figure 3.3: Example of compositional calculations for 0.7-quality CO₂ foam.

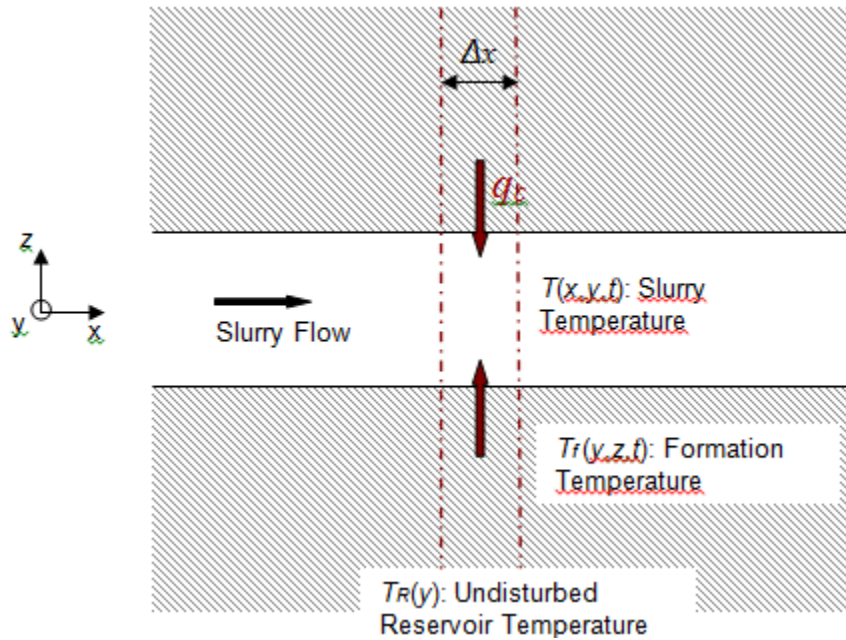


Figure 3.4: Pseudo 1D transient heat transfer between the fracture and the reservoir (top view).

NOMENCLATURE

A_j^*	= intermediate variable defined by Eq. 3.13, $\text{ft}^5/(\text{lbf}\cdot\text{min})$	$q_{p,j,y}^*$	= flow rate per unit height of proppant in phase j in the vertical direction, ft^2/min
c	= proppant concentration (volume fraction)	m_{pumped}	= mass rate imposed at the perforations, lbm/min
$C_{p,j}$	= heat capacity of fluid phase j , $\text{BTU}/(\text{lbm}\cdot^\circ\text{F})$	M_w	= molecular weight, atomic mass unit
$C_{p,j}^*$	= heat capacity of slurry phase j , $\text{BTU}/(\text{lbm}\cdot^\circ\text{F})$	n	= normal direction
$C_{w,j}$	= leakoff coefficient of fluid phase j , $\text{ft}/\sqrt{\text{min}}$	n_j	= flow behavior index of slurry phase j
g	= gravity of earth, ft/s^2	NC	= number of components
G	= shear modulus of the rock, psi	NP	= number of phases
H	= enthalpy, $\text{psi}\cdot\text{ft}^3$	P	= fluid pressure, psi
K_j	= flow consistency index of slurry phase j , $\text{lbm}\cdot\text{min}^n/\text{ft}^2$	P_c	= critical pressure, psi
$k_{ret,j}$	= retardation factor for slurry phase j in the horizontal direction	P_r	= reduced pressure (P/P_c)
K_i	= K -value for component i	P_0	= reference pressure, psi
K_I	= stress intensity factor, $\text{psi}\cdot\sqrt{\text{in}}$	r	= distance between the source and the field point in Eq. 3.66, ft
K_{IC}	= fracture toughness, $\text{psi}\cdot\sqrt{\text{in}}$	r_{tip}	= distance to the fracture tip, ft
K_R	= thermal conductivity of rock, $\text{BTU}/(\text{min}\cdot\text{ft}\cdot^\circ\text{F})$	R	= gas constant, $\text{ft}\cdot\text{lbf}/(\text{lbm}\cdot^\circ\text{R})$
K_γ	= proppant split between two phases (γ_2/γ_1)	S_j	= saturation of fluid phase j
$q_{j,x}$	= flow rate per unit height of fluid phase j in the horizontal direction, ft^2/min	S_j^*	= saturation of slurry phase j
$q_{j,y}$	= flow rate per unit height of fluid phase j in the vertical direction, ft^2/min	t	= time, min
$q_{j,x}^*$	= flow rate per unit height of slurry phase j in the horizontal direction, ft^2/min	T	= fluid temperature, $^\circ\text{F}$
$q_{j,y}^*$	= flow rate per unit height of slurry phase j in the vertical direction, ft^2/min	T_c	= critical temperature, $^\circ\text{F}$
$q_{L,j}^*$	= fluid loss flow rate per unit height of fluid phase j , ft/min	T_r	= reduced temperature (T/T_c)
$q_{p,j,x}^*$	= flow rate per unit height of proppant in phase j in the horizontal direction, ft^2/min	T_R	= reservoir temperature, $^\circ\text{F}$
		T_0	= reference temperature, $^\circ\text{F}$
		V_{fluid}	= total volume of fluid, ft^3
		V_j	= volume of fluid phase j , ft^3
		V_j^*	= volume of slurry phase j , ft^3
		V_P	= total volume of proppant, ft^3
		$V_{P,j}$	= volume of proppant in slurry phase j , ft^3
		V_{set}	= settling velocity, ft/min
		V_{stokes}	= Stokes settling velocity, ft/min
		V_T	= total slurry volume, ft^3
		w	= fracture width, ft
		x	= horizontal location, ft
		y	= vertical location, ft
		Z	= compressibility factor

Subscripts

i = component i

inj = boundary conditions at the perforations
 j = phase j
 $p/prop$ = proppant
 R = reservoir
 T = total

Superscripts

n = time step n
 $*$ = slurry property
 $'$ = field point in Eq. 3.66

Greek Symbols

α_T = thermal expansion, $1/^\circ\text{F}$
 β_P = isothermal compressibility, $1/\text{psi}$
 γ_j = proppant concentration (volume fraction) in slurry phase j
 Δd = displacement of the fracture front in the normal direction, ft
 Δd_{max} = maximum displacement of the fracture front, ft
 $\partial\Omega$ = boundary of the fracture domain
 $\partial\Omega_c$ = non-perforated portion along the wellbore
 $\partial\Omega_f$ = fracture front
 $\partial\Omega_p$ = perforated interval along the wellbore

$\Delta m_{fracture}$ = change in fracturing fluid mass during Δt^n , lbm
 $\Delta m_{leakoff}$ = mass of fluid that leaked off during Δt^n , lbm
 $\Delta P_{toughness}$ = initiation net pressure, psi
 Δt^n = time step increment, min
 $\lambda_{j,x}$ $\lambda_{j,y}$ = retardation factor for proppant in phase j in the horizontal and vertical direction
 μ = fluid viscosity, cp
 ρ_j = density of fluid phase j , lbm/ft^3
 ρ_j^* = density of slurry phase j , lbm/ft^3
 ρ_p = density of proppant, lbm/ft^3
 ρ_R = density of reservoir rock, lbm/ft^3
 ρ_T^* = density of slurry, lbm/ft^3
 ρ_0 = density of reference at (P_0, T_0) , lbm/ft^3
 σ_{hmin} = *in-situ* minimum horizontal stress, psi
 τ = retardation factor, min
 ν = Poisson's ratio of the rock
 ω_{ij} = mass fraction of component i in phase j
 Ω = fracture domain

REFERENCES

- Abou-Sayed, A.S, Sinha, K.P., and Clifton, R.J 1984. Evaluation of the Influence of *In-Situ* Reservoir Conditions on the Geometry of Hydraulic Fractures Using a 3-D Simulator: Part 1–Technical Approach, Paper SPE/DOE/GRI 12877, Unconventional Gas Recovery Symposium, Pittsburg, Pennsylvania, 13-15 May.
- Adachi, J.I, Siebrits, E., Peirce, A., and Desroches, J. 2007. Computer Simulation of Hydraulic Fractures, *Int. J. Rock Mech. and Min. Sci. & Geomech.* **44**: 739-757.
- Barree, R.D. 1983. A Practical Numerical Simulator for Three-Dimensional Hydraulic Fracture Propagation in Heterogeneous Media. Paper SPE 12273 presented at the SPE Symposium on Reservoir Simulation, San Francisco, California, 15-18 November.
- Bui, H. 1977. An Integral Equations Method for Solving the Problem of a Plane Crack of Arbitrary Shape. *J. Mech. Phys. Solids* **25**: 29-39.
- Carslaw, H.S. and Jaeger, J.C. 1959, *Conduction of Heat in Solids*, 2nd edition, Clarendon Press, Oxford, UK.
- Carter, R.D. 1957. Derivation of the general equation for estimating the extent of the fractured area, Appendix to *Optimum Fluid Characteristics for Fracture Extension*, by Howard, G.C. and Fast, C.R., *Drilling and Production Practices*, API: 261-270.
- Cleary, M.P., Kawadas, M., and Lam, K.Y. 1983. Development of a Fully Three-Dimensional Simulator for Analysis and Design of Hydraulic Fracturing. Paper SPE 11631 presented at the Symposium on Low-Permeability Gas Reservoirs, 14-16 March 1983, Denver, Colorado.
- Clifton, R.J. and Abou-Sayed, A.S. 1981. A Variational Approach to the Prediction of the Three-Dimensional Geometry of Hydraulic Fractures. Paper SPE 9879 presented at the SPE/DOE Low Permeability Gas Reservoirs Symposium, Denver, Colorado, 27-29 May.
- Economides, M. and Nolte, K.G. 2000, *Reservoir Stimulation, Third Edition*, John Wiley and Sons, New York City, New York.
- Friehauf, K.E. 2009. Simulation and Design of Energized Hydraulic Fractures. Ph.D. Dissertation, The University of Texas at Austin, Austin, Texas (August 2009).
- Friehauf, K.E. and Sharma, M.M. 2009. A New Compositional Model for Hydraulic Fracturing With Energized Fluids. *SPE Prod & Oper* **24**(4): 562-572. SPE 115750-PA.
- Gadde P. B., Liu Y., Norman J., Bonnecaze, R. and Sharma, M. M. 2004. Modeling Proppant Settling in Water-Fracs. Paper SPE 89875 presented at the SPE Annual Technical Conference and Exhibition, Houston, Texas, 26-29 September.
- Gu, H. 1987. A Study of Propagation of Hydraulically Induced Fractures, Ph.D. Dissertation, The University of Texas at Austin, Austin, Texas (December 1987).

- Hasan, A. and Kabir, S. 2002, *Fluid Flow and Heat Transfer in Wellbores*, Society of Petroleum Engineers, 2002.
- Khade, K. and Shah, S. 2004. New Rheological Correlations for Guar Foam Fluids. *SPE Prod & Fac* **19**(2): 77-85. SPE 88032-PA.
- Kossecka, E. 1971. Defects as Surface Distribution of Double Forces. *Arch. Mech.* **23**: 481-494.
- Liu, Y. 2006. Settling and Hydrodynamic Retardation of Proppants in Hydraulic Fractures, Ph.D. Dissertation. The University of Texas at Austin, Austin, Texas (May 2006).
- Mastrojannis, E.N., Keer, L.M., and Mura, T. 1979. Stress Intensity Factor for a Plane Crack under Normal Pressure. *Int. J. Fracture* **15**: 247-258.
- Meyer, B.R. 1989. Heat Transfer in Hydraulic Fracturing. *SPE Prod Eng* **4**: 423-429. SPE 17041-PA.
- Ouyang, S. 1994. Propagation of Hydraulically Induced Fractures with Proppant Transport, Ph.D. Dissertation. The University of Texas at Austin, Austin, Texas (May 1994).
- Reidenbach, V.G., Harris, P.C., Lee, Y.N, and Lord, D.L. 1986. Rheological Study of Foam Fracturing Fluids using Nitrogen and Carbon Dioxide. *SPE Prod Eng* **1**(1): 31-41. SPE 12026-PA.
- Ribeiro, L.H. and Sharma, M.M 2013. A New 3D Compositional Model for Hydraulic Fracturing with Energized Fluids. *SPE Prod & Oper* **28**(3): 259-267. SPE 159812-PA.
- Settari, A. and Cleary, M.P. 1984. Three-Dimensional Simulation of Hydraulic Fracturing. *J. Pet Tech* **36**(7): 1177-1190. SPE 10504-PA.
- Standing, M.B. and Katz, D.L. 1942. Density of Natural Gases. *Trans. AIME* **146**(1): 140-149. SPE 942140-G.
- Valkó, P. and Economides, M.J. 1997. Foam-Proppant Transport. *SPE Prod & Fac* **12**(4): 244-249. SPE 27897-PA.
- Weaver, J. 1977. Three-Dimensional Crack Analysis. *Int. J. Solids Structures* **13**: 321-330.
- Yew, C.H. 1997, *Mechanics of Hydraulic Fracturing*, Gulf Publishing Company, Houston, Texas.

Chapter 4: Finite-Element Formulation and Main Algorithm

The objective of Chapter 4¹ is to derive a finite-element formulation of the compositional fracturing problem presented in Chapter 3. The problem encompasses five non-linear, time-dependent, moving-boundary, partial differential equations (PDEs) that govern pressure, proppant concentration, component mass fractions, temperature, and fracture width. The numerical solution is complicated by the fact that three different classes of equations need to be solved: an elliptic diffusivity equation, a parabolic-hyperbolic convection-dominated equation, and a singular boundary integral equation.

The strong coupling between the equations makes the numerical solution cumbersome. To ease this process, we propose an iterative procedure and a time-step decoupling scheme to solve the system of equations simultaneously. First, we compute fracture width and pressure using a relaxation iterative procedure. Then, we solve the transport equations using a time-forward loop. The two loops constitute an essential part of the main algorithm implemented in the computer program.

In order to ensure the accuracy of the computations, a grid generation scheme is incorporated into the program. The meshing scheme consists of a dynamic unstructured 2D mesh that is suitable for all of the equations. Complex algorithms are used to efficiently re-generate the mesh as the fracture propagates. The gridding scheme encompasses unstructured Delaunay triangulation with the convection, insertion, and redistribution of nodal points. The construction of a smooth and efficient grid plays a critical role in the stability of the calculations.

¹ Many of the ideas expressed in this chapter were first written in SPE 159812 (Ribeiro and Sharma 2013).

4.1 SOLUTION OF THE PRESSURE EQUATION

In this chapter, we follow the nomenclature typically used in numerical methods: subscripts i and j refer to the nodal numbering; N refers to the total number of nodes; and the superscript n refers to the time step number. The component and phase numbers are now referred to by the subscripts I and J , respectively. The derivations presented in this chapter follow the general methods presented in the finite-element textbook written by Becker, Carey, and Oden (1981).

The pressure equation derived in Chapter 3 has the form of a diffusivity equation:

$$\begin{aligned} & \frac{\partial}{\partial t} \left\{ w \left(\sum_{j=1}^{NP} \rho_j^* S_j^* \right) \right\} + \frac{\partial}{\partial x} \left\{ \left(\sum_{j=1}^{NP} \rho_j^* A_j^* S_j^* \right) \frac{\partial P}{\partial x} \right\} + \frac{\partial}{\partial y} \left\{ \left(\sum_{j=1}^{NP} \rho_j^* A_j^* S_j^* \right) \frac{\partial P}{\partial y} \right\} \\ & + \frac{\partial}{\partial y} \left\{ \left(\sum_{j=1}^{NP} \rho_j^{*2} A_j^* S_j^* \right) g \right\} + \sum_{j=1}^{NP} \frac{2C_{w,j} \rho_j}{\sqrt{t-\tau}} = 0 \end{aligned} \quad (4.1)$$

$$\underline{BCs}: \begin{cases} A^* \frac{\partial P}{\partial n} = (q_x)_{inj} & \text{on } \partial\Omega_p \\ \frac{\partial P}{\partial n} = 0 & \text{on } \partial\Omega_f \text{ and } \partial\Omega_c \end{cases}$$

To make the derivations more compact, Eq. 4.1 is replaced by a generic diffusivity equation that has the same type of boundary conditions (BCs). The generic equation reduces to the pressure equation with a proper choice of coefficients. The unknown is a smooth function $u(x,y,t)$, which is a function of time and location.

$$\begin{aligned} & \frac{\partial \alpha}{\partial t} + \nabla \cdot \vec{q} + \frac{2}{\sqrt{t-\tau}} q_L = 0 \quad \text{where} \quad \vec{q} = \beta \vec{\nabla} u + \gamma \vec{n}_y \\ & \underline{BCs}: \begin{cases} \vec{q} = q_{inj} \vec{n} & \text{on } \partial\Omega_p \\ \vec{q} = 0 & \text{on } \partial\Omega_f \text{ and } \partial\Omega_c \end{cases} \end{aligned} \quad (4.2)$$

A weak formulation of the problem defined in Eq. 4.2 requires the introduction of a test function $v(x,y)$. We multiply the PDE defined in Eq. 4.2 by the test function v , and integrate the equation over the domain Ω :

$$\int_{\Omega} v \frac{\partial \alpha}{\partial t} d\Omega + \int_{\Omega} v (\nabla \cdot \vec{q}) d\Omega + \int_{\Omega} v \frac{2}{\sqrt{t-\tau}} q_L d\Omega = 0 \quad (4.3)$$

Eq. 4.3 is integrated by parts:

$$\int_{\Omega} v \frac{\partial \alpha}{\partial t} d\Omega + \int_{\Omega} \nabla \cdot (v \vec{q}) d\Omega - \int_{\Omega} (\vec{\nabla} v \cdot \vec{q}) d\Omega + \int_{\Omega} v \frac{2}{\sqrt{t-\tau}} q_L d\Omega = 0 \quad (4.4)$$

The divergence theorem (also known as Gauss theorem) transforms the surface integral to a line integral:

$$\int_{\Omega} \nabla \cdot (v \vec{q}) d\Omega = \int_{\partial \Omega} v (\vec{q} \cdot \vec{n}) ds \quad (4.5)$$

The domain boundary $\partial \Omega$ is the summation of the sub-regions $\partial \Omega_p$, $\partial \Omega_f$ and $\partial \Omega_c$. The flux along $\partial \Omega_f$ and $\partial \Omega_c$ is zero, so the line integral is zero along these sub-regions. The flux along $\partial \Omega_p$ is prescribed as a BC, and the line integral becomes:

$$\int_{\partial \Omega} v (\vec{q} \cdot \vec{n}) ds = \int_{\partial \Omega_p} v q_{inj} ds \quad \text{since} \quad \begin{cases} \vec{q} = q_{inj} \vec{n} & \text{on } \partial \Omega_p \\ \vec{q} = 0 & \text{on } \partial \Omega_f \text{ and } \partial \Omega_c \end{cases} \quad (4.6)$$

Using Eqs. 4.5 and 4.6, Eq. 4.4 reduces to:

$$\int_{\Omega} v \frac{\partial \alpha}{\partial t} d\Omega + \int_{\partial \Omega_p} v q_{inj} ds - \int_{\Omega} (\vec{\nabla} v \cdot \vec{q}) d\Omega + \frac{2}{\sqrt{t-\tau}} \int_{\Omega} v q_L d\Omega = 0 \quad (4.7)$$

The flux is now expressed in terms of the gradient of the function of interest u :

$$\int_{\Omega} v \frac{\partial \alpha}{\partial t} d\Omega + \int_{\partial\Omega_p} v q_{inj} ds - \int_{\Omega} \gamma (\vec{\nabla} v \cdot \vec{n}_y) d\Omega - \int_{\Omega} \beta (\vec{\nabla} v \cdot \vec{\nabla} u) d\Omega + \frac{2}{\sqrt{t-\tau}} \int_{\Omega} v q_L d\Omega = 0 \quad (4.8)$$

Eq. 4.8 constitutes a variational statement of the problem defined in Eq. 4.2. Our goal is to find the function u such that the PDE, together with the BCs, are satisfied in the sense of weighted averages. To do so, we determine approximate solutions of Eq. 4.8 over subsets of Ω . The domain Ω is divided in N sub-domains, and we introduce N basis functions $\{\phi_1(x, y), \phi_2(x, y), \dots, \phi_N(x, y)\}$ that define an N -dimensional subspace covering the domain. The unknown function u and the test function v are continuous functions that can be represented by a linear combination of the N basis functions. u_N and v_N are the so-called Galerkin approximations of the functions u and v :

$$\begin{aligned} u(x, y, t) &\approx u_N(x, y, t) = \sum_{j=1}^N u_j(t) \phi_j(x, y) \\ v(x, y) &\approx v_N(x, y) = \sum_{i=1}^N v_i \phi_i(x, y) \end{aligned} \quad (4.9)$$

Since the N basis functions are known, the function u is completely determined at a given time t once the N coefficients $u_j(t)$ are determined. These coefficients are referred to as the degrees of freedom of the approximation. Inserting the Galerkin approximations of functions u and v in the variational statement of the problem, we obtain N independent equations:

$$\begin{aligned} \int_{\Omega} \frac{\partial \alpha}{\partial t} \phi_i d\Omega + \int_{\partial\Omega_p} q_{inj} \phi_i ds - \int_{\Omega} \gamma \frac{\partial \phi_i}{\partial y} d\Omega - \sum_{j=1}^N \int_{\Omega} \beta \left(\frac{\partial \phi_i}{\partial x} \frac{\partial \phi_j}{\partial x} + \frac{\partial \phi_i}{\partial y} \frac{\partial \phi_j}{\partial y} \right) u_j d\Omega \\ + \frac{2}{\sqrt{t-\tau}} \int_{\Omega} q_L \phi_i d\Omega = 0 \quad ; i = 1 \dots N \end{aligned} \quad (4.10)$$

The first term of Eq. 4.10 includes a time derivative, and the fifth term includes a time-dependent leak-off rate. The time derivative for an arbitrary function f between t^n and $t^n + \Delta t^n$ is given by:

$$\left. \frac{\partial f(x, y, t)}{\partial t} \right|_{t^n + \Delta t^n} = \frac{1}{\Delta t^n} [f(x, y, t^n + \Delta t^n) - f(x, y, t^n)] \quad (4.11)$$

The fluid-loss term involves the inverse of the square root of time. The average rate between t^n and $t^n + \Delta t^n$ is approximated by the following time integration:

$$\int_{t^n}^{t^n + \Delta t^n} \frac{f(x, y, t)}{\sqrt{t - \tau}} dt = \frac{2}{\Delta t^n} f(x, y, t^n) (\sqrt{t^n + \Delta t^n - \tau} - \sqrt{t^n - \tau}) \quad (4.12)$$

Inserting Eqs. 4.11 and 4.12 in Eq. 4.10, we obtain:

$$\begin{aligned} & \frac{1}{\Delta t^n} \int_{\Omega} (\alpha^{n+1} - \alpha^n) \phi_i d\Omega + \int_{\partial\Omega_p} q_{inj} \phi_i ds - \int_{\Omega} \gamma \frac{\partial \phi_i}{\partial y} d\Omega - \sum_{j=1}^N \int_{\Omega} \beta \left(\frac{\partial \phi_i}{\partial x} \frac{\partial \phi_j}{\partial x} + \frac{\partial \phi_i}{\partial y} \frac{\partial \phi_j}{\partial y} \right) u_j d\Omega \\ & + \frac{4}{\Delta t^n} (\sqrt{t^n + \Delta t^n - \tau} - \sqrt{t^n - \tau}) \int_{\Omega} q_L^n \phi_i d\Omega = 0 \quad ; i = 1 \dots N \end{aligned} \quad (4.13)$$

The structure of Eq. 4.13 is most easily seen by isolating the N unknowns u_j , and by rewriting the equation in the more compact form:

$$\sum_{j=1}^N K_{ij} u_j = \frac{1}{\Delta t^n} (f_{w,i}^{n+1} - f_{w,i}^n) + f_{inj,i} - f_{g,i} + \frac{1}{\Delta t^n} f_{L,i}^{n \rightarrow n+1} \quad ; i = 1 \dots N$$

$$K_{ij} = \int_{\Omega} \beta \left(\frac{\partial \phi_i}{\partial x} \frac{\partial \phi_j}{\partial x} + \frac{\partial \phi_i}{\partial y} \frac{\partial \phi_j}{\partial y} \right) d\Omega \quad ; \quad \begin{cases} f_{w,i}^{n+1} = \int_{\Omega} \alpha^{n+1} \phi_i d\Omega & ; \quad f_{w,i}^n = \int_{\Omega} \alpha^n \phi_i d\Omega \\ f_{inj,i} = \int_{\partial\Omega_p} q_{inj} \phi_i ds \\ f_{g,i} = \int_{\Omega} \gamma \frac{\partial \phi_i}{\partial y} d\Omega \\ f_{L,i}^{n \rightarrow n+1} = 4 (\sqrt{t^n + \Delta t^n - \tau} - \sqrt{t^n - \tau}) \int_{\Omega} \phi_i q_L d\Omega \end{cases} \quad (4.14)$$

The $N \times N$ rectangular array of components K_{ij} constitutes a matrix K commonly referred to as a *stiffness* matrix. The right side of Eq. 4.14 forms a $N \times 1$ vector of components f_i , which is commonly referred to as *load* vector F . The unknown is the vector U made of N components u_j :

$$\bar{K}\tilde{U} = \tilde{F} \quad (4.15)$$

The pressure equation may be obtained from the generic equation defined in Eq. 4.2 by using the following coefficients:

$$\left\{ \begin{array}{l} \alpha = w \left(\sum_{J=1}^{NP} \rho_J^* S_J^* \right) \\ \beta = \left(\sum_{J=1}^{NP} A_J^* \rho_J^* S_J^* \right) \\ \gamma = g \left(\sum_{J=1}^{NP} (\rho_J^*)^2 A_J^* S_J^* \right) \end{array} \right. ; \left\{ \begin{array}{l} q_L = \sum_{J=1}^{NP} C_{w,J} \rho_J \\ q_{inj} = \sum_{J=1}^{NP} (\rho_J^* q_J^*)_{inj} \end{array} \right. \quad (4.16)$$

Inserting Eq. 4.16 into Eq. 4.14, the discretized finite-element formulation of the pressure equation is given in a matrix form as:

$$\begin{aligned} \bar{K}.\tilde{P} = \tilde{F} \quad \text{or} \quad \sum_{j=1}^N K_{p,ij} P_j &= \frac{1}{\Delta t^n} (f_{w,i}^{n+1} - f_{w,i}^n) + f_{inj,i} - f_{g,i} \frac{1}{\Delta t^n} f_{L,i}^{n \rightarrow n+1} \quad ; i = 1 \dots N \\ K_{p,ij} &= \int_{\Omega} \left(\sum_{J=1}^{NP} A_J^* \rho_J^* S_J^* \right) \left(\frac{\partial \phi_j}{\partial x} \frac{\partial \phi_i}{\partial x} + \frac{\partial \phi_j}{\partial y} \frac{\partial \phi_i}{\partial y} \right) d\Omega \\ \left\{ \begin{array}{l} f_{w,i}^{n+1} = \int_{\Omega} \left\{ w \left(\sum_{J=1}^{NP} \rho_J^* S_J^* \right) \right\}^{n+1} \phi_i d\Omega \quad ; \quad f_{w,i}^n = \int_{\Omega} \left\{ w \left(\sum_{J=1}^{NP} \rho_J^* S_J^* \right) \right\}^n \phi_i d\Omega \\ f_{inj,i} = \int_{\partial\Omega_p} \left(\sum_{J=1}^{NP} \rho_J^* q_J^* \right)_{inj} \phi_i ds \\ f_{g,i} = \int_{\Omega} g \left(\sum_{J=1}^{NP} (\rho_J^*)^2 A_J^* S_J^* \right) \frac{\partial \phi_i}{\partial y} d\Omega \\ f_{L,i}^{n \rightarrow n+1} = 4 \left(\sqrt{t^n + \Delta t^n} - \tau - \sqrt{t^n - \tau} \right) \int_{\Omega} \left(\sum_{J=1}^{NP} C_{w,J} \rho_J \right) \phi_i d\Omega \end{array} \right. \quad (4.17) \end{aligned}$$

4.2 SOLUTION OF THE COMPATIBILITY CONDITION

As discussed in Chapter 3, satisfying the compatibility equation is a necessary condition for the existence of a solution to the pressure equation. The increase in fracture mass must equal the mass of fluid pumped minus the mass of fluid that leaked off. This requirement yields the following time step increment:

$$\Delta t^n = \frac{\Delta m_{fracture} + \Delta m_{leakoff}}{\dot{m}_{pumped}} \quad (4.18)$$

The derivation of Eq. 4.18 is similar to the derivation used for the pressure equation. The overall conservation of mass ensures that the summation of the accumulation, injection, and fluid-loss terms is zero on a global basis. Using Eq. 4.13 as the starting point for the derivations of the compatibility equation, the overall mass balance is given in a discrete form by:

$$\begin{aligned} & \sum_{i=1}^N \frac{1}{\Delta t^n} \int_{\Omega} (\alpha^{n+1} - \alpha^n) \phi_i d\Omega + \sum_{i=1}^N \int_{\partial\Omega_p} q_{inj} \phi_i ds + \\ & \sum_{i=1}^N \frac{4}{\Delta t^n} \left(\sqrt{t^n + \Delta t^n - \tau} - \sqrt{t^n - \tau} \right) \int_{\Omega} q_L^n \phi_i d\Omega = 0 \end{aligned} \quad (4.19)$$

Eq. 4.19 may be rewritten as:

$$\Delta t^n = \frac{\sum_{i=1}^N \int_{\Omega} (\alpha^{n+1} - \alpha^n) \phi_i d\Omega + \frac{4}{\Delta t^n} \left(\sqrt{t^n + \Delta t^n - \tau} - \sqrt{t^n - \tau} \right) \sum_{i=1}^N \int_{\Omega} q_L^n \phi_i d\Omega}{\sum_{i=1}^N \int_{\partial\Omega_p} |q_{inj}| \phi_i ds} \quad (4.20)$$

Using the coefficients defined in Eq. 4.16, we can rewrite the compatibility condition as:

$$\Delta t^n = \frac{\sum_{i=1}^N f_{w,i}^{n+1} - \sum_{i=1}^N f_{w,i}^n + \sum_{i=1}^N f_{L,i}^{n \rightarrow n+1}}{\sum_{i=1}^N f_{inj,i}}$$

$$\begin{cases} f_{w,i}^{n+1} = \int_{\Omega} \left\{ w \left(\sum_{J=1}^{NP} \rho_J^* S_J^* \right) \right\}^{n+1} \phi_i d\Omega ; & f_{w,i}^n = \int_{\Omega} \left\{ w \left(\sum_{J=1}^{NP} \rho_J^* S_J^* \right) \right\}^n \phi_i d\Omega \\ f_{inj,i} = \int_{\partial\Omega_p} \left(\sum_{J=1}^{NP} \rho_J^* q_J^* \right)_{inj} \phi_i ds \\ f_{L,i}^{n \rightarrow n+1} = 4 \left(\sqrt{t^n + \Delta t^n - \tau} - \sqrt{t^n - \tau} \right) \int_{\Omega} \left(\sum_{J=1}^{NP} C_{w,J} \rho_J \right) \phi_i d\Omega \end{cases} \quad (4.21)$$

The fluid-loss term in Eq. 4.21 is itself a function of the time increment; therefore, an iterative scheme is used to solve this convoluted problem. The time increment for the new iteration $k+1$ is given by:

$$\left(\Delta t^n \right)_{k+1} = \left(\frac{\sum_{i=1}^N f_{w,i}^{n+1} - \sum_{i=1}^N f_{w,i}^n + \sum_{i=1}^N f_{L,i}^{n \rightarrow n+1}}{\sum_{i=1}^N f_{inj,i}} \right)_k \quad (4.22)$$

When this value of the time increment is used in solving the pressure equation, the compatibility condition is automatically satisfied.

4.3 SOLUTION OF THE CONVECTION-DOMINATED EQUATIONS

The proppant transport, component transport, and temperature equations are convection-dominated equations of the same mathematical form. The BCs are similar, and these problems are different formulations of the same generic problem (as seen in **Table 4.1**); therefore, these equations are solved in a similar fashion.

Convection-dominated equations often lead to oscillations even when the analytical solution is smooth and monotonic. Several approaches have been used to treat

this problem. One of the most popular approaches is to use *upwind* discretization schemes for solving this type of equations. According to such a scheme, the spatial differences are skewed in the upwind direction, i.e. the direction from which the flow originates, so that the numerical scheme “follows” the transport of the quantity of interest. This approach has not been used here; it is one of our recommendations for future work (Section 9.3.1).

In this work, we introduce a dispersion term to reduce oscillations. This term accounts for both physical diffusion (due to concentration gradients) and numerical dispersion. Moreover, the temperature equation is rewritten in a dimensionless form to dampen oscillations. The dimensionless temperature is introduced as:

$$T_D = \frac{T - T_{inj}}{T_R - T_{inj}} \quad (4.23)$$

By definition, T_D is between 0 and 1; and the new BC along the perforations is $T_D=0$. To make the derivations more compact, the three convection-dominated problems are replaced by the generic problem given in Eq. 4.24. The unknown is a smooth function $u(x,y,t)$, which is a function of time and location.

$$\begin{aligned} \frac{\partial}{\partial t}(\alpha u) + \nabla \cdot (\vec{q}u) - \nabla \cdot (w\varepsilon_d \vec{\nabla} u) + \frac{2}{\sqrt{t-\tau}}(q_L + q_{cond})u &= f_R \\ \underline{BCs}: \begin{cases} u = u_{inj} & \text{on } \partial\Omega_p \\ \vec{q} = 0 & \text{on } \partial\Omega_f \text{ and } \partial\Omega_c \end{cases} \end{aligned} \quad (4.24)$$

Introducing the test function $v(x,y)$, and integrating the PDE over the domain Ω gives:

$$\begin{aligned}
& \int_{\Omega} v \frac{\partial}{\partial t} (\alpha u) d\Omega + \int_{\Omega} v \nabla \cdot (\vec{q} u) d\Omega - \int_{\Omega} v \nabla \cdot (w \varepsilon_d \vec{\nabla} u) d\Omega \\
& + \int_{\Omega} v \frac{2}{\sqrt{t-\tau}} (q_L + q_{cond}) u d\Omega = \int_{\Omega} v f_R d\Omega
\end{aligned} \tag{4.25}$$

Eq. 4.25 is integrated by parts:

$$\begin{aligned}
& \int_{\Omega} v \alpha \frac{\partial u}{\partial t} d\Omega + \int_{\Omega} v u \frac{\partial \alpha}{\partial t} d\Omega + \int_{\Omega} \nabla \cdot (u v \vec{q}) d\Omega - \int_{\Omega} u (\vec{\nabla} v \cdot \vec{q}) d\Omega - \int_{\Omega} \nabla \cdot (w \varepsilon_d v \vec{\nabla} u) d\Omega \\
& + \int_{\Omega} w \varepsilon_d (\vec{\nabla} v \cdot \vec{\nabla} u) d\Omega + \int_{\Omega} v \frac{2}{\sqrt{t-\tau}} (q_L + q_{cond}) u d\Omega = \int_{\Omega} v f_R d\Omega
\end{aligned} \tag{4.26}$$

The divergence theorem transforms the surface integrals to line integrals:

$$\begin{aligned}
& \int_{\Omega} \nabla \cdot (u v \vec{q}) d\Omega = \int_{\partial\Omega} v u (\vec{n} \cdot \vec{q}) ds \\
& \int_{\Omega} \nabla \cdot (w \varepsilon_d v \vec{\nabla} u) d\Omega = \int_{\partial\Omega} v w \varepsilon_d \frac{\partial u}{\partial n} ds
\end{aligned} \tag{4.27}$$

The flux along $\partial\Omega_f$ and $\partial\Omega_c$ is zero, so the line integral is zero along these sub-regions. Dirichlet BCs are prescribed along $\partial\Omega_p$, so the test function equals zero over this sub-domain:

$$\begin{cases} \int_{\partial\Omega} v w \varepsilon_d \frac{\partial u}{\partial n} ds = 0 \\ \int_{\partial\Omega} v u (\vec{n} \cdot \vec{q}) ds = 0 \end{cases} \quad \text{since} \quad \begin{cases} u = u_{inj} \Rightarrow v = 0 \text{ on } \partial\Omega_p \\ \frac{\partial u}{\partial n} = 0 \text{ and } \vec{n} \cdot \vec{q} = 0 \text{ on } \partial\Omega_f \text{ and } \partial\Omega_c \end{cases} \tag{4.28}$$

Using Eqs. 4.27 and 4.28, Eq. 4.26 reduces to:

$$\begin{aligned}
& \int_{\Omega} v \alpha \frac{\partial u}{\partial t} d\Omega + \int_{\Omega} v u \frac{\partial \alpha}{\partial t} d\Omega - \int_{\Omega} u (\vec{\nabla} v \cdot \vec{q}) d\Omega + \int_{\Omega} w \varepsilon_d (\vec{\nabla} v \cdot \vec{\nabla} u) d\Omega \\
& + \frac{2}{\sqrt{t-\tau}} \int_{\Omega} v (q_L + q_{cond}) u d\Omega = \int_{\Omega} v f_R d\Omega
\end{aligned} \tag{4.29}$$

Using the Galerkin discretization introduced in section 4.1, we obtain a discretized finite-element formulation of the convection-dominated problem:

$$\begin{aligned}
& \sum_{j=1}^N \int_{\Omega} \alpha \phi_i \phi_j \frac{du_j}{dt} d\Omega + \sum_{j=1}^N \int_{\Omega} \frac{\partial \alpha}{\partial t} \phi_i \phi_j u_j d\Omega - \sum_{j=1}^N \int_{\Omega} \left(q_x \frac{\partial \phi_i}{\partial x} + q_y \frac{\partial \phi_i}{\partial y} \right) \phi_j u_j d\Omega \\
& + \varepsilon_d \sum_{j=1}^N \int_{\Omega} \left(\frac{\partial \phi_j}{\partial x} \frac{\partial \phi_i}{\partial x} + \frac{\partial \phi_j}{\partial y} \frac{\partial \phi_i}{\partial y} \right) w u_j d\Omega + \frac{2}{\sqrt{t-\tau}} \sum_{j=1}^N \int_{\Omega} (q_L + q_{cond}) \phi_i \phi_j u_j d\Omega \\
& = \int_{\Omega} \phi_i f_R d\Omega \quad ; i = 1 \dots N
\end{aligned} \tag{4.30}$$

The N independent equations may be rewritten in a more compact form:

$$\begin{aligned}
& \sum_{j=1}^N A_{ij} \frac{du_j}{dt} + \sum_{j=1}^N (B_{1,ij} + B_{2,ij} + B_{3,ij} + B_{4,ij} + B_{5,ij}) u_j = C_i \quad ; i = 1 \dots N \\
& \left\{ \begin{aligned} A_{ij} &= \int_{\Omega} \alpha \phi_i \phi_j d\Omega \\ B_{1,ij} &= \int_{\Omega} \frac{\partial \alpha}{\partial t} \phi_i \phi_j d\Omega \\ B_{2,ij} &= - \int_{\Omega} \left(q_x \frac{\partial \phi_i}{\partial x} + q_y \frac{\partial \phi_i}{\partial y} \right) \phi_j d\Omega \\ B_{3,ij} &= \varepsilon_d \int_{\Omega} \left(\frac{\partial \phi_j}{\partial x} \frac{\partial \phi_i}{\partial x} + \frac{\partial \phi_j}{\partial y} \frac{\partial \phi_i}{\partial y} \right) w d\Omega \end{aligned} \right. ; \left\{ \begin{aligned} B_{4,ij} &= \frac{2}{\sqrt{t-\tau}} \int_{\Omega} q_L \phi_i \phi_j d\Omega \\ B_{5,ij} &= \frac{2}{\sqrt{t-\tau}} \int_{\Omega} q_{cond} \phi_i \phi_j d\Omega \\ C_i &= \int_{\Omega} \phi_i f_R d\Omega \end{aligned} \right. \tag{4.31}
\end{aligned}$$

Using an implicit time scheme discretization, Eq. 4.31 becomes:

$$\sum_{j=1}^N A_{ij} \frac{u_j^{n+1} - u_j^n}{\Delta t^n} + \sum_{j=1}^N (B_{1,ij} + B_{2,ij} + B_{3,ij} + B_{4,ij} + B_{5,ij})^{n+1} u_j^{n+1} = C_i^{n+1} \quad ; i = 1 \dots N \tag{4.32}$$

The N independent equations may be written in a typical matrix form with the following choice of coefficients:

$$\bar{K}\tilde{U} = \tilde{F} \quad \text{or} \quad \sum_{j=1}^N K_{ij} u_j^{n+1} = F_i \quad ; \quad i=1\dots N$$

$$\text{where} \quad \begin{cases} K_{ij} = A_{ij} + \Delta t^n (B_{1,ij} + B_{2,ij} + B_{3,ij} + B_{4,ij} + B_{5,ij}) \\ F_i = \sum_{j=1}^N A_{ij} u_j^n + \Delta t^n C_i \end{cases} \quad (4.33)$$

Eq. 4.33 is a finite-element matrix formulation of the generic problem defined in Eq. 4.24. The corresponding finite-element formulations of the proppant, component, and temperature equations are obtained using the coefficients given in **Table 4.2**. The corresponding matrix equations are given in **Table 4.3**.

4.4 SOLUTION OF THE FRACTURE OPENING EQUATION

The fracture opening equation relates the net pressure and the fracture opening displacement. Along the fracture edge, the fracture opening is zero. The strong form of the problem is given by:

$$-P(x, y) + \sigma_{h\min}(x, y) = \frac{G}{4\pi(1-\nu)} \int_{\Omega} \left[\frac{\partial}{\partial x} \left(\frac{1}{r} \right) \frac{\partial w(x, y)}{\partial x'} + \frac{\partial}{\partial y} \left(\frac{1}{r} \right) \frac{\partial w(x, y)}{\partial y'} \right] d\Omega$$

$$\text{where } r = \sqrt{(x' - x)^2 + (y' - y)^2} \quad (4.34)$$

$$\underline{BC} : w = 0 \quad \text{on } \partial\Omega_f$$

This boundary integral equation is singular, and its solution requires complex numerical techniques. We refer here to the work of Gu (1987), who solved the equation by forming a weak formulation of the equation in which the differentiation of the singular term $(1/r)$ is transferred to the test function v . The derivations of the finite-element formulation of the problem are included in Gu (1987). The fracture width w is approximated by a finite number N of terms using a Galerkin approximation:

$$w(x, y, t) \approx w_N(x, y, t) = \sum_{j=1}^N w_j(t) \phi_j(x, y) \quad (4.35)$$

The matrix form of the weak formulation is given by:

$$\begin{aligned} \bar{K} \cdot \tilde{W} = \tilde{F} \quad \text{or} \quad \sum_{j=1}^N K_{w,ij} w_j = -f_{p,i} + f_{\sigma,i} \quad ; i=1 \dots N \\ \left\{ \begin{aligned} K_{w,ij} &= \frac{G}{4\pi(1-\nu)} \iint_{\Omega \Omega'} \left(\frac{1}{r} \right) \left(\frac{\partial \phi_i}{\partial x} \frac{\partial \phi_j}{\partial x'} + \frac{\partial \phi_i}{\partial y} \frac{\partial \phi_j}{\partial y'} \right) d\Omega' d\Omega \\ f_{p,i} &= \int_{\Omega} \phi_i P d\Omega \\ f_{\sigma,i} &= \int_{\Omega} \phi_i \sigma_{hmin} d\Omega \end{aligned} \right. \quad (4.36) \end{aligned}$$

Eq. 4.36 requires a double integration over the fracture domain; one integral comes from the strong form of the equation (since the equation is a boundary integral equation), and the second integral appears during the formulation of the weak statement of the problem.

4.5 MAIN ALGORITHM

4.5.1 Overview of the Main Algorithm

Fig. 4.1 shows a simplified version of the main algorithm implemented in *EFRAC-3D*. The algorithm shows the main interactions between the different equations presented thus far. The algorithm also includes a wellbore model, which relates the surface and bottomhole conditions, and a productivity model, which assesses the productivity of the fractured well during flowback. The wellbore and productivity models are described in Chapter 5.

As seen in Fig. 4.1, the main algorithm solves the pressure and fracture opening equations together using an iterative scheme. This choice is motivated by the strong

coupling between these equations, as the presence of the $1/w^3$ term in the pressure equation makes this equation highly sensitive to changes in fracture width. The simultaneous resolution of the compatibility condition is also required because it is a necessary condition to the existence of a solution for the pressure equation. The iterative scheme is shown on the left side of **Fig. 4.2**, which is a more detailed version of the simplified algorithm presented in Fig. 4.1. As seen on the right side of Fig. 4.2, we use a second algorithm to solve the transport equations separately. The main features of the main algorithm are discussed in the following sections.

4.5.2 Fracture Propagation

An incremental process approximates fracture propagation. For a short period of time, the fracture remains stationary. The fracture front is temporarily arrested by the fracture toughness or by the *in-situ* stress contrast. During this time, fluid is pumped into the fracture causing an increase of fluid pressure, fracture width, and stress intensity factor at the fracture front. When the stress intensity factor exceeds the fracture toughness, the fracture front propagates. The maximum displacement of the fracture front (Δd_{max}) controls the motion of the fracture. This maximum displacement occurs at the node where the stress intensity factor is maximum ($K_{I_{max}}$). For the other nodes located along the fracture tip, their displacement is governed by the criterion established by Mastrojannis *et al.* (1979):

$$\Delta d = \max \left(\Delta d_{max} \left(\frac{K_I - K_{IC}}{K_{IC}} \right); 0 \right) \quad (4.37)$$

This method guarantees that the fracture front is not propagating artificially if the local value of K_I does not exceed K_{IC} . **Figs. 4.3** and **4.4** show the motion of the fracture

between consecutive time steps. In our algorithm, the fracture is forced to propagate at each time step to avoid unnecessary re-meshing. We accomplish this by adjusting the fluid pressure so that the critical value is exceeded at each time step. In other words, the period of time necessary to reach the maximum front displacement is calculated from the compatibility condition, which is a mass balance over the entire fracture. It should be noted that the motion of the front shown in Fig. 4.3 is exaggerated for display purposes; the two fracture fronts are actually separated by twenty successive time steps.

4.5.3 Adaptive Fracture Front Displacement

The speed of the propagation process is indirectly controlled by Δd_{max} . If Δd_{max} increases, the mass required to fill the gap between the old and the new fracture front increases, so the value of Δt^n calculated from the compatibility condition increases. Although we cannot freely choose the value of Δt^n , we can control the speed at which the fracture propagates using Δd_{max} . Several options may be used for Δd_{max} :

- Δd_{max} remains constant: the user chooses its value.
- Δd_{max} is a function of the difference between K_I and K_{IC} : the front displacement increases as the stress intensity factor increases.
- Δd_{max} is a function of the velocity of the fluid front: this method ensures that the fracture propagates at a velocity comparable to the fluid front. (This approach is similar to the one proposed by Linkov (2011)).
- Δd_{max} changes over time to ensure that the value of Δt^n calculated from the compatibility condition remains within a prescribed range.

Regardless of the method we use, Δd_{max} is the numerical parameter that is not estimated from experimental data. Although it provides some flexibility to improve the

numerical stability, this flexibility is artificial, and its impact on the fracture propagation process is undesirable. The fracture propagation criterion is intrinsically grid-dependent. This numerical artifact is common in fracture modeling, as discussed by Economides and Nolte (2000).

4.5.4 Time-Decoupling Scheme

We chose to use an implicit backward finite-differencing scheme for the time derivatives. This scheme is unconditionally stable, which makes it particularly suitable for calculations in which the step increment is not chosen arbitrarily by the user. As the fracture grows, the time step calculated from the compatibility equation increases significantly. **Fig. 4.5** shows such an example for the validation case proposed in Section 6.2.3. After a few minutes, the time increment may be too large for convection-dominated equations, which are more prone to oscillations than the elliptic diffusivity equation.

We introduce a new time-decoupling scheme to improve numerical stability and dampen oscillations. First, we compute the fracture width and fluid pressure using the relaxation iterative procedure described in section 4.5.5. Then, we solve the transport equations using a time-forward loop. For the time-forward loop, the time step Δt^n is divided in smaller time steps, which can be adjusted by the user (Δt_{cc}). For each time step Δt^n , fracture width and fluid pressure are interpolated linearly using the values obtained at times t^n and $t^n + \Delta t^n$, as seen on the right side of **Fig. 4.6**. Since the coupling between the transport equations is not as strong as the coupling between the fracture opening and pressure equations, individual iterative schemes are used for solving each equation. The time-forward loop appears on the right side of the main algorithm presented in Fig. 4.2. A second approach to dampen oscillations would be to use an *upwind* discretization scheme

for solving the transport equations. This approach, which has not been used in his work, is discussed in Section 9.3.1.

4.5.5 Relaxation Process

We use an adaptive relaxation iterative scheme to solve the fracture mechanics, pressure equation, and compatibility condition together. The process consists of constructing a succession of approximations that converge toward the desired solution. For a given iteration, the new estimate is based on the approximation obtained at the previous iteration and the solution obtained at the previous time step. This is done by using a linear extrapolation of the solution:

$$w^{n(k+1)} = \alpha_r F[w^{n(k)}] + (1 - \alpha_r) w^{n-1} \quad (4.38)$$

In Eq. 4.38, α_r is the relaxation parameter ($0 \leq \alpha_r \leq 1$); n is the time step number; k is the iteration number; and F refers to the process of substituting $w^{n(k)}$ into the fracture opening equation. The relaxation parameter controls the convergence of the iterative process. Since the problem is highly non-linear, large values of α_r may result in the divergence or oscillation of the iterative process. On the other hand, a low value of α_r slows down the computations. The typical value used in this work is 0.3. The actual value of α_r varies over time based on the behavior of the solution, and the iterative process is said to be *adaptive*. The value of α_r is decreased if the change in fracture width becomes more dramatic, and it is increased for smooth problems with slow changes in fracture width.

4.5.6 Linear Solvers

The numerical resolution of the different PDEs consists of solving different versions of the matrix equation $\bar{K}\tilde{U} = \tilde{F}$ where K is a $N \times N$ stiffness matrix; F is a $N \times 1$ load vector; and U is a $N \times 1$ unknown vector. The properties of the matrices differ for the various PDEs; hence, different solvers can be used. In this work, we use the *LAPACK* library, which is a software library for numerical linear algebra. We use version 3.3 of the library, which is provided by the University of Tennessee, the University of California Berkeley, the University of Colorado, and NAG Ltd.

The resolution of the matrix equation is a two-step process: the first subroutine computes the LU factorization of the stiffness matrix, and the second subroutine solves the factorized equation. The list of subroutines² used in this work includes:

- *SPOTRF-SPOTRS*: These subroutines are used for solving the fracture opening equation. The first subroutine computes the Cholesky factorization of a real symmetric positive definite matrix K .
- *SSYTRF-SSYTRS*: These subroutines are used for solving the pressure equation. The first subroutine factors a real symmetric matrix K .
- *SGETFR-SGETRS*: These subroutines are used for solving the proppant transport, component transport, and temperature equations. The first subroutine factors a general matrix K using Gaussian elimination with partial pivoting.

Improving the resolution of the matrix equations was non-essential to this work, and the performance of the *LAPACK* solvers was considered satisfactory. More efficient

² The names of the subroutines correspond to the version 3.3.1 of the *LAPACK* library. These names are susceptible to change in future releases.

solvers are nonetheless available, and their future implementation could improve the computation time and accuracy.

4.6 MAIN FEATURES OF THE DYNAMIC UNSTRUCTURED MESH

4.6.1 Past Developments

The meshing and interpolation techniques discussed in this dissertation are based on the work of several authors. The original grid was implemented by Gu (1987), who introduced tip-specific elements along the fracture edge to overcome the singularity arising near the fracture tip. The gridding scheme, however, lacked flexibility and was not suitable for propagating elongated fractures. The number of nodes and the number of elements were constant, and the elements were constructed by connecting the adjacent nodes in a fixed relation among them. Then, Ouyang (1994) improved the gridding scheme by developing an adaptive re-meshing scheme. In his algorithm, additional nodes were implemented along the boundary and inside the domain, as the fracture grows over time. The elements were constructed in an optimized manner using the Delaunay triangulation and tactically assigned pivot points. Finally, additional criteria for node insertions have been implemented to optimize the construction of the elements. These criteria were developed by researchers at the Oak Ridge National Laboratories, and particularly by Renka who initiated these gridding capabilities (1981).

4.6.2 Mesh Structure

As the fracture grows during pumping, the fracture shape depends primarily on the vertical distribution of the minimum horizontal stress and on the fracturing treatment. The fracture is represented by a 2D dynamic unstructured mesh, of which its shape is an integral part of the solution of the moving boundary problem. The mesh is periodically

remeshed for maintaining an optimal grid for the numerical evaluation of the solutions. However, the mesh may be distorted in some cases, and the irregularly shaped domain can create numerical instabilities. Therefore, building an efficient mesh generator is critical to obtain smooth solutions to the fracture propagation problem.

As seen in Fig. 4.3, the mesh consists of triangular elements and quadrilateral elements located along the fracture edge. Inside the fracture, none of the governing equations are singular, so the same element and shape functions are suitable for all the equations. The fracture opening equation becomes singular near the fracture edge. The singularity is removed by using tip-specific quadrilaterals along the fracture boundary.

4.6.3 Elements and Shape Functions

As there are different types of elements, there are different types of shape functions. For all the equations, we use linear triangular elements inside the domain. The master element for the regular triangles is shown on the left side of Fig. 4.7. The associated shape functions ψ_i^t are given by:

$$\psi_1^t = 1 - \xi - \eta \quad ; \quad \psi_2^t = \xi \quad ; \quad \psi_3^t = \eta \quad (4.39)$$

ξ and η are the coordinates in the *master* element, which are mapped in the x - y fracture referential using simple coordinate transformations (Becker, Carey, and Oden 1981). Two types of shape functions are used for the quadrilateral elements: regular bilinear shape functions and singular root shape functions. The bilinear shape functions ψ_i^q are used for the regular quadrilaterals:

$$\begin{aligned} \psi_1^q &= \frac{1}{4}(1-\eta)(1-\xi) \quad ; \quad \psi_2^q = \frac{1}{4}(1-\eta)(1+\xi) \\ \psi_3^q &= \frac{1}{4}(1+\eta)(1+\xi) \quad ; \quad \psi_4^q = \frac{1}{4}(1+\eta)(1-\xi) \end{aligned} \quad (4.40)$$

We use singular root shape functions to solve the singular fracture opening equation over the quadrilateral elements. The shape of these functions is consistent with the work of Kassir and Sih (1966), who observed that the fracture opening displacement decreases with the square root of the distance towards the fracture tip. The master element for the singular quadrilaterals is shown on the right side of Fig. 4.7. The associated shape functions ψ_i^s and their derivatives are given by:

$$\begin{aligned}
\psi_1^s &= \frac{1}{2}(1-\eta)(1-\xi)^{1/2} & ; & \quad \psi_2^s = 0 & ; & \quad \psi_3^s = 0 & ; & \quad \psi_4^s = \frac{1}{2}(1+\eta)(1-\xi)^{1/2} \\
\frac{\partial \psi_1^s}{\partial \xi} &= -\frac{1}{4}(1-\eta)(1-\xi)^{-1/2} & ; & \quad \frac{\partial \psi_4^s}{\partial \xi} = -\frac{1}{4}(1+\eta)(1-\xi)^{-1/2} & & & & (4.41) \\
\frac{\partial \psi_1^s}{\partial \eta} &= -\frac{1}{2}(1-\xi)^{1/2} & ; & \quad \frac{\partial \psi_4^s}{\partial \eta} = \frac{1}{2}(1-\xi)^{1/2} & & & &
\end{aligned}$$

By construction, the side 2-3 of the singular quadrilateral always coincides with the fracture front where the width is zero. The side 1-4 of the singular quadrilateral is connected to the base of the adjacent triangle, as seen in **Fig. 4.8**. The displacement along the side 1-4 of the quadrilateral is a linear function, which is completely determined by its nodal values at nodes 1 and 4. On the adjacent triangle, the displacement is also a linear function along the nodes connected to side 1-4. Therefore, there is no gap in the opening displacement between the singular and the regular elements. This arrangement is shown on the right side of Fig. 4.8.

We use Gaussian quadrature rules to perform numerical integrations. The order of the quadrature depends on the type of element. The following quadrature rules are used in this work:

- 12-point integral rule for 1D integration along a segment;
- 7-point integral rule for 2D integration along a regular triangle;

- 9-point integral rule for 2D integration along a bilinear regular quadrilateral (which is used for the pressure and transport equations); and
- 9-point integral rule for 2D integration along a bilinear singular quadrilateral (which is used for the fracture opening equation).

4.6.4 Boundary Node Generation

We use different re-meshing techniques for constructing the boundary nodes and the interior nodes. At each time step Δt^n , the fracture front advances along its outward normal direction, as seen in Fig. 4.4. The nodal points from the previous fracture front $\partial\Omega_f^n$ are repositioned to form the new fracture front $\partial\Omega_f^{n+1}$. This movement of the boundary nodes is the first step performed by the re-meshing algorithm. These nodes delimit the fracture domain.

The spacing between the boundary nodes control the size of the quadrilaterals and adjacent triangles placed near the fracture front. These elements play a critical role in determining the shape of the fracture. An efficient optimization scheme is required to refine the shape of the front and avoid numerical instabilities, particularly for cases where the distribution of the *in-situ* stresses promotes fracture propagation across multiple layers. As the fracture crosses boundaries, re-entrant corners may form and hinder the numerical calculations.

We use several refinement criteria for boundary node generation and re-distribution. A new boundary node is inserted if the ratio of the spacing between two nodes divided by the minimum spacing along the front exceeds a critical value. Similarly, a new boundary node is inserted if the ratio of the spacing between two nodes divided by the spacing between the adjacent nodes exceeds a critical value. Once we determined the

number of boundary nodes, the nodes are re-distributed using a technique referred to as *smoothing*. The position of a given node is modified if the ratio between adjacent nodes is lower than a critical value, or if this ratio exceeds a critical value. The user can change these parameters to control the distribution of the boundary nodes along the fracture edge.

4.6.5 Interior Node Generation

Once the quadrilaterals are positioned along the boundary, the triangular elements are distributed within the newly formed domain. The location of the nodes, as well as the total number of nodes, is critical to ensure the stability of the numerical calculations. The construction of the interior mesh encompasses the redistribution of the existing nodes and the insertion of new nodes.

Several meshing techniques are used for interior node generation. First, we re-distribute the interior nodes using an angle-weighted average smoothing method. This method, referred to as node *convection*, reduces the occurrence of elongated elements (Ouyang 1997). Then, we remove large elements by inserting additional nodes. If the area of a triangle exceeds a critical value, a node is inserted so the triangle is divided into three smaller elements. In addition, if the ratio of the area of a triangle divided by the area of the smallest triangle exceeds a critical value, a node is inserted into the larger triangle. Finally, we construct the triangles from the interior nodes using the Delaunay triangulation, which reduces the formation of elongated elements.

The meshing techniques presented in this chapter were satisfactory for most cases, but they sometimes led to inaccurate numerical results for complex fracture shapes. Over the past decade, there have been significant developments in re-meshing techniques and adaptive schemes for moving boundary problems. In particular, the video game industry has developed fast and flexible unstructured meshing schemes that could be applicable to

fracturing. Some of these techniques could be implemented in the future to improve the current gridding capabilities. These techniques are out of the scope of this work, and they will not be addressed in this dissertation.

4.7 MAIN DIFFERENCES WITH *UTFRAC-3D*

UTFRAC-3D refers to the current version of the fracturing code initially developed by Gu (1987), Ouyang (1994), and Yew (1997) at the University of Texas. The work of these authors has been instrumental in the pursuit of the work presented in this dissertation. Specifically, *UTFRAC-3D* is the basis of our new model for: (1) solving the fracture opening equation, (2) solving the stress intensity factor calculations, and (3) coupling the pressure and fracture opening equations. We also use similar shape functions and elements.

However, there are many differences between their model and the one we are proposing in this dissertation; therefore, we rewrote the finite element code these authors initially proposed. The following list shows some of the features of our model that differ from their work:

- The pressure equation accounts for multi-phase, compressible fluid flow.
- The compatibility equation expresses the overall conservation of mass (as opposed to the conservation of volume implemented into *UTFRAC-3D*).
- We implemented an adaptive fracture front displacement method.
- The proppant transport equation is significantly different.
- We incorporated an energy balance equation and *NC* component transport equations.

- The model predicts changes in phase behavior.
- A new time-decoupling scheme dissociates the resolution of the transport equations from the resolution of the pressure equation.
- A time-slicing scheme improves the stability of the solution of the convection-dominated equations.
- We used different numerical solvers (from the *LAPACK* library).
- The meshing scheme incorporates additional features.
- The full model also includes a wellbore model, which relates the surface and bottomhole conditions, and a productivity model, which assesses the productivity of the fractured well during flowback.

Table 4.1: Comparison of the proppant transport, component transport, and temperature equations.

Proppant c	Component ω_{I1}	Temperature T_D
$\frac{\partial}{\partial t}(\alpha c) + \nabla \cdot (\vec{q}c)$ $-\nabla \cdot (w\varepsilon \vec{\nabla} c) = 0$ $\begin{cases} c = c_{inj} \text{ on } \partial\Omega_p \\ \vec{q} = 0 \text{ on } \partial\Omega_f \text{ and } \partial\Omega_c \end{cases}$	$\frac{\partial}{\partial t}(\alpha \omega_{I1}) + \nabla \cdot (\vec{q} \omega_{I1})$ $-\nabla \cdot (w\varepsilon \vec{\nabla} \omega_{I1}) + \frac{2}{\sqrt{t-\tau}} q_L \omega_{I1} = 0$ $\begin{cases} \omega_{I1} = \omega_{I1, inj} \text{ on } \partial\Omega_p \\ \vec{q} = 0 \text{ on } \partial\Omega_f \text{ and } \partial\Omega_c \end{cases}$	$\frac{\partial}{\partial t}(\alpha T_D) + \nabla \cdot (\vec{q} T_D) - \nabla \cdot (w\varepsilon \vec{\nabla} T_D)$ $+ \frac{2T_D}{\sqrt{t-\tau}} (q_L + q_{cond}) = \frac{2}{\sqrt{t-\tau}} \left(q_L \frac{T_{inj}}{T_{inj} - T_R} + q_{cond} \right)$ $\begin{cases} T_D = 0 \text{ on } \partial\Omega_p \\ \vec{q}_T = 0 \text{ on } \partial\Omega_f \text{ and } \partial\Omega_c \end{cases}$

Table 4.2: Choice of coefficients to obtain the proppant transport, component transport, and temperature equations from the generic problem given in Eq. 4.24.

	Proppant c	Component ω_{I1}	Temperature T_D
α	w	$w(1-c)(\rho_1 S_1 + K_I \rho_2 S_2)$	$w(S_1^* \rho_1^* C_{p,1}^* + S_2^* \rho_2^* C_{p,2}^*)$
q_x	$\frac{\lambda_{1,x} q_{1,x}^* + K_\gamma \lambda_{2,x} q_{2,x}^*}{K_\gamma + S_1^* (1 - K_\gamma)}$	$\rho_1 q_{1,x}^* \left((1 - \gamma_1) + \frac{\rho_p}{\rho_1} \gamma_1 (1 - \lambda_{1,x}) \right) +$ $K_I \rho_2 q_{2,x}^* \left((1 - \gamma_2) + \frac{\rho_p}{\rho_2} \gamma_2 (1 - \lambda_{2,x}) \right)$	$q_{1,x}^* \rho_1^* C_{p,1}^* + q_{2,x}^* \rho_2^* C_{p,2}^*$
q_y	$\frac{\lambda_{1,y} q_{1,y}^* + K_\gamma \lambda_{2,y} q_{2,y}^*}{K_\gamma + S_1^* (1 - K_\gamma)}$	$\rho_1 q_{1,y}^* \left((1 - \gamma_1) + \frac{\rho_p}{\rho_1} \gamma_1 (1 - \lambda_{1,y}) \right) +$ $K_I \rho_2 q_{2,y}^* \left((1 - \gamma_2) + \frac{\rho_p}{\rho_2} \gamma_2 (1 - \lambda_{2,y}) \right)$	$q_{1,y}^* \rho_1^* C_{p,1}^* + q_{2,y}^* \rho_2^* C_{p,2}^*$
q_L	0	$\rho_1 C_{w,1} + K_I \rho_2 C_{w,2}$	$\rho_1 C_{p,1} C_{w,1} + \rho_2 C_{p,2} C_{w,2}$
q_{cond}	0	0	$\sqrt{\frac{K_R \rho_R C_{p,R}}{\pi}} \psi(c) \phi(c)$
f_R	0	0	$q_L \frac{T_{inj}}{T_{inj} - T_R} + q_{cond}$

Table 4.3: Matrix coefficients in Eq. 4.33 to solve the proppant transport, component transport, and temperature equations.

	Proppant c	Component ω_{1i}	Temperature T_D
A_{ij}	$\int_{\Omega} \alpha \phi_i \phi_j d\Omega$	$\int_{\Omega} \alpha \phi_i \phi_j d\Omega$	$\int_{\Omega} \alpha \phi_i \phi_j d\Omega$
$B_{1,ij}$	$\int_{\Omega} \frac{\partial \alpha}{\partial t} \phi_i \phi_j d\Omega$	$\int_{\Omega} \frac{\partial \alpha}{\partial t} \phi_i \phi_j d\Omega$	$\int_{\Omega} \frac{\partial \alpha}{\partial t} \phi_i \phi_j d\Omega$
$B_{2,ij}$	$-\int_{\Omega} \left(q_x \frac{\partial \phi_i}{\partial x} + q_y \frac{\partial \phi_i}{\partial y} \right) \phi_j d\Omega$	$-\int_{\Omega} \left(q_x \frac{\partial \phi_i}{\partial x} + q_y \frac{\partial \phi_i}{\partial y} \right) \phi_j d\Omega$	$-\int_{\Omega} \left(q_x \frac{\partial \phi_i}{\partial x} + q_y \frac{\partial \phi_i}{\partial y} \right) \phi_j d\Omega$
$B_{3,ij}$	$\varepsilon \int_{\Omega} \left(\frac{\partial \phi_j}{\partial x} \frac{\partial \phi_i}{\partial x} + \frac{\partial \phi_j}{\partial y} \frac{\partial \phi_i}{\partial y} \right) wd\Omega$	$\varepsilon \int_{\Omega} \left(\frac{\partial \phi_j}{\partial x} \frac{\partial \phi_i}{\partial x} + \frac{\partial \phi_j}{\partial y} \frac{\partial \phi_i}{\partial y} \right) wd\Omega$	$\varepsilon \int_{\Omega} \left(\frac{\partial \phi_j}{\partial x} \frac{\partial \phi_i}{\partial x} + \frac{\partial \phi_j}{\partial y} \frac{\partial \phi_i}{\partial y} \right) wd\Omega$
$B_{4,ij}$	0	$\frac{2}{\sqrt{t-\tau}} \int_{\Omega} q_L \phi_i \phi_j d\Omega$	$\frac{2}{\sqrt{t-\tau}} \int_{\Omega} q_L \phi_i \phi_j d\Omega$
$B_{5,ij}$	0	0	$\frac{2}{\sqrt{t-\tau}} \int_{\Omega} q_{cond} \phi_i \phi_j d\Omega$
C_i	0	0	$\frac{2}{\sqrt{t-\tau}} \int_{\Omega} \left(q_L \frac{T_{inj}}{T_{inj} - T_R} + q_{cond} \right) \phi_i d\Omega$

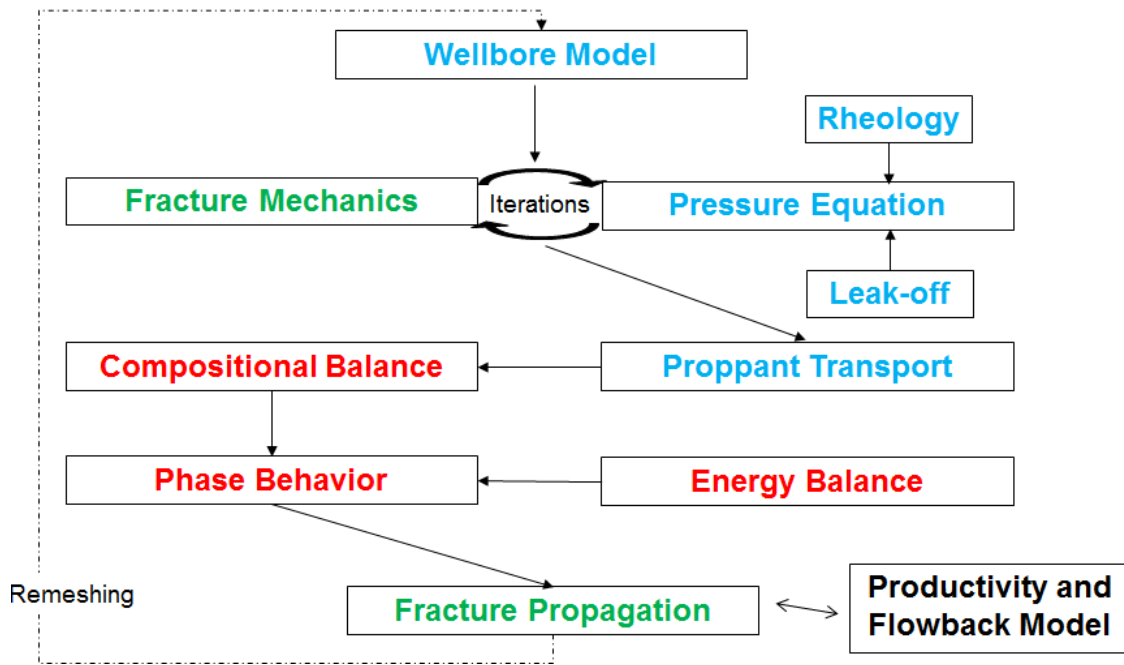


Figure 4.1: Simplified version of the main algorithm. The green color indicates equations that are used in conventional fracturing simulators; blue indicates equations that are modified to account for multi-phase compressible fluid flow; and red indicates equations that are not present in traditional fracturing models.

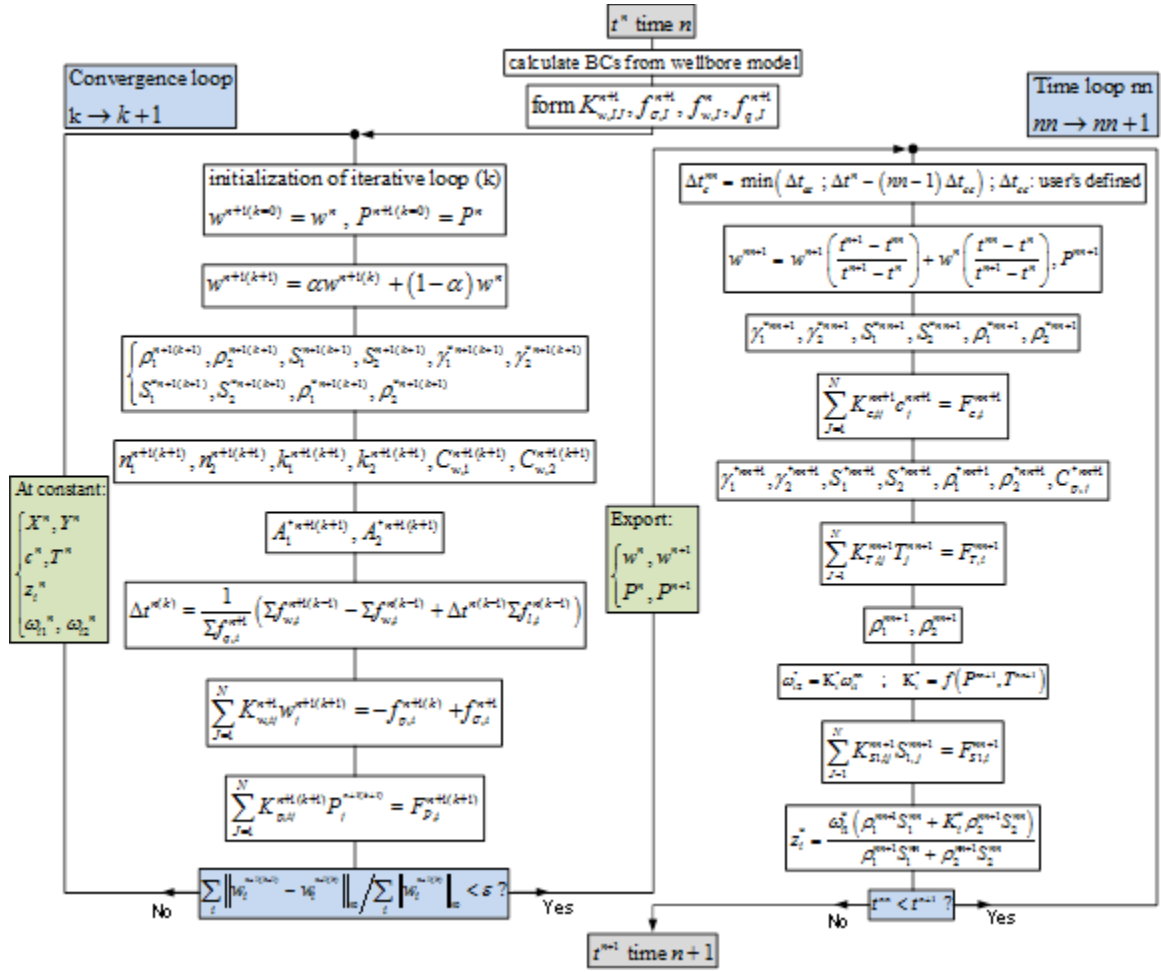


Figure 4.2: General structure of the algorithm implemented in EFRAC-3D. The left side shows the iterative process used to compute pressure and width for a calculated time step Δt^n . The right side shows the time-forward loop used to compute proppant concentration, fluid temperature, and fluid composition.

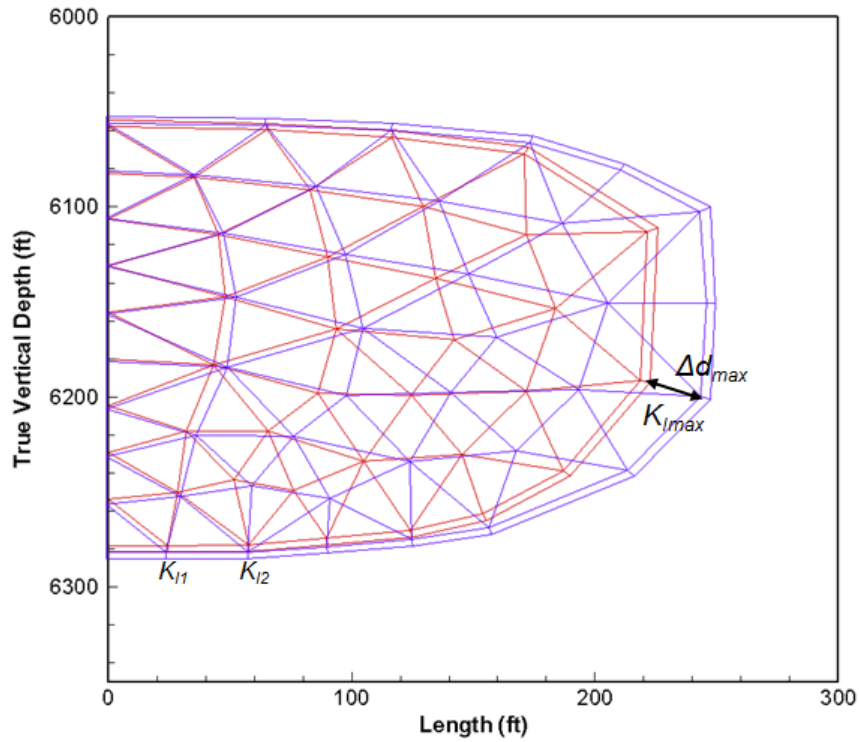


Figure 4.3: Fracture propagation scheme. The node with the maximum stress intensity factor (K_{imax}) advances by a distance equal to the maximum front displacement (Δd_{max}). The motion of the other boundary nodes is governed by Eq. 4.37. The old fracture is indicated in red, and the new fracture is indicated in blue.

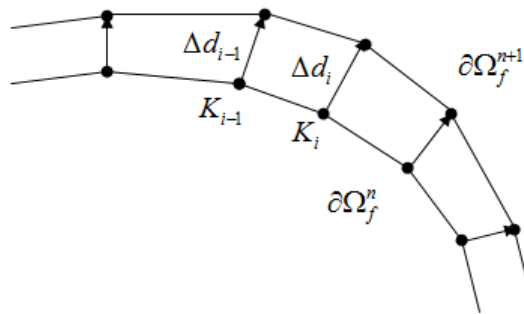


Figure 4.4: Movement of the boundary nodes between times t^n and t^{n+1} . Each node advances along its outward normal direction (adapted from Gu 1987).

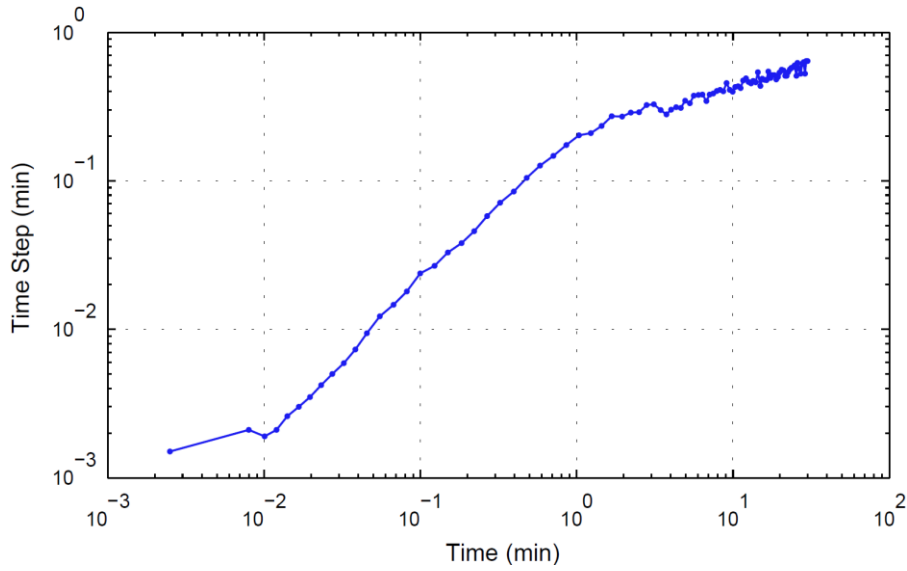


Figure 4.5: Example illustrating the evolution of the time step calculated from the compatibility condition (for the validation case presented in Section 6.2.3).

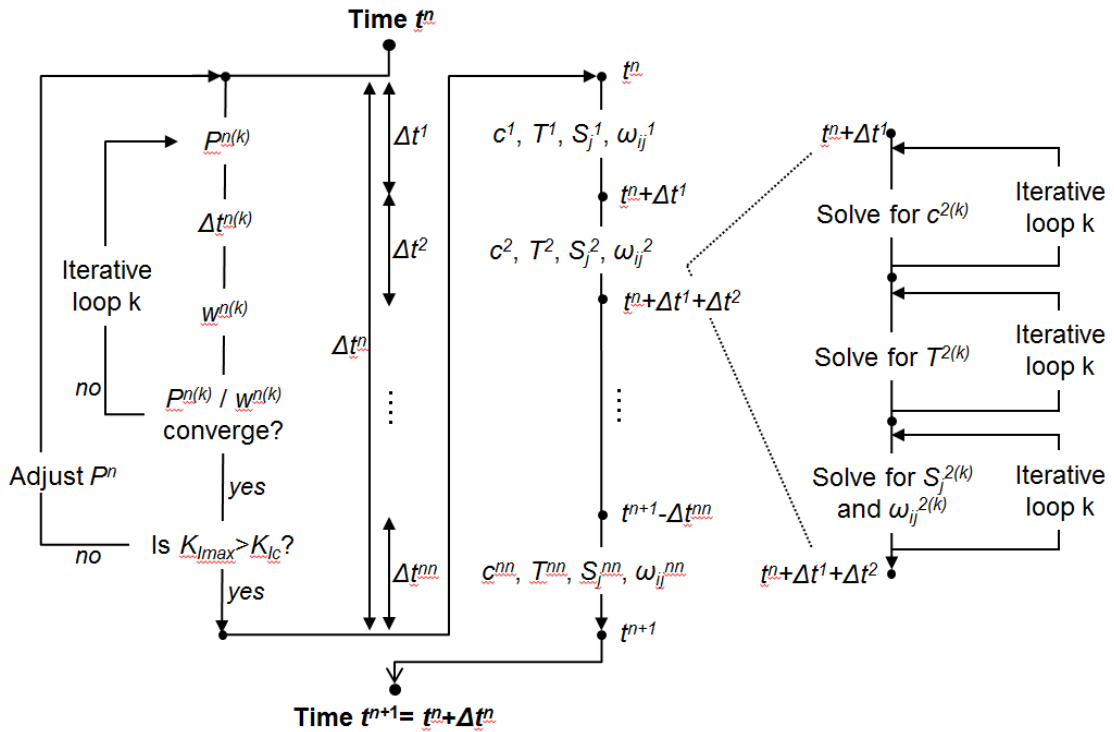


Figure 4.6: Time decoupling scheme. First, we compute fracture width and pressure using a relaxation iterative procedure. Then, we solve the transport equations using a time-forward loop and individual iterative schemes.

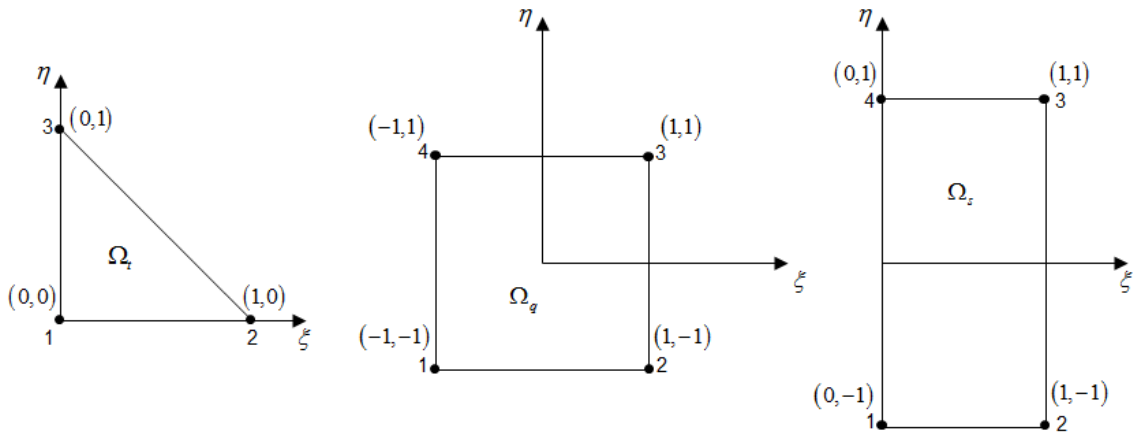


Figure 4.7: Master elements for the regular triangular (Ω_t), regular quadrilateral (Ω_q), and singular quadrilateral (Ω_s) elements.

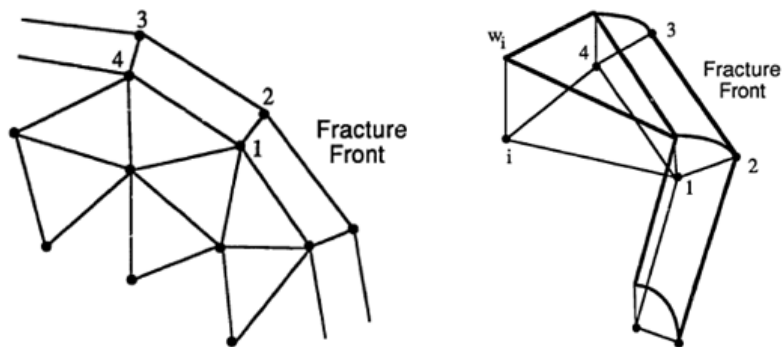


Figure 4.8: Node arrangement at the fracture tip. By construction, each pair of triangle and quadrilateral shares a side (from Gu 1987).

NOMENCLATURE

$A_{ij}, B_{l,ij}, C_{ij}, F_{ij}, K_{ij}, U_i$	= matrix coefficients at nodes i and j .	n	= normal direction
A_j^*	= Intermediate variable defined in Eq. 3.9, $\text{ft}^5/(\text{lb-f-min})$	n_J	= flow behavior index of slurry phase J
c	= proppant concentration (volume fraction)	NC	= number of components
C_p	= heat capacity, $\text{BTU}/(\text{lbm-}^\circ\text{F})$	NP	= number of phases
C_w	= leakoff coefficient, $\text{ft}/\sqrt{\text{min}}$	P	= fluid pressure, psi
f	= arbitrary function	r	= distance between the source and the field point in Eq. 4.34, ft
g	= gravity of earth, ft/s^2	R	= gas constant, $\text{ft-lbf}/(\text{lbm-}^\circ\text{R})$
G	= shear modulus of the rock, psi	S_J	= saturation of fluid phase J
K_J	= flow consistency index of slurry phase J , $\text{lbm-min}^n/\text{ft}^2$	S_J^*	= saturation of slurry phase J
$k_{ret,J}$	= retardation factor for slurry phase J in the horizontal direction	t	= time, min
K_I	= stress intensity factor, $\text{psi-}\sqrt{\text{in}}$	T	= fluid temperature, $^\circ\text{F}$
K_{IC}	= fracture toughness, $\text{psi-}\sqrt{\text{in}}$	T_D	= dimensionless temperature
K_R	= thermal conductivity of rock, $\text{BTU}/(\text{min-ft-}^\circ\text{F})$	T_R	= reservoir temperature, $^\circ\text{F}$
K_γ	= proppant split between two phases (γ_2/γ_1)	u	= unknown function
q_{cond}	= conductive flux, ft/min	v	= test function
$q_{J,x}$	= flow rate per unit height of fluid phase J in the horizontal direction, ft^2/min	w	= fracture width, ft
$q_{J,y}$	= flow rate per unit height of fluid phase J in the vertical direction, ft^2/min	x	= horizontal location, ft
$q_{J,x}^*$	= flow rate per unit height of slurry phase J in the horizontal direction, ft^2/min	y	= vertical location, ft
$q_{J,y}^*$	= flow rate per unit height of slurry phase J in the vertical direction, ft^2/min		
$q_{L,j}$	= fluid-loss flow rate per unit height of fluid phase J , ft/min		
$q_{p,J,x}^*$	= flow rate per unit height of proppant in phase J in the horizontal direction, ft^2/min		
$q_{p,J,y}^*$	= flow rate per unit height of proppant in phase J in the vertical direction, ft^2/min		
m_{pumped}	= mass rate imposed at the perforations, lbm/min		
		Subscripts	
		i	= node i
		I	= component I
		inj	= BCs at the perforations
		j	= node j
		J	= phase J
		N	= order the of the Galerkin approximation
		p	= proppant
		R	= reservoir
		Superscripts	
		k	= iteration k
		n	= time step n
		*	= slurry property
		.	= field point in Eq. 4.34
		Greek Symbols	
		α, β, γ	= coefficients in generic PDEs
		α_r	= relaxation parameter
		γ_J	= proppant concentration (volume fraction) in slurry phase J
		Δd	= displacement of the fracture front in the normal direction, ft

Δd_{max}	= maximum displacement of the fracture front, ft	ϕ_N	= basis function of order N
$\partial\Omega$	= boundary of the fracture domain	ρ_J	= density of fluid phase J , lbm/ft ³
$\partial\Omega_c$	= non-perforated portion along the wellbore	ρ_J^*	= density of slurry phase J , lbm/ft ³
$\partial\Omega_f$	= fracture front	ρ_p	= density of proppant, lbm/ft ³
$\partial\Omega_p$	= perforated interval along the wellbore	ρ_R	= density of reservoir rock, lbm/ft ³
$\Delta m_{fracture}$	= change in fracturing fluid mass during Δt^n , lbm	ρ_T^*	= density of slurry, lbm/ft ³
$\Delta m_{leakoff}$	= mass of fluid that leaked off during Δt^n , lbm	σ_{hmin}	= <i>in-situ</i> minimum horizontal stress, psi
Δt^n	= time step increment, min	τ	= retardation factor, min
ε_D	= diffusion coefficient in Eq. 4.24	ν	= Poisson's ratio of the rock
ζ	= coordinate in the master element	ω_{IJ}	= mass fraction of component I in phase J
$\lambda_{J,x}, \lambda_{J,y}$	= retardation factor for proppant in phase J in the horizontal and vertical direction	Ω	= fracture domain
η	= coordinate in the master element	Ω_q	= regular quadrilateral master element
		Ω_s	= singular quadrilateral master element
		Ω_t	= regular triangular master element

REFERENCES

- Becker, E.B., Carey, G.F., and Oden, J.T. 1981, *Finite Elements: An Introduction*, Volume 1, Prentice-Hall, Inc., Englewood Cliffs, NJ.
- Economides, M. and Nolte, K.G. 2000, *Reservoir Stimulation, Third Edition*, John Wiley and Sons, New York City, New York.
- Gu, H. 1987. A Study of Propagation of Hydraulically Induced Fractures, Ph.D. Dissertation, The University of Texas at Austin, Austin, Texas (December 1987).
- Kassir, M.K. and Sih, G.C. 1966. Three-Dimensional Stress Distribution Around an Elliptical Crack Under Arbitrary Loadings. *ASME J. Appl. Mech.* **33**: 601–611.
- LAPACK, Linear Algebra PACKage, information available at www.netlib.org/lapack/.
- Linkov, A.M. 2011. On Efficient Simulation of Hydraulic Fracturing in terms of particle Velocity. *Int. Journ. Eng. Sci.* **52**: 77-88.
- Mastrojannis, E.N., Keer, L.M., and Mura, T. 1979. Stress Intensity Factor for a Plane Crack under Normal Pressure. *Int. J. Fracture* **15**: 247-258.
- Ouyang, S. 1994. Propagation of Hydraulically Induced Fractures with Proppant Transport, Ph.D. Dissertation. The University of Texas at Austin, Austin, Texas (December 1987).
- Renka, R.J. 1981. Triangulation and bivariate interpolation for irregularly distributed data points. Ph.D. Dissertation, The University of Texas at Austin, Austin, Texas (December 1981).
- Ribeiro, L.H. and Sharma, M.M 2013. A New 3D Compositional Model for Hydraulic Fracturing with Energized Fluids. *SPE Prod & Oper* **28**(3): 259-267. SPE 159812-PA.
- Yew, C.H. 1997, *Mechanics of Hydraulic Fracturing*, Gulf Publishing Company, Houston, Texas.

Chapter 5: Wellbore and Fracture Productivity Models

Fracturing fluid properties change not only inside the fracture, but also along the wellbore, as the fluid travels from the surface to the perforations. Operators regularly collect temperature and pressure data at the surface, but they rarely collect *in-situ* data. A wellbore model is thus required to estimate the variations in temperature and pressure along the wellbore. The wellbore model we implemented is very similar to the popular heat-transfer model proposed by Hasan and Kabir (1994, 2002, and 2012). Although variations in density and composition are negligible for traditional water-based fluids, changes in pressure and temperature affect the density and composition of compressible fluids. Heat transfers are usually amplified when we use energized fluids, as the gas component is injected at very low temperatures. Thus, a rigorous treatment of the wellbore calculations is critical when designing energized treatments.

Evaluating the performance of a fracture treatment is not about determining the final geometry of the fracture, but rather determining the associated hydrocarbon production; therefore, we developed a fractured well productivity model to assess fracture performance. It consists of a two-phase, pseudo 1D, fractured well productivity model that is very similar to the model developed by Frieauf, Suri and Sharma (2010). The fracture communicates with the reservoir via a 2D interpolation scheme that maps the properties of the unstructured grid into the Cartesian reservoir grid. The interpolation scheme constitutes the interface between the fracture and the reservoir; it monitors the amount of fluid invading the reservoir during pumping and shut-in, as well as the amount of fluid recovered during flowback.

The combination of the fracture, wellbore, and productivity models constitutes a design tool particularly suitable for designing and optimizing energized fracture treatments. This single modeling tool enables us to quantify the potential benefits of energizing the fracturing fluid.

5.1 TEMPERATURE VARIATION IN THE WELLBORE

An energy balance equation models the heat transfers occurring between the fracturing fluid and the reservoir. A rigorous treatment of heat transfers is important, as changes in temperature affect the fracturing fluid's composition, density, and rheology. Our model is very similar to the wellbore model proposed by Hasan and Kabir (1994, 2002, and 2012). We chose to use their model because of its simplicity, robustness, and popularity in the industry. The implementation of the wellbore model into our code is similar to the work of Frieauf (2009). The main difference is that our formulation applies to any wellbore geometry while the formulation used by Frieauf (2009) was restricted to a vertical wellbore configuration. The main features and derivations of the model are presented in this chapter.

5.1.1 Definition and Formulation of Heat Exchanges

The primary heat transfers are the heat conduction between the reservoir and the wellbore, and the forced convection that occurs as the fluid travels down the well. The heat conduction in the vertical direction is negligible compared to the heat transfer in the horizontal plane. This assumption reduces the heat conduction problem to a pseudo 1D problem for each horizontal slice of the reservoir. The *undisturbed* reservoir temperature T_{ei} (also referred to as *far-field* temperature) is a known function of depth, so the heat conduction flux remains dependent on depth:

$$T_{ei}(z) = T_{ei}(TVD) = T_{es} + g_G \times TVD \quad (5.1)$$

Following the work of Ramey (1962) and Hasan and Kabir (1994), the surrounding earth is modeled as an infinite sink, and the wellbore is modeled as a line source of finite diameter. The heat diffusion per unit well depth (Q) between the well and the reservoir has the following expression, irrespective of the well configuration:

$$Q = \frac{2\pi k_R}{T_D} (T_{wb} - T_{ei}) \quad (5.2)$$

In Eq. 5.2, T_{wb} is the temperature of the interface between the well and the reservoir; T_{ei} is the undisturbed reservoir temperature; and T_D is a dimensionless function given by:

$$T_D = \ln\left(e^{-0.2t_D} + (1.5 - 0.3719e^{-t_D})\sqrt{t_D}\right) \quad (5.3)$$

Eq. 5.3 expresses the cooling (heating) of the reservoir resulting from the heating (cooling) of the wellbore. The variable t_d is the dimensionless producing time:

$$t_D = \frac{4k_R}{\rho_e C_{p,R} d_{wb}^2} t \quad (5.4)$$

Even for steady-state heat transfers, the temperature of the reservoir in contact with the well is a function of time. As the reservoir heats the fracturing fluid, T_{wb} decreases, but the time dependence decreases over time, as seen on Eq. 5.3.

The heat exchanged by diffusion inside the reservoir is transferred radially from the outer layer of the wellbore to the fluid in the well. The heat transfer is given by:

$$Q = -\pi d_{io} U_{io} (T_f - T_{wb}) \quad (5.5)$$

U_{to} is an overall heat transfer coefficient (based on the outer tubing area) that represents the equivalent thermal resistance offered by the wellbore. As seen in **Fig. 5.1**, the equivalent resistance is the summation of the multiple resistances offered by the cement, casing wall, annulus, thermal insulation, and tubing wall. Because heat transfer is dominant in the radial direction, we assume that the resistances are in a series; therefore, the overall heat-transfer coefficient is given by the following summation:

$$\frac{1}{U_{to}} = \frac{r_{to}}{r_i h_t} + \frac{r_{to} \ln(r_{to} / r_{ti})}{k_t} + \frac{r_{to} \ln(r_{ins} / r_{to})}{k_{ins}} + \frac{r_{to}}{r_{ins} h_a} + \frac{r_{to} \ln(r_{caso} / r_{casi})}{k_{cas}} + \frac{r_{to} \ln(r_{wb} / r_{caso})}{k_{cem}} \quad (5.6)$$

If any part of the completion does not exist in a particular well configuration, the thermal resistance of that part is set to zero. The heat transfer coefficients for the natural convection in the annulus (h_a) and convection inside the tubing (h_t) are calculated from empirical correlations (Hasan and Kabir 2002).

The heat received by the fluid must equal that coming from the reservoir; therefore, the expression of the heat transfer coefficient is given by equating Eqs. 5.2 and 5.5:

$$Q = -L_R (T_f - T_{ei}) = -\frac{2\pi}{c_p m} \left(\frac{r_{to} U_{to} k_R}{k_R + r_{to} U_{to} T_D} \right) (T_f - T_{ei}) \quad (5.7)$$

The parameter L_R defined in Eq. 5.7 is an overall heat transfer coefficient that depends on the thermal properties of both the wellbore and the rock formation.

5.1.2 Energy Balance Equation along the Wellbore

The temperature distribution is obtained from an energy balance equation for the fluid in the wellbore. Assuming that the heat transfers occur in a pseudo steady-state manner, the energy balance equation is given by:

$$\frac{dT_f}{dz} = -L_R (T_f - T_{ei}) + \frac{g \sin \alpha}{c_p} - \left(\frac{v}{c_p} \frac{dv}{dz} - C_{JT} \frac{dP}{dz} \right) \quad (5.8)$$

We assume that the kinetic energy (dv/dz) and Joule-Thompson (C_{JT}) effects are negligible; therefore Eq. 5.8 becomes:

$$\frac{dT_f}{dz} = -L_R (T_f - T_{ei}) + \frac{g \sin \alpha}{c_p} \quad (5.9)$$

We follow the work of Hasan and Kabir (2012) and represent the wellbore as a series of segments of constant diameter, as seen in **Fig. 5.2**. The parameter L_R is uniform for a given well segment, and its time dependence is weak; hence, Eq. 5.9 is a first-order linear differential equation, which can be solved with the integrating factor method:

$$T_f = T_{ei} + \frac{1}{L_R} \left(1 - e^{L_R(z-z_j)} \right) \left(g_G \sin \alpha - \frac{g \sin \alpha}{c_p} \right) + e^{L_R(z-z_j)} (T_{fj} - T_{ei_j}) \quad (5.10)$$

In Eq. 5.10, T_{fj} is the local boundary condition that specifies that the temperature at the distance z_j is known. This expression is used to account for changes in wellbore inclination and diameter.

5.2 PRESSURE VARIATION IN THE WELLBORE

A rigorous treatment of fluid flow along the wellbore is important because energized fluids are compressible. The changes in pressure affect the fracturing fluid

composition and density. Similarly to the temperature model, we chose to use the model proposed by Hasan and Kabir (2002) because of its simplicity, robustness, and popularity. The flow problem reduces to a pseudo 1D flow problem, in which the fluid properties are averaged along each cross-section of the wellbore.

5.2.1 Pressure Equation

The total pressure gradient is the sum of the hydrostatic head caused by the weight of the fluid, the frictional pressure drop, and the kinetic gradient:

$$\frac{dP}{dz} = \rho g - \left(\frac{dP}{dz} \right)_{fr} - \rho v \frac{dv}{dz} \quad (5.11)$$

In this study, we assume that the kinetic gradient (dv/dz) is negligible compared to the hydrostatic gradient and the frictional pressure drop. The hydrostatic head per unit of length is simply the density of the fluid multiplied by the gravitational constant. The frictional pressure drop is estimated from friction factor correlations or from actual pressure data measured along the wellbore.

For foams, we assume that the two-phase mixture remains stable; therefore, the velocity is the same for both phases, and the two-phase flow problem reduces to a pseudo single-phase flow problem. Because energized fluids are compressible, the density of the fluid is itself a function of pressure in Eq. 5.11. This effect is accounted for by updating the fluid density and composition at intermediate locations along the wellbore. We use a similar procedure to update fluid rheology along the well.

5.2.2 Frictional Loss

The frictional pressure loss depends on the rate of injection, fluid rheology, and tubing diameter. The pressure loss is usually estimated from empirical correlations that

invoke the Fanning friction factor (f), which is a function of the roughness of the pipe and the level of turbulence within fluid flow:

$$\left(\frac{dP}{dz}\right)_{fr} = \frac{2f\rho v^2}{d_{ii}} \quad (5.12)$$

Many laboratory and field studies have been conducted to estimate the frictional pressure loss. In our model, three options are available:

- the frictional pressure gradient is prescribed by the user;
- the Fanning friction factor is prescribed by the user; or
- the Fanning friction factor is estimated from empirical correlations.

When field data are available, the user can directly prescribe the frictional pressure gradient per unit length for a given injection rate. This is the most accurate representation of the flow behavior inside the well. Similarly, the user can prescribe the value of the fanning friction coefficient when it is determined from carefully-controlled experiments. These formulations are particularly useful for history-matching purposes.

Often, the frictional pressure loss is unknown *a priori*, so empirical models are required to estimate it. The injection rates, viscosities, and tubing diameters used in fracturing typically result in turbulent flow at high Reynolds numbers (Re higher than 10^4). A common correlation for the friction factor under turbulent flow (Denn 1980) is given by:

$$f = \left(-1.737 \ln \left[0.269 \frac{\varepsilon}{d_{ii}} - \frac{2.185}{Re} \ln \left(0.269 \frac{\varepsilon}{d_{ii}} + \frac{14.5}{Re} \right) \right] \right)^{-2} \quad (5.13)$$

This correlation predicts unreasonably large pressure drops for most fracturing applications, as fracturing fluids usually contain friction-reducing polymers that have been known to cause a drag reduction. As shown by Virk (1975) and Denn (1980), long polymer molecules dampen flow instabilities and hence reduce the turbulent energy dissipation. For high Reynolds numbers, Denn (1980) proposed the following friction factor correlation:

$$\ln(f) = 28.135 + \left[-29.379 + (8.2405 - 0.86227x_{Re})x_{Re} \right] x_{Re} \quad (5.14)$$

where $x_{Re} = \ln[\ln(Re_w)]$

In the oil industry, Valkó and Economides (1995) notably used Eq. 5.14 to account for the addition of gelling agents in fracturing fluids. The wall Reynolds number, Re_w , is used in Eq. 5.14 so the shear-thinning behavior of the fluid is taken into account. The wall Reynolds number is related to the general Reynolds number Re as follows:

$$Re_w = \left(\frac{1+3n}{4n} \right) Re \quad (5.15)$$

5.3 NEAR-WELLBORE FRICTIONAL LOSS

High near-wellbore friction losses have been observed in fracturing treatments, particularly in deviated wells or when the perforations are inadequate or poorly designed. The friction losses are attributed to several phenomena, such as poor wellbore communication through the perforations, tortuosity as the fracture turns and twists, and perforation phasing misalignment. A close study of fracture initiation and near-wellbore complexities requires the use of complex models, which are applicable only in a research environment under limited assumptions. These models are computationally intensive and generally require a specialist to obtain and interpret the results. One example of such a

study was recently published by Alekseenko *et al.* (2013). Instead of conducting a comprehensive study of near-wellbore phenomena, we chose to use simple empirical correlations to account for near-wellbore pressure losses.

5.3.1 Perforation Frictional Loss

Improper perforating can result in near-wellbore screenouts if the perforations do not provide an adequate pathway between the wellbore and the fracture. The equation commonly used to calculate the perforation friction loss was proposed by McClain (1963):

$$\Delta P_{perf} = 0.2369 \frac{\rho q^2}{d_{perf}^4 N^2 C_{disc}^2} \quad (5.16)$$

In Eq. 5.16, the fluid density ρ is in lbm/gal, the total flow rate q is in bpm; the perforation diameter d_{perf} is in inches; N is the number of active perforations contributing to fluid flow into the fracture; and C_{disc} is a dimensionless discharge coefficient. The form of Eq. 5.16 is based on the assumption that the perforations are short cylindrical tunnels of the same length and diameter. C_{disc} accounts for the effect of the perforation shape on the friction pressure; so this empirical coefficient provides some flexibility for matching field and experimental data.

When proppant is pumped at high flow rates, an erosion process alters the shape of the perforation, thereby reducing the friction loss through the eroded perforations (Crump and Conway 1988). As seen in **Fig. 5.3**, sand erosion increases the value of the discharge coefficient, which results in a decrease in the pressure drop:

$$C_{disc} = \min(0.56 + 1.65 \times 10^{-4} m_{sand,cum}; 0.95) \quad (5.17)$$

The erosion process reaches equilibrium after enough sand has been produced; therefore, Eq. 5.17 contains an upper limit for the value of C_{disc} .

Alternatively, we can use direct empirical correlations to assess the perforation friction loss. When properly calibrated, these empirical correlations are the most accurate representation of the fluid behavior through the perforations. This correlation is not limited by any assumption:

$$\Delta P_{perf} = a_{perf} q^{b_{perf}} \quad (5.18)$$

Eq. 5.18 is a more general representation of the problem, which encompasses the model formulation proposed by McClain (1963) when using:

$$a_{perf} = 0.2369 \frac{\rho}{d_{perf}^4 N^2 C_{disc}^2} \quad \text{and} \quad b_{perf} = 2 \quad (5.19)$$

The user has three options to estimate the perforation friction loss: using Eq. 5.16 with a constant value of C_{disc} , using Eqs. 5.16 and 5.17, or using Eq. 5.18.

5.3.2 Tortuosity Effects

The expression of the perforation friction loss given in Eq. 5.16 assumes that the fracture is properly aligned with the perforations along the wellbore. The friction loss increases when this is not the case, due to phase misalignment, tortuosity, or other near-wellbore phenomena. In this work, the effect of phase misalignment is not explicitly accounted for. Rather, it can be incorporated by decreasing the value of N in Eq. 5.16. N refers to the number of active perforations contributing to fluid flow into the fracture; therefore, if the perforations are misaligned with the fractures, the effective number of active perforations decreases.

Another phenomenon is the turning and twisting of the fracture near the perforations in deviated and horizontal wells (**Fig. 5.4**). In a vertical well, the contact between the fracture and the wellbore extends over several tens of feet, which constitutes a large pathway for the fluid. The flow communication is much more restrained in horizontal wells, as the contact between the fracture and the wellbore is about the size of the wellbore diameter. In a vertical well, the flow regime inside the fracture and near the wellbore is linear. In a horizontal well, the flow regime inside the fracture remains linear, but the flow regime converges toward radial flow near the wellbore. The consequence is an additional pressure drop. Mukherjee and Economides (1991) modeled this behavior as a skin effect, referred to as *choke effect*. In their work, the dimensionless productivity index of a transverse fracture intersecting a horizontal well (J_{DH}) can be obtained from the productivity index of the corresponding fractured vertical well (J_{DV}) as follows:

$$J_{DH} = \frac{1}{\frac{1}{J_{DV}} + s_c} \quad ; \quad s_c = \frac{kh}{k_f w} \left[\ln \left(\frac{h}{2r_{wb}} - \frac{\pi}{2} \right) \right] \quad (5.20)$$

Alternatively, the impact of the different mechanisms responsible for increased friction loss near the wellbore may be accounted for by using Eq. 5.18 with an appropriate choice of coefficients. This is the method we recommend for deviated (and horizontal) wells. Indeed, the current model does not explicitly solve for the local twisting and turning of the fracture near the perforations (as illustrated in Fig. 5.4). For deviated wells, the well trajectory impacts the flow calculations inside the wellbore, but it does not explicitly impact the friction loss caused by the fracture tortuosity. As of now, this effect is accounted for by increasing the value of the friction drop using Eq. 5.18. We recommend an explicit formulation of this effect in the future.

5.4 INTERPOLATION SCHEME BETWEEN THE FRACTURE AND THE RESERVOIR

The performance of the fracturing treatment depends on the interactions between the created fracture and the reservoir. Good communication is essential for the hydrocarbon to flow from the reservoir into the fracture. Thus far, all the computations have been performed inside the fracture using a dynamic unstructured mesh for the propagating fracture, thereby ignoring what happens inside the reservoir. On the other hand, a productivity model estimates the amount of hydrocarbon recovered from the stimulated portion of the reservoir by considering the fracture as a boundary condition for the reservoir. The link between the two approaches is the interpolation scheme presented in this section. The interpolation scheme connects the propagating reservoir and the static reservoir by mapping the dynamic unstructured mesh into a static Cartesian grid.

5.4.1 Algorithm for Interpolation

We developed an efficient algorithm to perform the interpolation between the fracture grid and the reservoir grid. **Fig. 5.5** shows the main steps performed by the algorithm for an arbitrary fracture element T_{elem} . In Fig. 5.5, the smaller black points are the nodes of the reservoir grid. The spacing between the reservoir nodes in the x - and y -directions is a constant prescribed by the user. The three large black points refer to the vertices of the triangular element T_{elem} . The coordinates of these nodes are obtained as part of the solution of the moving-boundary fracturing problem; therefore, the orientation of the triangle is unknown *a priori*. We use the following algorithm (also shown in **Fig. 5.6**) to perform the interpolation scheme over all the fracture elements:

1. Start an outer loop over all the fracture elements.
2. Identify the minimum and maximum along the x - and y - directions for a given element T_{elem} . In this example: $x_{min}=x_1$, $x_{max}=x_2$, $y_{min}=y_2$, and $y_{max}=y_3$.

3. Define the interval of reservoir nodes that encompasses T_{elem} (shown in red in Fig. 5.5). The corresponding indices are denoted by i_{min} , i_{max} , j_{min} , and j_{max} .
4. Start an inner loop over all the reservoir nodes inside this interval. We consider here node i_{node} .
5. Check whether node i_{node} has been used already. A given reservoir node can only belong to one fracture element at most; therefore, if this node has already been identified as part of an element, it is not considered for the following steps.
6. Test whether node i_{node} is strictly inside triangle T_{elem} using a 2D barycentric test referred to as *triangle inclusion test*. An additional test is performed to check if i_{node} lies along one of the triangle edges.
7. If the node is inside the triangle, perform a 2D barycentric interpolation using the values of the property of interest at the vertices of T_{elem} . These nodes, which are indicated by a blue circle in Fig. 5.5, are then discarded for the computations over the next fracture elements.
8. Stop the inner loop over the nodes contained in the interval defined in step 3.
9. Stop the outer loop over the fracture elements.

5.4.2 Barycentric Method

The 2D barycentric method is a simple test to determine if a given node belongs to a given triangle of arbitrary size and orientation. As shown in Fig. 5.5, we consider a node located at (x_p, y_p) and a triangle T_{elem} formed by three nodes of coordinates (x_1, y_1) , (x_2, y_2) , and (x_3, y_3) . The node is inside the triangle if the node always lies on the same side of the vectors formed by the triangle edges. This is the case if the three quantities (t_{p1} , t_{p2} , and t_{p3}) have the same sign:

$$\begin{cases} t_{p1} = (x_p - x_1)(y_2 - y_1) - (y_p - x_1)(x_2 - x_1) \\ t_{p2} = (x_p - x_2)(y_3 - y_2) - (y_p - x_2)(x_3 - x_2) \\ t_{p3} = (x_p - x_3)(y_1 - y_3) - (y_p - x_3)(x_1 - x_3) \end{cases} \quad (5.21)$$

If the node of coordinates (x_p, y_p) is inside the triangle T_{elem} , the interpolated value z_p at this node is given by:

$$\begin{cases} z_p = \alpha_1 x_p + \alpha_2 y_p + \alpha_3 \\ \alpha_0 = x_1 y_2 - x_2 y_1 + x_2 y_3 - x_3 y_2 + x_3 y_1 - x_1 y_3 \\ \alpha_1 = \frac{1}{\alpha_0} [z_1 (y_2 - y_3) + z_2 (y_3 - y_1) + z_3 (y_1 - y_2)] \\ \alpha_2 = \frac{1}{\alpha_0} [z_1 (x_3 - x_2) + z_2 (x_1 - x_3) + z_3 (x_2 - x_1)] \\ \alpha_3 = \frac{1}{\alpha_0} [z_1 (x_2 y_3 - x_3 y_2) + z_2 (x_3 y_1 - x_1 y_3) + z_3 (x_1 y_2 - x_2 y_1)] \end{cases} \quad (5.22)$$

where

5.4.3 Interpolation Examples

Figs. 5.7 and **5.8** provide an example of results obtained with this interpolation scheme. Fig. 5.7 shows the fracture width calculated by solving the fracture mechanics equation inside the 2D unstructured fracture grid, and Fig. 5.8 shows the corresponding fracture width mapped into the static reservoir grid using the interpolation scheme. The match between the two meshes shown in this example is very good, and a similar match has been observed for all the simulations ran in this dissertation.

The intent of the previous example was to show that the interpolation scheme is reliable and efficient by showing the fracture width in both grids. The main purpose of the interpolation scheme is not to merely map properties in the two grids, but to allow us to track the fluid exchanges that occur between the propagating fracture and the static reservoir over time. One of the key factors when evaluating the fracture productivity is

the amount of fluid trapped in the reservoir. **Figs. 5.9** and **5.10** show the mass of water (per unit area) placed into the reservoir immediately after pumping, and after an extended shut-in. The corresponding values for the length of the invaded zone are given in **Figs. 5.11** and **5.12**. These examples show how the interactions between the two grids enable us to dissociate what happens in the fracture from what happens in the reservoir. This feature is critical to evaluate the flowback performance using a productivity model. For instance, at a given time during pumping, the fluid saturation in the fracture is different from the fluid saturation in the reservoir.

5.5 PRODUCTIVITY MODEL FOR FRACTURED WELL

We use a two-phase, pseudo 1D, fractured well productivity model to assess the performance of the fracturing treatment (Ribeiro and Sharma 2013). Our model is almost identical to the model developed by Friehauf, Suri and Sharma (2010), and the reader may refer to their work for more details regarding the derivations of the model. Our formulation is different because the fracture height is not necessarily equal to the pay zone height. A height correction factor (h_c) is used to assess how much of the vertical section of the pay zone is actually covered by the fracture. The fluid and reservoir properties are averaged vertically for each location along the fracture. These assumptions make the model a pseudo 1D model; therefore, there is no cross-flow, and gravity effects are not accounted for inside the reservoir. These assumptions are too simplistic to evaluate a gravity-driven liquid unloading process (Agrawal and Sharma 2013). Nevertheless, the model provides valuable insight regarding the impact of the fracturing fluid on hydrocarbon production.

5.5.1 Formulation of the Productivity Model

Well productivity is typically represented by the productivity index (J), which is defined as the rate of production divided by the applied drawdown. The applied drawdown is the pressure difference between the initial reservoir pressure and the bottomhole flowing pressure. Using the electronic-hydraulic analogy, the productivity index equals the inverse of the total hydraulic resistance R_{tot} :

$$J = \frac{q}{\Delta P} = \frac{q}{P_e - P_{wf}} = \frac{1}{R_{tot}} \quad (5.23)$$

For comparison purposes, J may be normalized by a base productivity index. For example, we define the base productivity J_0 as the productivity of an unfractured, undamaged well in a circular drainage area. Assuming steady state flow of a single hydrocarbon phase, the ratio of the productivity index becomes:

$$\frac{J}{J_0} = \frac{q/\Delta P}{q_0/\Delta P} = \frac{2\mu \ln(r_e / r_w)}{\pi kh} \frac{1}{R_{tot}} \quad (5.24)$$

The total flow resistance R_{tot} is calculated from the combination of the flow resistances that constitute the circuit shown in **Fig. 5.13**. For reasons of symmetry, the reservoir is split into four quarters. The definition of each resistance and the algorithm used for combining the resistances for a constant-height 2D fracture are provided in Friehauf (2009) and Friehauf, Suri and Sharma (2010). We have modified their formulation to account for 3D fracture geometry. Fig. 5.13 only shows a horizontal slice of the reservoir, but the calculations are performed for multiple horizontal slices of the reservoir. Because we do not consider any cross-flow, the horizontal slices of the reservoir are merely superposed.

During flowback, we assume Darcy's law in both the reservoir and into the propped fracture, which is modeled as a channel of known permeability and width. Depending on the flow geometry, the flow is modeled as elliptical, radial, or linear, and a flow resistance is appropriately defined. R_{tot} is the sum of the outer resistance (R_{out}), which connects the outer boundary of the drainage zone to the inner ellipse, and the inner resistance (R_{in}), which accounts for the flow from the boundary of the inner ellipse to the fracture:

$$R_{tot} = R_{out} + R_{in} \quad (5.25)$$

The outer resistance is delimited by the constant pressure ellipse, which is the limit of the drainage area, and the inner ellipse that encloses the stimulated fracture region. The ellipse dimensions are calculated in a similar fashion to Prats (1961) and Suri and Sharma (2007). In the outer ellipse, fluid flow is not altered by the fracturing treatment; therefore, the flow resistance is given by:

$$R_{out} = \frac{1}{h_c} \frac{2\mu}{\pi hk} \ln \left(\frac{a_2 + b_2}{a_1 + b_1} \right) \quad (5.26)$$

The distance a_1 is assumed to be slightly longer than the fracture length. The distance b_1 is a function of the dimensionless quantity a_{Prats} , which is defined in Eq. 5.27. A graphical representation of the inner equi-pressure boundary around the fractured well is shown in **Fig. 5.14**. As shown by Friehauf (2009), a_{Prats} is the dominating factor in controlling the inner ellipse size b_1 . The dimensions of the outer drainage ellipse are calculated by assuming a confocal ellipse around points $x=-L$ and $x=L$, with an area equal to the drainage area of the reservoir (A). The dimensions of the inner and outer ellipses are given by:

$$\left\{ \begin{array}{l} b_1 = L(1 + \varepsilon_{drained}) \\ a_1 = f(a_{prats}, b_1) \\ a_{prats} = \frac{\pi}{2} \frac{kL}{k_f w_{ave}} \end{array} \right. ; \left\{ \begin{array}{l} b_2 = \frac{\sqrt{2(\sqrt{\pi^2 L^4 + 4A^2} - \pi L^2)}}{2\sqrt{\pi}} \\ a_2 = \frac{A}{\pi(b_2)} \end{array} \right. \quad (5.27)$$

Within the inner ellipse, the fluid travels through three successive zones: (1) the virgin zone, which is at the initial reservoir conditions, (2) the invaded zone, in which the saturation and the relative permeability to gas (oil) depend on fluid leak-off, and (3) the fracture, in which the conductivity is a function of fracture width, proppant concentration, and fluid saturation. These three zones are represented in Fig. 5.13: $R_{el,i}$ refers to a resistance in the virgin zone; $R_{d,i}$ refers to a resistance in the invaded zone; and $R_{f,i}$ refers to a resistance along the fracture. The length of the virgin and invaded zones is itself a function of the amount of fluid leak-off. For calculations purposes, the inner ellipse ($b_{1,i}$), the fracture width (w_i), the fracture height (h_i), and the length of the invaded zone ($h_{leak,i}$) are divided into segments of length ΔX . The flow resistances in the inner ellipse are given by:

$$\left\{ \begin{array}{l} R_{el,0} = \frac{1}{h_{c,i}} \frac{2\mu}{\pi kh} \left[\frac{k}{k_s} \ln(r_s / r_w) + \ln(b_{1,0} / r_s) \right] \\ R_{el,i} = \frac{1}{h_{c,i}} \frac{\mu}{kh} \frac{(b_{1,i} - h_{leak,i})}{\Delta X} \\ R_{d,i} = \frac{1}{h_{c,i}} \frac{\mu}{kh} \frac{kh_{leak,i}}{k_d \Delta X} \end{array} \right. ; \left\{ \begin{array}{l} h_{c,i} = \max\left(\frac{h_i}{h}, 1\right) \\ R_{el,t} = \frac{1}{h_{c,i}} \frac{\mu}{kh} \frac{b_{1,t}}{(a_1 - L)} \\ R_{f,i} = \frac{1}{h_{c,i}} \frac{\mu}{kh} \frac{2k\Delta X}{k_f w_i} \end{array} \right. \quad (5.28)$$

Using the circuit shown in Fig. 5.13, these resistances are combined to obtain the inner resistance through the stimulated zone. This is done numerically using the

algorithm proposed by Friehauf, Suri, and Sharma (2010). The inner flow resistance is a series that takes the form of:

$$\frac{1}{R_m} = \frac{1}{R_{el,0}} + \frac{1}{R_{f,1} + \frac{1}{R_{f,2} + \frac{1}{R_{el,1} + R_{d,1}} + \frac{1}{R_{f,3} + \frac{1}{R_{el,2} + R_{d,2}} + \frac{1}{R_{f,4} + \frac{1}{R_{el,3} + R_{d,3}} + \dots}}}} \quad (5.29)$$

5.5.2 Properties of the Virgin Zone, Invaded Zone, and Fracture

The flow properties in the virgin zone are known because the initial fluid distribution has not been altered. Along the fracture, the fracture model calculates the fracture width and proppant concentration at each location. We assume that the saturation of the hydrocarbon phase inside the fracture is constant and provided by the user; however, this assumption is not rigorous as the liquid unloading occurs over time and is not uniform in the fracture (Economides and Nolte 2000; Agrawal and Sharma 2013). A reservoir simulator coupled with the fracturing model would be required to model the unloading process over time. In this study, our intent was to formulate a standalone simulator that can estimate the fractured well productivity, so the addition of an external reservoir simulator was not a desirable option. This potential future development is discussed in Chapter 9.

The flow properties in the invaded zone are altered by fluid leak-off. A damaged zone is formed when water leak-off occurs during the creation of the fracture. The zone may or may not cause significant damage to the fracture productivity based on the extent of leak-off and on the reservoir properties. For cases where the permeability and drawdown pressures are high, water is removed efficiently, and the flow is not

significantly impeded by the damage zone. In cases with low permeability and low drawdown pressure, the damage remains significant because the viscous forces are not sufficient to overcome the capillary forces. The high-water saturation zone impedes hydrocarbon production by reducing the relative permeability to the hydrocarbon phase. This water-blocking effect is illustrated in **Fig. 5.15**. One of the motivations behind using energized fluids is precisely to eliminate (or reduce) the water-blocking effect, by limiting the amount of water placed in the formation.

We assume that the capillary force is the main force trapping the water, and that the relative permeability to gas (oil) is a function of the capillary properties of the rock and the drawdown pressure only. Any *a priori* model may be used to model the changes in permeability as a function of saturation. For illustration purposes, the Brooks and Corey models (1966) are used to calculate the capillary pressure and relative permeability to gas (oil) as a function of the phase saturations:

$$P_c = P_c^o (S_w^*)^{-1/b} \quad \text{where} \quad S_w^* = \frac{S_w - S_{wr}}{1 - S_{wr}} \quad (5.30)$$

$$\frac{k_d}{k} = k_{r_{mw}} = k_{r_{mwo}} (1 - S)^n \quad \text{where} \quad S = \frac{S_w - S_{wr}}{1 - S_{wr} - S_{nwr}} \quad (5.31)$$

S_{wr} and S_{nwr} refer to the residual saturation of the wetting and non-wetting phases, respectively. Water is assumed to be the wetting phase, making the recovery of water by gas (oil) a drainage process. If the capillary pressure is much higher in the damaged zone than in the fracture (which is likely to be the case), the capillary pressure in the invaded zone is equal to the drawdown pressure across the invaded zone. Combining Eqs. 5.29 and 5.30, we can relate the effective permeability of the damaged zone (k_d) to the drawdown pressure (ΔP) as follows:

$$\frac{k_d}{k} = k_{mwo} \left(1 - \frac{(1 - S_{wr}) \left(\frac{\Delta P}{P_c^0} \right)^{-b}}{1 - S_{nwr} - S_{wr}} \right)^n \quad (5.32)$$

The parameter P_c^0 defined in Eq. 5.30 is a measure of the capillary pressure at high wetting (typically water) saturation. If the region around the fracture is fully saturated with the wetting phase, P_c^0 represents the minimum drawdown that any wetting phase could be recovered from that region. If the drawdown is less than P_c^0 , the water saturation will remain high, causing relative permeability damage that can permanently inhibit gas from flowing into the fracture. The value of P_c^0 can be estimated from field measurements, laboratory tests, or estimates based on the work of Leverett (1940):

$$P_c^0 = 0.42\sigma \cos \theta \sqrt{\frac{\phi}{k}} \quad (5.33)$$

5.5.3 Determination of the Invaded Zone Length

The length of the invading zone (h_{leak}) is unknown *a priori*. It depends on fluid invasion, applied drawdown and shut-in strategy, and reservoir petrophysical properties. During pumping, a fraction of the fracturing fluid leaks off into the reservoir. We use the interpolation scheme presented in Section 5.4 to track the cumulative mass distribution of each component that invades the reservoir. The mass (per unit area) of component i invading the reservoir during Δt^n is given by:

$$\left(\frac{\Delta m_{lk,i}}{\Delta X \Delta Y} \right)_{pumping}^{t^n \rightarrow t^n + \Delta t^n} = 4 \left(\sqrt{t^n + \Delta t^n - \tau} - \sqrt{t^n - \tau} \right) (\rho_1 C_{w,1} x_i + \rho_2 C_{w,2} y_i) \quad ; \quad i = 1 \dots NC \quad (5.34)$$

At the end of pumping, the operator can choose to flow back immediately or shut-in the well for a period of time. If the operator immediately flows back, the fracturing fluid left in the fracture at the end of pumping is recovered at the surface; therefore, the total amount of fluid invading the reservoir is equal to the time integral of Eq. 5.34. Alternatively, if the operator waits for an extended (infinite) time, the totality of the fracturing fluid left in the fracture at the end of pumping invades the formation, as the rock closes on the proppant. The additional mass (per unit area) of component i invading the reservoir for an extended shut-in is given by:

$$\left(\frac{\Delta m_{lk,i}}{\Delta X \Delta Y} \right)_{shutin}^{\infty} = w \frac{(1-c)}{(1-\phi_{frac})} (\rho_1 S_1 x_i + \rho_2 S_2 y_i) \quad ; \quad i=1...NC \quad (5.35)$$

In practice, the shut-in is a finite period of time, so only a fraction of the fracturing fluid left in the fracture after pumping invades the formation during shut-in. This process is not modeled explicitly; rather, it is modeled by a simple parameter ε_{shutin} , which can be estimated from the amount of fracturing fluid immediately recovered when the well is brought back in production:

$$\left(\frac{\Delta m_{lk,i}}{\Delta X \Delta Y} \right)_{shutin} = \varepsilon_{shutin} w \frac{(1-c)}{(1-\phi_{frac})} (\rho_1 S_1 x_i + \rho_2 S_2 y_i) \quad ; \quad i=1...NC \quad (5.36)$$

By definition, ε_{shutin} ranges between 0 and 1, where 0 is the immediate flowback case, and 1 is the extended (infinite) shut-in case.

Once we know the mass of each component placed into the reservoir, we can estimate the length of the invaded zone. To do so, we perform Flash calculations under the reservoir conditions to assess the composition and density of each phase in the invaded zone. Assuming a pseudo 1D piston-like displacement of the reservoir fluids by

the fracturing fluid, we calculate the volume (per unit area) of each phase inside the reservoir. This volume is then converted to an invaded zone length (h_{leak}):

$$h_{leak} = \frac{m_{lk,1}/\rho_1}{\phi S_1 \Delta X \Delta Y} \quad (5.37)$$

Based on the fractional flow curve and the initial fluid saturations in the reservoir, the value of h_{leak} and S_1 are corrected to agree with the rock petrophysical properties.

5.5.4 Comments Regarding Foams

The productivity model used to assess the performance of the fracturing treatment during flowback is a two-phase model that considers an aqueous phase and a hydrocarbon phase. Foams are themselves two-phase mixtures. They typically contain a water phase and a second phase that is miscible with hydrocarbons. During pumping, we assumed that foams remain stable along the wellbore and inside the fracture; therefore, they have been treated as pseudo single-phase fluids. During flowback, we consider, however, that foams break and split in two separate phases. This is primarily because of the filtration mechanism that occurs when the fracturing fluid invades the reservoir. As shown by Ribeiro and Sharma (2012), the filter cake created at the surface of the rock breaks the foam structure and allows for separate leak-off of each phase. Thus, we consider two separate phases in the reservoir and inside the fracture for the productivity calculations. Each phase can mix with a different fluid present in the reservoir. For instance, in the case of CO₂ foam invading a gas reservoir, the liquid (water-rich) phase mixes with connate water, while the gas (CO₂-rich) phase mixes with the hydrocarbon phase. The displacement of the two phases is no longer affected by the presence of the surfactant.

5.6 CONCLUSIONS

This chapter introduced a wellbore model that relates the surface and bottomhole conditions for any well configuration. The model estimates the temperature and pressure distribution along the well, and the subsequent changes in fluid properties. We also introduced a flow resistance model that assesses the productivity of a fractured well with damage in the invaded zone and finite fracture conductivity. The model identified four primary factors governing fracture performance: (1) the dimensions of the fracture, (2) the conductivity of the fracture, (3) the extent of the invaded zone, and (4) the relative permeability to gas (oil) in the invaded zone.

The wellbore and productivity models complement the fracture model presented in Chapter 3. The combination of these models forms a standalone modeling tool to design and optimize energized treatments. The model is built in a modular fashion so that each element can be easily updated or improved in the future. The modules are written in a *FORTTRAN* code that is compiled into an executable program. The program is connected to a graphical user interface (GUI), and the full model is referred to as *EFRAC-3D*. We use this program to generate the simulations shown in the following chapters.

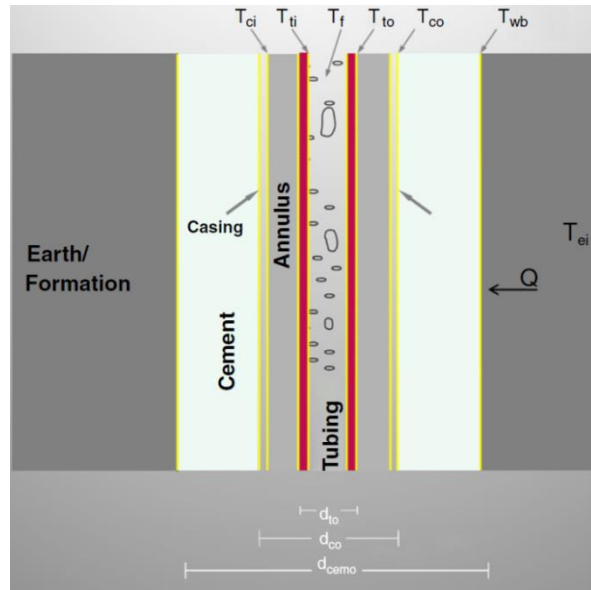


Figure 5.1: Wellbore configuration and heat flow through a series of resistances (from Hasan and Kabir 2012).

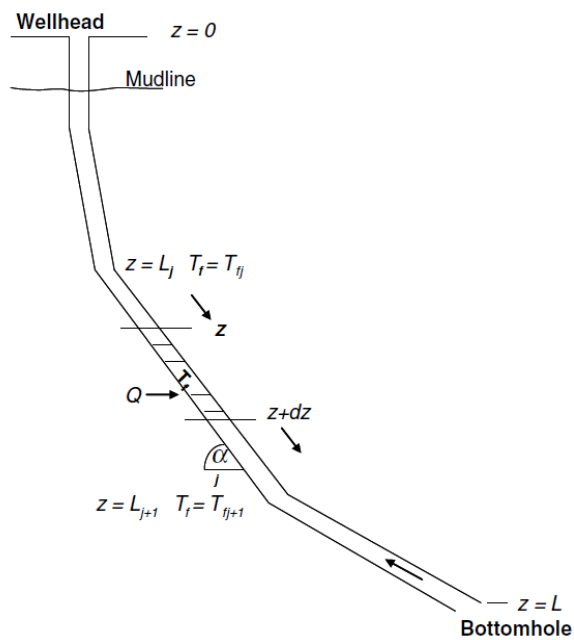


Figure 5.2: Well made of segments of variable inclination and pipe diameter (from Hasan and Kabir 2012).

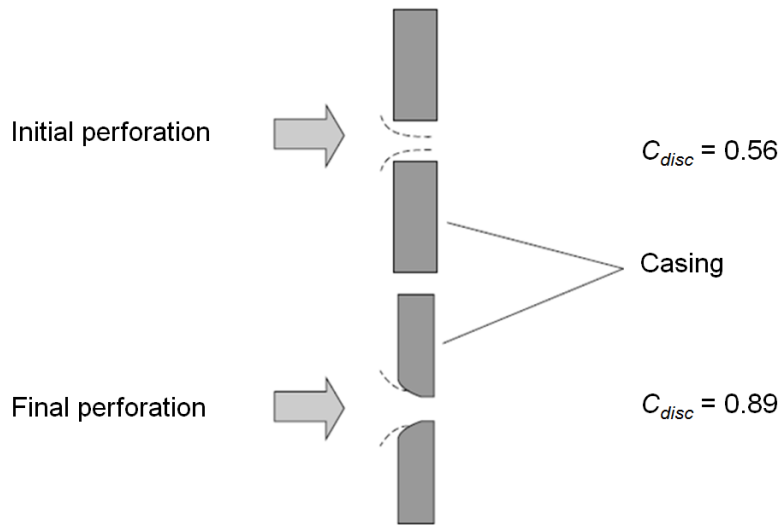


Figure 5.3: Evolution of the discharge coefficient due to sand erosion (from Crump and Conway 1988).

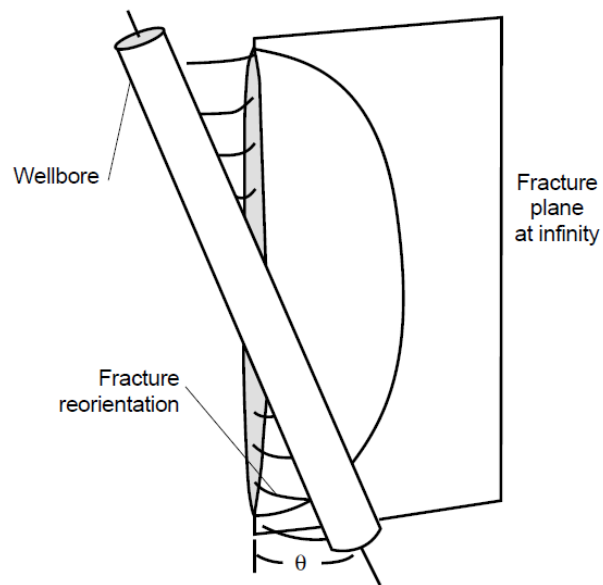


Figure 5.4: Tortuosity effect: the fracture twists and turns to align itself with the preferred direction of propagation (from Economides and Nolte 2000).

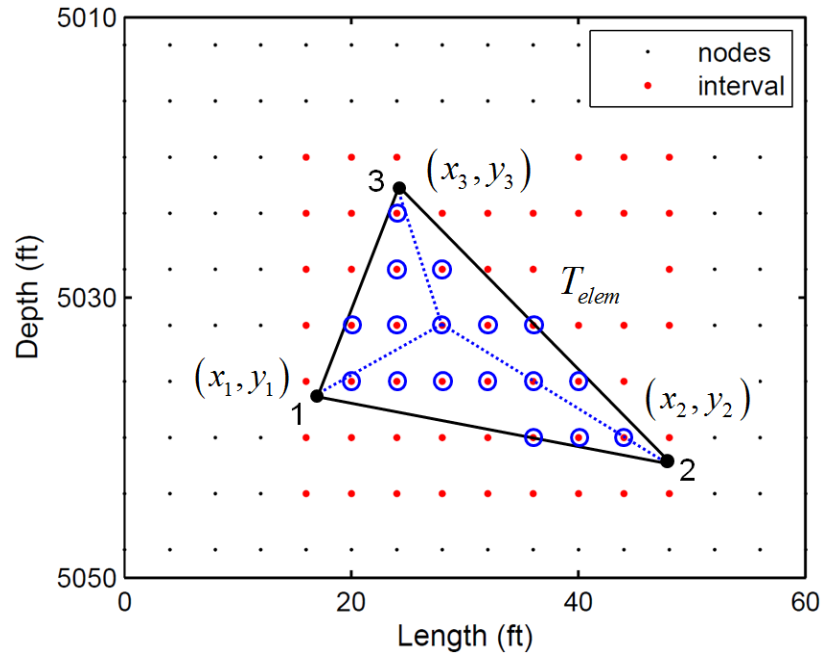


Figure 5.5: Interpolation scheme that relates the unstructured fracture grid to the Cartesian reservoir grid. Only the nodes indicated in blue are interpolated for this element.

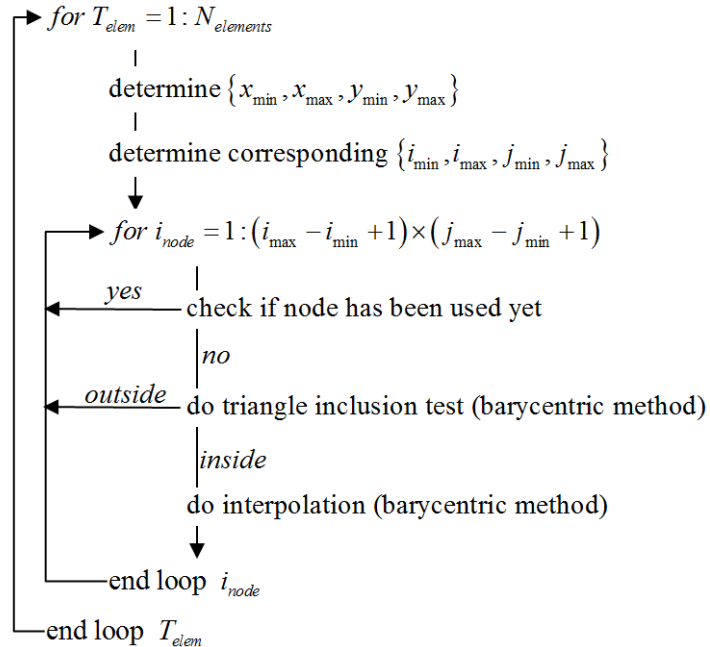


Figure 5.6: Algorithm used for the interpolation scheme.

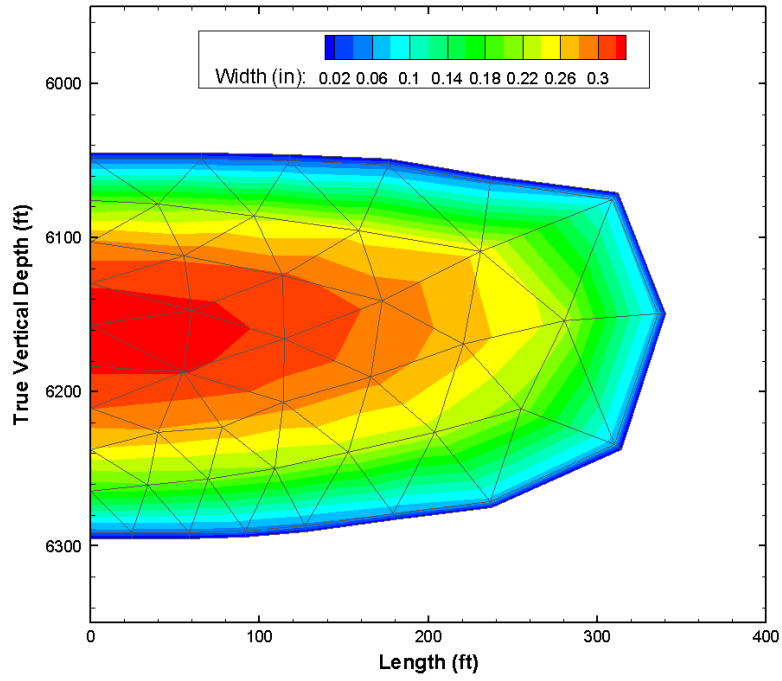


Figure 5.7: Fracture width calculated from the fracture mechanics equation in the unstructured fracture mesh.

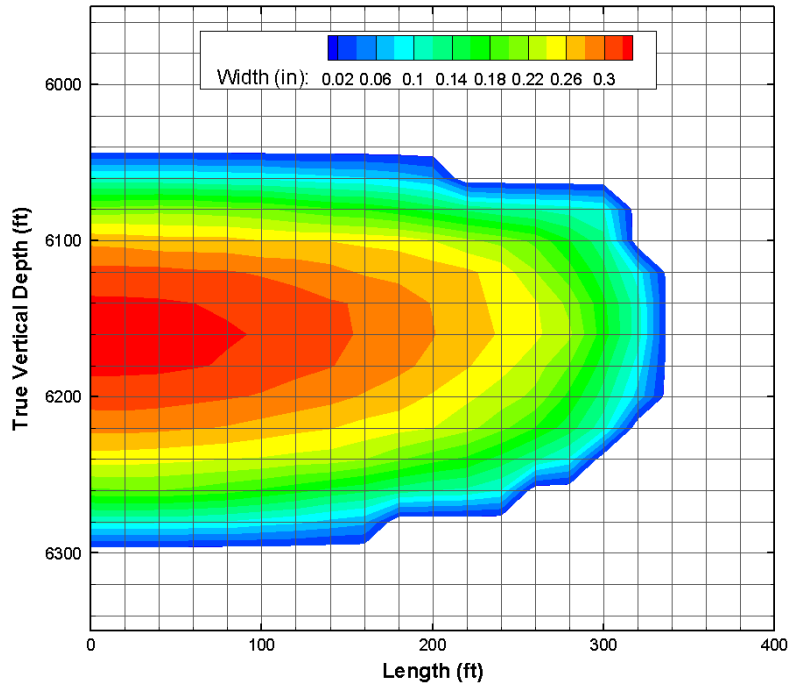


Figure 5.8: Fracture width mapped in the reservoir mesh using the interpolation scheme.

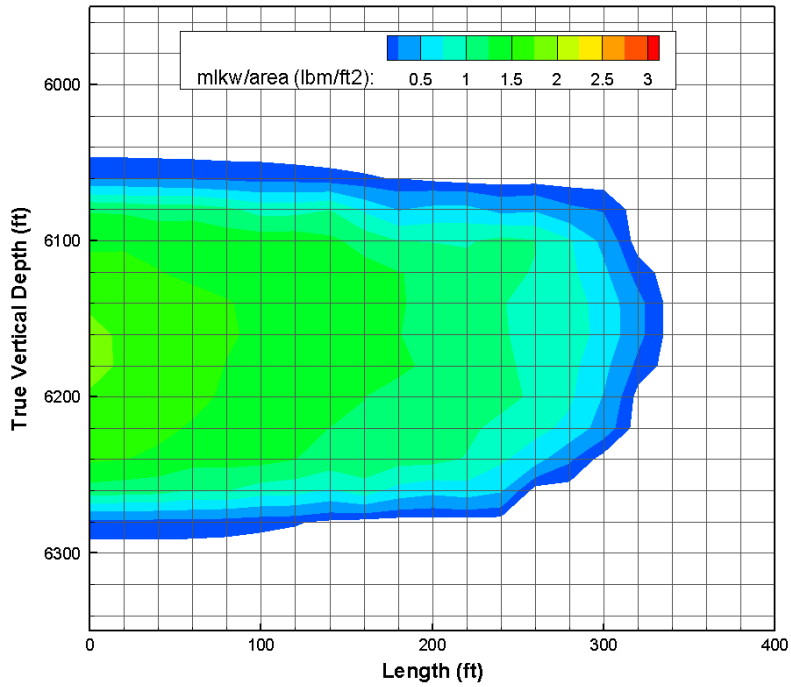


Figure 5.9: Mass of water per unit area placed into the reservoir at the end of pumping.

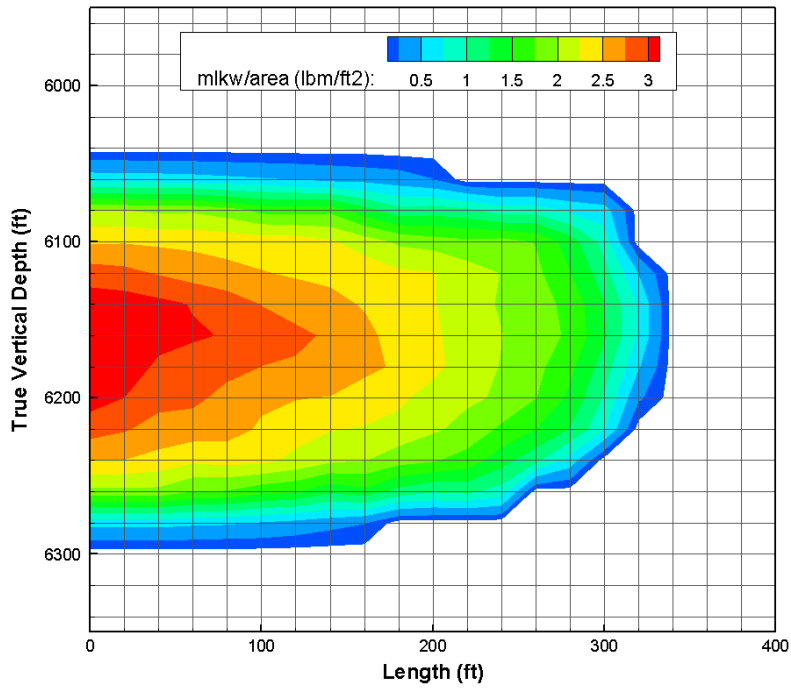


Figure 5.10: Mass of water per unit area placed into the reservoir after shut-in.

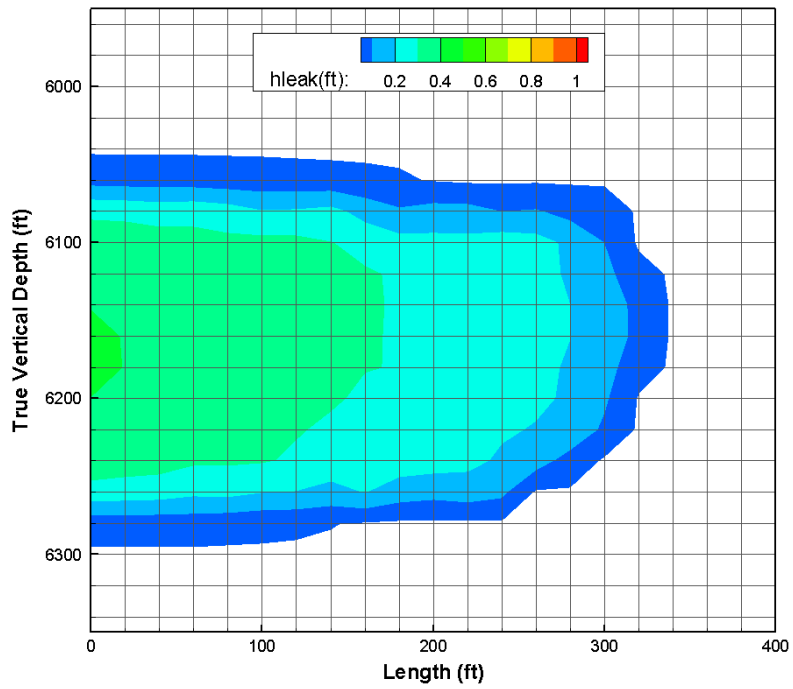


Figure 5.11: Length of the invaded zone at the end of pumping.

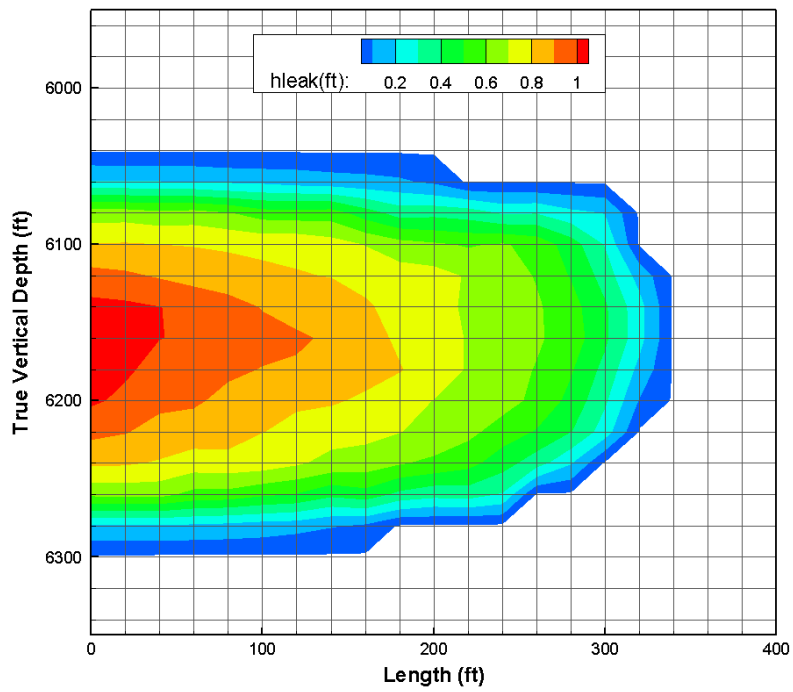


Figure 5.12: Length of the invaded zone after shut-in.

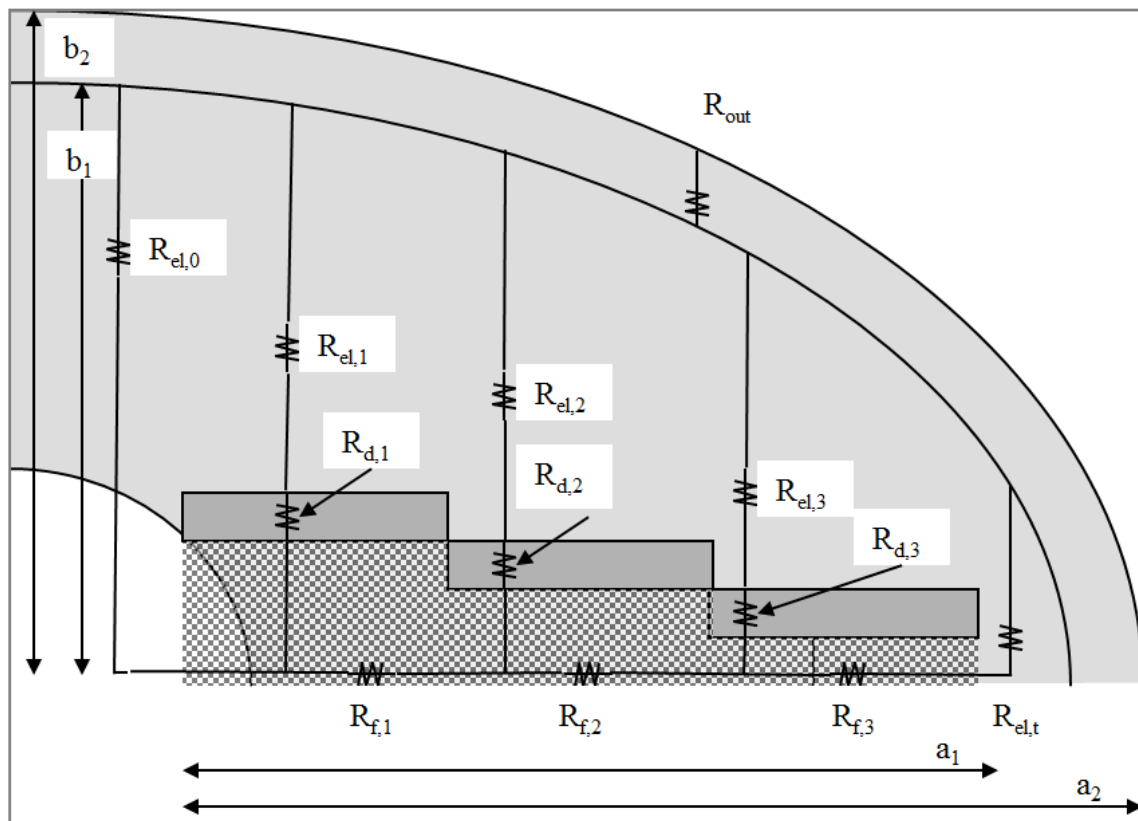


Figure 5.13: Association of flow resistances forming the productivity model (from Frieauf, Suri, and Sharma 2010). Because of the symmetry, only a quarter of the fractured well system is shown. R_{out} is the resistance in the outer ellipse; $R_{el,i}$ is a resistance in the virgin zone; $R_{d,i}$ is a resistance in the invaded zone; and $R_{f,i}$ is to a resistance along the fracture. The outer ellipse is delimited by a_2 and b_2 ; and the inner ellipse is delimited by a_1 and b_1 .

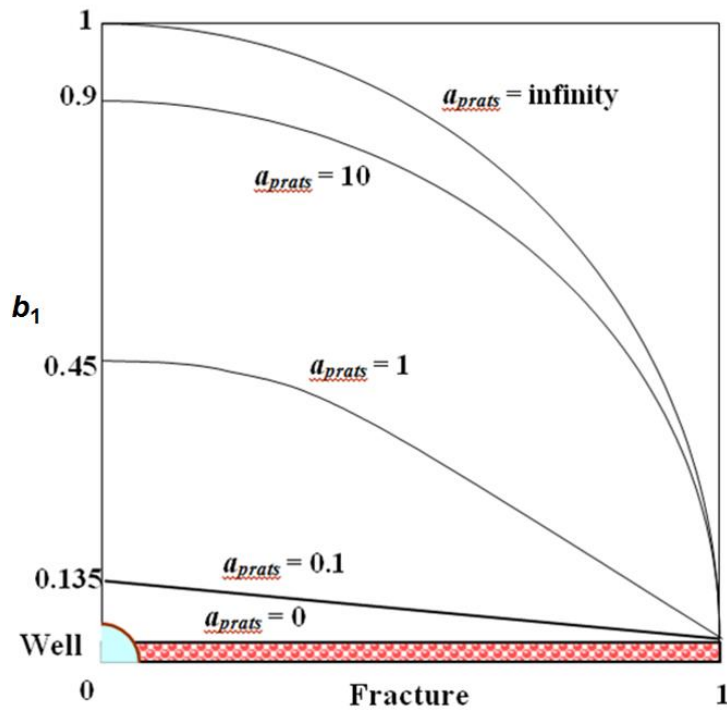


Figure 5.14: Inner ellipse minor axis versus a_{prats} conductivity (from Frieauf, Suri, and Sharma 2010).

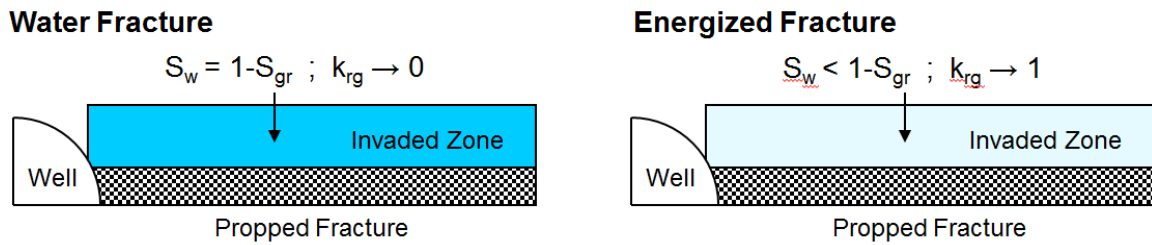


Figure 5.15: Illustration of the water blocking effect. The water that is not recovered creates a high-water saturation zone that impedes the flow of oil and gas. The use of energized fluids improves clean-up in and around the fracture.

NOMENCLATURE

a_1	= inner ellipse dimension parallel to the fracture, ft	J_{DV}	= productivity index for vertical well, BPD/psi
a_2	= outer ellipse dimension parallel to the fracture, ft	k	= reservoir permeability, mD
a_{perf}	= empirical correction factor defined in Eq. 5.18	k_{cas}	= thermal conductivity of casing, BTU/min-ft-°F
a_{prats}	= fracture conductivity defined by Prats (1961)	k_{cem}	= thermal conductivity of cement, BTU/min-ft-°F
A	= drainage area, acre	k_d	= damaged zone permeability (effective permeability of the producing phase i.e. oil/gas)
b	= Brooks-Corey model for capillary pressure exponent	k_f	= fracture permeability, mD
$b_{1,i}$	= inner ellipse dimension perpendicular to the fracture, ft	k_{ins}	= thermal conductivity of insulation, BTU/min-ft-°F
b_2	= outer ellipse dimension perpendicular to the fracture, ft	k_R	= thermal conductivity of reservoir, BTU/(min-ft-°F)
b_{perf}	= empirical correction factor defined in Eq. 5.18.	k_{rnw}	= relative permeability of non-wetting phase
c	= proppant concentration (volume fraction)	k_{rnw0}	= endpoint relative permeability of non-wetting phase
C_{disc}	= discharge coefficient defined in Eq. 5.16	k_s	= permeability of (mechanical) damage around the wellbore, mD
C_{JT}	= Joule-Thompson coefficient, °F/psi	k_t	= thermal conductivity of tubing, BTU/min-ft-°F
C_p	= heat capacity, BTU/(lbm-°F)	L	= fracture half-length, ft
$C_{w,j}$	= leakoff coefficient phase j , ft/ $\sqrt{\text{min}}$	L_R	= coefficient defined in Eq. 5.7
d_{perf}	= perforation diameter, in	m	= mass flux, lbm/ft
d_{ti}	= inner tubing diameter, ft	$m_{sand,cum}$	= cumulative mass of sand produced, lbm
d_{to}	= outside tubing diameter, ft	n	= flow behavior index in Eq. 5.15
d_{wb}	= wellbore diameter, ft	n	= Corey exponent in Eq. 5.31
f	= Fanning friction factor	N	= number of open perforations
g	= gravity of earth, ft/s ²	NC	= number of components
g_G	= geothermal gradient, °F/ft	P	= fluid pressure, psi
h	= height of pay zone, ft	P_c	= capillary pressure, psi
h_a	= heat-transfer coefficient in annulus, BTU/min-ft ² -°F	P_c^0	= endpoint capillary pressure psi
$h_{c,i}$	= height correction factor	P_e	= outer boundary pressure, psi
h_i	= height of fracture, ft	P_{wf}	= bottomhole flowing pressure, psi
$h_{leak,i}$	= lateral extent of damaged zone, ft	q	= flow rate, BPM
h_t	= heat-transfer coefficient in tubing, BTU/min-ft ² -F°	Q	= thermal flux, BTU/min-ft
J	= productivity index, BPD/psi	r_{casi}	= inner casing radius, ft
J_0	= productivity index for unfractured, undamaged well, BPD/psi	r_{caso}	= outside casing radius, ft
J_{DH}	= productivity index for transverse fractured well, BPD/psi	r_{ins}	= insulation radius, ft
		r_s	= radius of (mechanical) damage around the wellbore, ft
		r_{ti}	= inner tubing radius, ft

r_{to} = outside tubing radius, ft
 r_{wb} = wellbore radius, ft
 Re = Reynolds number
 Re_w = wall Reynolds number
 $R_{d,i}$ = damage zone flow resistance
 $R_{el,i}$ = virgin zone flow resistance
 $R_{f,i}$ = fracture flow resistance
 R_{in} = inner flow resistance
 R_{out} = outer flow resistance
 R_{tot} = total flow resistance
 s_c = choke skin factor
 S_J = saturation of fluid phase J
 S_{nwr} = residual non-wetting phase saturation
 S_w = wetting phase saturation
 S_{wr} = residual wetting phase saturation
 t = time, min
 t_D = dimensionless producing time
 t_{pi} = quantity defined in Eq. 5.21
 T or T_f = fluid temperature, °F
 T_D = dimensionless temperature
 T_{ei} = undisturbed reservoir temperature, °F
 T_{es} = surface reservoir temperature, °F
 T_R = reservoir temperature, °F
 T_{wb} = wellbore/reservoir interface temperature, °F
 TVD = true vertical depth, ft
 U_{to} = overall heat-transfer coefficient, BTU/min-ft²-°F
 v = fluid velocity, ft/min
 w = fracture width, ft
 w_{ave} = average fracture width, ft
 x = horizontal location, ft
 x_i = mass fraction of component i in the liquid phase
 x_{Re} = coefficient defined in Eq. 5.14
 y = vertical location, ft

y_i = mass fraction of component i in the gas phase
 z = well depth, ft
 z_p = extrapolated value in Eq. 5.22

Subscripts

i = segment i
 p = proppant
 R = reservoir
 s = skin factor

Greek Symbols

α = well inclination from horizontal, deg
 α_i = quantities defined in Eq. 5.22
 $\Delta m_{lk,i}$ = mass of fluid component i that leaked off, lbm
 Δt^n = time step, min
 ΔP = drawdown pressure, psi
 ΔP_{perf} = perforation friction loss, psi
 Δt^n = time increment, min
 ΔX = length of fracture segment, ft
 ΔY = height of fracture segment, ft
 ε = pipe roughness
 $\varepsilon_{drained}$ = coefficient defined in Eq. 5.27
 ε_{shutin} = coefficient defined in Eq. 5.36
 μ = reservoir fluid viscosity, cp
 ρ = density of fluid mixture in Eq. 5.16, lbm/gal
 ρ_e = density of reservoir, lbm/ft³
 ρ_j = density of fluid phase j , lbm/ft³
 ϕ = reservoir porosity
 ϕ_{frac} = fracture porosity
 $\sigma \cos \theta$ = interfacial tension, dynes/cm
 τ = retardation factor, min
 ω_{IJ} = mass fraction of component I in phase J

REFERENCES

- Agrawal, S. and Sharma, M.M 2013. Impact of Liquid Loading in Hydraulic Fractures on Well Productivity. Paper SPE 163837 presented at the SPE Hydraulic Fracturing Technology Conference, The Woodlands, Texas, 4-6 February.
- Alekseenko, O.P., Potapenko, D.I., Cherny, S.G., Esipov, D.V., Kuranakov, D.S., and Lapin, V.N. 2013. 3D Modeling of Fracture Initiation From Perforated Non-cemented Wellbore. *SPE J.* (to be published). SPE 151585-PA.
- Brooks, R.H. and Corey, A.T. 1966. Properties of Porous Media Affecting Fluid Flow. *J. Irrigation and Drainage Div., Proc. ASCE* **92**: 61-88.
- Crump, J. and Conway, M. 1988. Effects of Perforation-Entry Friction on Bottomhole Treating Analysis. *J. Pet Tech* **40**(8): 1041-1048. SPE 15474-PA.
- Denn, M.M. 1980, *Process Fluid Mechanics*, Prentice Hall, Englewood Cliffs, New Jersey.
- Economides, M. and Nolte, K.G. 2000, *Reservoir Stimulation, Third Edition*, John Wiley and Sons, New York City, New York.
- Friehauf, K.E. 2009. Simulation and Design of Energized Hydraulic Fractures. Ph.D. Dissertation, The University of Texas at Austin, Austin, Texas (August 2009).
- Friehauf, K.E. and Sharma, M.M. 2009. A New Compositional Model for Hydraulic Fracturing With Energized Fluids. *SPE Prod & Oper* **24**(4): 562-572. SPE 115750-PA.
- Friehauf, K.E., Suri, A., and Sharma, M.M. 2010. A Simple and Accurate Model for Well Productivity for Hydraulically Fractured Wells. *SPE Prod & Oper* **25**(4): 453-460. SPE 119264-PA.
- Hasan, A. and Kabir, S. 1994. Aspects of heat Transfer During Two-Phase Flow in Wellbores. *SPE Prod & Fac* **9**(1): 12-16. SPE 22948-PA.
- Hasan, A. and Kabir, S. 2002, *Fluid Flow and Heat Transfer in Wellbores*, Society of Petroleum Engineers, 2002.
- Hasan, A. and Kabir, S. 2012. Wellbore Heat-Transfer Modeling and Applications. *J. Pet Sci. & Eng.* **86**: 127-136.
- Leverett, M.C. 1940. Capillary Behavior in Porous Solids. *Trans. AIME* **142**(1): 152-169. SPE 941152-G.
- McClain, C. 1963, *Fluid Flow in Pipes*, The Industrial press, New York City, New York.
- Mukherjee, H. and Economides, M.J. 1991. A Parametric Comparison of Horizontal and Vertical Well Performance, *SPE Form Eval* **6**(2): 209-216. SPE 18303-PA.
- Prats, M. 1961. Effect of Vertical Fractures on Reservoir Behavior – Incompressible Fluid Case. *SPE J.* **1**(2): 105-117. SPE 1575-G.

- Ramey, H.J. 1962. Wellbore Heat Transmission. *J. Pet Tech* **14**(4): 427-435. *Trans. AIME* 225. SPE 96-PA.
- Ribeiro, L.H. and Sharma, M.M. 2012. Multi-Phase Fluid-Loss Properties and Return Permeability of Energized Fracturing Fluids. *SPE Prod & Oper* **27**(3): 265-277. SPE 139622-PA.
- Ribeiro, L.H. and Sharma, M.M. 2013. Fluid Selection for Energized Fracture Treatments. Paper SPE 163867 presented at the SPE Hydraulic Fracturing Technology Conference, The Woodlands, Texas, 4-6 February.
- Suri, A. and Sharma, M.M. 2007. A Model for Water Injection in Frac-Packed Wells. Paper SPE 110084 presented at the 2007 SPE Annual Technical Conference and Exhibition held in Anaheim, California. 11-14 November.
- Valkó, P. and Economides, M.J. 1995, *Hydraulic Fracture Mechanics, First Edition*, John Wiley and Sons, New York City, New York.
- Virk, P.S. 1975. Drag Reduction Fundamentals, *AIChE J.* **21**(4): 625-656.

Chapter 6: Preliminary Results and Model Capabilities

Chapters 4 and 5 described the formulation of the fracture, wellbore, and reservoir models that constitute our compositional fracturing simulator (*EFRAC-3D*). To make the code more attractive and ergonomic, we linked the program to a modern graphical user interface (GUI). This chapter does not describe the interface in detail; rather, it introduces the main inputs and outputs, which are organized in a modular fashion, so the user can easily modify each section and upload individually.

As our formulation is intended to be as general as possible, the model offers a wide range of capabilities, making the simulator suitable for many different applications. First, we validate the new model with several comparisons for single-phase, incompressible fluids against analytical solutions and against a popular 3D fracturing simulator. Then, we consider more realistic stress distributions and present results for a wide range of treatment designs, ranging from multi-phase energized fracturing treatments to long-term CO₂ injection. These various examples illustrate the numerous capabilities of the simulator.

6.1 INPUTS AND OUTPUTS

This section presents the main inputs required to run the program and the outputs that are available to the user. We developed a user-friendly interface under the *Microsoft .NET* framework with the intent to build an interface as compact and accessible as possible.

6.1.1 Main Inputs

The input file consists of five independent modules and two dynamic libraries:

1. *Geological properties*: This section defines the reservoir layers for fracture propagation purposes. It includes the depth of the reservoir layers, the vertical distribution of the *in-situ* stress distribution, the mechanical properties of each layer, the multi-phase leak-off properties in each layer, and the length and location of the perforated interval.
2. *Reservoir properties*: This section contains the reservoir properties used for productivity calculations. It includes the definition of the reservoir grid, the petrophysical reservoir properties, the relative permeability curve, and the fracture properties following flowback.
3. *Pumping schedule*: This section defines the desired pumping schedule over time. For each pumping stage¹, it contains the stage duration, injection rate, proppant loading, fluid type, and proppant type. The properties of the different types of fluid and proppant are stored in separate libraries, which can be updated and uploaded by the user:
 - i. *Fluid properties*: The library describes the fluid's density, composition, viscosity, and thermal properties.
 - ii. *Proppant properties*: The library defines the proppant's density, diameter, and thermal properties.
4. *Wellbore configuration*: This section defines the wellbore path, the tubing dimensions, the perforations, and the thermal properties of the wellbore. The wellbore path can be uploaded from a separate survey file.

¹ We do not refer to pumping stages as separated fractures or clusters, but as fluid stages that are pumped to generate a single fracture. The injection remains identical during a given fluid stage.

5. *Numerical parameters*: This section contains the meshing parameters, algorithm preferences, and initial grid parameters.

The modular organization enables the user to update individual sections of the input file by saving and uploading them separately. For example, the user can select a given reservoir and upload different fluid types to optimize fluid selection. Alternatively, the user can change the pumping schedule to optimize the proppant loading over time.

6.1.2 Main Outputs

The program generates several output files that are updated over time:

1. *Main fracture properties*: This section contains x - y plots showing the evolution of the main fracture properties over time. Specifically, it includes the evolution of the fracture length, height, maximum width, average width, and proppant volume over time.
2. *Fracture-level description*: This section displays a 2D spatial representation of a given variable inside the fracture at any given time. Section 3.3.2 shows such examples for the fracture width, fluid temperature, proppant coverage, proppant volumetric concentration, and fluid saturation along the fracture.
3. *Reservoir-level description*: This section is the counterpart of the fracture-level description on the reservoir side; it displays a 2D spatial representation of a given variable inside the reservoir at any given time. Notably, it includes the mass of each component invading the reservoir, fluid saturation, relative permeability to hydrocarbon, and invaded zone length.
4. *Wellbore calculations*: This section shows the spatial evolution of different properties along the wellbore at any given time. Because the wellbore radius is

negligible compared to its length, the outputs are averaged for any cross-section of the wellbore. This section is particularly important for determining pumping requirements because it contains the net pressure, bottomhole pressure, and surface pressure over time. The file also provides the surface pumping rate corresponding to a given downhole fluid design.

5. *Productivity estimates*: This section contains the key parameters for assessing fracture performance, particularly the productivity index of the fracturing treatment.

6.2 MODEL VALIDATION

Validation and comparison with prior models is essential before attempting to model energized treatments. To validate the new model, we compared our results to analytical solutions and to a popular 3D fracturing simulator under a wide range of reservoir conditions. We chose to present results for the radial and PKN geometries since they constitute extreme cases for single-layer fracture propagation. To make the comparison with analytical expressions relevant, the fluid was assumed to be single-component, single-phase, incompressible, isothermal, and Newtonian. **Table 6.1** contains the main inputs for the three validation cases.

6.2.1 Radial Example

In the radial example, the minimum horizontal stress remains constant throughout the reservoir (**Fig. 6.1**). The stress barriers at the interfaces are removed so the perforation interval can be seen as a point source. When the vertical distribution of the *in-situ* stress is uniform, the fracture is expected to take the shape of a circle in the x - y plane. **Fig. 6.3** shows the final width profile predicted by the model. As expected, the fracture

follows a circular shape, and the length is equal to the height (also referred to as *radius* for circular fractures). The growth of the circular fracture compares very well with the analytical expression derived by Geertsma and de Klerk (1969) for radial fractures with no leak-off, and with the numerical solution obtained with the standard 3D simulator (Fig. 6.4).

6.2.2 PKN Example – No fluid leak-off

When a large stress contrast occurs at the interface with the bounding layers, the stress distribution prohibits fracture growth out of the target zone, so the fracture height is bounded by the pay zone height. In our three-layer reservoir model, we introduced strong stress barriers of 1000 psi at the interface between layers to maintain a constant fracture height. The stress remains constant within each layer (Fig. 6.1). Because analytical expressions exist for the non-leak-off and high-leak-off cases, we ran two simulations, with a leak-off coefficient set to zero in the first example and set to 0.002 ft/ $\sqrt{\text{min}}$ in the second example.

Fig. 6.5 shows the final width profile predicted by the new model for the non-leak-off example. As expected, the fracture is well-constrained in height, and the fracture width tends to follow an elliptical shape. Fig. 6.6 compares the fracture growth and maximum width predicted by the analytical solution derived by Nordgren (1972), the standard 3D simulator, and the new model. The match is not as good as the other examples but remains satisfactory. As observed in Fig. 6.5, the final mesh contains several elongated elements, and the width profile is not perfectly elliptical. We could have obtained a better fit using different meshing parameters, but mesh refinement is out of the scope of this chapter. In general, our simulator tends to have a bias toward shorter and wider fractures as compared to 2D, pseudo 3D, and several 3D models.

6.2.3 PKN Example – Fluid Leak-off

Fig. 6.7 shows the final width profile predicted by our model, and **Fig. 6.8** compares the fracture growth and maximum width predicted by the analytical solution derived by Nordgren (1972), the standard 3D simulator, and our model for the leak-off example. The new model compares well with past predictions, particularly for the prediction of the maximum fracture width and net pressure. The final width profile (Fig. 6.7) follows an elliptical shape, and the mesh is not distorted.

Figs. 6.3, 6.5, and 6.7 all have an aspect ratio of 1 (length versus height) for comparisons purposes. These figures demonstrate that a wide range of fracture shapes can be predicted by the simulator. As expected, fluid leak-off plays a critical role in fracture design. As the leak-off coefficient increases from 0 to 0.002 ft/ $\sqrt{\text{min}}$, the fracture half-length decreases from 770 to 275 ft, and the maximum fracture width decreases from 0.27 to 0.19 in.

The few comparisons presented in this section demonstrate that the new model can be validated against well-established models under restrictive assumptions. The radial and the PKN geometries constitute the two ends of the spectrum for single-layer fracture propagation. The PKN model is better suited for long-duration treatments, whereas the radial model is better-suited at the beginning of the treatment, when the stress boundaries are not affecting fracture propagation.

6.2.4 Comparison with a Planar 3D Fracturing Simulator

The new model can also be used in more complex stress environments, as it allows vertical migration in the overlaying layers and fracture growth in multiple layers. We compared our model to *UTFRAC-3D* for single-phase incompressible fluids propagating in complex stress distributions. *UTFRAC-3D* refers to the current version of

the code initially developed by Gu (1987), Ouyang (1994), and Yew (1997) at the University of Texas. This simulator has been extensively benchmarked against current fracturing simulators since the early nineties (Weng 1992). The results of the new model were almost identical (within 2%) to the results obtained with *UTFRAC-3D* for all the simulations performed with incompressible fluids. This match is not surprising, as *UTFRAC-3D* was the original basis of *EFRAC-3D*. Notably, both models share the same subroutines for solving the fracture opening equation.

6.2.5 Comparison with Field Data

The most direct validation would be a thorough comparison of model predictions against actual field data. Unfortunately, we did not have the chance to do a formal comparison between the model and field data in this study. Although we worked in close collaboration with major gas providers, we did not have the opportunity to calibrate the model because field data were usually confidential, and because access to direct experimental measurements is challenging. In practice, very little is known regarding downhole fracture dimensions and existing reservoir heterogeneities. Often, the only calibration tool is the surface pressure. In some cases, micro-seismic data may be used to estimate fracture dimensions. The calibration and field validation of the model is one of the key areas of improvement for this work, and we recommend history-matching the rate and net-pressure response of several treatments in the future. A comparison with micro-seismic data would benefit this work, as it would give us reasonable confidence that the essential physics of the problem have been captured.

Nevertheless, we believe that our model provides reasonable results based on indirect comparisons. For non-energized treatments, the model agreed with *UTFRAC-3D*, which has been extensively calibrated and validated in the industry. Under limiting

assumptions, the model matched well-accepted analytical expressions. For energized treatments, the model predictions agree, at least qualitatively, with common field observations. For instance, our results indicate that viscous fluids tend to create shorter and wider fractures with minimum vertical migration.

6.3 MODEL CAPABILITIES: ENERGIZED FLUID EXAMPLES

Our primary goal is to apply the new model to cases for which conventional models do not apply, i.e. energized fractures. To illustrate the capabilities of the model, we present three examples: (1) a gelled LPG fracturing treatment, (2) a long-term CO₂ injection, and (3) a CO₂ foam fracturing treatment. The corresponding stress distributions, referred to as *Stress A*, *Stress B*, and *Stress C*, respectively, are represented in **Fig. 6.2**. These stress distributions are more realistic than the simplistic radial and PKN stress distributions used for model validation.

6.3.1 Gelled LPG Fracturing Treatment

The reservoir is a soft, tight-gas sand modeled with three distinct layers. The mechanical properties are presented in **Table 6.2**, and the stress distribution is indicated as *Stress A* in Fig. 6.2. The fracture gradient is equal to 0.6 psi/ft in the pay zone and to 0.8 and 0.75 psi/ft in the bounding layers. A stress contrast of 80 psi is present at the interfaces. This representation is typical of many reservoirs, for which the basement and overburden layers are stiffer than the target rock. The leak-off coefficient is 0.0005 ft/ $\sqrt{\text{min}}$ in the pay zone and 10^{-6} ft/ $\sqrt{\text{min}}$ in the bounding layers, which is typical for gelled fluids in tight-gas reservoirs.

We consider a vertical well with a 40-ft perforated interval located in the middle of the target zone. The pumping schedule and fluid properties are indicated in Table 6.2.

These properties are given at a temperature of 100°F and a pressure of 5000 psi simply for reference; they are actually evaluated as a function of pressure and temperature in the model. The fluid pressure in the fracture was above the critical pressure; therefore, there was no change of state.

6.3.1.1 Compositional Case

Fig. 6.9 shows the final width profile for the gelled LPG injection; **Fig. 6.11** shows the evolution of the fracture height and maximum fracture width over time; and **Fig. 6.12** provides the resulting net pressure and pressure drop occurring along the wellbore. The fracture does not penetrate the lower layer that offers a larger resistance (higher stress). Rather, the fracture migrates upward as the stress decreases in the pay zone. The stress contrast is relatively small at the interface, so the fracture overcomes the stress contrast and penetrates the upper layer.

Under these specific conditions, the density contrast between the fracturing fluid and the *in-situ* stress promotes vertical growth. As the fracture moves upward, the stress it encounters decreases significantly, so the fracture starts growing primarily in the upper layer (which constitutes the path of least resistance) while the growth is arrested in the target zone. This change in the fracture propagation pattern explains the non-uniform width profile and the increasing width at a depth of 7280 ft (Fig. 6.9). The out-of-zone growth causes a reduction in the net pressure, as observed after 12 minutes in Fig. 6.12a. 2D and pseudo 3D models cannot capture this type of fracture propagation pattern.

6.3.1.2 Incompressible Case

To quantify the impact of fluid expansion, we ran the exact same simulation with our simulator but with the assumption that the fluid was incompressible. The fluid density

was evaluated at the conditions of pressure and temperature experienced at the perforations (35.4 lbm/ft^3). **Fig. 6.10** shows the final width profile, and Figs. 6.11 and 6.12 emphasize the impact of fluid expansion on fracture propagation, by comparing the compositional and incompressible cases.

Even though the same volume of gelled LPG is injected, the final fracture volumes are different because of density variations. As temperature rises in the fracture, the density decreases from 35.5 to 30.3 lbm/ft^3 . This significant fluid expansion increases the fracture volume. This effect is not captured by traditional isothermal fracturing simulators, which underestimate the fracture volume created by a compressible fluid. In this example, the reduction in fluid density also impacts the main direction of propagation, as the fracture grows primarily in the upper layer.

The incompressibility assumption also leads to inaccuracies when determining the pumping requirements. In the compressible case, the fracture started propagating primarily in the upper layer after 12 minutes of pumping; therefore, the net pressure decreased because the fracture required less energy to propagate. In the incompressible case, this particular behavior was not observed, and the net pressure kept increasing because more energy was required to widen the fracture, as opposed to promoting fracture length growth. This example illustrates the impact of fluid expansion on both fracture propagation and pumping requirements. In many other examples, the net pressure was underestimated when we used the incompressibility assumption. The impact of fluid expansion varies on a case-by-case basis, so a close study of the net pressure and fracture profile is required to assess how fluid expansion alters fracturing propagation.

As shown in Fig. 6.12b, the pressure drop in the incompressible case is overestimated as compared to the compositional case. This is because we assumed that the

fluid density equals the downhole fluid density along the wellbore. In practice, the density at the surface is less than at the perforations because of the significant decrease in pressure; therefore, the fluid column is lighter. If we assumed that the fluid density was equal to the density at the surface, the pressure drop in the incompressible case would be underestimated as compared to the compositional case. The variations in frictional pressure drop were negligible as compared to the variations in the weight of the fluid column.

In this example, the variations in fluid pressure along the wellbore are minor, but the changes in fracture volume and fracture shape are significant. This comparison highlights the importance of properly characterizing fluid density for energized fluids. Similar observations can be made regarding the changes in fluid composition and viscosity. As the fluid temperature increases, its viscosity typically decreases, thereby reducing the proppant-carrying capacity of the fluid.

6.3.2 Long-Term CO₂ Injection

We consider the slow injection of pure CO₂ in a three-layer reservoir for enhanced recovery purposes. The mechanical properties are included in Table 6.2, and the stress distribution is indicated as *Stress B* in Fig. 6.2. We consider the same vertical well with a 40-ft perforated interval located in the middle of the target zone.

Because our model formulation depends primarily on the speed at which the fracture front propagates (rather than being time-step dependent), our simulator is suitable for long-term injection processes. The purpose of the injection is to stimulate the reservoir, not to propagate a fracture; therefore, the CO₂ is not gelled. Consequently, the fluid viscosity is low (0.3 cp), and the leak-off coefficient is very high (0.01 ft/ $\sqrt{\text{min}}$). The

fracture is not propagated by design, but is the result of a slow increase in net pressure. In this example, we assume that the leak-off coefficient remains constant over time.

Figs. 6.13 and **6.14** show the width profile after the injection of CO₂ at 10 days and 200 days, respectively. **Fig. 6.15** provides the evolution of the fracture half-length, fracture height, and maximum fracture width over time. The fracture grows upward as the stress decreases in the pay zone. This behavior is particularly evident in Fig. 6.13, where the fracture reaches the upper boundary after less than 10 days. Contrary to the LPG example, the stress contrast at the interface is large enough to maintain the fracture in the target layer. As seen in Fig. 6.15, the fracture seems to reach pseudo steady-state equilibrium after 100 days, at a nearly constant net pressure. The fracture keeps propagating in length while the maximum fracture width remains approximately constant.

In addition, our model may be used for investigating the fracture propagation induced by the long-term injection of CO₂ in carbon sequestration and storage (CSS) processes. The injection time in CSS projects may be several decades, so a very large stress contrast is required to prohibit fracture propagation in the bounding layers. In the previous example, the stress contrast was not large enough to contain the fracture in the target zone over a long period of time. Typical candidates for CSS projects are aquifers with a stress contrast of more than 2000 psi to limit the risk of having the buoyant CO₂ migrating in the upper layer.

6.3.3 CO₂ Foam Fracturing Treatment

The reservoir chosen for this example is a low-permeability sand formation. The gas-bearing zone is 100 ft in height and is bounded by two shale layers. The fracture gradient equals 0.6 psi/ft in the pay zone, and 0.65 and 0.67 psi/ft in the bounding layers. A stress contrast of 130 and 160 psi is present between the target zone and the upper and

lower bounding layers. **Table 6.3** contains the mechanical properties of the layers, and the vertical stress distribution is indicated as *Stress C* in Fig. 6.2. A typical value of the leak-off coefficient for a gelled base-fluid formulation in this tight-gas reservoir is 0.0005 ft/ $\sqrt{\text{min}}$ in the pay zone and 10^{-6} ft/ $\sqrt{\text{min}}$ in the bounding layers. The leak-off coefficients for the foam formulation are scaled accordingly using the multi-phase leak-off results presented in Chapter 7.

We consider a horizontal well that is centered within the target zone. From a practical standpoint, the use of a horizontal well may not be necessary because the pay zone is high enough, but we chose a horizontal well configuration to illustrate one of the capabilities of the model. As seen in Table 6.3, the initial pad is followed by two stages of proppant (3 and 6 lbm per added gallon, respectively). We assumed an injection temperature of 110°F at the perforations, and the fluid is designed to be 0.7-quality CO₂ water foam at the perforations. Table 6.3 provides the foam properties for a 0.7-quality foam at 5000 psi and 110°F. To our knowledge, this example is the first published example² of a simulation of a 3D fracture initiated with a two-phase mixture using a compositional hydraulic fracturing simulator.

Figs. 6.16 to 6.19 show the final fracture width, fluid temperature, gas phase density, and proppant volumetric concentration, respectively. The combination of these plots forms a good diagnostic tool to tailor the fracturing treatment. Fig. 6.16 shows that the fracture penetrates both the upper and lower layers toward the end of pumping. The fracture grows upward as the stress difference between the rock (0.6 psi/ft) and the fluid pressure (0.39 psi/ft) decreases. The stress contrast is relatively small at the interface so the fracture overcomes the stress contrast and penetrates the upper layer. Height

² This example was originally given in SPE 163867 by Ribeiro and Sharma (2013).

containment remains nonetheless satisfactory, and the fracture is very thick and rather short. This result is explained by the high-viscosity of the stable foam, and by the low Young's modulus of the rock formation.

Fig. 6.17 shows the rise of the fluid temperature in the fracture from 110°F at the perforations to 180°F along the fracture tip. Subsequently, Fig. 6.18 shows how the gas phase expands as the temperature increases. Even though proppant settling is clearly visible in Fig. 6.19, the foam was effective at carrying proppant far into the fracture, and most of the fracture located inside the targeted zone is propped. At the bottom of the fracture, the volumetric proppant concentration reaches a maximum value (0.52), which corresponds to the maximum packing of spheres of equal diameter.

6.3.4 Example of Wellbore Flow Calculations

This section provides an example of wellbore flow calculations that can be used to design the fracturing treatment and to determine the pumping requirements. We use the previous CO₂ foam example that was initiated from a horizontal well. The well is 12,000-ft long, with a 2,500-ft lateral section placed in the middle of the pay zone at a TVD of 8,000 ft (**Fig. 6.20**). The treatment design consists of injecting three stages of 0.7-quality foam, where the 0.7-quality is evaluated at the perforations. **Figs. 6.21** and **6.22** are outputs of the program that constitute good diagnostic plots for fracture design purposes.

Fig. 6.21a shows the evolution of the fluid pressure over time located downstream of the perforations, upstream of the perforations (designed as bottomhole pressure), and at the surface. The perforation pressure is the summation of the minimum horizontal stress and the net pressure. This pressure is fairly constant once the fracture has initiated (after 2 minutes). The bottomhole pressure is slightly higher than the perforation pressure because of the frictional loss occurring through the perforations. As more proppant is

injected over time, an erosion process decreases the frictional loss, and the bottomhole pressure converges toward the perforation pressure. The surface pressure depends on the weight of the fluid column, the frictional pressure drop, and the bottomhole pressure. As we start injecting proppant after 15 min, the surface pressure slowly decreases because the weight of the fluid column increases. Six minutes later (at the 21-min mark), the proppant has reached the perforations, and the pressure stabilizes until the 25-min mark when the third stage with a higher proppant concentration starts. Six minutes later (at the 31-min mark), the proppant reaches the perforations, and the pressure stabilizes once again. In this particular example, the surface pressure decreases as we inject more proppant because the increase in the weight of the fluid column exceeds the increase in the frictional pressure drop.

Fig. 6.21b shows the corresponding gas saturation at the different locations shown in Fig. 6.21a. By design, the gas saturation is 0.7 at the perforations. As the pressure loss through the perforations decreases, the bottomhole saturation converges to 0.7. At the surface, the gas saturation is higher because the gas phase is compressed as it flows from the surface to the perforations. The gas saturation at the surface increases over time because the friction loss increases as the proppant loading increases.

Fig. 6.22a shows the evolution of the density of the gas phase, fluid phase, and slurry mixture along the well after five minutes of injection. At that time, the fluid column only contains fluid from the first stage, so there is no proppant in the mixture. As expected, the liquid phase is nearly incompressible while the gas density significantly varies. The gas density increases until the well inclination is almost horizontal (at the 8,500-ft measured depth). Before the 8,500-ft mark, the weight of the fluid column exceeds the frictional loss, so the pressure (and subsequently the gas density) increases as

the fluid travels down. Further along the well, the frictional loss exceeds the gravity head, which is zero in the lateral section, so the pressure (and subsequently the gas density) decreases.

Fig. 6.22b shows the density profile after eighteen minutes of injection. The liquid and gas densities follow a behavior similar to that observed in Fig. 6.12a, but the slurry density is dramatically different. At the 18-min mark, the well contains both the slurry injected in stage 2 (for which the injection started at the 15-min mark) and the fluid injected in stage 1. The transition occurs at a depth of 6,400 ft, which is the distance traveled by the slurry in three minutes. The significant increase in slurry density is due to the high density of the proppant (150 lbm/ft^3). The sharp transition occurring at 6,400 ft is explained by our assumption that the proppant does not settle inside the well. This assumption may be challenged in the future if necessary.

6.4 CONCLUSIONS

This chapter illustrated the wide range of capabilities offered by the model:

1. The stress distribution may be refined to any number of layers to account for variations in stresses and mechanical properties. Nevertheless, the addition of reservoir layers comes at the expense of a longer computing time.
2. The model accounts for gravity effects.
3. The fracturing fluid can be single-phase or two-phase.
4. The model is suitable for many different applications ranging from hydraulic fracturing to long-term injections for enhanced oil recovery, well clean-up, or carbon sequestration purposes.
5. The model is suitable for any well configuration: vertical, deviated, or horizontal.

Table 6.1: Main input parameters for the validation examples (radial and PKN geometries).

Parameter	Unit	Radial	PKN #1	PKN #2
Pay Zone Height	ft	∞	150	150
Stress Contrast	psi	/	1000	1000
Young's Modulus	psi ($\times 10^6$)	2.5	2.5	2.5
Poisson's Ratio	/	0.25	0.25	0.25
Pumping Time	min	30	30	30
Injection Flow Rate	bbl/min	20	20	20
Viscosity (Newtonian)	cp	40	40	40
Leak-off Coefficient	ft/ $\sqrt{\text{min}}$	0	0*	0.002*

*Note that the only difference between the two PKN cases is the value of the leak-off coefficient.

Table 6.2: Main input parameters for the gelled LPG and CO₂ examples.

Parameter	Unit	LPG, Stress A	CO ₂ , Stress B
Pay Zone Height	ft	200	200
Stress Contrast (top - bottom)	psi	80 - 80	280 - 160
Young's Modulus (pay zone)	psi ($\times 10^6$)	1.5	1.3
Poisson's Ratio (pay zone)	/	0.25	0.25
Reservoir Temperature	$^{\circ}\text{F}$	180	130
Pumping Time	/	30 min	200 days
Injection Flow Rate	bbl/min	20	0.55
Density*	lbm/ft ³	35.4	58.1
Viscosity at 51s ⁻¹ *	cp	16	0.3
Leak-off Coefficient	ft/ $\sqrt{\text{min}}$	0.0005	0.01

*Fluid properties evaluated at 5000 psi and 100 $^{\circ}\text{F}$.

Table 6.3: Main input parameters for the 0.7-quality CO₂ foam example.

Parameter	Unit	CO ₂ Foam, Stress C
Pay Zone Height	ft	100
Stress Contrast (top - bottom)	psi	130 - 160
Young's Modulus (pay zone)	psi (x10 ⁶)	1
Poisson's Ratio (pay zone)	/	0.25
Reservoir Temperature	°F	180
Number of Stages	/	3
Pumping Time (per stage)	min	15 - 10 - 25
Injection Flow Rate (per stage)	bbbl/min	25 - 20 - 20
Proppant Loading (per stage)	lbm/gal	0 - 3 - 6
Density*	lbm/ft ³	56
Viscosity at 51s ⁻¹ *	cp	208
Leak-off Coefficient (liquid - gas)	ft/ $\sqrt{\text{min}}$	0.00015 – 0.00008

**Fluid properties evaluated at 5000 psi and 100 °F.*

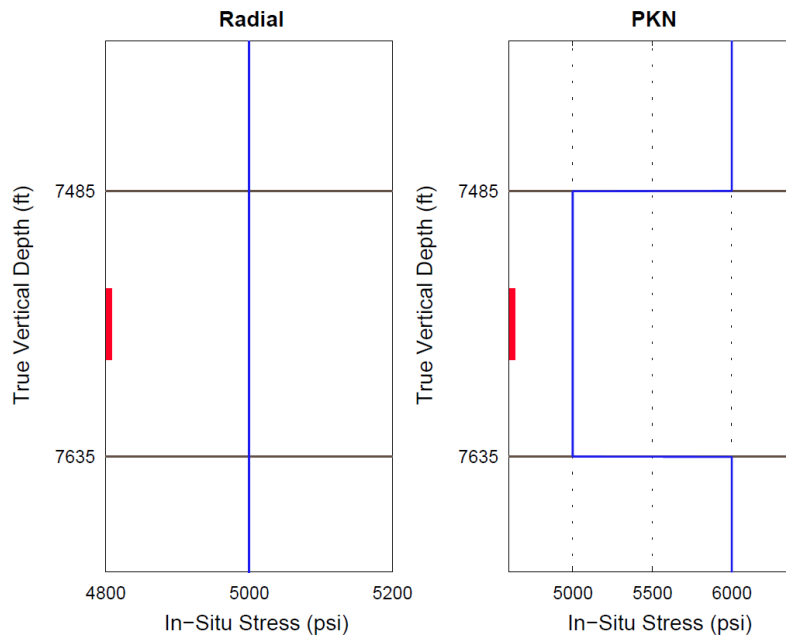


Figure 6.1: Vertical distribution of the *in-situ* minimum horizontal stress for the validation examples (radial and PKN geometries).

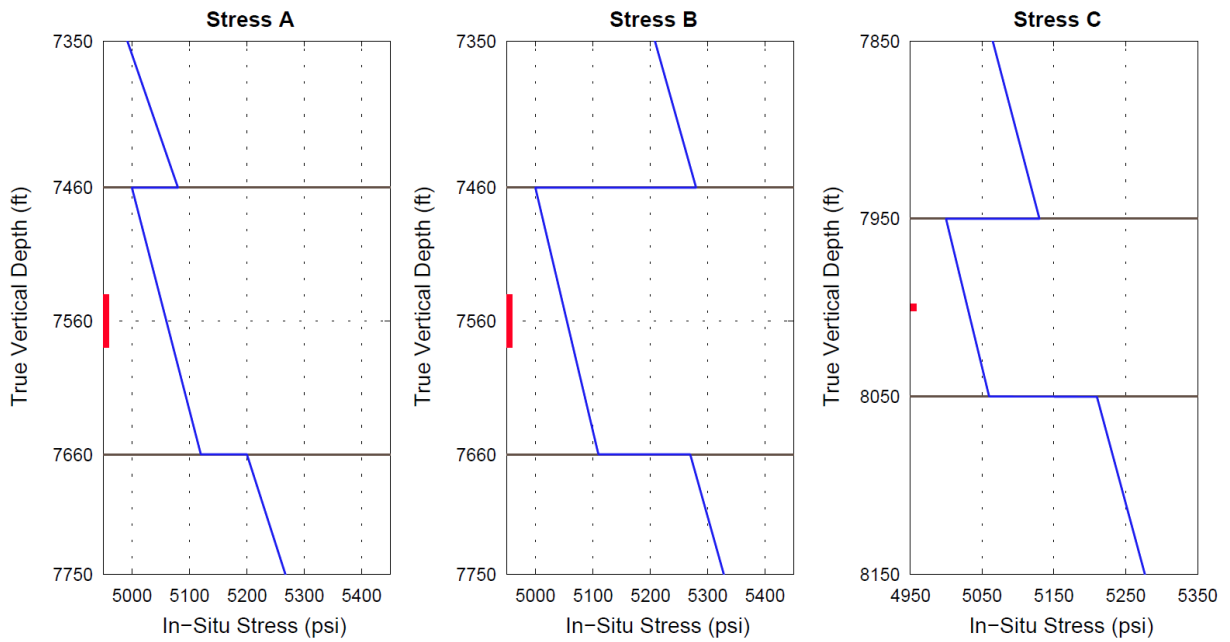


Figure 6.2: Vertical distribution of the *in-situ* minimum horizontal stress for the energized examples (LPG, CO₂, and CO₂ foam).

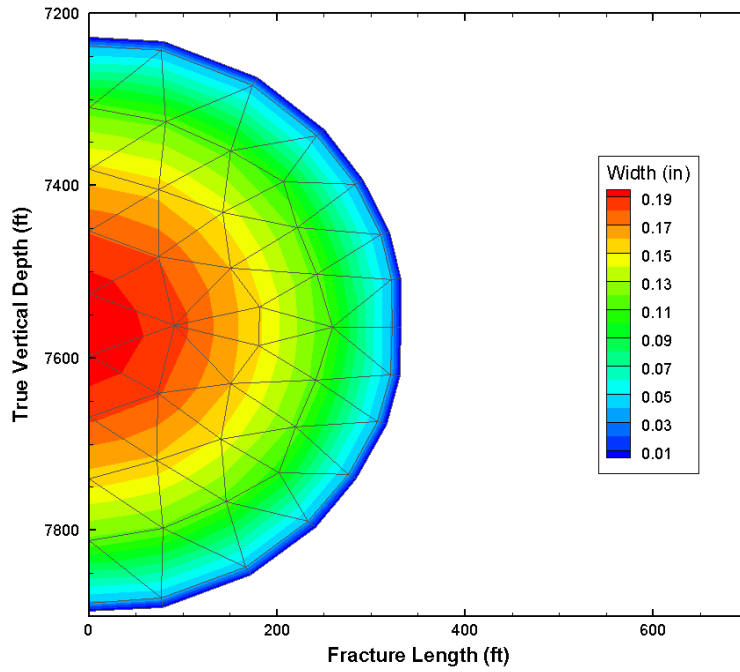


Figure 6.3: Final width profile (radial example, no leak-off).

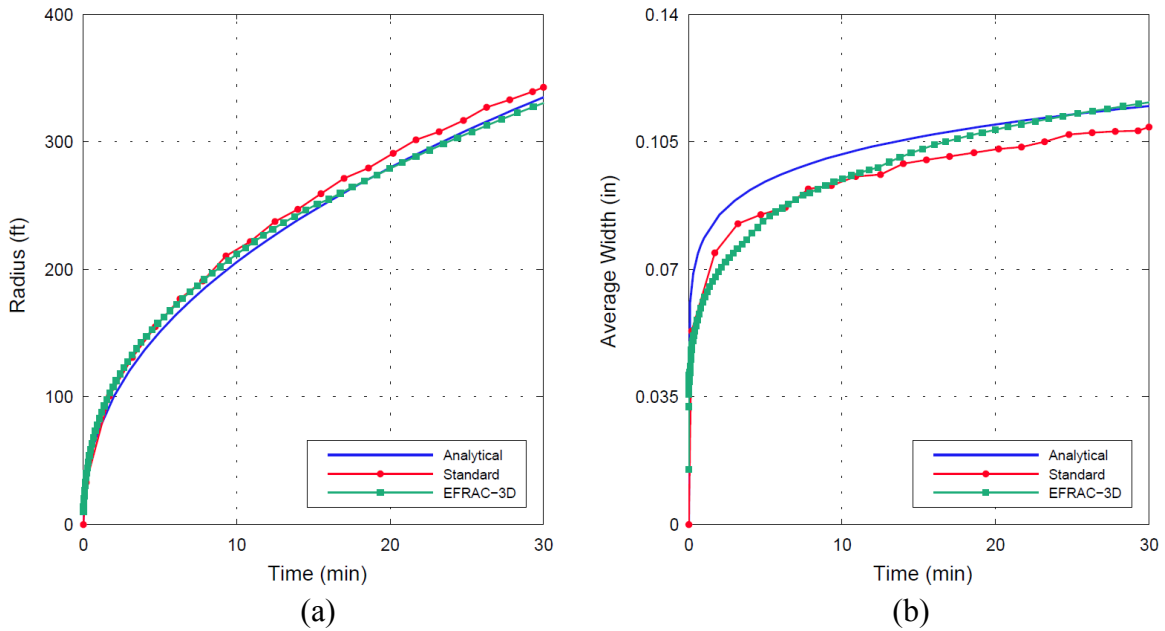


Figure 6.4: Comparison between fracturing models (radial example, no leak-off): (a) fracture radius over time and (b) average width over time.

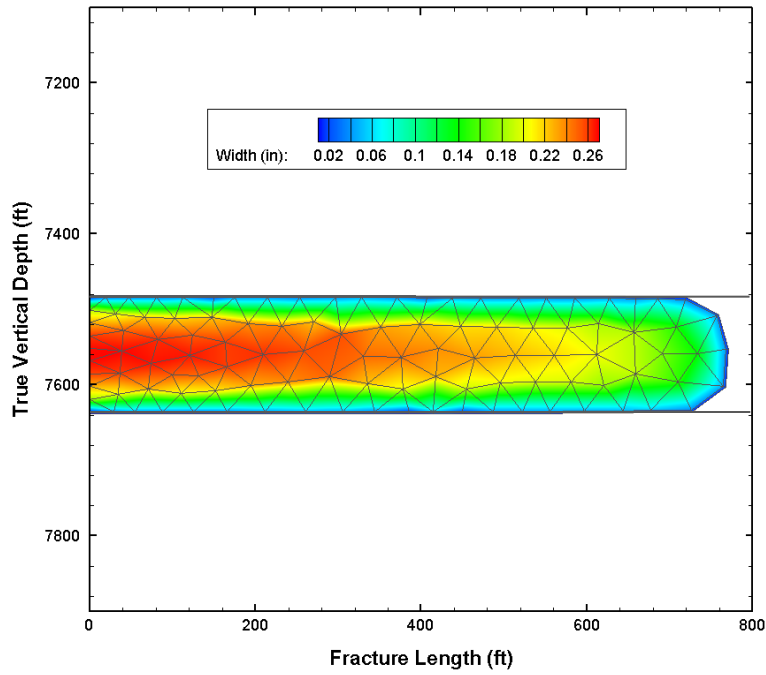


Figure 6.5: Final width profile (PKN example, no leak-off).

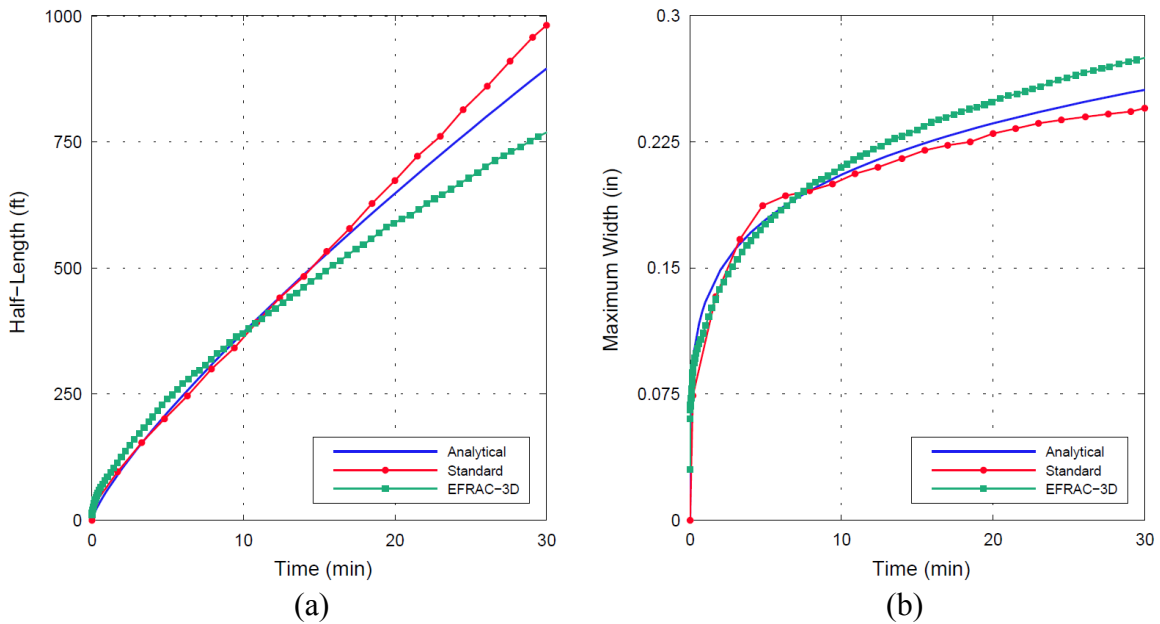


Figure 6.6: Comparison between fracturing models (PKN example, no leak-off): (a) fracture half-length over time and (b) maximum width over time.

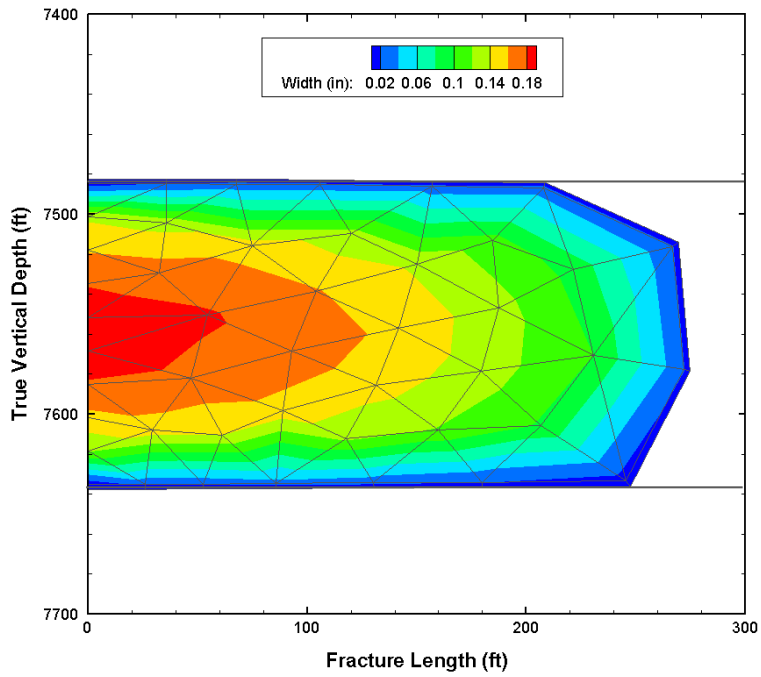


Figure 6.7: Final width profile (PKN example, with leak-off).

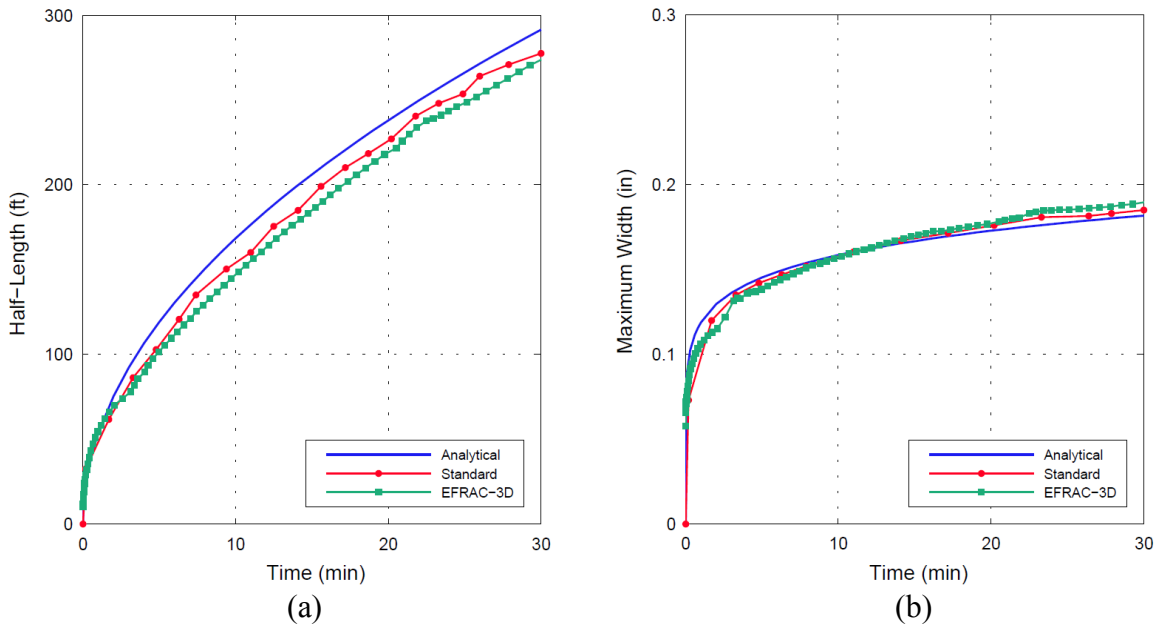


Figure 6.8: Comparison between fracturing models (PKN example, with leak-off): (a) half-length over time and (b) maximum width over time.

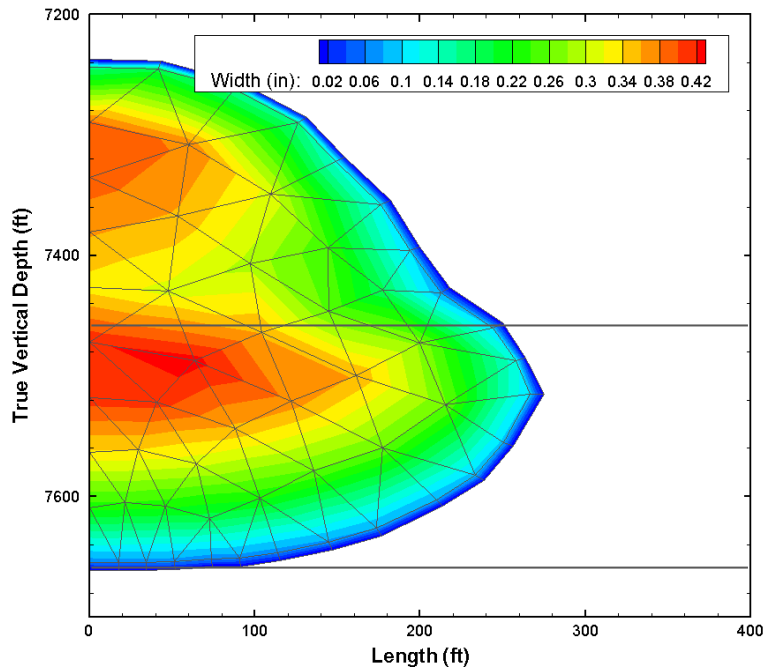


Figure 6.9: Final width profile for gelled LPG injection (*Stress A* distribution) using the compositional simulator. Fluid expansion is taken into account.

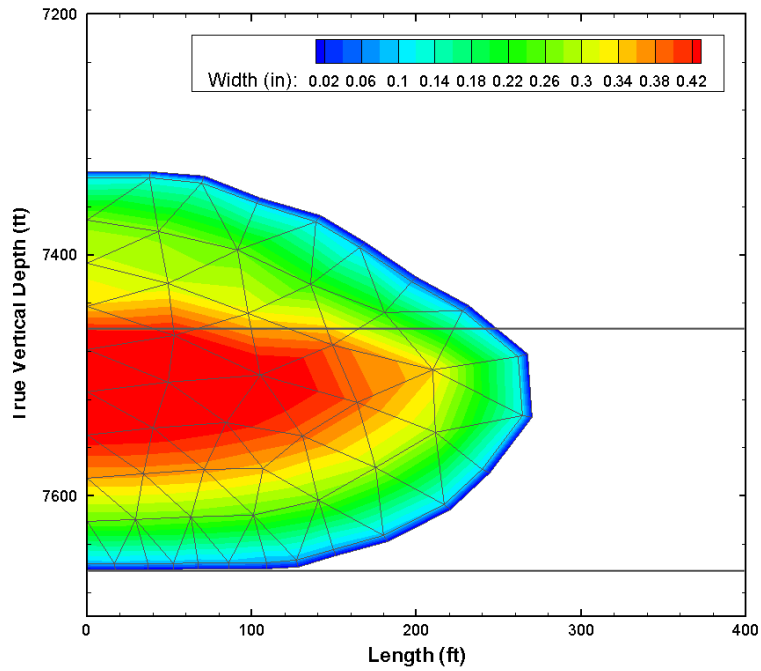


Figure 6.10: Final width profile for gelled LPG injection (*Stress A* distribution) assuming the fracturing fluid remains incompressible.

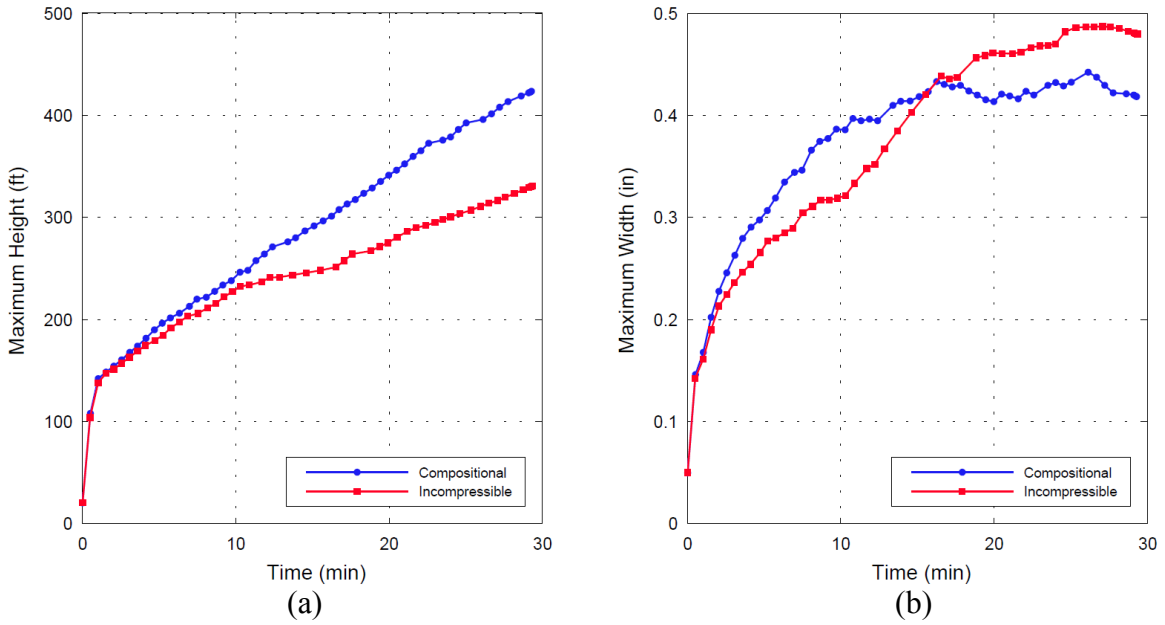


Figure 6.11: Impact of fluid expansion on fracture geometry (LPG example, *Stress A* distribution): (a) height over time and (b) maximum width over time.

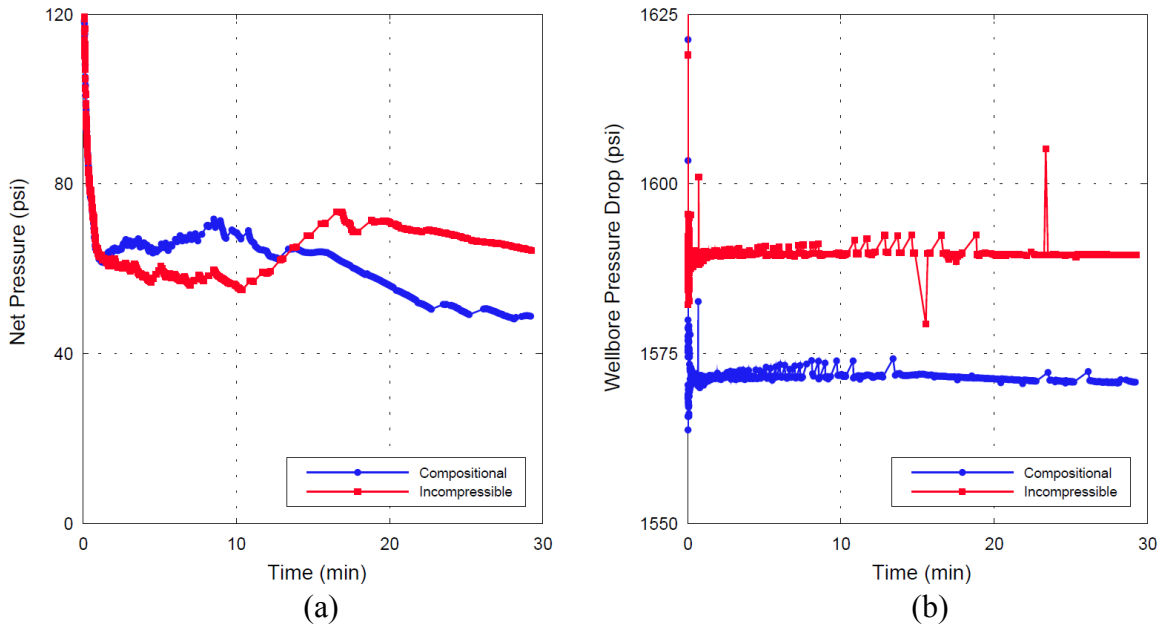


Figure 6.12: Impact of fluid expansion on pumping requirements (LPG example, *Stress A* distribution): (a) net pressure over time and (b) pressure drop along the wellbore over time.

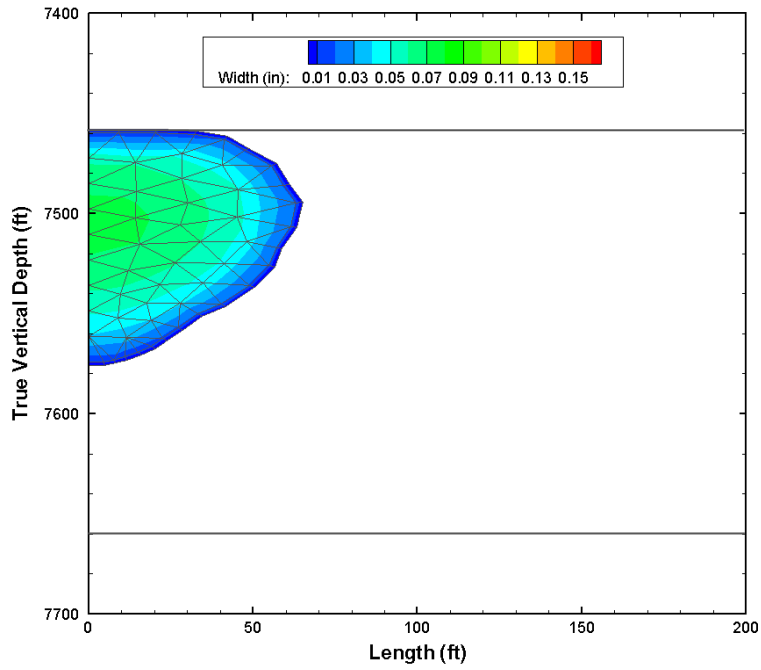


Figure 6.13: Width profile after 10 days of CO₂ injection (*Stress B* distribution).

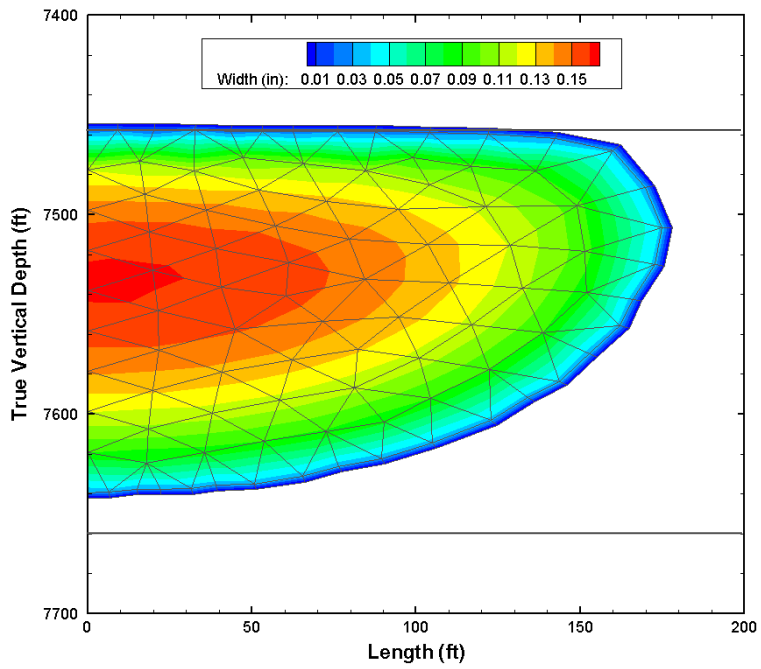


Figure 6.14: Width profile after 200 days of CO₂ injection (*Stress B* distribution).

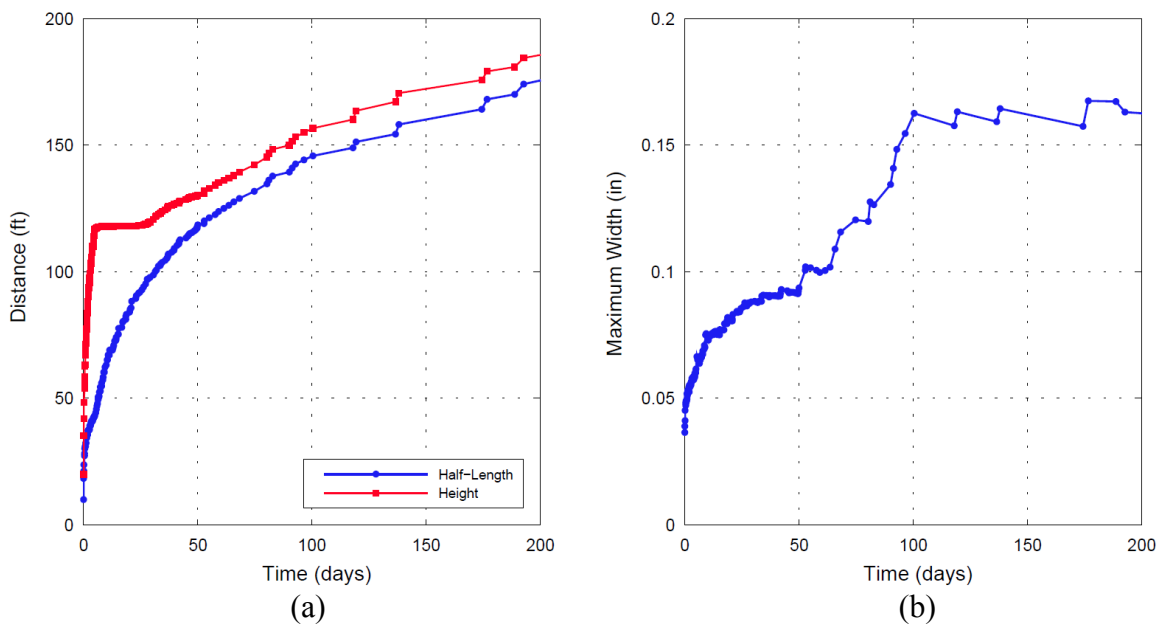


Figure 6.15: Evolution of fracture geometry for long-term CO₂ injection: (a) half-length and height over time and (b) maximum width over time. The time step increases over time, as indicated by the increasing gaps between markers.

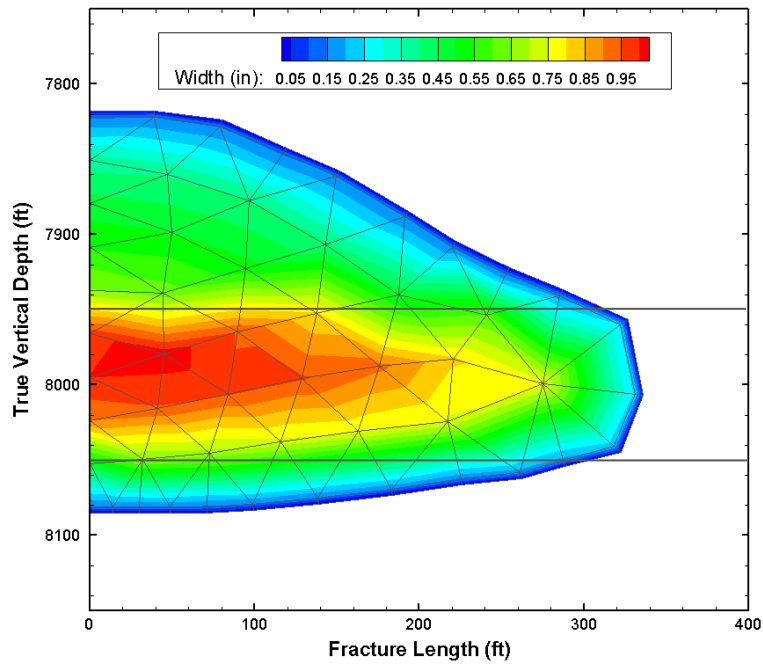


Figure 6.16: Fracture width for 0.7-quality CO₂ foam (*Stress C* distribution).

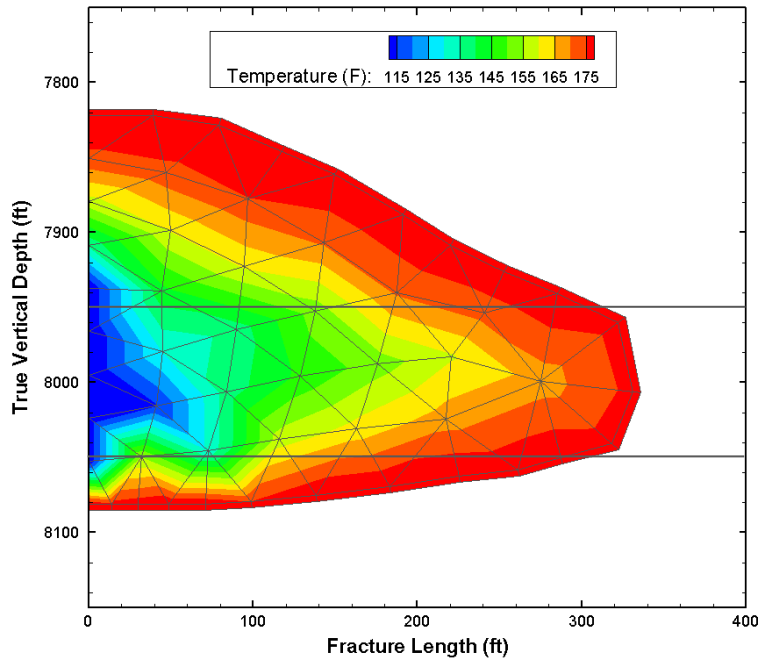


Figure 6.17: Fluid temperature for 0.7-quality CO₂ foam (*Stress C* distribution).

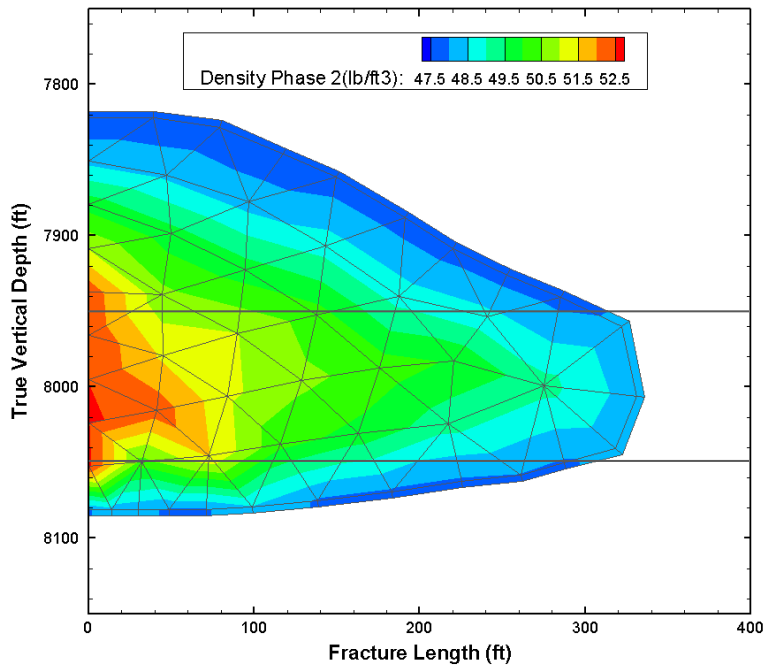


Figure 6.18: Gas phase density for 0.7-quality CO₂ foam (*Stress C* distribution).

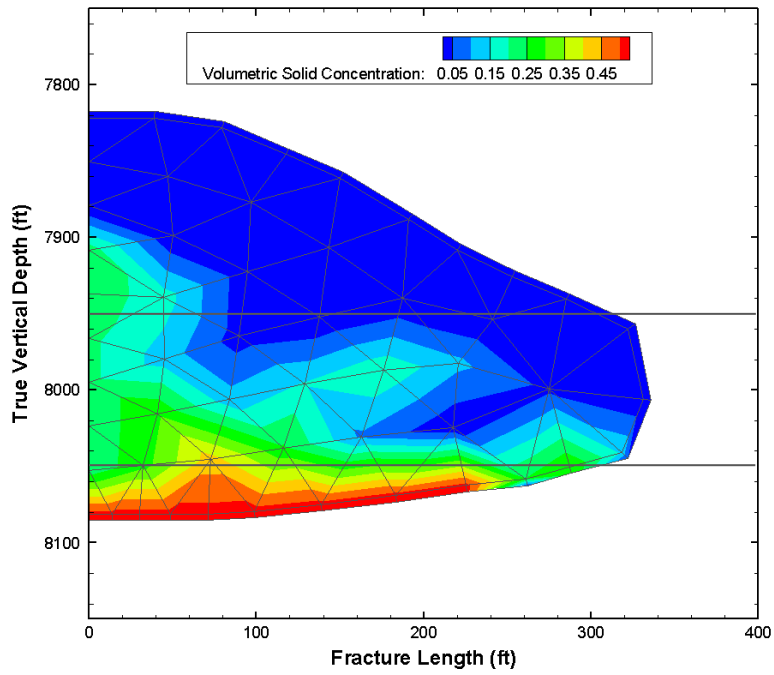


Figure 6.19: Proppant concentration (volume fraction) for 0.7-quality CO₂ foam (*Stress C* distribution).

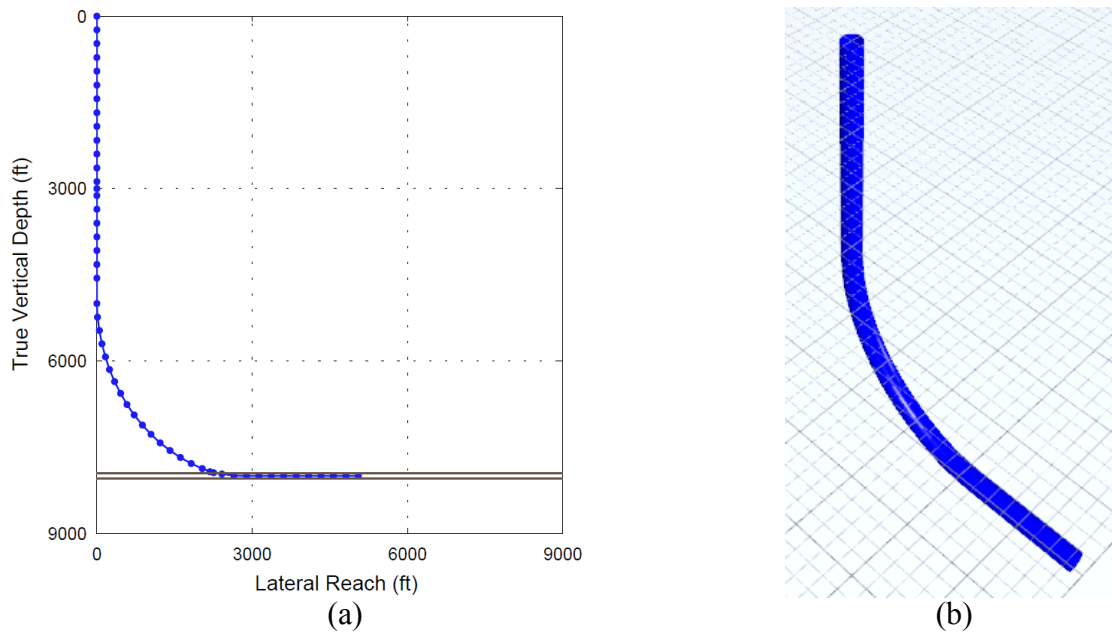


Figure 6.20: Horizontal well profile: (a) position of the survey stations in the vertical-lateral depth referential and (b) 3D isometric representation in our interface (not to scale).

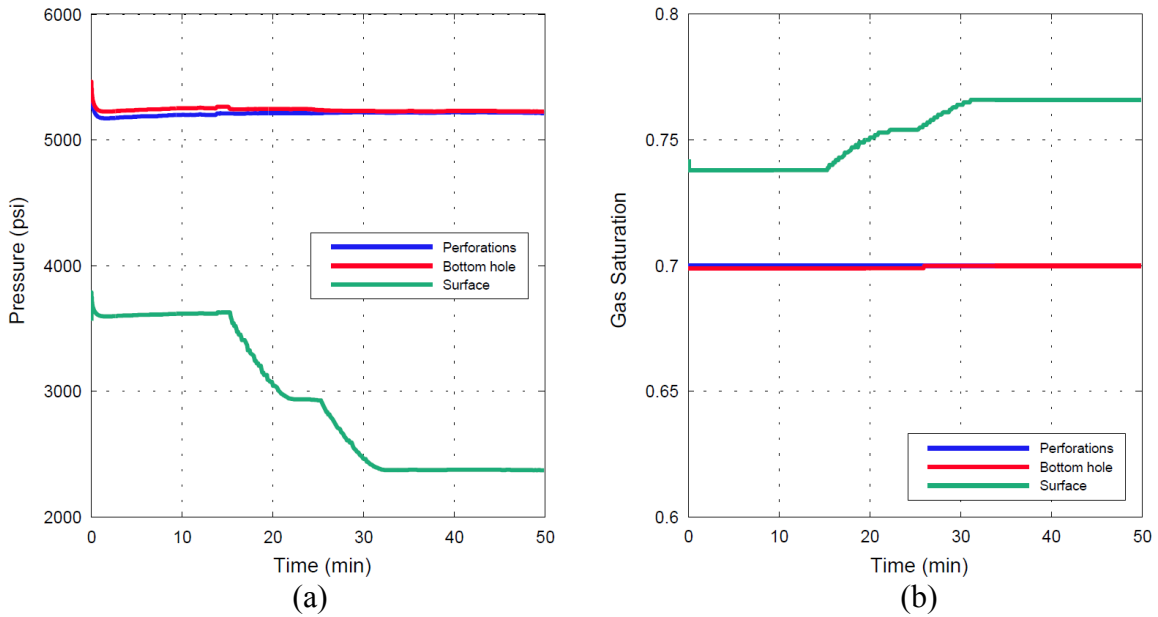


Figure 6.21: Pumping requirements: (a) fluid pressure over time and (b) gas saturation over time. Foam quality is higher at the surface than the designed quality at the perforations because of gas compressibility.

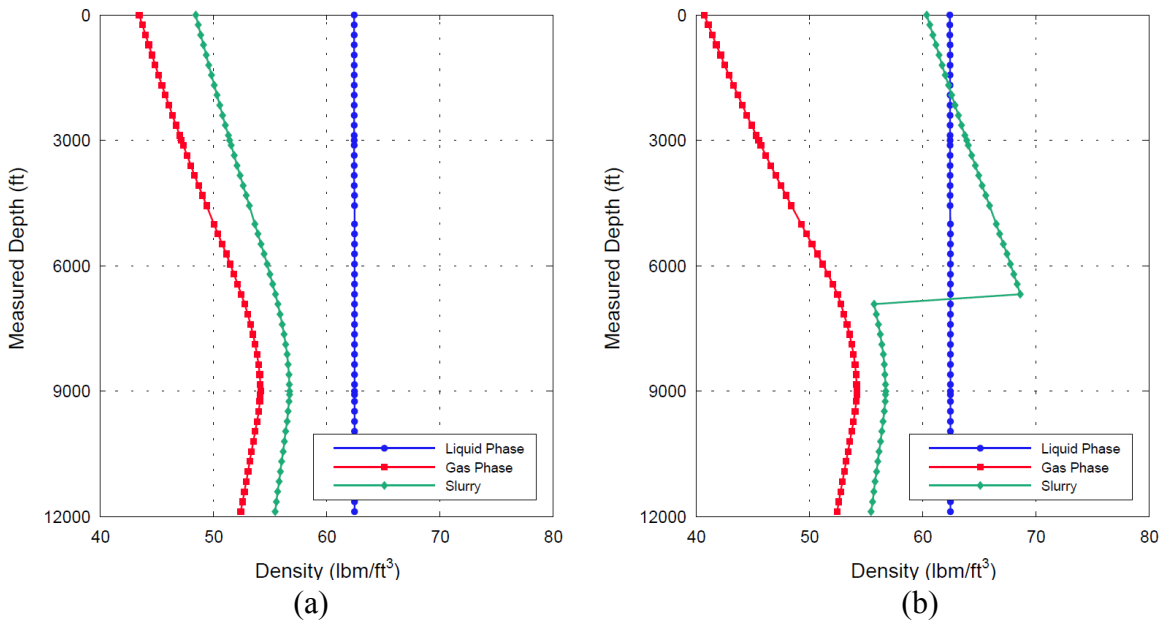


Figure 6.22: Density of the liquid phase, gas phase, and slurry mixture along the wellbore: (a) after 5 minutes of pumping and (b) after 18 minutes of pumping. The markers indicate the position of the survey stations.

REFERENCES

- Geertsma, J. and de Klerk, F. 1969. A Rapid Method of Predicting Width and Extent of Hydraulically Induced Fractures. *J. Pet Tech* **21**(12): 1571-1581. SPE 2458-PA.
- Gu, H. 1987. A Study of Propagation of Hydraulically Induced Fractures, Ph.D. Dissertation, The University of Texas at Austin, Austin, Texas.
- Nordgren, R.P. 1972. Propagation of a Vertical Hydraulic Fracture. *SPE J.* **12**(4): 306-314. SPE 3009-PA.
- Ouyang, S. 1994. Propagation of Hydraulically Induced Fractures with Proppant Transport, Ph.D. Dissertation. The University of Texas at Austin, Austin, Texas (May 1994).
- Weng, X. 1992. Incorporation of 2D Fluid Flow Into a Pseudo-3D Hydraulic Fracturing Simulator. *SPE Prod Eng* **7**(4): 331-337. SPE 21849-PA.
- Yew, C.H. 1997, *Mechanics of Hydraulic Fracturing*, Gulf Publishing Company, Houston, Texas.

Chapter 7: Phase Behavior, Rheology, and Leak-off of Energized Fluids

The examples presented in Chapter 6 demonstrated the impact of fluid properties on fracture performance, with a particular emphasis on the fluid's density, phase behavior, rheology, and leak-off. The main advantage of our compositional fracturing model is to capture a more realistic representation of the fluid behavior, as opposed to the simplistic fluid characterization assumed in traditional fracturing models. The additional complexity of the compositional model enables us to model the unique properties of energized fluids; however, this modeling effort is futile if it is not supported by an accurate fluid characterization that is consistent with experimental data. Thus, the objective of this chapter is to review key fluid properties and provide meaningful data to the reader.

If the qualitative benefits of energized fluids are known, the lack of experimental data has hindered their field implementation. This chapter addresses the main experimental challenges in measuring multi-phase rheology and leak-off. It introduces the experimental work we conducted to characterize foam behavior, using a new laboratory apparatus that enabled us to (1) measure foam rheology and stability, (2) measure dynamic liquid and gas leak-off, and (3) evaluate regain permeability during flowback¹ (Ribeiro 2012; Ribeiro and Sharma 2012).

Foams exhibit unique properties that set them apart from traditional fluid formulations. Variations in pressure and temperature cause changes in fluid density and behavior, thereby impacting the fracture volume and the flowback performance. Foams

¹ The details regarding the experimental work conducted by the author are not included in this dissertation, as they are included in Ribeiro (2012) and Ribeiro and Sharma (2012).

experience dramatic changes in viscosity across different flow regimes, and the fracturing engineer can take advantage of this wide range of viscosities to optimize fluid design. Moreover, foams typically present superior fluid-loss control properties, and the reduction in liquid leak-off significantly bolsters oil and gas production.

7.1 PHASE DENSITY

Fluid density primarily affects fracture geometry, pump horsepower requirements, and proppant transport. Common additives do not modify fluid density because their concentration is too low; and they do not impact phase behavior because they are not chemically reactive. The density of water-based fracturing fluids is generally assumed to be constant, which is a reasonable assumption because the water density typically varies by less than 1% in most fracturing applications. For energized fluids, significant fluid expansion increases the fracture volume as temperature increases, but this effect is not captured by traditional isothermal fracturing simulators. Our compositional model captures this effect; therefore, it requires the knowledge of fluid density as a function of temperature, pressure, and composition. The densities of the many fluid formulations encountered in this dissertation are well-documented, and we use empirical correlations to determine phase density.

7.1.1 Model Formulation

As mentioned in Chapter 3, Friehauf and Sharma (2009) used the Peng-Robinson equation of state (EoS) to determine phase density. This approach is comprehensive and flexible, but the Peng-Robinson EoS is not well-suited for polar fluids like water. Since water is the most common component used in fracturing, this choice may not be judicious. Also, the use of an EoS significantly slows down the computations.

An alternative approach for estimating phase density is to use empirical correlations. For liquid-like fluids, thermal expansion (α_T) and isothermal compressibility (β_P) are taken into account. For gas-like fluids, phase density can be calculated from the real gas EoS, for which the compressibility factor is obtained from a mathematical fit of experimental data.

$$\rho(P, T) = \rho_0(P_0, T_0) \times e^{[-\alpha_T(T-T_0)]} \times e^{[\beta_P(P-P_0)]} \quad (7.1)$$

$$\rho(P, T) = \frac{M_w P}{Z(P_r, T_r) RT} \quad (7.2)$$

We used a combination of Eqs. 7.1 and 7.2 to generate the examples shown in the following sections. In fact, any *a priori* correlation or equation of state may be implemented into the code. We tuned Eq. 7.1 so that the thermal expansion (α_T) and isothermal compressibility (β_P) are functions of pressure and temperature, respectively. For the compressibility factor, we used a mathematical model similar to the one proposed by Beggs and Brill (1973) to fit the work of Standing and Katz (1942). These correlations provide a simple and effective way to estimate fluid density:

$$z(P, T) = \alpha_1(T_r) + \alpha_2(T_r)P_r + \frac{(1 - \alpha_1(T_r))}{e^{\alpha_7(T_r, P_r)}} + \alpha_6(T_r) \left(\frac{P_r}{10} \right)^4$$

$$\left\{ \begin{array}{l} \alpha_1 = -0.101 - 0.36T_r + 1.3868\sqrt{T_r - 0.919} \\ \alpha_2 = 0.021 + \frac{0.04275}{T_r - 0.65} \\ \alpha_3 = 0.6222 - 0.224T_r \\ \alpha_4 = \frac{0.0657}{T_r - 0.86} - 0.037 \end{array} \right. ; \quad \left\{ \begin{array}{l} \alpha_5 = 0.32 \exp(-19.53(T_r - 1)) \\ \alpha_6 = 0.122 \exp(-11.3(T_r - 1)) \\ \alpha_7 = P_r (\alpha_3 + \alpha_4 \times P_r + \alpha_5 \times P_r^4) \end{array} \right. \quad (7.3)$$

7.1.2 Phase Density of Common Fracturing Fluids

This section compares our model formulation to well-established data sets for validation purposes. **Figs. 7.1** through **7.4** show the density of a pure water phase, pure nitrogen phase, pure CO₂ phase, and LPG mixture, respectively. The figures show the variations of density under a wide range of pressures for three different temperatures. All the plots presented in this chapter follow the same convention: solid lines refer to our model predictions and markers refer to external references (typically experimental data).

As seen in Fig. 7.1, the model predictions for water are in agreement with the measured data provided in the textbook compiled by Sandler (2007). For practical purposes, the range of density is narrow enough to assume that water is incompressible; therefore, the additional model complexity is not required for simple water-based cases. **Fig. 7.2** shows a good match between our N₂ density predictions and the data provided by Saddington and Krase (1934). For pressures higher than approximately 3500 psi, Eq. 7.2 tends to underestimate the N₂ density, so we used Eq. 7.1 at high pressures to guarantee a good match across the entire spectrum. A smooth transition between the two regimes is enforced by using a combination of Eqs. 7.1 and 7.2 for pressures ranging between 2500 and 3500 psi.

Fig. 7.3 compares the density of a pure CO₂ phase against predictions obtained with a well-established software package, *PVTsim*. At moderate pressures (1000 to 2500 psi) and temperatures (90 to 130 °F), the match between our model and the reference data weakens, and, accordingly, one of the future recommendations for improving this model is to improve the quality of the model predictions for CO₂ density. Nevertheless, we assume that the fit is satisfactory enough for the results presented in this study because this range of pressures and temperatures is infrequently encountered in fracturing.

Indeed, low-to-moderate pressures are mostly observed in the upper section of the well, where the fluid temperature is lower than the indicated range.

Fig. 7.4 shows a good match between our model and the data obtained with *PVTsim* for a LPG mixture. For this example, the LPG composition is 90% of propane (C_3) and 10% of n-butane ($n-C_4$) on a volume basis, which is a typical composition for LPG. In practice, the LPG composition varies geographically and seasonally. For instance, heavier components may be added to decrease the risk of flammability.

7.2 COMPONENT SOLUBILITY

For two-phase fluids, component solubility primarily affects the flowback performance of the fracture treatment. Because liquid leak-off is usually higher than gas leak-off (Harris 1985; Harris 1987; Ribeiro and Sharma 2012), an energized component is more likely to invade the reservoir rock when that component is leaking off with the liquid phase. As the bottomhole pressure is decreased during flowback, the soluble component comes out of solution, thereby increasing gas saturation. This phenomenon significantly facilitates the flow of the hydrocarbon fluids to the wellbore.

7.2.1 Model Formulation

Friehauf and Sharma (2009) used the Peng-Robinson EoS to determine the component split between phases. This method is computationally demanding, particularly for a 3D code; therefore, we used K -values to assess component solubility in two-phase fluids. For a given component, the K -value is a function of pressure and temperature. Fundamentally, the K -values express Henry's Law, which states that the solubility of a gas in a liquid is directly proportional to the partial pressure of the gas above the liquid. These K -values can be obtained from an empirical fit of solubility data, and we chose to

use a Langmuir-type equation (Eq. 7.4) to fit the data. This choice was motivated by the fact that the solubility process is analogous to the adsorption of molecules on a solid surface, which was the process originally modeled by the Langmuir equation. The equation is bounded, which is necessary to represent the intrinsic limit of solubility. The solubility estimate ($x_{i,sol}$) is converted to the mass fraction of component i (x_i) in the liquid phase as follows:

$$x_{i,sol} = \beta(T) \frac{\alpha(T)P}{1 + \alpha(T)P} \quad \text{and} \quad x_i = \frac{x_{i,sol}}{100 + x_{i,sol}} \quad (7.4)$$

7.2.2 Component Solubility of Common Fracturing Fluids

This section compares our model formulation to well-established data sets under a wide range of pressures and temperatures. **Figs. 7.5** through **7.7** show the solubility of N₂ in water, CO₂ in water, and CO₂ in an equimolar mixture of water and methanol, respectively. The y -axis indicates the solubility as the mass (in grams) of component we can add to a liquid solution of 100 g.

As seen in Fig. 7.5, N₂ is practically insoluble in water, and these predictions are supported by the experimental data given by Goodman and Krase (1931). Because water does not partition in the gas phase, N₂ foams only contain water in the liquid phase and N₂ in the gas phase. Fig. 7.6 compares our model to the solubility data for CO₂ in water given by Rumpf *et al.* (1994), and Fig. 7.7 compares our model to the solubility data for CO₂ in an equimolar mixture of water and methanol given by Xia *et al.* (2004). The match is satisfactory in both cases. CO₂ is appreciably more soluble than N₂ in water, and the addition of methanol further promotes the solubility of CO₂ to high concentrations. Fluids with higher solubility in the liquid phase have an increased ability to reduce

damage by increasing the relative permeability to gas (oil) in the invaded zone, which in turn improves the gas (oil) production.

7.3 RHEOLOGY

One of the most important considerations in fluid selection is viscosity, which impacts fracture geometry, fluid-loss control, and proppant transport. For non-energized fluids, fluid design primarily consists in selecting the optimum fluid rheology for a given reservoir. Depending on the nature of the reservoir, high viscosities may or may not be desirable. Viscous fluids tend to create wider and shorter fractures because the frictional loss dramatically increases in a narrow opening. The gelling agents and other viscosifying additives typically used in fracturing form a competent filter-cake on the fracture face, leading to a reduction in fluid leak-off. Increasing fluid viscosity also improves proppant placement by reducing proppant settling. For these reasons, the fluid rheology plays a critical role in fracturing.

7.3.1 Base-Fluid Rheology

The rheology of water-based fluids is well documented, with numerous textbooks and monographs on the subject (Gidley *et al.* 1989; Economides and Nolte 2000). Rheology primarily depends on the gelling agents and fluid additives that are used. A large cocktail of additives is available, sometimes with major differences between the providers; therefore, few comprehensive models and/or databases describe the rheology of water-based fluids. The study of water-based fluid rheology is out of the scope of this dissertation, but knowledge of the based-fluid rheology is necessary to assess the rheology of the two-phase mixture. For the experiments presented in this chapter, the

base-fluid is a 30 lbm/Mgal linear Guar gel with 3% KCl per weight. If the base-fluid was different, the absolute values of viscosity would be different.

Rheological data for gelled CO₂ and LPG formulations are very scarce in the literature (Taylor *et al.* 2005; Lestz *et al.* 2007). Often, rheology data and protocols for gelling and mixing remain confidential. LPG is compatible with most of the common gelling agents, and the gelling process has been done routinely in the field. This is not the case for single-phase CO₂ because of incompatibilities between the gelling agents and CO₂. In some cases, the alternative approach is to mix the CO₂ with another fluid that is easily gelled (Taylor *et al.* 2005; Lestz *et al.* 2007). In this study, we assume that the gelling process is efficient enough to increase the CO₂ or LPG viscosity. Without any additives, pure CO₂ and LPG are about three to five times less viscous than water under typical fracturing conditions; therefore, we will assume that gelled CO₂ and LPG remain less viscous than their gelled water counterparts.

7.3.2 Foam Stability

Foam rheology is inherently dependent on foam stability, which results from the quasi-equilibrium between buoyancy and inertial forces (that favor gas bubble coalescence), and shear forces (that dynamically breaks the gas bubbles and mixes them with the internal phase). Unstable foams can be seen as mixtures of dissociated gas and liquid phases. The phases may travel at different velocities based on their intrinsic rheology. For stable foams, the two phases travel at the same velocity, so there is no slippage. Also, interfacial forces prevent gravity segregation. From a transport standpoint, stable foam is seen as a single “pseudo phase” that contains gas bubbles and liquid together. For unstable foams, the interfacial forces are not capable of holding the gas

bubbles inside the external liquid phase. As gas bubbles coalesce, the subsequent gas pocket migrates upward because of gravity segregation.

The foam stability assumption is critical, as evidenced by Figs. 7.8 and 7.9. Fig. 7.8 shows the water saturation inside the fracture after pumping stable 0.7-quality CO₂ foam for 5 minutes (min). In this case, the water saturation slowly decreases from 0.3 at the perforations to 0.25 along the fracture tip. The fracture is slightly enriched in the gas phase because liquid leak-off is higher than gas leak-off, and because the gas phase expands as temperature increases near the fracture tip. Alternatively, Fig. 7.9 shows the water saturation inside the fracture after pumping unstable 0.7-quality CO₂ foam for 5 min. The water and the gas phases are completely separated after a few minutes, and the mixture loses its viscosity. Gravity segregation occurs because of the contrast between the liquid and the gas densities.

7.3.3 Stable Foam Rheology

7.3.3.1 Literature Review

Foam² rheology depends on both the rheology of the sole continuous liquid phase, and the interactions between the dispersed gas bubbles and the liquid phase. These interactions are related to the texture, or bubble-size distribution, of the foam. It should be noted that our discussion is restricted to bulk foams, which are formed in a volume that is much larger than the individual gas bubbles. The bulk foam rheology differs from the transport of foam in a porous medium, which is well-documented (Kovscek and Radke 1994).

² In this dissertation, we use the term *foam* to refer to both the foam and the comingled flow regimes. Although a misnomer, this terminology is commonly used in practice.

A critical parameter for foam rheology is quality, which is defined as the volume fraction of the external phase (gas). At high qualities, interactions between bubbles cause energy dissipation resulting in a high effective viscosity. The internal phase remains stable until very high qualities are reached (~95%). Then, the gas becomes the external phase, and the mixture is referred to as a mist. At low qualities (typically lower than 50%), the interactions between bubbles are minimal, so the fluid viscosity resembles that of the base fluids. At low qualities, the fluid is typically referred to as a comingled fluid. These three flow regimes (i.e., comingled, foam, and mist) are indicated in **Fig. 7.10**. In practice, the transition between the regimes can be vague, and the scarcity of rheology data does not allow a proper characterization of the fluid behavior over a large spectrum. As seen in Fig. 7.10, multiple interpretations of the same data set are often possible.

Reidenbach *et al.* (1986) studied the rheology of foams under laminar and turbulent flow conditions. They described the rheology of N₂-hydroxypropyl guar (HPG) foam with a Herschel-Buckley model that depends on foam quality, gas type, and base-fluid rheology. The Herschel-Buckley model is a non-linear rheology model characterized by three parameters: the fluid consistency K , the flow index n , and the yield shear stress τ_0 . The model relates the shear stress τ experienced by the fluid to the shear rate $\dot{\gamma}$ as:

$$\tau = \tau_0 + K\dot{\gamma}^n \quad (7.5)$$

According to Reidenbach *et al.* (1986), the foam yield shear stress is only a function of quality for linear-gel-based foams. The yield stress significantly increases for qualities higher than 0.6, which is related to the large energy dissipation associated with the bubbles interactions at high foam qualities. Reidenbach *et al.* (1986) also assumed

that the foam flow index equals the flow index of the liquid phase, and the consistency index is a function of quality and gel loading, as seen in **Table 7.1** and Eq. 7.6:

$$\begin{cases} \tau_{0,foam} = 0.07\Gamma \text{ if } \Gamma \leq 0.6 \\ \tau_{0,foam} = 0.0002e^{9\Gamma} \text{ if } \Gamma > 0.6 \end{cases} ; \quad n_{foam} = n_0 \quad ; \quad K_{foam} = K_0 \exp(C_1\Gamma + 0.75\Gamma^2) \quad (7.6)$$

The assumption that n remains constant has been challenged by Khade and Shah (2004), who claimed that the flow index n should decrease as the flow consistency K decreases:

$$\begin{cases} n_{foam} = n_0 (1 - 2.1006\Gamma^{7.3003}) \\ K_{foam} = K_0 \exp(-1.9913\Gamma + 8.9722\Gamma^2) \end{cases} \text{ for } 20\text{lbm} / \text{Mgal guar} \\ \begin{cases} n_{foam} = n_0 (1 - 0.1535\Gamma^{6.5152}) \\ K_{foam} = K_0 \exp(-2.3761\Gamma + 8.8830\Gamma^2) \end{cases} \text{ for } 30\text{lbm} / \text{Mgal guar} \\ \begin{cases} n_{foam} = n_0 (1 - 0.6633\Gamma^{5.168}) \\ K_{foam} = K_0 \exp(-0.4891\Gamma + 5.6203\Gamma^2) \end{cases} \text{ for } 40\text{lbm} / \text{Mgal guar} \end{cases} \quad (7.7)$$

Valkó and Economides (1992, 1997) proposed an alternative approach using a volume-equalized power-law model to describe polymer-based foams. In their formulation, volume fraction is the key variable for fluid flow, irrespective of the constituents of the internal phase. For rheology purposes, they assimilated the addition of proppant as a mere addition to the internal phase, by introducing an equivalent foam quality as the volume fraction of gas and proppant altogether. Harris *et al.* (1991) first implemented this approach in the field; proposing a constant internal-phase design in which the gas fraction is reduced as proppant is injected. Their strategy yielded more predictable wellhead treating pressures that used less hydraulic horsepower.

7.3.3.2 In-House Experimental Work

To complement the few data sets available in the literature, we decided to design and build a new laboratory apparatus to measure foam rheology and stability over time (Ribeiro and Sharma 2012). As discussed later in Section 7.4.2, the unique feature of this apparatus is to combine multi-phase fluid-loss and rheology measurements. A simplified schematic of the system is provided in **Fig. 7.11**. It consists of an 850-cc closed-loop system in which the fluid is prepared and circulated at fracturing conditions. The foam-loop includes a foam generator (in-line screen), a circulating pump (high-flow-rate gear pump), a mass flow meter, and backpressure and reducing regulators (denoted by BPR and RR, respectively). Our rheology setup is comparable to the apparatus introduced by Hutchins and Miller (2005), and the reader is encouraged to refer to Ribeiro and Sharma (2012) for a more detailed description of the apparatus. The main steps of the laboratory procedures are also presented in Section 7.4.2.

Fig. 7.12 presents rheology data for N₂ foams with qualities ranging from 0 to 0.7. For the experiments presented here, the base gel was 30 lbm/Mgal linear guar; the temperature was 80 °F; the pressure in the foam loop was 1000 psi; and the flow rate was controlled by the circulating pump. We measured the flow rate and the pressure drop occurring along a segment of the foam loop, and we converted these measurements into apparent viscosity versus shear rate, as shown in Fig. 7.12.

Our measurements support the fact that guar-N₂ foams are shear-thinning, as the apparent viscosity decreases when the shear rate increases (regardless of quality). At every shear rate, foam viscosity increases as quality increases. The increase in viscosity is more dramatic as the quality goes from 0.48 to 0.6. This is in agreement with the widely

known observation that foam viscosity surges once the interactions between gas bubbles become dominant and cause large energy dissipations.

We further compared our viscosity measurements to the data published by Reidenbach *et al.* (1986) and Khade and Shah (2004), which are references widely accepted in the industry. **Fig. 7.13** shows the apparent viscosity measured at a stabilized shear rate of 100 s^{-1} for 30 lbm/Mgal guar-N₂ foams of different qualities. The first set of data is taken from Table 1 of Reidenbach *et al.* (1986). These correlations were obtained with HPG-N₂ foam circulated in a foam loop at ambient temperature and at a pressure of 1000 psi. Based on these correlations, a 30 lbm/Mgal HPG-N₂ foam is characterized as follows: $n=0.4788$, $C_1=1.32$, and $K=0.0065 \text{ lbf}\cdot\text{min}^n/\text{ft}^2$. The apparent viscosity was then calculated from the equation presented in Table 1. The second data set is from Table 2 of Khade and Shah (2004). The rheology data correspond to a 30 lbm/Mgal guar-N₂ foam circulating in a loop set at a temperature of 100 °F and a pressure of 1000 psi.

As shown in Fig. 7.13, our rheology data are consistent with other published data. We made similar comparisons under different testing conditions to validate our apparatus and laboratory protocols for foam generation and circulation. We hope that the test protocols and procedures we proposed will contribute to the adoption of a standard technique to experimentally evaluate the rheology of multi-phase fluids.

7.3.3.3 Influence of Proppant Concentration

The impact of proppant concentration on foam rheology is a topic open to discussion, as the literature of this subject is virtually nonexistent. The constant-internal-phase assumption proposed by Harris *et al.* (1991) and Valkó and Economides (1997) assimilated the proppant as part of the internal phase. They considered volume fraction as the key variable for fluid flow, irrespective of the composition of the internal phase. This

approach assumes that proppant settling is negligible and does not modify the flow pattern. An alternative approach is to consider that the foam has its own viscosity, and the addition of proppant modifies it, as this is typically assumed in single-phase slurry flow. The proppant effect on rheology is represented by an empirical correlation, such as:

$$\begin{cases} n_{prop} = n_{fluid} \exp(n_c \times c) \\ K_{prop} = K_{fluid} \exp(k_c \times c) \end{cases} \quad (7.8)$$

For stable foams, n_{fluid} and K_{fluid} are the rheology parameters at a given foam quality. Additional experimental work is required to properly characterize the flow behavior of foam slurries.

7.4 CHALLENGES IN MEASURING MULTI-PHASE LEAK-OFF COEFFICIENTS

The rate of fluid leak-off is one of the most critical parameters involved in fracture design, as it directly impact production by affecting fracture geometry, fracture-closure time, and proppant distribution. Fracture productivity is largely related to the amount of damaging fluid placed into the formation. If an operator overestimates leak-off, the pumping rate may be unnecessarily high and cause excessive pump pressures. Alternatively, an operator is likely to lower the pumping rate if he underestimates leak-off. In this case, the fracturing fluid may not be able to propagate large quantities of proppant. As the proppant accumulates and the frictional pressure drop surges near the perforations, a premature screenout may occur and cause a premature job termination. Although the importance of fluid leak-off is widely acknowledged by the industry, the understanding of multi-phase fluid-loss is very limited. This section identifies and explores the experimental challenges that must be overcome to gain a better understanding of the behavior of energized fluids.

7.4.1 Field Determination

Fluid leak-off is typically evaluated from a mini-frac (or leak-off) test, in which one injects a small volume of fluid at a pressure sufficient enough to initiate a fracture. Once the pressure breakdown is observed, the well is shut-in and the pressure response is monitored over time. The analysis of the pressure decline provides an average leak-off value that is representative of the region of the reservoir in contact with the fracture volume.

Data interpretation of leak-off tests with energized treatments is not trivial. Liquid and gas leak-off occur at different rates, but only one pressure response is available. The problem is ill-posed because we have two variables ($C_{w,l}$ and $C_{w,g}$) for only one equation (the pressure response). In addition, the pressure response is often measured from surface gauges, so the downhole pressure is obtained by estimating the weight of the fluid column in the wellbore. While this approach may be reasonable for incompressible fluids, the compressibility effects complicate the analysis of the pressure response in energized treatments.

For both non-energized and energized treatments, mini-frac tests have several shortcomings in unconventional formations. In shales, the matrix permeability is not necessarily the key parameter for fluid leak-off because leak-off primarily occurs through natural fractures. Mini-frac tests are short duration tests that span a small fraction of the reservoir, so the area of investigation is not likely representative of the reservoir. Thus, if the induced fracture does not intersect any major fractures, the average leak-off will be underestimated, whereas it will be overestimated if the induced fracture intersects an abnormally large number of natural fractures. Also, the timing is critical because the opening of pre-existing fractures may require a larger pressure than the one experienced

during the mini-frac test. In this case, the leak-off is pressure-dependent and highly location-dependent; therefore, the use of a “Carter-type” leak-off model may lead to large discrepancies.

7.4.2 Experimental Determination

In the laboratory, the determination of dynamic multi-phase leak-off coefficients is challenging because it involves two experimental tasks that are not well understood by the industry: the generation of stable foams at high pressures, and the measurement of dynamic leak-off coefficients. These challenges have hindered the development of experimental studies on multi-phase leak-off.

As mentioned in Section 7.3.4, we developed a new laboratory apparatus that enables us to (1) measure foam rheology and stability, (2) measure the liquid and gas dynamic leak-off coefficients, and (3) evaluate the rock regain permeability during flowback (Ribeiro and Sharma 2012). The foam loop presented in Section 7.3.4 is connected to a fluid-loss cell, which is a Hassler-type core holder with a special end-design allowing for dynamic testing of fluid invasion into core samples (**Fig. 7.14**). In conventional core holders, the flow injection is parallel to the core. Instead, we used a core holder with a flow-through slot that allows us to flow the fracturing fluid in the direction perpendicular to the core face. This flow pattern is intended to mimic the flow path experienced by the fracturing fluid within the fracture.

All the experiments presented in Section 7.5 were performed for at least 90 minutes at ambient temperature (about 80 °F). We used Berea and Nugget sandstone samples, ranging from 0.5 to 400 mD, to evaluate the effects of the rock permeability. The base fluid for both linear gels and nitrogen foams was a blend of guar powder mixed with a 3% by weight potassium chloride solution. We added surfactants (provided by BJ

Services) to lower the surface tension between the internal gas phase and the external liquid phase. We used the following procedures to generate foam and measure leak-off:

1. Load the circulating loop with the base-fluid at a pressure P_{loop} by setting up the BPR at that particular pressure.
2. Load the accumulator with N_2 (or CO_2) and pressurize the gas at a pressure slightly above P_{loop} . A RR connects the accumulator (upstream side) to the loop (downstream side).
3. Open the valve downstream of the RR, and apply a pressure at the RR slightly above the BPR pressure. The gas slowly displaces the base-fluid initially present in the loop.
4. Collect the amount of liquid coming out of the loop, monitor the density of the fluid via the mass flow meter, and inspect the foam texture via the high-pressure view cell.
5. Close the valve downstream of the RR, and set the circulating pump at high speed to promote turbulent mixing through the foam generator.
6. Repeat steps 3 to 6 to safely ensure foam mixing. The foam quality increases at each step as gas displaces some of the liquid phase out of the loop.
7. Stop steps 3 to 6 when the quality of interest is reached. The quality is calculated from the density measurements provided by the mass flow meter.
8. Circulate the foam at the shear rate of interest and monitor the pressure drop through the in-line differential pressure transmitter.

9. Once the foam is stable, start the leak-off test by closing the bypass and opening the valve connecting the loop to the fluid-loss cell.
10. Monitor the amount of gas and liquid exiting the core over time.
11. Conduct a regain permeability test to evaluate the fluid-induced damages.

The leak-off tests presented in this dissertation were conducted at ambient temperature and with a back pressure set to zero (the pressure downstream of the core sample was atmospheric); therefore, the foam leak-off results presented in Section 7.5 may not be quantitatively correct under reservoir conditions. However, the underlying mechanisms of leak-off and the overall trends and conclusions should remain valid.

7.5 MULTI-PHASE LEAK-OFF COEFFICIENTS

The petroleum literature contains numerous experimental studies on the leak-off behavior of linear gels, and the reader may refer to the summaries compiled by Penny and Conway (1989) and McGowen and Vitthal (1996a, 1996b). However, very little data is available for multi-phase fluids. Until recently, Harris conducted the only systematic published multi-phase leak-off study on N₂ (Harris 1985) and CO₂ foams (Harris 1987). We supplemented his work by presenting the first systematic experimental study of multi-phase fluid-loss for fracturing fluids under dynamic conditions.

The objective of this study is not to build a comprehensive library of foam leak-off coefficients. Rather, our intent was to improve the general understanding of the multi-phase leak-off process, providing a springboard for further research, and encourage researchers in both academia and the industry to study this subject more closely. For practical purposes, the reference values we provide in Section 7.5.1 may be scaled to estimate multi-phase leak-off in different reservoirs.

7.5.1 In-House Experimental Results

Under all conditions, foams showed superior fluid-loss control properties than linear gels, regardless of the foam quality (Ribeiro and Sharma 2012). As seen in **Fig. 7.15**, the different foam formulations (which contain a gelling agent in the liquid phase) built a competent filter-cake on top of the rock surface. The thick, polymer-rich, cake constitutes a low-permeability barrier that impedes the flow of gas and liquid. The ability of the foam to form a rapid wall-building filter-cake is critical in reducing the fluid-loss. The leak-off coefficient data do not capture this transient behavior, so we would also refer to spurt-loss data when evaluating the fluid-loss properties of a fluid. Under all the testing conditions reported here, energizing the fracturing fluid has reduced the total amount of fluid lost into the formation.

Fig. 7.16 indicates a clear reduction in liquid leak-off as quality increases. This observation is intuitive because less liquid is used at higher foam qualities. Additionally, the invasion of gas into the porous medium reduces liquid invasion because of relative permeability effects. When compared to the non-energized leak-off, the liquid leak-off decreased by a factor of ten in the 55-mD case, and by a factor of three in the 1-mD case. It should be noted that *outlet* refers to the downstream side of the rock sample, which represents the reservoir, whereas *inlet* refers to the upstream side of the rock sample, which represents the fracture.

Figs. 7.17 and **7.18** show the ability of the free gas phase to leak-off under various testing conditions. To the best of our knowledge, this work presented the first quantitative study of dynamic gas leak-off over time. It establishes the ability of the gas bubbles to break from the foam structure and to flow through the porous medium by a mechanism other than solubility. **Fig. 7.17** seems to indicate that gas leak-off increases as quality

increases, at least in the lower range of foam qualities. At qualities higher than about 60%, the gas leak-off seems to stabilize or to even decrease. This behavior might be explained by the fundamental change occurring within the fluid at the microscopic scale. At qualities above 50% or so, the interactions between gas bubbles become preponderant, thereby increasing the internal friction and the viscosity of the foam. There is nonetheless some scatter in the data at qualities above 60%, and it is premature to conclude that the gas leak-off decreases as inlet quality increases at high qualities. Additional tests at high qualities and at high back pressures are needed to further investigate this behavior.

Fig. 7.18 indicates that the outlet quality is always enriched in the liquid phase, as all the data points lie under the unit slope. Figs. 7.16 to 7.18 clearly show the effect of the foam quality on multi-phase leak-off, and the data seem to follow some general trends. While it is still premature to extend the general trends to lower rock permeabilities, this is encouraging when deriving empirical correlations for both the liquid and the gas leak-off coefficients. A systematic comparison between the bubble size distribution and the pore size distribution would benefit our understanding of the physics of the multi-phase filtration process.

7.5.2 Comparison with Published Data

We compared our N₂ foam leak-off data with the data published by Harris (1985) and Penny *et al.* (1985), which are the only known references on N₂ foam leak-off. Harris (1985) measured leak-off data with a semi-static apparatus, which is not representative of the flow experienced in a fracture, and Penny *et al.* (1985) used a static apparatus. This significantly differs from our study, as we present truly dynamic leak-off data. Also, former researchers used a linear HPG base-fluid that is different from the linear guar

formulation we used. Despite these limitations, we compare the data to see whether our findings are consistent.

Table 7.1 compares our leak-off data on guar-N₂ foams and linear gels to the data on HPG-N₂ foams reported by Harris (1985) and Penny *et al.* (1985). A direct comparison with public data is cumbersome because there is very little published data for foam leak-off, and there are a multitude of parameters. The first set of data is taken from Table 1 in Harris (1985), and the second set of data is taken from Figure 10 in Penny *et al.* (1985). The main experimental conditions are included in Table 7.1. The dynamic leak-off coefficients we measured were typically lower than the values reported previously. They are nonetheless of the same order of magnitude, and the overall trends are consistent.

7.6 CONCLUSIONS

This chapter highlighted some of the unique properties of foams, which have a significant impact on the hydrocarbon production. It is thus critical to characterize these fluids accurately using experimental data, in order to take advantage of these properties when designing the fracturing treatment. The following properties make the use of foams particularly attractive in fracturing:

1. *Fluid expansion*: As the fluid temperature increases, the fluid volume increases; therefore, a smaller volume of fluid at the wellhead is required to generate the same downhole fracture volume.
2. *Leak-off*: Foams provide superior fluid-loss control without using excessive amounts of gelling agents and additives. The filter-cake is supplemented by the presence of gas bubbles (non-wetting phase), which reduce liquid-flow into the

porous medium. A smaller volume of fluid (downhole) is required to generate the same fracture volume downhole.

3. *Solubility*: When soluble components are used in foams, a larger fraction of the energized component invades the reservoir. As pressure decreases, the energized component enhances fluid clean-up in and around the fracture.
4. *Flow behavior*: Foams offer a wide range of viscosities without using excessive amounts of gelling agents and additives. The transition from the comingled to the foam regime is unique; it provides some flexibility when designing foam treatments.

By design, foams offer properties similar to any gelled water-based fluids in terms of fracture creation, proppant transport, and fracture conductivity; therefore, the decision to use foams primarily depend on formation damage and fluid recovery. As discussed in Chapter 8, foams are preferred over water-based fluids when the damage induced by the latter is *too* detrimental to hydrocarbon production. Obviously, costs, safety concerns, and environmental considerations also play important roles in fluid selection. Typically, the use of energized fluids requires larger capital expenditures than the use of water-based fluids, which largely explains why energized fluids are not used as frequently despite their apparent advantages over water-based fluids. The following chapter helps us decide when - and why - energized fluids should be preferred over traditional fluids in certain reservoirs.

Table 7.1: Rheology correlation values for N₂ foams (from Reidenbach *et al.* 1986).

HPG Load (lbm/Mgal)	n (-)	K (lbf-sec ^{n} /ft ²)	C_1 (-)
0	1	0.00002	3.6
10	0.75	0.0053	2.1
20	0.607	0.00256	1.7
40	0.45	0.0152	1.2

Table 7.2: Comparison of foam leak-off data.

N ₂ foam leak-off data (SPE 139622) $\Gamma=0.6, T=80^\circ\text{F}, \gamma=20\text{s}^{-1}, \text{loading}=30\text{lbm/Mgal}$			Linear guar leak-off data (SPE 139622) $T=80^\circ\text{F}, \gamma=40\text{s}^{-1}, \text{loading}=30\text{lbm/Mgal}$		
k (mD)	ΔP (psi)	C_{wtotal} (ft/ $\sqrt{\text{min}}$)	k (mD)	ΔP (psi)	C_{wtotal} (ft/ $\sqrt{\text{min}}$)
1.5	450	0.0013	1.5	550	0.0032
1.5	950	0.0041	1.5	1000	0.0033
55	500	0.0048	25	500	0.0167
55	950	0.0053	25	1000	0.0178
390	465	0.0089	390	550	0.051
390	800	0.0163	390	1000	0.055
N ₂ foam leak-off data (SPE 11065) $\Gamma=0.75, T=75^\circ\text{F}, \gamma=20\text{s}^{-1}, \text{loading}=20\text{lbm/Mgal}$			N ₂ foam leak-off data (SPE 12486) $\Gamma=0.75, T=75^\circ\text{F}, \gamma=0\text{s}^{-1}, \text{loading}=20\text{lbm/Mgal}$		
k (mD)	ΔP (psi)	C_{wtotal} (ft/ $\sqrt{\text{min}}$)	k (mD)	ΔP (psi)	C_{wtotal} (ft/ $\sqrt{\text{min}}$)
0.3	500	0.00069	0.1	1000	0.0008
0.3	1000	0.00134	1	1000	0.0025
13	1000	0.0112	10	1000	0.0078
18.6	500	0.0108	55	1000	0.018
17	200	0.0097	100	1000	0.029
137	200	0.0265	390	1000	0.048

*In SPE 11065, Harris (1985) used a semi-static leak-off apparatus, in which the shear rate was estimated to be 20 s^{-1} .

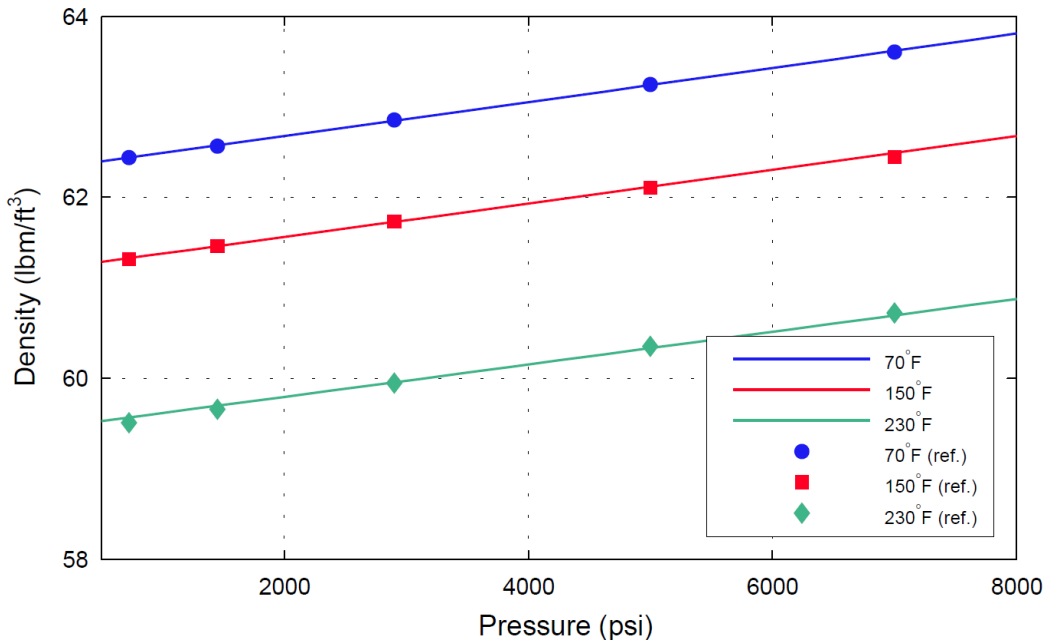


Figure 7.1: Density of pure water phase: comparison between our model and the experimental data compiled in Sandler (2007).

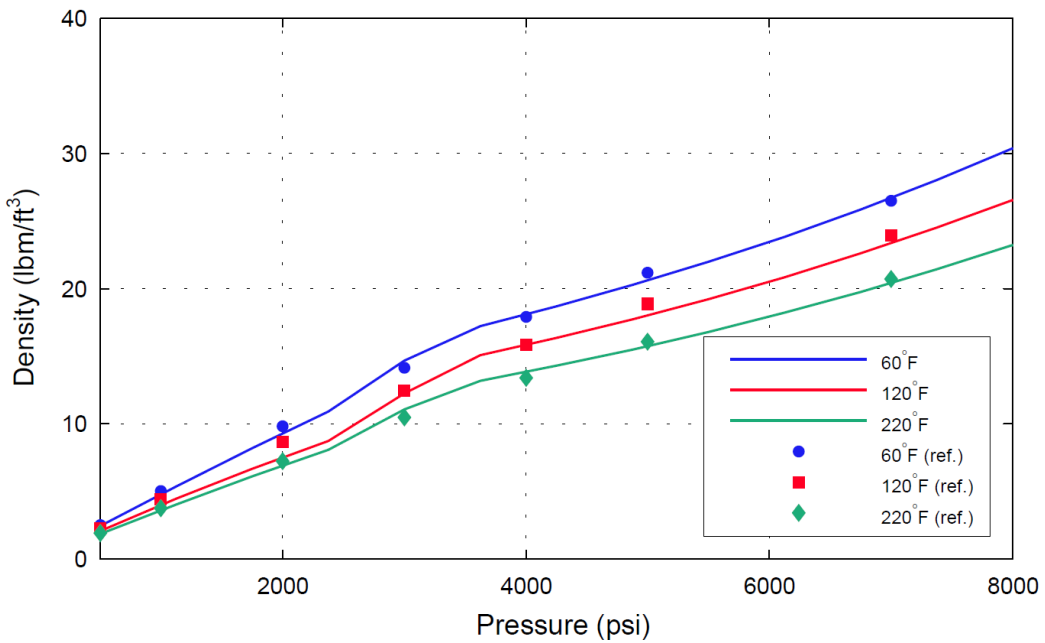


Figure 7.2: Density of pure N₂ phase: comparison between our model and the experimental data provided by Saddington and Krase (1934).

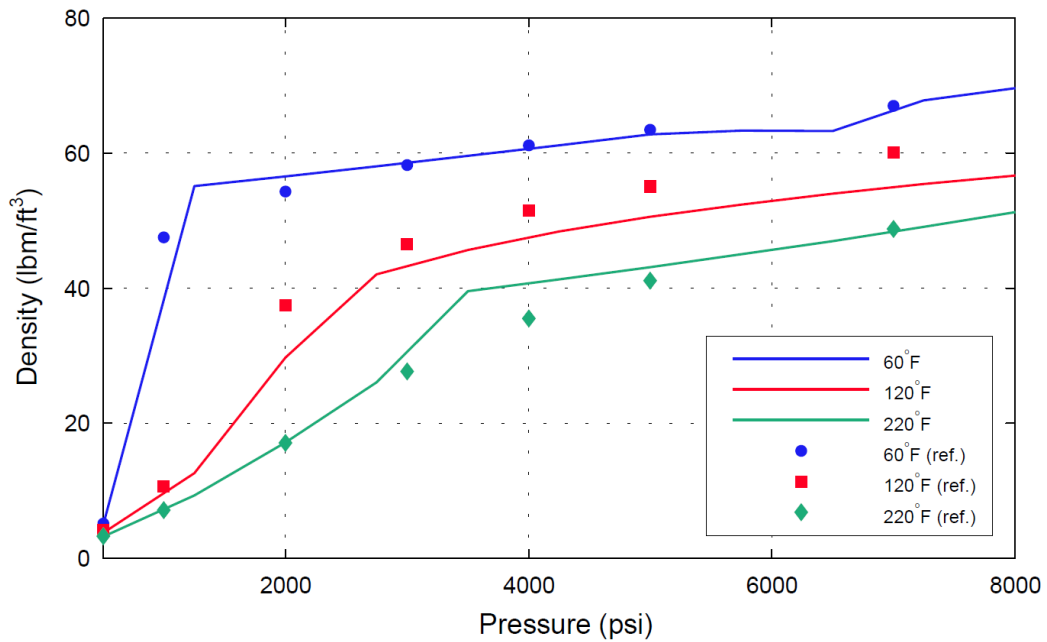


Figure 7.3: Density of pure CO₂ phase: comparison between our model and the data obtained with *PVTsim*.

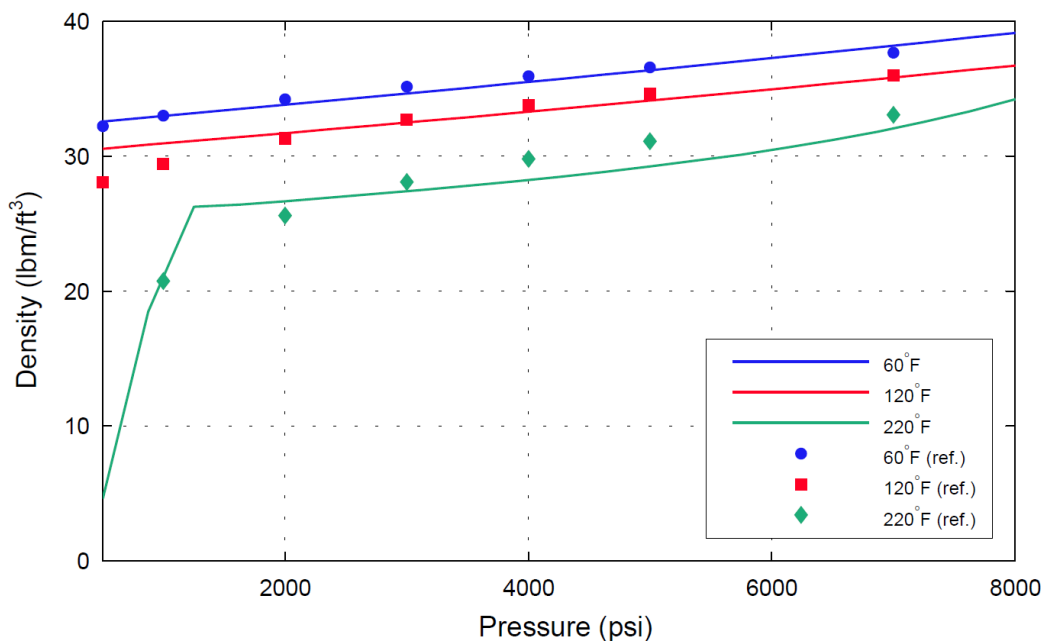


Figure 7.4: Density of a LPG mixture of 90% of C₃ and 10% of n-C₄ per volume: comparison between our model and the data obtained with *PVTsim*.

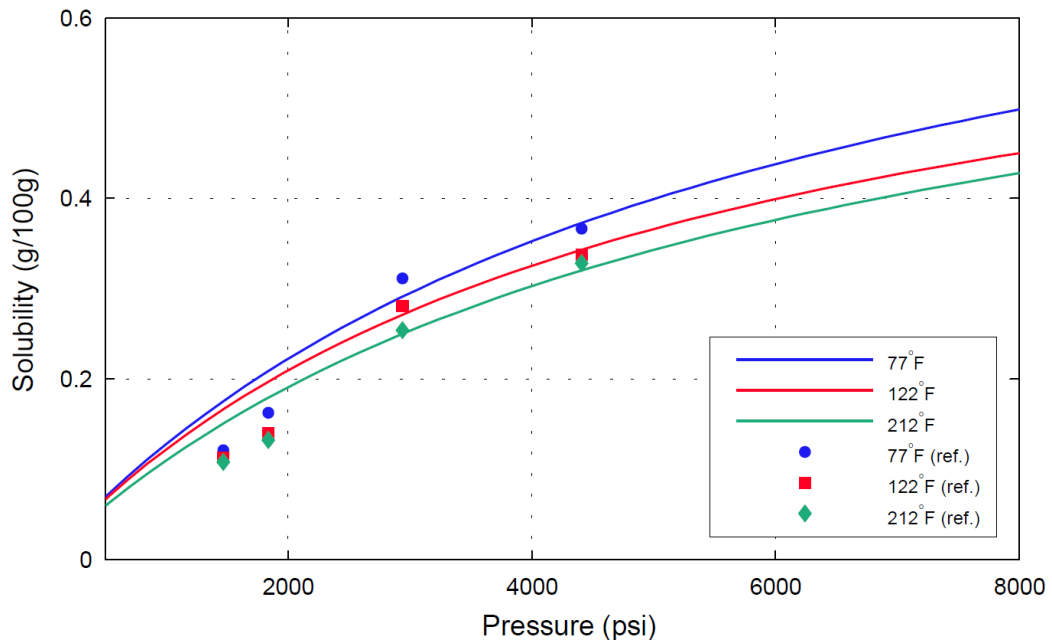


Figure 7.5: Solubility of N₂ in water: comparison between our model and the experimental data provided by Goodman and Krase (1931).

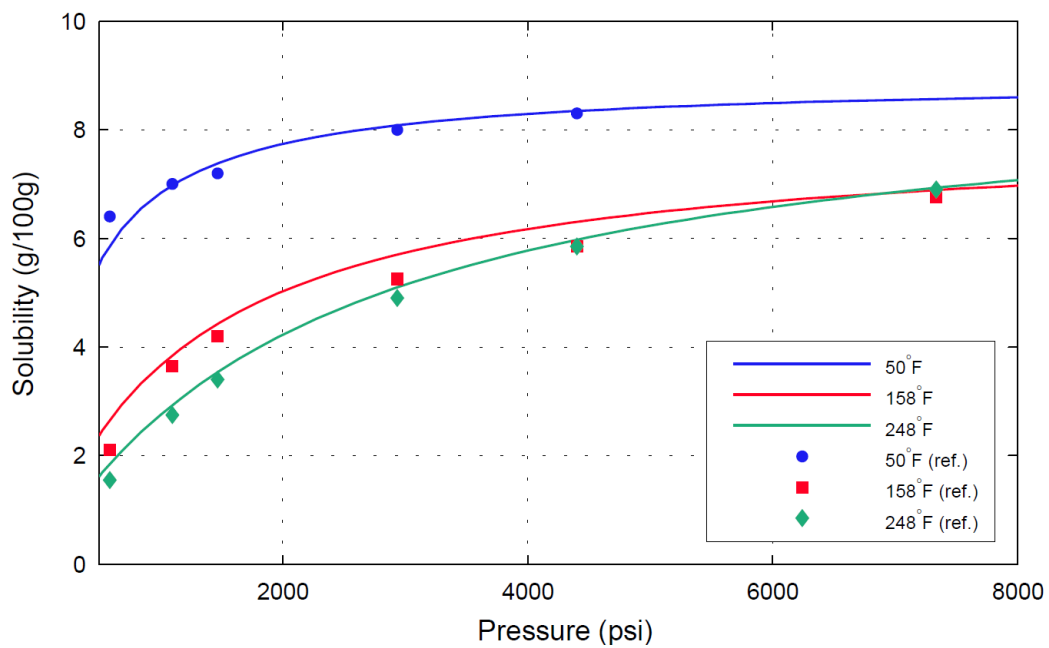


Figure 7.6: Solubility of CO₂ in water: comparison between our model and the experimental data provided by Rumpf *et al.* (1994).

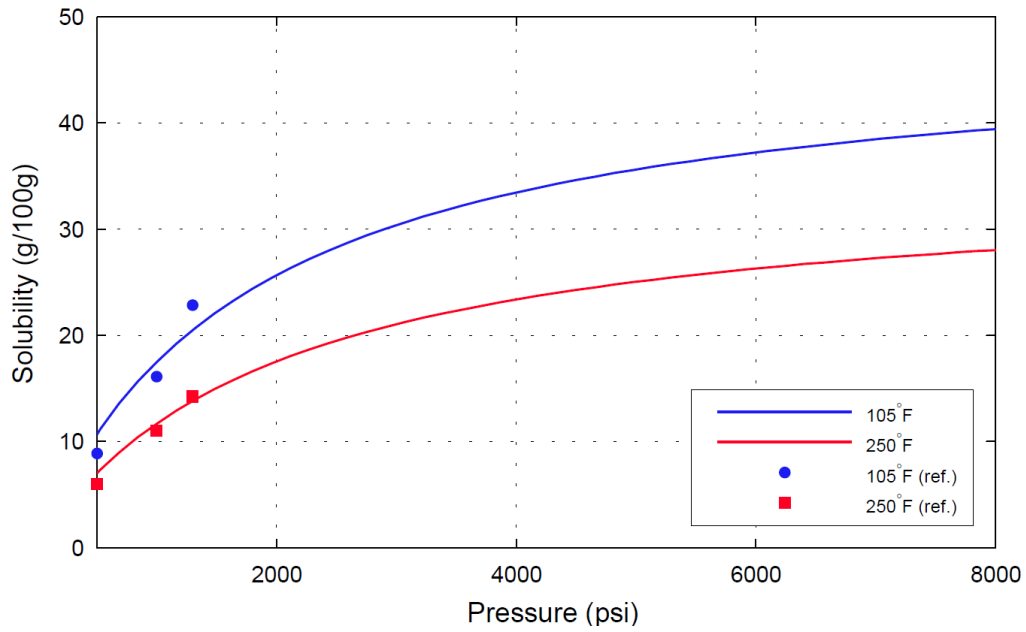


Figure 7.7: Solubility of CO₂ in an equimolar mixture of water and methanol: comparison between our model and the experimental data provided by Xia *et al.* (2004).

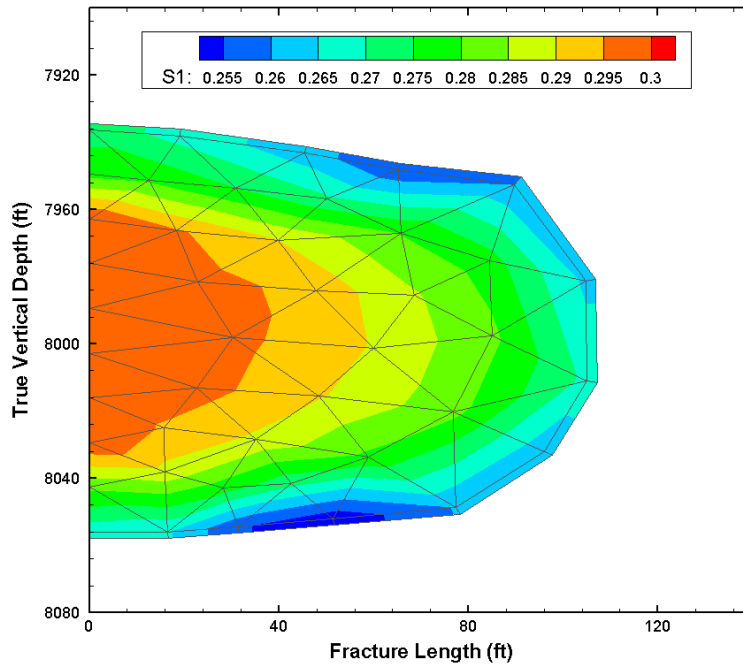


Figure 7.8: Water saturation for stable 0.7-quality CO₂ foam after 5 min.

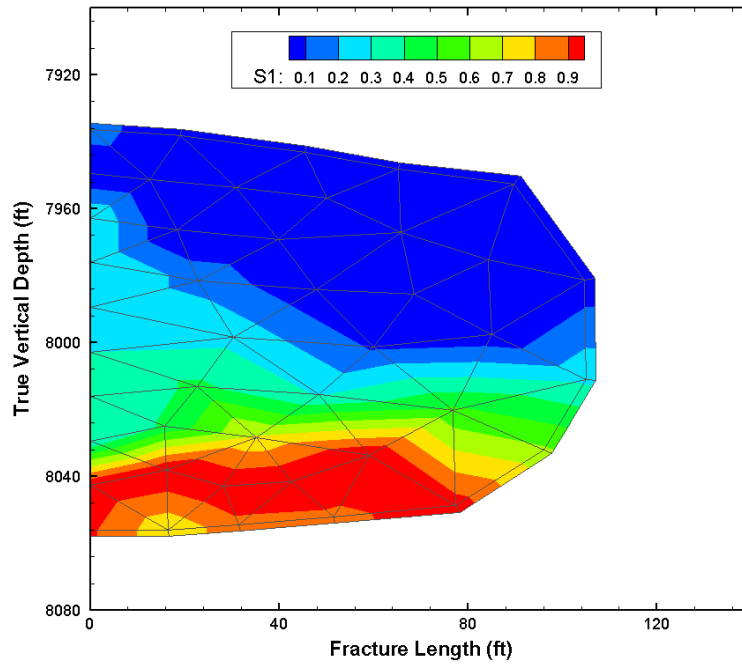


Figure 7.9: Water saturation for unstable 0.7-quality CO₂ foam after 5 min.

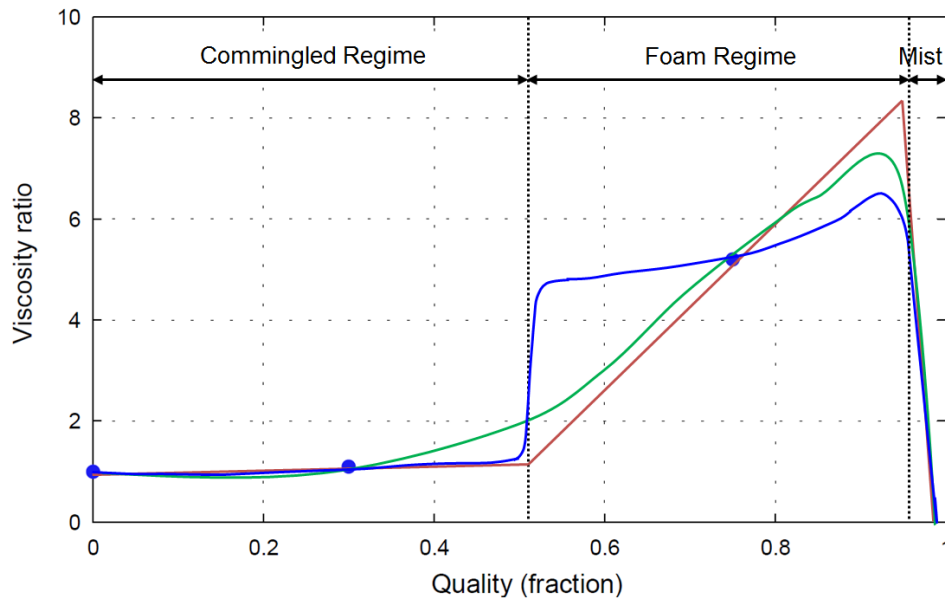


Figure 7.10: Illustration of the three flow regimes: commingled, foam, and mist. The transition between the regimes can be vague, and the scarcity of rheology data does not allow a proper characterization of the fluid behavior over a large spectrum. Often, multiple interpretations are possible because of the limited number of data points (indicated by the blue markers).

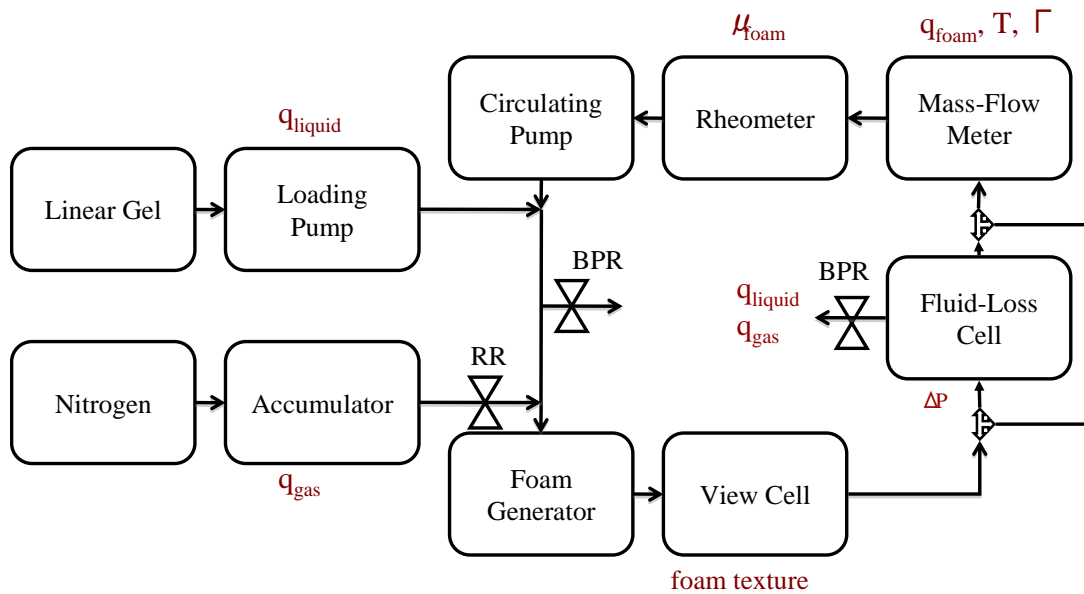


Figure 7.11: Simplified schematic of the foam-loop system, with relevant measurements shown in red.

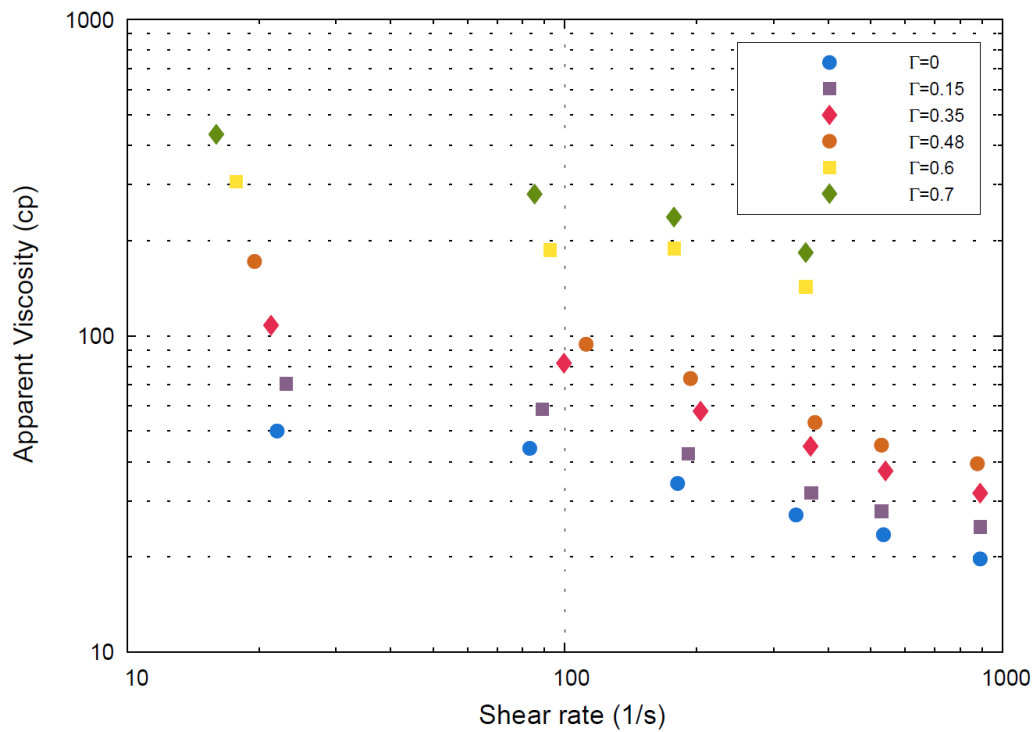


Figure 7.12: N_2 foam apparent viscosity versus shear rate for multiple form qualities.

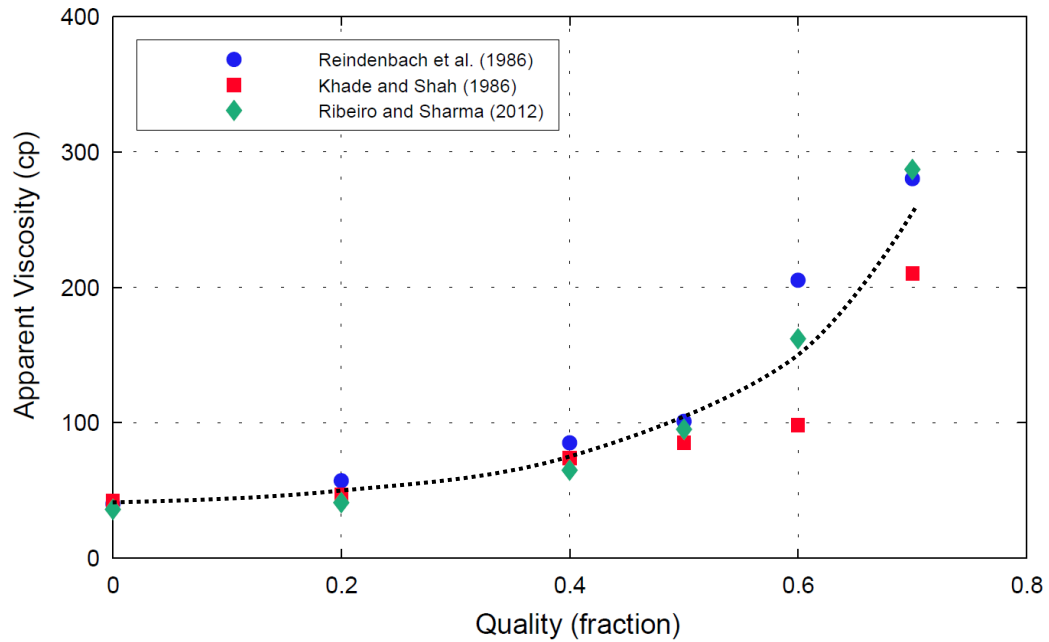


Figure 7.13: Comparison of N_2 foam apparent viscosity measurements for multiple qualities (at a shear rate of 100 s^{-1}).

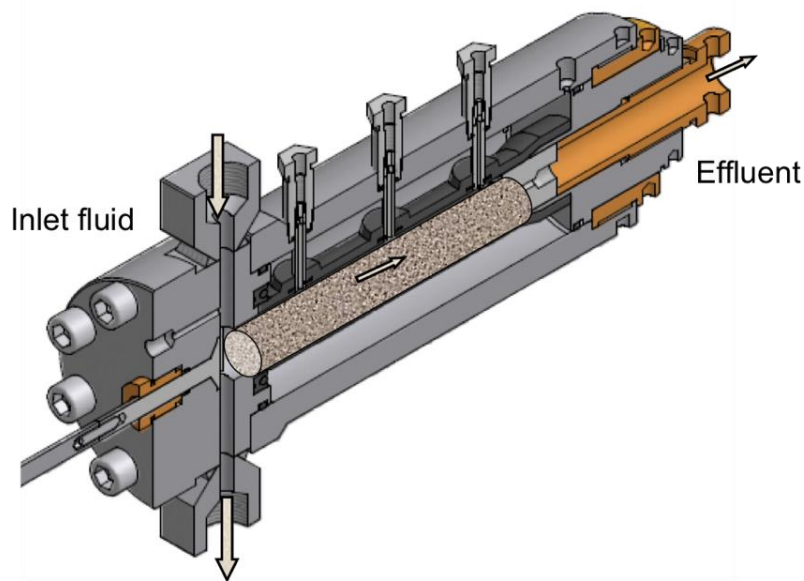


Figure 7.14: Drawing of the fluid-loss cell (courtesy of TEMCO). The thick arrows indicate the direction of flow imposed in the circulating loop, and the thin arrows indicate the direction of fluid leak-off.

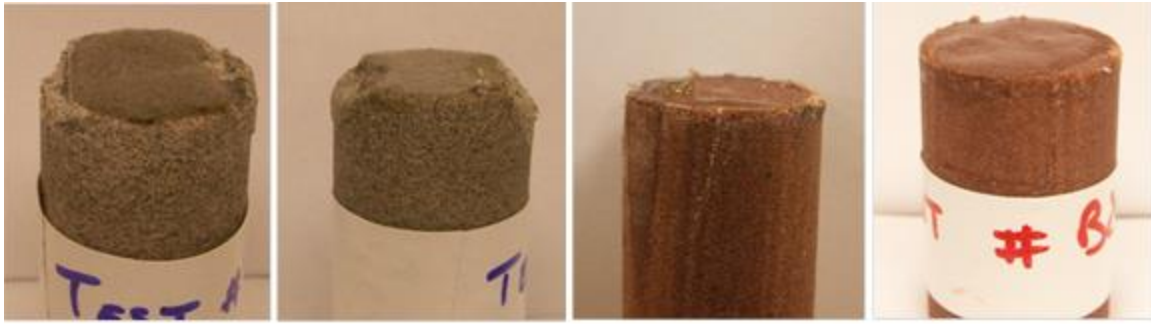


Figure 7.15: External filter-cakes observed after leak-off tests on Berea (left side) and Nugget (right side) sandstone samples. The ability of the fluid to form a rapid polymer-rich filter-cake is critical in reducing fluid-loss.

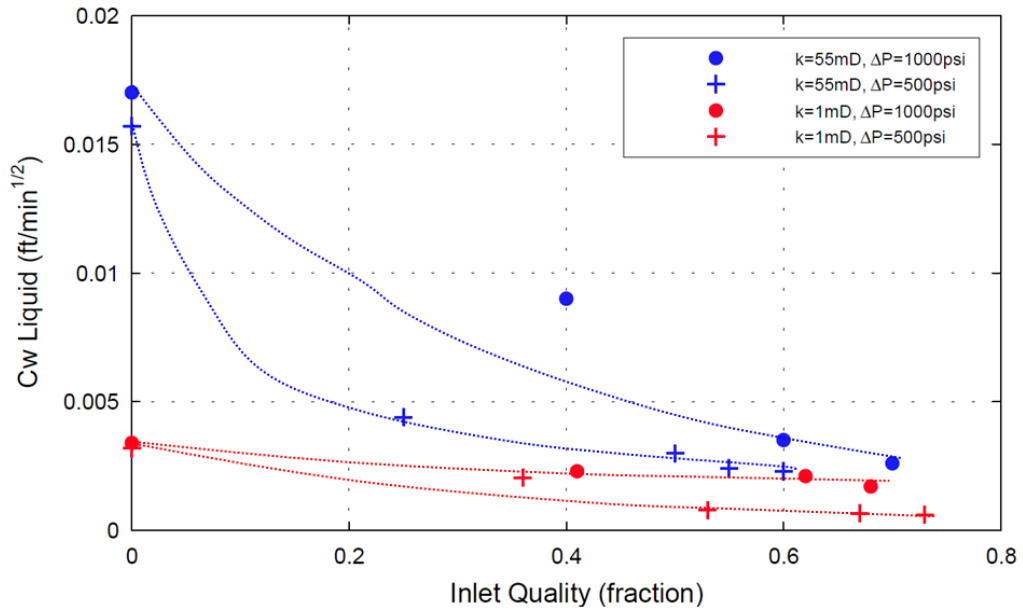


Figure 7.16: Effect of foam quality on liquid leak-off under various testing conditions. A significant decrease in liquid leak-off limits the fluid-induced damage.

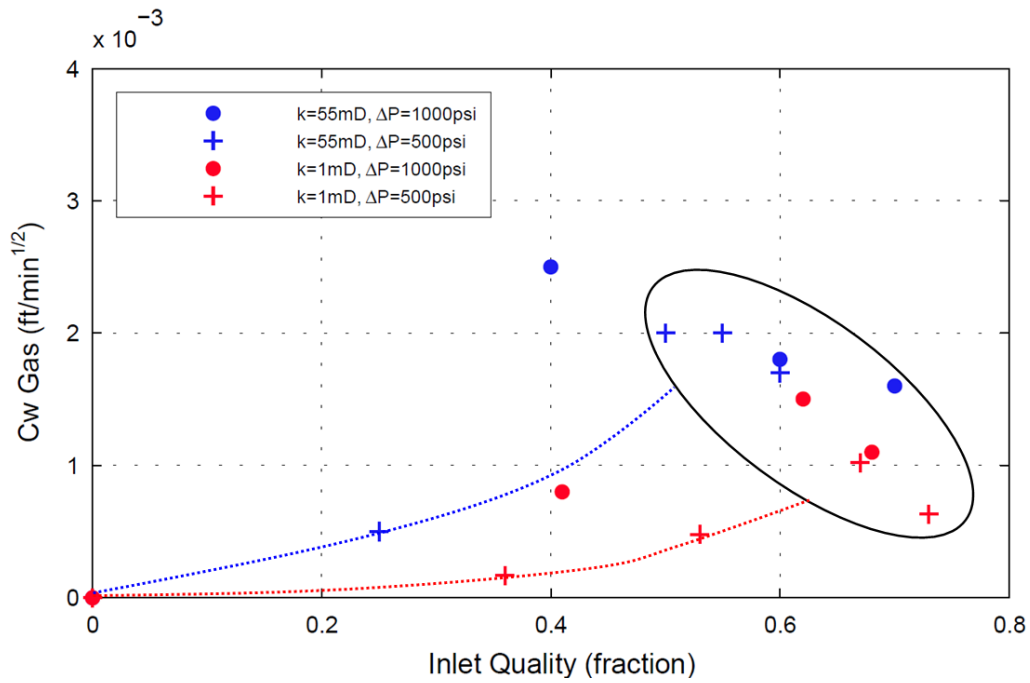


Figure 7.17: Effect of foam quality on gas leak-off under various testing conditions. The behavior at high qualities is poorly understood.

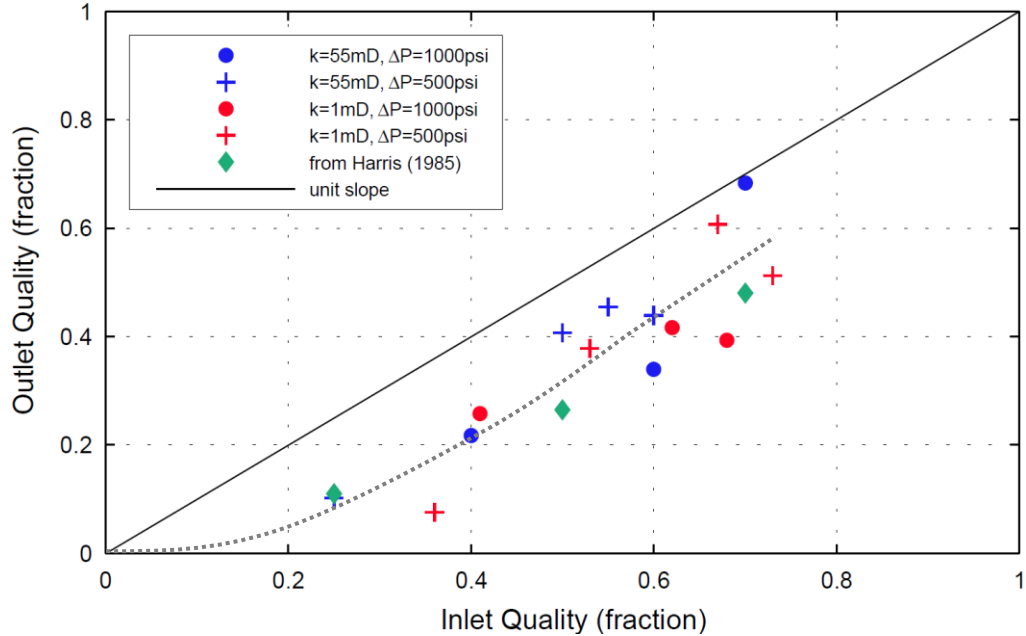


Figure 7.18: Outlet composition enriched in the liquid phase as the result of filtration.

NOMENCLATURE

$C_{w,g}$	= leakoff coefficient of the gas phase, ft/ $\sqrt{\text{min}}$	P_r	= reduced pressure (P/P_c)
$C_{w,l}$	= leakoff coefficient of the liquid phase, ft/ $\sqrt{\text{min}}$	P_0	= reference pressure, psi
C_1	= coefficient defined in Table 7.1	R	= gas constant, ft-lbf/(lbm- $^{\circ}\text{R}$)
k_c	= coefficient in Eq. 7.8	T	= fluid temperature, $^{\circ}\text{F}$
K	= flow consistency index, lbm-min $^n/\text{ft}^2$	T_c	= critical temperature, $^{\circ}\text{F}$
K_{fluid}	= flow consistency index of the clean fluid, lbm-min $^n/\text{ft}^2$	T_r	= reduced temperature (T/T_c)
K_{foam}	= flow consistency index, lbm-min $^n/\text{ft}^2$	T_0	= reference temperature, $^{\circ}\text{F}$
K_{prop}	= flow consistency index of the slurry, lbm-min $^n/\text{ft}^2$	x_i	= mass fraction of component i in the liquid phase
K_0	= flow consistency index of the base-fluid, lbm-min $^n/\text{ft}^2$	$x_{i,sol}$	= solubility of component i in the liquid phase
M_w	= molecular weight, atomic mass unit	Z	= compressibility factor
n	= flow behavior index	Greek Symbols	
n_c	= coefficient in Eq. 7.8	α	= Langmuir coefficient in Eq. 7.4
n_{fluid}	= flow behavior index of the clean fluid	α_i	= coefficients defined in Eq. 7.3
n_{foam}	= flow behavior index	α_T	= thermal expansion, $1/^{\circ}\text{F}$
n_{prop}	= flow behavior index of the slurry	β	= Langmuir coefficient in Eq. 7.4
n_0	= flow behavior index of the base-fluid	β_P	= isothermal compressibility, $1/\text{psi}$
P	= fluid pressure, psi	γ	= shear rate, s^{-1}
P_c	= critical pressure, psi	Γ	= foam quality (volume fraction)
		ρ	= density, lbm/ ft^3
		ρ_0	= density of reference at (P_0, T_0), lbm/ ft^3
		τ	= yield shear stress, lbf/ ft^2
		$\tau_{0,foam}$	= yield shear stress of foam, lbf/ ft^2
		τ_0	= yield shear stress of the base-fluid, lbf/ ft^2

REFERENCES

- Beggs, D.H. and Brill, J.P. 1973. A Study of Two-Phase Flow in Inclined Pipes. *J. Pet Tech* **25**(5): 607-617. SPE 4007-PA.
- Friehauf, K.E. and Sharma, M.M. 2009. A New Compositional Model for Hydraulic Fracturing With Energized Fluids. *SPE Prod & Oper* **24**(4): 562-572. SPE 115750-PA.
- Gidley, J.L., Holditch, S.A., Nierode, D.E., and Veatch, R.W. Jr. 1989. *Recent Advances in Hydraulic Fracturing*. Monograph Series **12**, SPE, Richardson, Texas.
- Goodman, J.B and Krase, N.W. 1931. Solubility of Nitrogen in Water at High Pressures and Temperatures. *Ind. Eng. Chem*, **23**: 401-404
- Harris, P.C. 1985. Dynamic Fluid-Loss Characteristics of Nitrogen Foam Fracturing Fluids. *J. Pet Tech* **37**(11): 1847-1852. SPE 11065-PA.
- Harris, P.C. 1987. Dynamic Fluid-Loss Characteristics of CO₂-Foam Fracturing Fluids. *SPE Prod Eng* **2**(2): 89-94. SPE 13180-PA.
- Harris, P.C., Klebenow, D.E., and Kundert, D.P. 1991. Constant-Internal-Phase Design Improves Stimulation Results. *SPE Prod Eng* **6**(1): 15-19. SPE 17532-PA
- Hutchins, R.D. and Miller, M.J. 2005. A Circulating-Foam Loop for Evaluating Foam at Conditions of Use. *SPE Prod & Fac* **20**(4): 286-294. SPE 80242-PA.
- Khade, K. and Shah, S. 2004. New Rheological Correlations for Guar Foam Fluids. *SPE Prod & Fac* **19**(2): 77-85. SPE 88032-PA.
- Kovscek, A. and Radke, C. 1994. *Foams: Fundamentals and Applications in the Petroleum Industry*, Schramm, L., Editor, American Chemical Society, Washington D.C.
- Lestz, R.S., Wilson, L., Taylor, R.S., Funkhouser, G.P., Watkins, H., and Attaway, D. 2007. Liquid Petroleum Gas Fracturing Fluids for Unconventional Gas Reservoirs. *J Cdn. Pet Tech* **46**(12): 68-72.
- McGowen, J.M and Vitthal, S. 1996a. Fracturing-Fluid Leakoff Under Dynamic Conditions Part 1: Development of a realistic Laboratory testing Procedure. Paper SPE 36492 presented at the 1996 Annual Technical Conference held in Denver, Colorado, 6-9 October.
- McGowen, J.M and Vitthal, S. 1996b. Fracturing-Fluid Leakoff Under Dynamic Conditions Part 2: Effect of Shear Rate, Permeability and Pressure. Paper SPE 36493 presented at the 1996 Annual Technical Conference held in Denver, Colorado, 6-9 October.
- Penny, G.S. and Conway, M.W. 1989. *Recent Advances in Hydraulic Fracturing*. Monograph Series, SPE, Richardson, Texas **1**: 147-176.
- Penny, G.S., Conway, M.W, and Lee, W. 1985. Control and Modeling of Fluid Leakoff During Hydraulic Fracturing. *J. Pet Tech* **37**(6): 1071-1081. SPE 12486-PA.

- Reidenbach, V.G., Harris, P.C., Lee, Y.N, and Lord, D.L. 1986. Rheological Study of Foam Fracturing Fluids using Nitrogen and Carbon Dioxide. *SPE Prod Eng* **1**(1): 31-41. SPE 12026-PA.
- Ribeiro, L.H. 2012. Multi-Phase Fluid-Loss Properties and Return Permeability of Energized Fracturing Fluids. Master's Report, The University of Texas at Austin, Austin, Texas (May 2012).
- Ribeiro, L.H. and Sharma, M.M. 2012. Multi-Phase Fluid-Loss Properties and Return Permeability of Energized Fracturing Fluids. *SPE Prod & Oper* **27**(3): 265-277. SPE 139622-PA.
- Rumpf, B., Nicolaisen, H., and Maurer, G. 1994. Solubility of Carbon Dioxide in Aqueous Solutions of Sodium Chloride: Experimental Results and Correlation. *J. Solution Chem.* **23**(3): 431-448.
- Saddington, A.W. and Krase, N.W. 1934. Vapor-Liquid Equilibria in the System Nitrogen-Water. *J. Amer. Chem. Soc.* **56**: 353-361
- Sandler, S.I. 2006, *Chemical, Biochemical, & Engineering Thermodynamics, Fourth Edition*, John Wiley and Sons, New York City, New York.
- Standing, M.B. and Katz, D.L. 1942. Density of Natural Gases. *Trans. AIME* **146**(1): 140-149. SPE 942140-G.
- Taylor, R.S., Lestz, R.S., Bennion, D.B., Funkhouser, G.P., and Geddes, I.R. 2005. Rheological Evaluations of COMiscible Hydrocarbon Fracturing Fluids. Paper 2005-023 presented at the Canadian International Petroleum Conference, held in Calgary, Alberta, June 7-9.
- Valkó, P. and Economides, M.J. 1992. Volume Equalized Constitutive Equations for Foamed Polymer Solutions. *J. Rheol.* **36**(6): 1033-1055.
- Valkó, P. and Economides, M.J. 1997. Foam-Proppant Transport. *SPE Prod & Fac* **12**(4): 244-249. SPE 27897-PA.
- Xia, J, Jdecke, M, Prez-Salado Kamps, I, and Maurer, G. 2004. Solubility of CO₂ in (CH₃OH + H₂O). *J. Chem. Eng. Data* **49**(6): 1756-1759.

Chapter 8: Impact of Fluid and Reservoir Properties on Fracture Productivity: Identification of Key Parameters

In this chapter¹, we discuss the factors that are important in energized fracture design. The objective is to evaluate the impact of various fluids on fracture performance and to identify the fluid candidates that yield the highest hydrocarbon production. This chapter intends to answer common design questions, such as:

- When should we use energized fluids?
- Which energized component should we use?
- What is the optimum foam quality?
- What are the pumping requirements?

In the field, a trial-and-error approach can be used to optimize the pumping schedule, primarily by adjusting fluid rheology and proppant loading at each stage. A similar approach is not feasible for optimizing fluid selection, as the deployment of various fluid types would require unreasonably large capital expenditures and the development of new infrastructure. The use of the compositional model enables us to screen fracturing fluids and identify potential fracturing fluid candidates with minimal field testing, saving time and money. This modeling approach does not replace field trials; rather, it complements them. Once the best fluid candidates have been identified with the modeling tool, these fluid formulations can be implemented in the field with an optimized pumping schedule.

¹ Many of the ideas expressed in this chapter were first written in SPE 163867 (Ribeiro and Sharma 2013a) and ARMA 13-409 (Ribeiro and Sharma 2013b).

The first part of this chapter presents a fluid sensitivity study in a low-permeability gas reservoir. The study considers five fluid formulations: water-based fluids, supercritical CO₂, LPG, N₂ foams, and CO₂ foams. We placed a particular emphasis on the 0.3-quality N₂ foam example to show how the model predictions constitute a suitable diagnostic tool. We compare the fracture propagation, productivity, and pumping requirements of the various fluids to identify the best candidate in that particular reservoir.

Furthermore, we conduct a comprehensive sensitivity study under a wide range of reservoir conditions. We address the impact of five critical fluid properties on fracture productivity: density, composition, rheology, leak-off, and compatibility with reservoir fluids. We also identify prime reservoir candidates for using energized treatments by assessing five key reservoir parameters: relative permeability curve, initial gas saturation, reservoir pressure, changes to rock mechanical properties, and sensitivity to water. These factors control well productivity and, thus, fluid selection.

8.1 CASE STUDY: RESULTS FOR 0.3-QUALITY N₂ FOAM

The case study demonstrates how the compositional model can be used to assess the performance of different fracturing fluids in a given reservoir. This section discusses the results for the 0.3-quality N₂ foam treatment in more detail; the performance of the other candidates is discussed in Section 8.2.

8.1.1 Reservoir Properties and Pumping Schedule

The reservoir chosen for this case study is a low-permeability gas formation made of five distinct layers. **Fig. 8.1** shows the vertical stress distribution across the five layers, as well as Young's modulus, Poisson's ratio, and leak-off coefficient for each layer. The

gas-bearing zone is 135 feet in height and is bounded by layers of lower permeabilities. The fracture gradient equals 0.48 psi/ft in the pay zone. The stress contrast between the target zone and the bounding layers is limited. We assume that the odd-numbered layers indicated in Fig. 8.1 share the same mechanical and leak-off properties. Similarly, the even-numbered layers share the same properties. The mechanical and petrophysical properties of the target zone are given in **Table 8.1**.

We consider a 10,000-ft vertical well with an inner tubing diameter of 4 in. The target zone is perforated along a 40-ft interval that is located near the bottom of the target zone (as indicated by the red segment in Fig. 8.1). We consider the same pumping schedule for all the treatments (**Table 8.2**). The initial pad is followed by four stages containing 20/40-mesh proppant. The flow rate and proppant loading is gradually increased during the 60-min treatment. The main inputs for the case study are presented in two separate tables indicating reservoir inputs and pumping schedule inputs. Only the pumping schedule inputs are under the control of the fracturing engineer.

Eight fluids are considered in this case study: linear gel, cross-linked gel, LPG, supercritical CO₂, 0.3-quality CO₂ foam, 0.65-quality CO₂ foam, 0.3-quality N₂ foam, and 0.65-quality N₂ foam. The corresponding fluid properties are given in **Table 8.3**. These properties are given at a temperature of 150°F and a pressure of 6200 psi simply for reference; they are actually evaluated as a function of pressure and temperature in the model. For the foam cases, Table 8.3 provides the fluid properties at the foam quality of interest. By design, this quality is obtained at the perforations; therefore, the fluid saturation at the surface is unknown *a priori*. The corresponding injection rate at the surface is an output of the simulation.

The different fluids are shear-thinning, and their rheology is provided for reference purposes at shear rates representative of flow in the wellbore (500 s^{-1}) and flow in the fracture (50 s^{-1}). We follow the work of Reidenbach *et al.* (1986) and assume that low-quality foams have the same rheology than their base-fluid counterpart (i.e., linear gel in this study). The liquid and gas leak-off coefficients provided in Table 8.3 refer to the values in the odd-numbered layers (denoted as C_a in Fig. 8.1).

8.1.2 Pumping Requirements

Fig. 8.2 shows the evolution of pressure located downstream of the perforations, upstream of the perforations, and at the surface for the 0.3-quality N_2 foam treatment. The perforation pressure is the summation of the minimum horizontal stress and the net pressure, which increases over time as more energy is needed to further propagate the fracture. The bottomhole pressure is slightly higher than the perforation pressure because of the frictional loss occurring through the perforations. The pressure difference increases when the injection rate increases (as seen at the 10-min mark). As more proppant is injected over time, an erosion process decreases the frictional loss, and the bottomhole pressure slowly decreases toward the perforation pressure.

The pressure drop in the wellbore is the result of the competition between the weight of the fluid column and the frictional loss. As we increase flow rate and inject proppant after ten minutes, the surface pressure increases because the increase in friction exceeds the increase in the weight of the slurry column. We observe the same behavior at the beginning of the third stage (at the 20-min mark). At the 45-min mark, we increase the proppant concentration significantly while maintaining a constant injection rate; therefore, the surface pressure decreases because the increase in the slurry column weight exceeds the increase in friction. The variations in surface pressure are significant in this

example, and the variations would be even more dramatic at higher pumping rates. Thus, it is critical to properly estimate the variation in pressures when designing the pumping facilities.

8.1.3 Fracture Propagation

Fig. 8.3 presents the main characteristics of the fracture created by the 0.3-quality N₂ foam treatment. As seen in Fig. 8.3a, the fracture penetrates both the upper and lower layers rapidly. The fracture primarily grows upward, where the *in-situ* stress is lower. The stress contrast is small at the interfaces, and the fracture penetrates four layers (labeled as layers 1 to 4 in Fig. 8.1). The width profile shown in Fig. 8.3b is relatively uniform because the mechanical properties of the different layers are very similar.

Fig. 8.3c shows the rise of the fluid temperature in the fracture from 70°F at the perforations to 180°F along the fracture tip. Energized components are typically injected at low temperatures, so significant changes in fluid temperature are expected in energized treatments. Even though proppant settling is clearly visible in Fig. 8.3d, the foam is effective at carrying proppant. A larger proppant volume would have been required to further pack the fracture with proppant. For comparison purposes, we decided to keep the same volume of proppant for all the treatments, but a higher volume would have been acceptable because the fluid viscosity was high enough to carry higher proppant concentrations. At the bottom of the fracture, the volumetric proppant concentration reaches 0.52, which is the maximum volumetric concentration corresponding to the packing of spheres of equal diameter.

8.1.4 Fluid Invasion

Fig. 8.4 presents the extent of fluid invasion in the reservoir. Figs. 8.4a and 8.4b show the mass (per unit area) of water and N_2 that have invaded the reservoir during pumping. The profiles observed in Fig. 8.4 are different from the smooth width profiles shown in Fig. 8.3 because of the differences between the leak-off coefficients in each layer. The amount of gas placed in the reservoir is significantly lower than the amount of liquid (by approximately a factor of four), which is consistent with the values of the leak-off coefficients provided in Table 8.3. N_2 is practically insoluble in water, so the only way for N_2 to invade the reservoir during pumping is by leaking-off with the gas phase.

Figs. 8.4c and 8.4d show the mass (per unit area) of water and N_2 that have invaded the reservoir after an extended shut-in. During shut-in, the fluid remaining inside the fracture slowly invades the reservoir, as the fracture closes on the proppant. In this example, approximately 70% of the fluid injected was left in the fracture at the end of pumping, so the invaded zone length increases by more than a factor of two after shut-in.

8.1.5 Invaded Zone Properties

Fig. 8.5 shows the properties of the invaded zone at the end of pumping and after an extended shut-in. Using the fluid distribution given in Fig. 8.4, we determine the gas saturation and the length of the invasion zone with flash calculations. The range of allowable saturations is governed by the petrophysical properties provided in Table 8.1. The initial water saturation is 0.35, and the corresponding relative permeability to gas is 0.45.

Figs. 8.5a and 8.5b show the length and the water saturation of the invaded zone at the end of pumping. Similarly, Figs. 8.5c and 8.5d show the length and the water saturation of the invaded zone after an extended shut-in. Gas saturation increases during

shut-in. This is because the gas leak-off was lower than the liquid leak-off (as compared to the foam quality), and because the pressure decreases over time as the fracturing fluid bleeds into the reservoir. As a result, the invaded zone is enriched in the gas phase, and the relative permeability to gas increases. Nevertheless, the invaded zone length also increased, so the well productivity after shut-in is not necessarily better than the well productivity after an immediate flowback.

8.1.6 Fracture Productivity

The productivity model presented in Chapter 5 is used to estimate the fracture productivity of the 0.3-quality N₂ foam treatment. As seen in **Tables 8.4** and **8.5**, the dimensionless well productivity is 3.7 after immediate flowback and 3.6 after an extended shut-in. At the end of pumping, the invaded zone length is limited because the addition of gas reduced liquid leak-off. As seen in Fig. 8.5b, the water saturation is not uniform, and only part of the invaded zone contains gas. In the zone not invaded by the gas component, the reduction in permeability exceeds two orders of magnitude, which severely impedes gas flow. During flowback, significant gas expansion occurs as pressure decreases. As a result, water saturation decreases to an acceptable level ($S_g=0.54$), and the water blocking effect is limited ($k_{dl}/k=0.08$). Gas expansion during flowback is one of the main benefits of using energized fluids, as it improves liquid clean-up around the fracture.

Instead of bringing the well back to production immediately, an alternative strategy is to shut-in the well for an extended period. As the fluid left in the fracture invades the reservoir, the invaded zone length increases significantly (Fig. 8.5c). The water saturation decreases (Fig. 8.5d) because more gas invades the formation (as compared to water), and because the gas phase expands when pressure decreases. The

addition of gas further reduces the liquid blocking effect; however, it does not translate to an improvement in productivity (3.6 versus 3.7 in the immediate flowback case) because the water blocking was already low in the immediate flowback case. In fact, the productivity slightly decreases because the invaded zone is longer. The decision to shut-in the well should be made on a case-by-case basis, as discussed in Section 8.2.4.

8.2 CASE STUDY: COMPARISON BETWEEN SEVERAL FLUID CANDIDATES

We now compare the performance of eight fluids: linear gel, cross-linked gel, LPG, supercritical CO₂, LPG, 0.3-quality CO₂ foam, 0.65-quality CO₂ foam, 0.3-quality N₂ foam, and 0.65-quality N₂ foam. Our objective is not to optimize the pumping schedule; therefore, the same volume of fluid and proppant is pumped at each stage. We follow the pumping schedule indicated in Table 8.2 and consider the reservoir and the well introduced in Section 8.1.1. The comparative study highlights the differences in pumping requirements, fracture properties, and productivity.

8.2.1 Pumping Requirements

Fig. 8.6 shows the evolution of surface pressure for the different treatments. The behavior of each individual pressure signal is similar to the behavior observed in Fig. 8.2. For the first stages, the addition of proppant and the increasing injection rate causes an increase in the frictional loss that exceeds the increase in slurry density. For the fifth stage, the increase in proppant concentration causes an increase in the fluid column weight that exceeds the increase in frictional loss.

The comparison between the different curves clearly illustrates the competition between gravity head and frictional losses. Essentially, the surface pressure increases

either because the slurry viscosity increases, the injection rate increases, and/or because the slurry density decreases. This behavior is consistent with the following observations:

- Linear and cross-linked gels have the same density but the cross-linked gel is ten times more viscous; hence, the surface pressure is much higher for the cross-linked gel treatment.
- Supercritical CO₂ and LPG have a similar viscosity, but LPG is lighter than CO₂ (by 30 to 40%); hence, the surface pressure is much higher for the LPG treatment. Similarly, the linear gel viscosity is comparable to the LPG and CO₂ viscosities, but water is heavier so the surface pressure is lower.
- N₂ and CO₂ foams of the same quality have a similar viscosity, but N₂ is lighter than CO₂, so the surface pressure is higher for the N₂ cases. The contrast in surface pressure increases as the gas volume fraction increases.
- As foam quality increases, the slurry becomes both lighter and more viscous, so the surface pressure increases dramatically. This is the case for both N₂ and CO₂ foams.

This example demonstrates that surface pressure requirements can be very different from one fluid to another. For instance, the use of N₂ is not practical in many deep wells because it requires excessive pumping pressures at the surface. Alternatively, slick-water is the only fluid that can be pumped at really high rates (up to 100 BPM). In those cases, the estimation of the required wellbore pressure constitutes a simple screening test for fluid selection.

8.2.2 Fracture Propagation

The use of different fluids impacts fracture propagation because of variations in fluid leak-off, viscosity, density, and compressibility. For the sake of brevity, we only show the final width profiles of the cross-linked gel, gelled LPG, 0.3-quality CO₂ foam, and 0.65-quality CO₂ foam cases in **Fig. 8.7**. These examples illustrate the following behaviors:

- The cross-linked and 0.65-quality foam fractures are bigger than the other fractures primarily because they have the lowest leak-off coefficients.
- Although the leak-off coefficient is higher for the 0.65-quality foam than for the cross-linked gel, gas expansion compensates for the slight difference in leak-off.
- The LPG fracture shows a more elongated profile because the fluid viscosity is significantly lower.
- The LPG fracture is the only case in which the fracture does not penetrate the lower layer. This is the result of a smaller fracture volume, lower viscosity, and lower fluid density. Lighter fluids are more likely to migrate upward and less likely to penetrate in lower layers because of the contrast between the gravity head and the fracture gradient.

The effects of fluid leak-off, viscosity, density, and compressibility are highly correlated, and a careful analysis is required to dissociate their individual impact. Our results correlate well with phenomena commonly observed in the field.

8.2.3 Invaded Zone Properties

Fig. 8.8 shows the invaded zone length at the end of pumping for the four cases presented in Section 8.2.2. The invaded zone length is proportional to the amount of fluid

leak-off in each layer. The cross-linked gel case yields the lowest invasion whereas the LPG case yields the largest invasion. The difference between the two cases exceeds a factor of ten. **Fig. 8.9** shows the corresponding water saturation at the end of pumping. Warm colors indicate fluid-induced damage, while cool colors indicate a stimulation of the reservoir. The initial water saturation is 0.35 in the reservoir.

Water filtrate mixes with connate water, and the saturation reaches the maximum value (0.75) in the cross-linked gel case. Alternatively, LPG mixes with the hydrocarbon phase, so water reaches its residual saturation (0.3). These results are consistent with our assumption of a pseudo 1D piston-like displacement for each horizontal slice of the reservoir. For the foam cases, the gas phase competes with water. The distribution is based on the relative amount of leak-off for each phase. As expected, the gas saturation is higher for high-quality foams.

The combination of Figs. 8.8 and 8.9 constitutes a good diagnostic tool to determine the water blocking effect. The analysis of Fig. 8.8 alone may suggest that the cross-linked gel shows the least fluid-induced damage, while LPG dramatically impedes gas flow. Nevertheless, LPG is not damaging, and water saturation decreases from 0.35 to 0.3. For the cross-linked gel case, the invasion zone is very narrow, but its impact on gas flow is not negligible because the high-water saturation impedes hydrocarbon flow.

Fig. 8.9 shows the saturation profile at the end of pumping, which provides a pessimistic view of the saturation profile. As the pressure decreases during flowback, any gas present in the reservoir expands, thereby reducing water saturation. This is why the water blocking effect remains low even in the low-quality foam example ($k_d/k=0.06$).

8.2.4 Fracture Productivity

Fig. 8.10 shows the dimensionless fracture productivity of all the treatments. The blue bars indicate the immediate flowback cases, and the green bars indicate the extended shut-in cases. This type of figure is a prime diagnostic tool for fluid selection purposes. For this particular example, high-quality foams appear to be the best fluid candidates, because they exhibit the best combination of low fluid leak-off, limited fluid damage, and reasonable fracture conductivity. The following observations can be made upon analysis of the results presented in this section:

- For damaging fluids (linear gel and cross-linked gels), an extended shut-in is detrimental because it causes the highly water-saturated damaging zone to increase.
- CO₂ and LPG are compatible with the reservoir, so the shut-in does not affect their performance. CO₂ outperforms LPG in this case because we assumed that CO₂ was more viscous, and its leak-off was slightly lower (Table 8.3).
- Foams outperform CO₂ and LPG because the reduction in fluid leak-off yields larger fractures, and they outperform the cross-linked gel treatment because of the limited fluid-induced damage.
- An extended shut-in slightly reduces fracture productivity for the 0.3-quality foams. The benefits of adding gas do not compensate for the detrimental addition of water. Although the relative permeability to gas increases in the invaded zone, the invaded zone length increases sufficiently to generate a larger resistance to flow.

8.2.5 Limitations of the Case Study

In the case study presented above, we used several assumptions that influenced our analysis:

- The proppant distribution was not altered by flowback. This may not hold true if a large pressure drawdown is generated during flowback, particularly when forcing an immediate flowback. The fraction of proppant recovered during flowback is an input to our model.
- The presence of an external filter-cake did not alter fluid flow. In some cases, the gelling agent may further reduce the relative permeability to gas because of the formation of an external and/or internal filter-cake. We can account for this effect by lowering the relative permeability to gas in our model.
- To reduce the number of variables, we designed the treatments so that they all follow the same pumping schedule. This limited the differences between the fluids in terms of proppant-carrying capabilities. More viscous fluids could have transported more proppant, which would have increased fracture conductivity.
- Alternatively, less viscous and denser fluids could have been pumped at higher rates.
- The reservoir was not particularly discriminating between some of the fluid formulations. We assumed that only the target zone contained gas, and the amount of fluid pumped was large enough to cover the target zone for all the fluids. The additional fracture height created was not useful for production purposes. If the target zone was larger, cross-linked gels and high-quality foams would perform better (as compared to other fluids) because they would span a larger portion of the pay zone.

- We assumed that the interactions between the reservoir rock and the invading fluid did not impact the reservoir rock permeability. This will not be the case for water-sensitive formations coming into contact with a water-based fracturing fluid. This behavior can be taken into account by lowering the permeability of the invaded zone in the model.

8.3 RESERVOIR SENSITIVITY STUDY

The case study presented in Section 8.2 demonstrated the impact of several fluid properties on fracture production. Nevertheless, the scope of this example was too limited to assess the performance of different fluids under a wide range of reservoir conditions. This section intends to provide a more comprehensive review of fracture performance, with a particular emphasis on the impact of fluid properties on fracture design.

8.3.1 Scope of the Study

The main output of the model is the fracture productivity (J) normalized by a base productivity, which in this chapter is the productivity of an unfractured, undamaged well in a circular drainage area (J_0). The main inputs of the well productivity model are the fracture geometry, mass of each component leaking off into the rock formation, and conductivity of the propped fracture. As shown by Friehauf, Suri, and Sharma (2010), the dimensionless fracture productivity is a function of four dimensionless parameters defined as: length ($L_f/L_{drained}$), conductivity (F_{cd}), relative permeability in the invaded zone (k_d/k), and invaded zone length (h_{leak}/w). In our 3D model formulation, we consider a fifth dimensionless parameter: height (h_f/h_{pay}).

These five parameters form a useful diagnostic tool to identify when and why a fracturing treatment may underperform. The use of dimensionless parameters reduces the

number of variables needed in the diagnostic. In this section, we show how fracture performance depends on these parameters, by generating type curves representative of a wide range of reservoir conditions. In Section 8.4, we will show how the fluid properties are related to these dimensionless parameters.

8.3.2 Impact of Invaded Zone Permeability

It is evident from the results presented thus far that the reduction in the gas (oil) relative permeability, both in the rock matrix and in the fracture, largely affects well productivity. The impact of water on the relative permeability to gas depends very much on the initial water saturation in the reservoir and on the end point gas permeability, both of which depend on the single phase permeability of the rock. **Fig. 8.11** shows three examples of relative permeability curves. Reservoir 1 refers to an under-saturated rock with low initial water saturation, which is typical of a dry gas reservoir ($S_{gr}=0.25$, $S_{wr}=0.1$, $n_g=2.7$, and $k_{rg,0}=0.8$); Reservoir 2 is a mixed-wet rock ($S_{gr}=0.25$, $S_{wr}=0.3$, $n_g=2.5$, and $k_{rg,0}=0.5$); and Reservoir 3 is a strongly water-wet reservoir with high initial water saturation ($S_{gr}=0.1$, $S_{wr}=0.5$, $n_g=2$, and $k_{rg,0}=0.2$). For the three cases, a small change in gas saturation can change the relative permeability to gas by up to two orders of magnitude (from 0.001 to 0.1). This sharp transition occurs at the transition from immobile to mobile gas, near the residual gas saturation. Then, a very large change in gas saturation is necessary to increase the relative permeability to gas from 0.1 to its maximum value.

The impact of water invasion in these reservoirs can be very different. **Fig. 8.12** shows the productivity index dependence on the effective permeability in the invaded zone for three invaded zone lengths (1, 10, and 100, respectively). These ratios correspond to depth of penetrations of approximately 1 in, 1 ft, and 10 ft. For this

example, we assumed that $L_f/L_{drained}=1$ and $F_{cd}=0.6$. The amount of permeability damage (k_d/k) is dependent on the capillary properties of the formation and the drawdown pressure across the invaded zone. This ratio is equal to the relative permeability to gas (as given by Fig. 8.11) if the rock formation does not appreciably react (both chemically and mechanically) with water. In this case, the petrophysics of the formation is modeled by simple relative permeability and capillary pressure models, and the damage is created by the presence of high water saturation. However, some rocks that contain clays and other fines are sensitive to water. Clay swelling, fines migration, and chemical reactions can further reduce the value of k_d/k . This ratio can, therefore, be used as a modeling parameter useful to account for water sensitivity effects in the invaded zone.

For cases with moderate leak-off, the reduction in well productivity is negligible if the ratio k_d/k is higher than 0.1 because the reduction in permeability only occurs across a small layer around the fracture. As the ratio k_d/k increases from 0.001 to 0.1, the productivity index increases by a factor of three. As mentioned previously, k_d/k is very sensitive to gas saturation; therefore, a small change in gas saturation (associated with fluid leak-off) can dramatically change the effective permeability in the invaded zone. For cases with large fluid leak-off, the change in well productivity is more gradual and permeability damage becomes significant at a higher range (k_d/k ranging from 0.005 to 0.2).

Figs. 8.11 and 8.12 constitute a simple diagnostic tool to identify when energized fluids are likely to outperform water-based fracturing fluids. Our analysis shows that it is critical to maintain a gas saturation slightly higher than the residual gas saturation to yield satisfactory gas flow. The transition between immobile and mobile gas is very steep, as shown in Fig. 8.11. If the gas saturation becomes close to the residual gas saturation after

water invasion, energized fluids should be used. When foams are used, knowing the amount of gas (which may be soluble gas) leaking into the rock formation is critical to evaluate the impact on gas saturation, and therefore on well productivity. As long as there is *enough* gas in and around the fracture, well productivity is satisfactory. A criteria to quantify what is meant by *enough* is to identify the foam quality that gives a saturation corresponding to a value of k_d/k higher than 0.1.

8.3.3 Impact of Invaded Zone Length

Fig. 8.13 shows the productivity index dependence on the invaded zone length for three effective permeabilities (0.001, 0.01, and 0.1, respectively). Similarly to Fig. 8.12, we assumed that $L_{fj}/L_{drained}=1$ and $F_{cd}=0.6$. Figs. 8.12 and 8.13 are thus type curves expressing similar information in different fashions. When comparing the performance of several treatments, one should keep in mind that fluids with different leak-off would result in different fracture geometries; therefore, a different set of type curves should be used.

The size of the invaded zone depends on fluid leak-off and reservoir properties. For a given volume of fluid leak-off, the invaded zone length increases if the reservoir porosity decreases; the residual saturation of the displacing phase increases; and/or the initial saturation of the phase in which the leak-off fluid mixes with increases. As seen in Fig. 8.13, the invaded zone length does not impact productivity if the invaded zone permeability remains higher than 0.1. Also, a very narrow invaded zone (h_{leak}/w less than 5) does not impede hydrocarbon flow, irrespective of the reduction in permeability. This was the case of the cross-linked fluid treatment with immediate flowback in Section 8.2. Although the invaded zone was saturated with water, the zone was narrow enough to have a limited impact on gas flow.

8.3.4 Impact of Fracture Length and Height

The impact of fracture height on productivity is similar to the impact of fracture length. This is because we assume that there are no cross-flow and gravity effects in the reservoir; therefore, the reservoir is represented by the superposition of independent horizontal sections. **Fig. 8.14** shows the productivity index dependence on fracture length for three dimensionless fracture conductivities (0.5, 5, and 50, respectively). In this example, $k_d/k=0.01$ and $h_{eak}/w =20$. Contrary to Figs. 8.12 and 8.13, the productivity index does not plateau for the given range of dimensionless lengths. This is because longer fractures contact more gas inside the drainage area. Of course, if the fracture length exceeds the drainage area ($L_f/L_{drained}$ higher than one), there is no further productivity enhancement. As fracture conductivity decreases ($F_{cd}=0.5$), the incremental benefit of creating length is reduced because the fracture becomes less effective at transporting gas (oil) over a long distance. For short fractures, conductivity plays a limited role because the gas (oil) does not have to travel long distances inside the fracture. On the other hand, maintaining high fracture conductivities is critical to ensure effective hydrocarbon flow in long fractures.

It should be noted that $L_{drained}$ is defined as the equivalent drainage radius, which is calculated from the estimated drainage area. For ultra-low permeability rocks, the definition of the drainage area is not trivial. In these rocks, the estimated drainage area may be unreasonably large because the pressure takes decades (or more) to reach the reservoir boundary. Instead, we can see the drainage area as the largest area one can possibly drain in a reasonable time. For horizontal wells with multiple fractures, the drainage zone may be seen as the product of the spacing between consecutive fractures from the same lateral, multiplied by the spacing between adjacent wells.

8.3.5 Impact of Fracture Conductivity

Fig. 8.15 through **Fig. 8.17** shows the productivity index dependence on fracture conductivity under a wide range of conditions. In **Fig. 8.15**, we assume that $k_d/k=0.005$ and $h_{leak}/w=20$ in an undamaged well. For low-conductivity fractures (F_{cd} lower than 0.1), increasing fracture length does not bolster production because the gas (oil) is not easily transported in the fracture. For fracture conductivities higher than 10, an increase in fracture conductivity only provides a marginal productivity enhancement. At high fracture conductivities, fracture length is the dominant factor, and the productivity seems to be directly proportional to fracture length (as observed in **Fig. 8.14**). For moderate conductivities (F_{cd} ranging from 0.2 to 1), a slight increase in conductivity yields a significant productivity enhancement.

Fig. 8.16 shows the productivity index dependence on fracture conductivity for three relative permeabilities (0.001, 0.01, and 0.1, respectively) in an undamaged reservoir. For this example, we assumed that $L_f/L_{drained}=0.8$ and $h_{leak}/w=50$. At low conductivities, the minimum productivity index equals one because the reservoir is undamaged. If there is no fracture, gas production results from circular hydrocarbon flow around the well. Fluid flow is redirected into the non-damaged wellbore instead of forcing it through a highly damaged fracture. In this example, a relative permeability of 0.01 is high enough that any improvement in permeability is marginal. This behavior implies that low-quality foams may perform as well as high-quality foams, at least from a fluid-induced damage standpoint.

Similarly to **Fig. 8.16**, **Fig. 8.17** shows the productivity index dependence on fracture conductivity for the same relative permeabilities except, here, the well is initially damaged. We assume that $L_f/L_{drained}=0.8$ and $h_{leak}/w=50$, with a mechanical skin of

$k_s/k=0.001$ and $r_s/r_w=3$. The mechanical skin typically results from mud filtrate invasion during drilling operations. The productivity index tends toward zero if there is no fracture because the skin effect impedes hydrocarbon flow. A fracture treatment is required to bypass the mechanical skin around the well. Under these conditions, fracture conductivities higher than 0.1 ensure that fluid flow is redirected through the fracture to generate productivity enhancement. For high values of fracture conductivities, the mechanical effect does not impact productivity because the conductive fractures bypass the mechanical skin.

8.4 KEY FRACTURING FLUID PROPERTIES

The previous sensitivity study demonstrated how fracture productivity depends on five critical parameters: fracture length, height, conductivity, relative permeability in the invaded zone, and invaded zone length. This section assesses how fluid properties relate to these parameters and, thus, to fracture productivity.

8.4.1 Density

Fluid density impacts primarily pumping requirements, proppant transport, and fracture geometry in the following ways:

- Lighter fluids require larger treating pressures as they generate a lower hydrostatic pressure.
- Lighter fluids favor proppant settling, as settling is governed by the competition between the gravity force and the drag force exerted by the fluid.
- Lighter fluids are more prone to upward migration and out-of-zone propagation because of the increasing difference between the stress gradient and the fluid

gradient, as illustrated by **Fig. 8.18**. Nevertheless, the presence of a significant stress contrast at the interface between layers may prevent vertical migration.

- Energized fluids are compressible, so they tend to expand as the rock formation heats the fracturing fluid. The subsequent increase in fracture volume can be significant (as seen in Section 6.3.1).

8.4.2 Rheology

Rheology primarily depends on the gelling agents and fluid additives that are used. A large cocktail of additives is available, sometimes with major differences between the providers. We will not discuss the differences in fluid additives here; rather, we review the main effects of fluid rheology on fracture productivity:

- Viscous fluids require higher treating pressures, as discussed in Section 8.2.
- Increasing fluid viscosity reduces proppant settling.
- Viscous fluids promote the propagation of wider and shorter fractures.
- Foams offer a wide range of viscosities without using excessive amounts of gelling agents and additives. The transition from the comingled regime to the foam regime is unique; it provides some flexibility when designing foam treatments.

8.4.3 Leak-off

Similarly to rheology, leak-off primarily depends on the gelling agents and fluid additives that are used. In addition, fluid leak-off is highly reservoir-dependent, which makes its estimation very tedious. Fluid leak-off influences treatment design and fluid selection in the following ways:

- High leak-off is detrimental, not only because of the reduction in fracture volume, but also because of the increasing fluid-induced damage.
- High leak-off reduces the ability of the fluid to carry proppant along the fracture. As proppant accumulates and the frictional pressure drop surges near the perforations, a premature screenout is likely to occur.
- LPG, CO₂, or any other non-damaging fluids that mix with the hydrocarbon phase do not impede hydrocarbon flow. A narrow high-water saturation zone is more detrimental than an extended low-water saturation zone.
- Fluids with higher solubility in the aqueous phase have an increased ability to reduce damage in the invaded zone. The presence of free gas and soluble gas coming out of solution improves clean-up in and around the fracture.
- Foams provide superior fluid-loss control without using excessive amount of gelling agents. The filter-cake is supplemented by the presence of gas bubbles that reduce liquid-flow in the porous medium.

8.4.4 Shut-in Strategy

Determining the optimum time to bring the well back to production is challenging because numerous factors are involved. In many cases, the shut-in time is a pre-defined company policy. Our productivity model provides some valuable insight in determining shut-in strategy:

- Immediate flowback is recommended when using damaging fluids such as water.
- For foams, an extended shut-in is recommended if the benefit of increasing the relative permeability to gas outweighs the increase in invaded zone length.

- If the permeability in the invaded zone is high *enough* at the end of pumping, a well shut-in is not necessary. This is the case when k_d/k is higher than 0.1.
- For non-damaging fluids, such as LPG and CO₂, a well shut-in does not modify well productivity.

There are other factors that influence the decision of shutting-in the well. These mechanisms were not considered in Section 8.3, but they can impact productivity in significant ways:

- More proppant is likely to be recovered when the well is immediately flowed back. An extended shut-in ensures that the fracture closes on the proppant.
- Fluids such as CO₂ can swell the oil phase and reduce its mobility, thereby affecting flowback and the subsequent hydrocarbon production.
- In naturally-fractured reservoirs, an extended shut-in contributes to the re-activation of pre-existing cracks. The creation of a large stimulated rock volume enhances productivity.

8.4.5 Safety Considerations

Fluid selection is not limited to identifying the fluid that will yield the highest production. Initial cost, fluid availability, and safety considerations also play important roles in fluid selection. Safety concerns regarding the use of gases have hindered the implementation of energized treatments in the field. These concerns partially explain why energized fluids only represent 2 to 3% of the fracturing treatments in the U.S., while they represent 20 to 30% of the fracturing treatments in Canada.

All the fluids listed in this dissertation can be implemented in the field safely, following proper procedures. Currently, the use of LPG fracturing fluids remains

marginal, and only one company (*GasFrac*) has a monopoly on this technology. Although field results indicate that LPG treatments are safe, there are still concerns in the industry regarding the risks associated with LPG because it is very flammable and volatile. The use of gases requires additional safety measures because of their compressibility. High-pressure storage units are required, with numerous instruments to prevent and monitor potential leaks. An extensive evaluation is required to identify the risks and to define the steps minimizing those risks. For CO₂, an additional concern is the formation of dry ice in the surface equipment.

Furthermore, field implementation is more challenging for energized treatments because many fracturing crews are not very experienced with the methodologies and the proper safety requirements for the use of gases. This lack of experience has hindered the field implementation of energized fluids. With foams, there is an additional concern with regard to the formation of extremely-high-viscosity foams. At high qualities, the interactions between gas bubbles can generate an increase in viscosity by a factor of 100. When this occurs, the surface pressure surges, and the pumping must stop. It is thus critical to operate foams in a controlled manner to prevent complications or operational delays.

8.4.6 Cost and Availability

The cost of the fluid itself plays a minor role in the cost evaluation, as the associated costs (for infrastructures, storage, disposal, etc.) far exceed the cost of the actual fluid. To fully appreciate the life-cycle costs of fluids used for hydraulic fracturing, one needs to examine the total costs of fluid acquisition, management and disposal (Watts 2013). The cost to acquire, transport, store, use, treat, recover, recycle, and dispose the fracturing fluid represents a significant investment for energy producers and service

companies. Much of the cost savings depend on the availability of the fluid and the structure of the pumping contractor's bid package, so a thorough fluid selection analysis requires a site-specific cost evaluation.

In certain areas, large quantities of CO₂ are available *via* pipelines; thus, in those cases, the cost of the fluid is reasonable. Alternatively, the use of large quantities of CO₂ in certain reservoirs requires the deployment of many trucks, pressurized storage units, and additional pumping equipment. Since a large volume of CO₂ is required in a very short time span, coordinating these efforts becomes very complex to such an extent that, sometimes, gas providers are reluctant to provide this service by themselves. The situation is similar when the operator chooses to use LPG or N₂. In many cases, concerns related to fluid availability and delivery severely hinder - or even prohibit - the use of energized fluids in the field.

In essence, energized fluids offer properties similar to any water-based fluids in terms of fracture creation, proppant transport, and fracture conductivity, while also offering the advantage of limited fluid-induced damage as compared to water-based fluids. Nevertheless, the use of energized fluids typically requires larger capital expenditures, so it would only make sense to use these fluids when the profits associated with increased production outweigh the additional expenditures.

8.5 KEY RESERVOIR PROPERTIES FOR FLUID SELECTION

As evidenced by the different type curves presented in Section 8.3, there are several reservoir parameters that are critical when evaluating fracture productivity and, therefore, fluid selection:

1. *Relative permeability curve*: The residual gas and water saturations determine the range of allowed gas saturations and control the fractional flow of gas and water. The endpoint relative permeability to gas controls the maximum rate of gas delivery.
2. *Initial gas saturation*: In under-saturated rocks, any water lost to the rock matrix will remain trapped, thereby lowering the relative permeability to gas. In reservoirs with high initial water saturations, small variations in gas saturation can have dramatic repercussions on fractional flow, and therefore on well productivity.
3. *Reservoir pressure*: Damage around the fracture face induced by the loss of water-based fracturing fluids can be removed during flowback if the drawdown pressure exceeds the capillary forces holding the liquid in place. When the reservoir pressure is too low to create a drawdown pressure larger than the capillary forces, energized fluids are recommended.
4. *Water sensitivity of the formation*: In some rock formations, clay swelling, fines migration, and chemical reactions with the fracturing fluid can significantly reduce the rock permeability. Non-aqueous fluids are thus preferred: oil-base muds, LPG, CO₂, etc. Foams reduce the amount of water in contact with clays, but they do not eliminate clay swelling.
5. *Proppant embedment*: Many shales soften (i.e., their Young's modulus decreases) when they are brought into contact with water-based fluids. This softening leads to additional proppant embedment that may cause a significant loss in propped fracture conductivity. When this is determined to be the case (based on shale

compatibility laboratory tests), non-aqueous fluids should be strongly considered as they can prevent or at least minimize this effect.

8.6 CONCLUSIONS

This chapter illustrated the wide range of capabilities offered by our compositional model, which forms a modeling tool particularly suitable for screening fluid candidates and optimizing fracturing treatments. We conducted a comprehensive sensitivity study under a wide range of reservoir conditions. The study emphasized the role of critical fluid properties for fluid selection: density, composition, rheology, leak-off, and compatibility with reservoir fluids. We also identified key reservoir parameters that impact fluid selection: relative permeability curve, initial gas saturation, reservoir pressure, changes to rock mechanical properties, and water-sensitivity. The following design recommendations can be made upon the analysis of the results presented in this section. Many of these recommendations are consistent with the findings of Friehauf (2009) and Friehauf and Sharma (2009):

1. *Relative permeability:* Reductions in relative permeability to gas (oil) by less than a factor of ten do not affect hydrocarbon production. When water blocking severely impedes gas flow, the use of energized fluids improves clean-up and well productivity.
2. *Reservoir pressure:* When the drawdown pressure is insufficient to remove the damaging phase (water), energized fluids constitute an attractive alternative. In depleted reservoirs, fluid expansion improves liquid clean-up.
3. *Initial saturation:* In under-saturated rocks, any water lost to the rock matrix remains trapped, thereby lowering the relative permeability to gas. When

- energized fluids are used, an extended shut-in can improve fluid clean-up by placing an additional amount of gas into the formation.
4. *Fracturing fluid solubility:* Fluids with higher solubility in the aqueous phase have an increased ability to reduce damage in the invaded zone. Adding a component such as methanol increases the solubility of CO₂ in the liquid phase and alleviates fines migration and clay swelling in some sandstone reservoirs.
 5. *Fracture conductivity:* In many cases, low-quality foams allow enough gas to limit the water blocking effect, while creating long fractures. High-quality foams are recommended if having high fracture conductivity is a priority.
 6. *Shut-in strategy:* An extended shut-in is detrimental when damaging fluids are used, as more liquid invades the rock formation. However, some of the proppant may be recovered when the fracturing fluid is flowed back immediately. If this is the case, it is important to slowly bring the well back to production by carefully ramping-up the production rate.
 7. *Water-sensitivity:* Non-aqueous fluids such as LPG and CO₂ are preferred in reservoirs that are prone to excessive fines migration and clay swelling. High-quality foams reduce the amount of water in contact with clays, but they do not eliminate clay swelling.
 8. *Operational considerations:* The use of gases requires additional safety measures because of their compressibility. High-pressure storage units are required, with numerous instruments to prevent and monitor potential leaks. This is also true when using LPG because of its flammability and volatility. When using foams,

care should be taken to avoid the formation of extremely-high-viscosity foams, which would halt the pumping operations.

9. *Cost and availability:* Much of the cost savings depend on the availability of the fluid and the structure of the pumping contractor's bid package. In certain areas, the use of large quantities of gas is prohibitive because of the costs associated with the deployment of many trucks and pressurized storage units.

Table 8.1: Main reservoir properties.

Parameter	Unit	Case Study
Drainage Area	acre	50
Pay Zone Height	ft	135
Young's Modulus (pay zone)	psi ($\times 10^6$)	3.6
Poisson's Ratio (pay zone)	/	0.25
Reservoir Temperature	°F	180
Porosity	%	13
Permeability	mD	0.005
Pore Pressure	psi	4000
Capillary Pressure	psi	500
Initial Water Saturation	%	35
Residual Water Saturation	%	30
Residual Gas Saturation	%	25
End-Point Permeability	cp	0.6
End-Point Exponent	/	2.5

Table 8.2: Pumping schedule for all the treatments used in the case study.

Parameter	Unit	1	2	3	4	5
Duration	min	10	10	10	15	15
Flow Rate	bbl/min	20	30	30	35	35
Proppant Volume Fraction	%	0	6	9	12	18
Proppant Diameter	in	n/a	0.007	0.007	0.007	0.007

Table 8.3: Fluid properties evaluated at 6200 psi and 150 °F.

Parameter* (Unit)	Linear Gel	Cross-Linked	LPG	CO ₂	30% CO ₂ foam	65% CO ₂ foam	30% N ₂ foam	65% N ₂ foam
Density (lbm/ft ³)	62.4	62.4	34.5	53.9	59.9	56.9	49.7	34.8
Viscosity at 500s ⁻¹ (cp)	16	112	7	10	16	50	16	50
Viscosity at 50s ⁻¹ (cp)	51	350	24	32	51	153	51	153
Leak-off (ft/√min) x10 ³	1.6	0.4	2	1.8	0.8 - 0.15	0.4 - 0.3	0.8 - 0.15	0.4 - 0.3

*500 and 50 s⁻¹ are representative of the shear-rate in the well and in the fracture, respectively. For foams, two leak-off coefficients are provided for the liquid and gas phases.

Table 8.4: Fracture productivity (immediate flowback).

Parameter* (unit)	Linear Gel	Cross-Linked	LPG	CO ₂	30% CO ₂ foam	65% CO ₂ foam	30% N ₂ foam	65% N ₂ foam
h_{leak} (ft)	0.36	0.06	0.48	0.42	0.17	0.09	0.17	0.07
S_w	0.75	0.75	0.3	0.3	0.55	0.31	0.54	0.31
k_d/k	0.0001	0.0001	0.6	0.6	0.06	0.55	0.08	0.56
F_{cd}	0.5	0.9	0.3	0.5	0.6	0.8	0.5	0.7
J/J_0	1.6	3	3.3	3.5	3.7	4.2	3.7	4.1

*These parameters are averaged in the target zone only. The productivity index is normalized by the productivity of an unfractured, undamaged reservoir in a circular drainage area.

Table 8.5: Fracture productivity (extended shut-in).

Parameter* (unit)	Linear Gel	Cross-Linked	LPG	CO ₂	30% CO ₂ foam	65% CO ₂ foam	30% N ₂ foam	65% N ₂ foam
h_{leak} (ft)	0.44	0.44	0.56	0.6	0.45	0.5	0.42	0.52
S_w	0.75	0.75	0.3	0.3	0.53	0.3	0.52	0.3
k_d/k	0.0001	0.0001	0.6	0.6	0.09	0.59	0.1	0.6
F_{cd}	0.5	0.9	0.3	0.5	0.6	0.8	0.5	0.7
J/J_0	1.5	1.7	3.3	3.5	3.6	4.2	3.6	4.1

*These parameters are averaged in the target zone only. The productivity index is normalized by the productivity of an unfractured, undamaged reservoir in a circular drainage area.

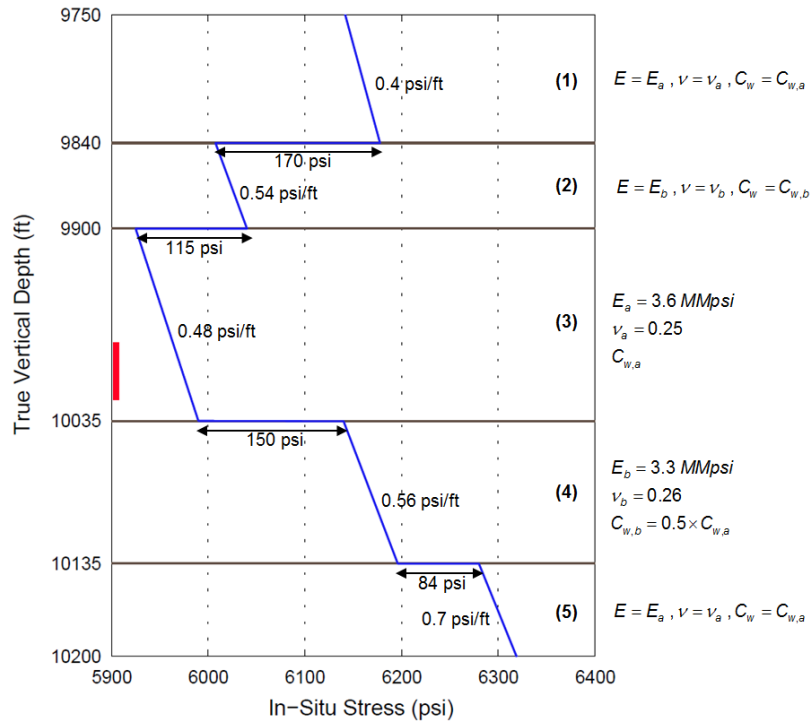


Figure 8.1: *In-situ* stress distribution and mechanical properties of each layer.

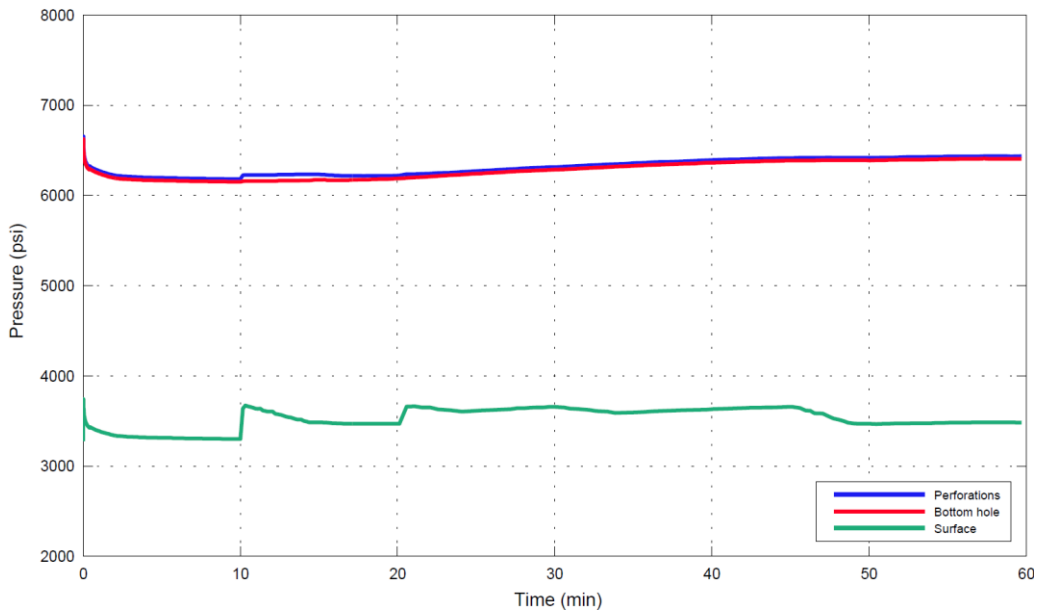


Figure 8.2: Evolution of pressure at different locations along the well.

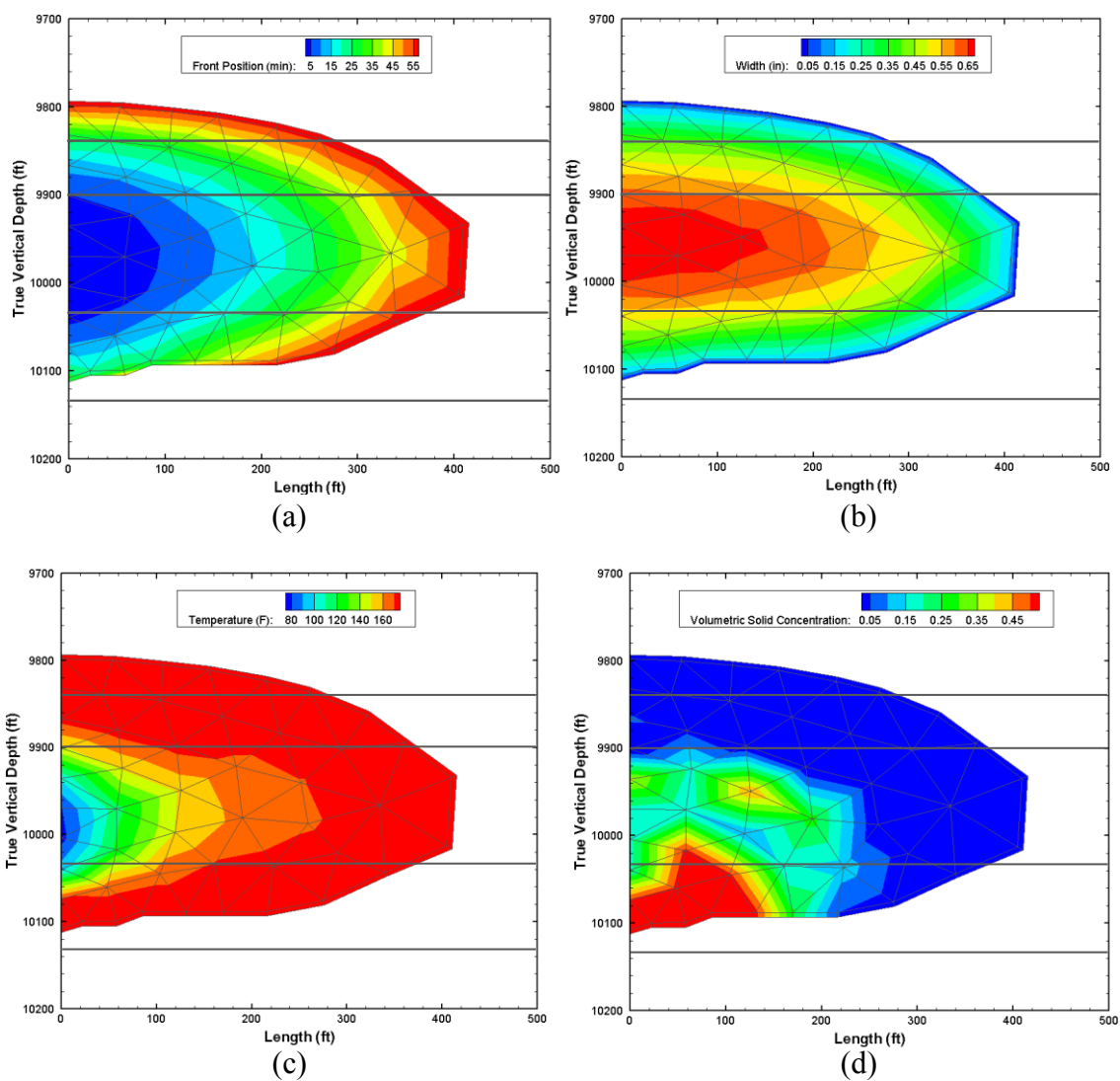


Figure 8.3: Fracture propagation for the 0.3-quality N_2 foam example: (a) position of the fracture front over time, (b) final fracture width, (c) final temperature distribution, and (d) final volumetric proppant concentration.

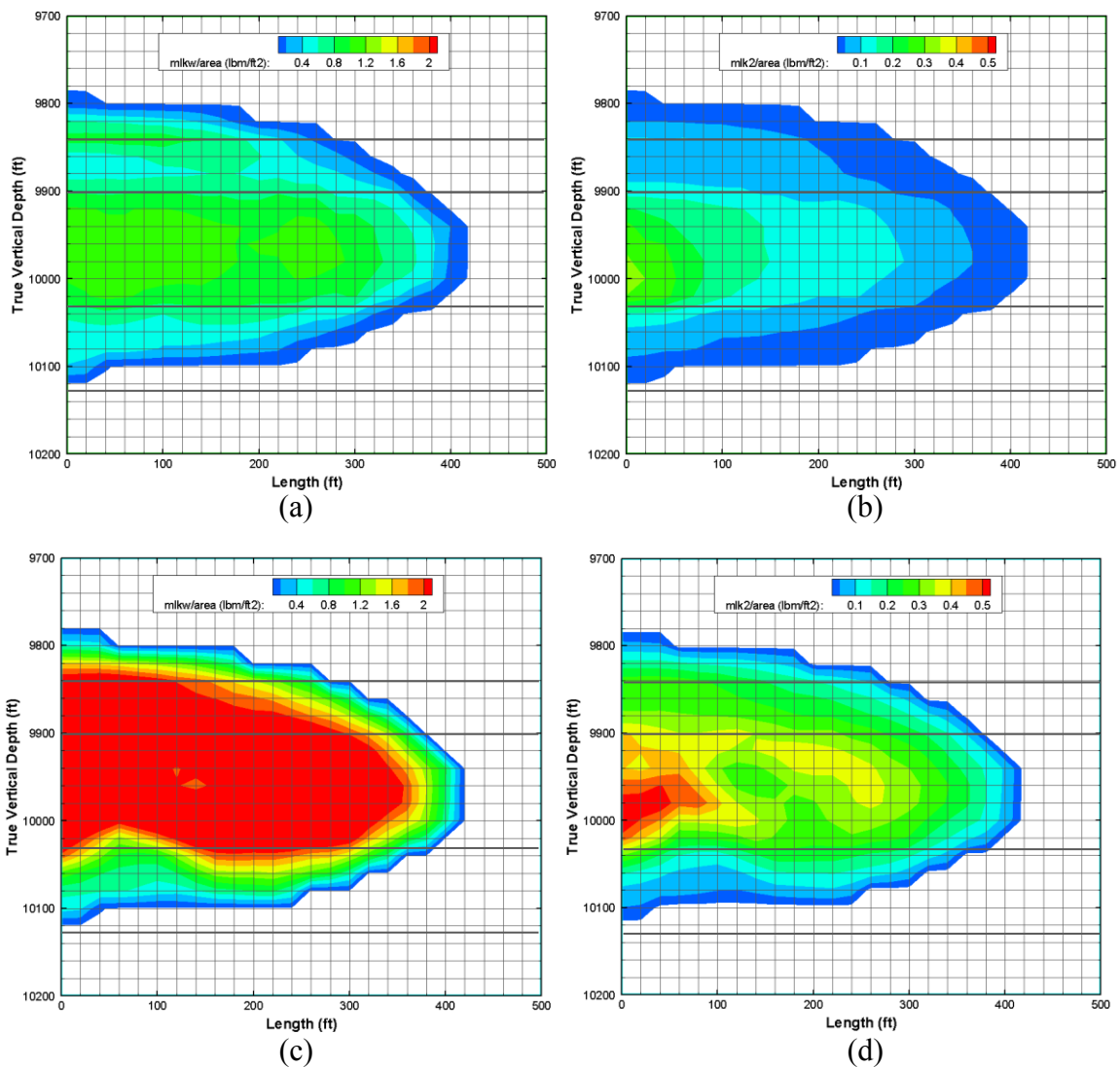


Figure 8.4: Mass per unit area of each component that has invaded the reservoir for the 0.3-quality N₂ foam example: (a) water invasion at the end of pumping, (b) N₂ invasion at the end of pumping, (c) water invasion after an extended shut-in, and (d) N₂ invasion after an extended shut-in.

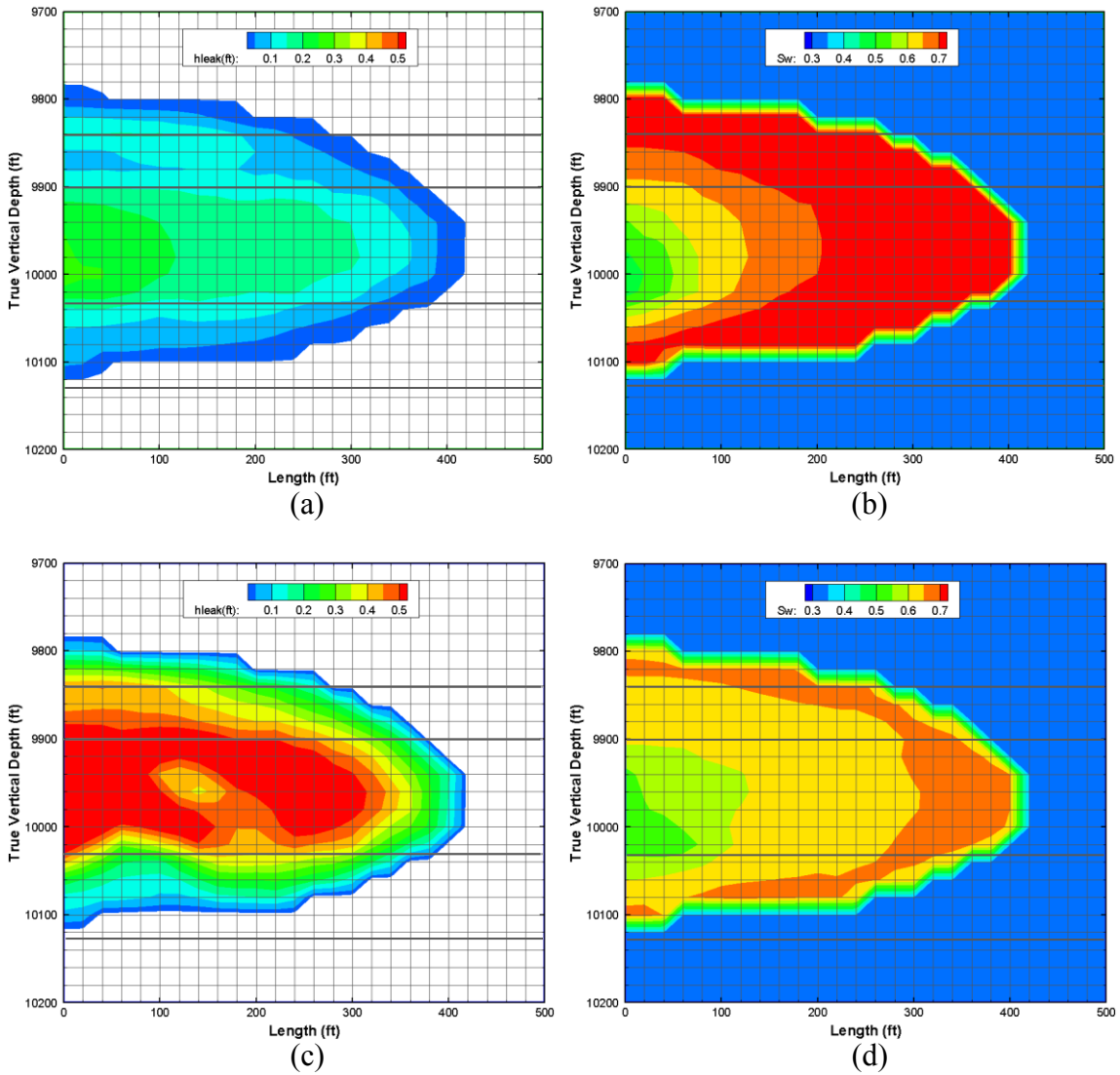


Figure 8.5: Properties of the invaded zone for the 0.3-quality N_2 foam example: (a) invaded zone length at the end of pumping, (b) water saturation in the invaded zone at the end of pumping, (c) invaded zone length after an extended shut-in, and (d) water saturation in the invaded zone after an extended shut-in. The initial water saturation in the reservoir is 0.35.

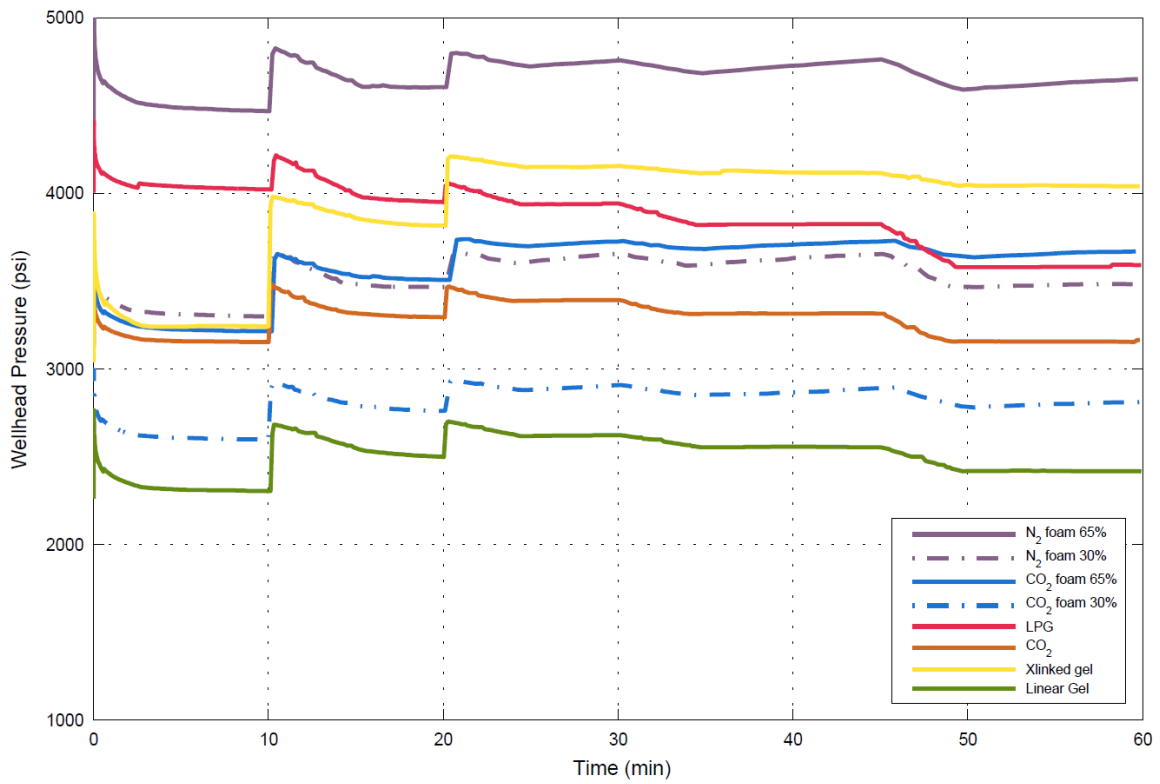


Figure 8.6: Evolution of the surface pressure for the different fluids considered in the case study.

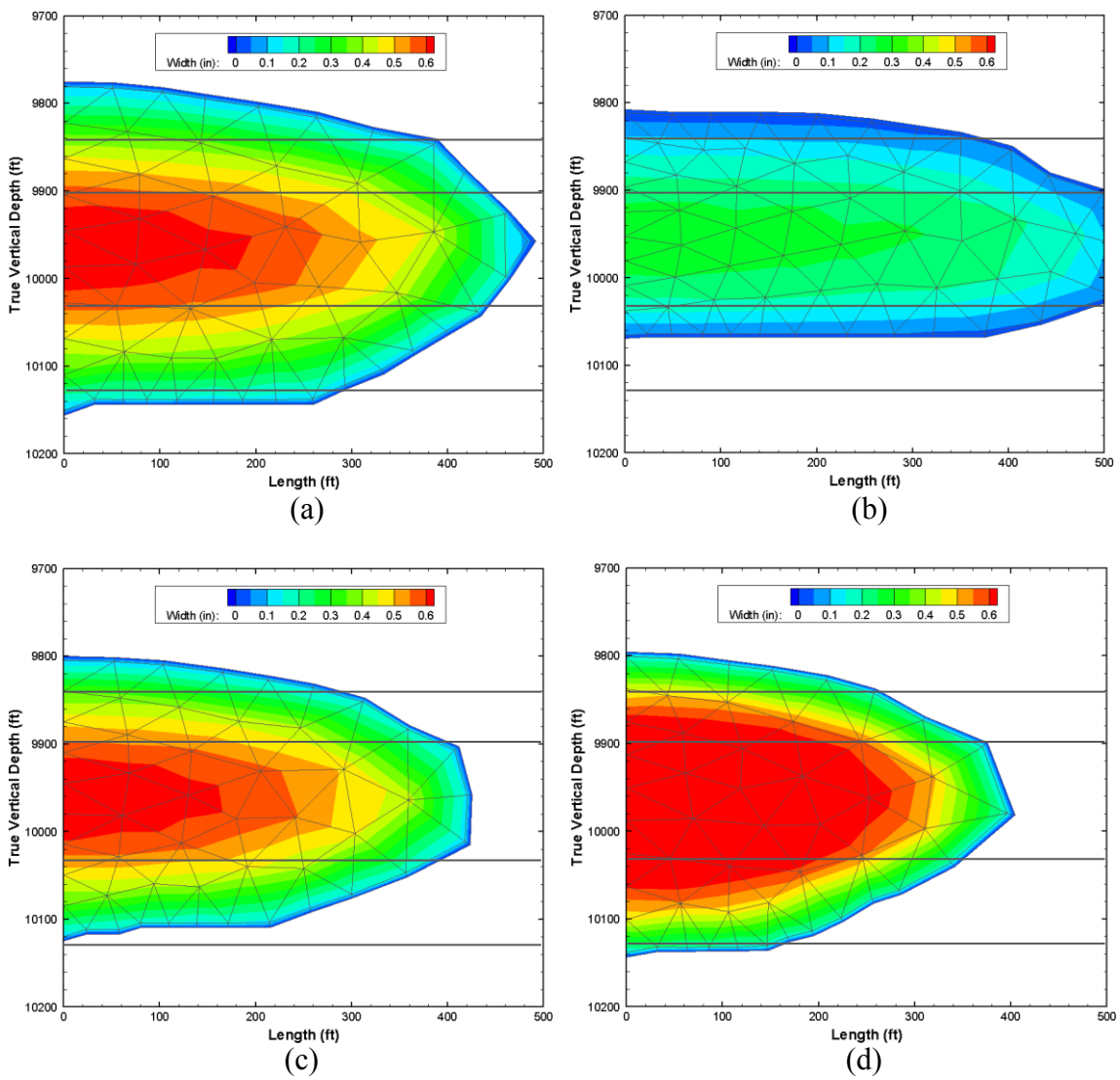


Figure 8.7: Final fracture geometry using: (a) cross-linked water-based gel, (b) gelled LPG, (c) 0.3-quality CO₂ foam, and (d) 0.65-quality CO₂ foam.

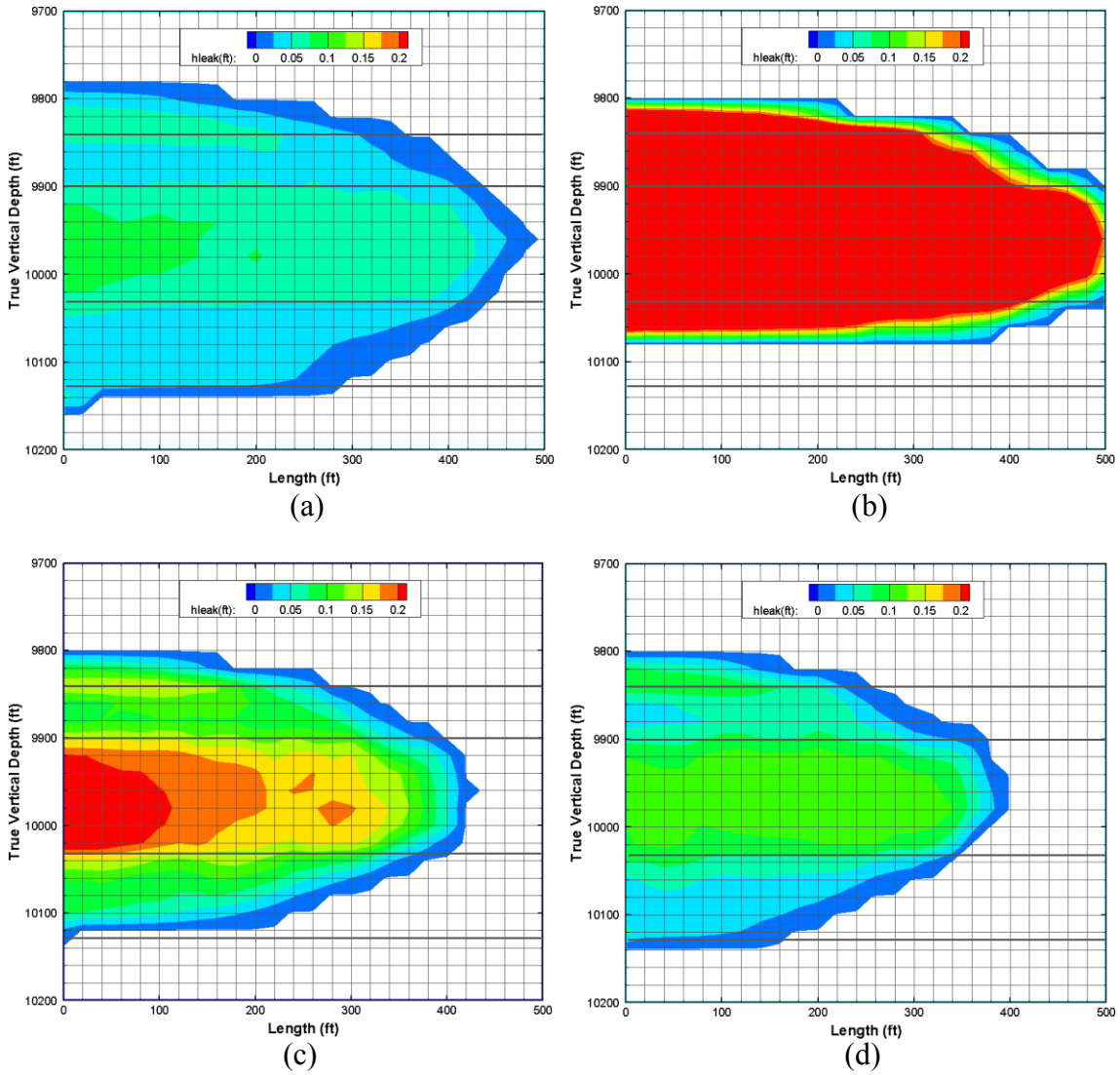


Figure 8.8: Invaded zone length at the end of pumping using: (a) cross-linked water-based gel, (b) gelled LPG, (c) 0.3-quality CO₂ foam, and (d) 0.65-quality CO₂ foam.

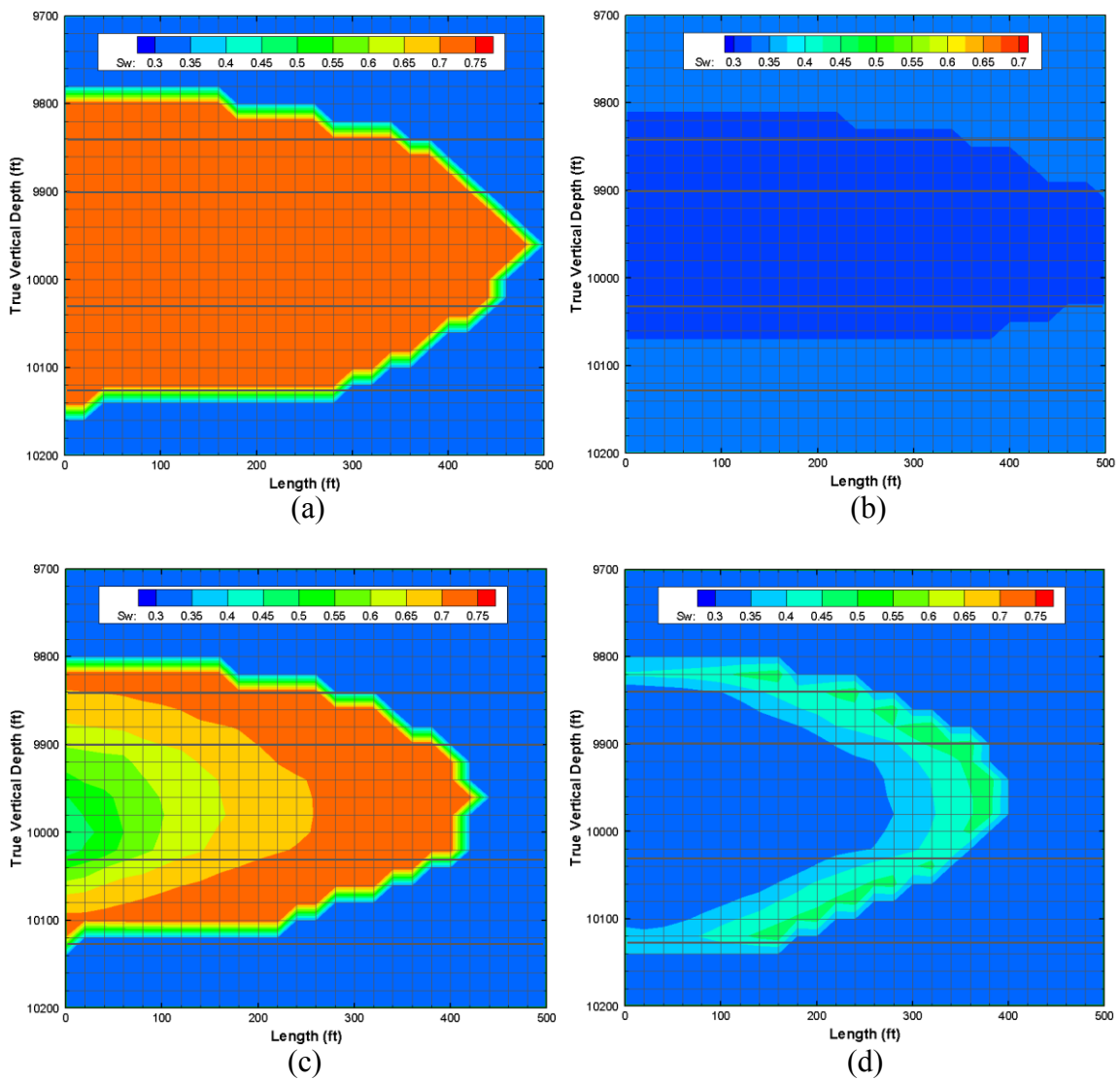


Figure 8.9: Water saturation at the end of pumping using: (a) cross-linked water-based gel, (b) gelled LPG, (c) 0.3-quality CO_2 foam, and (d) 0.65-quality CO_2 foam.

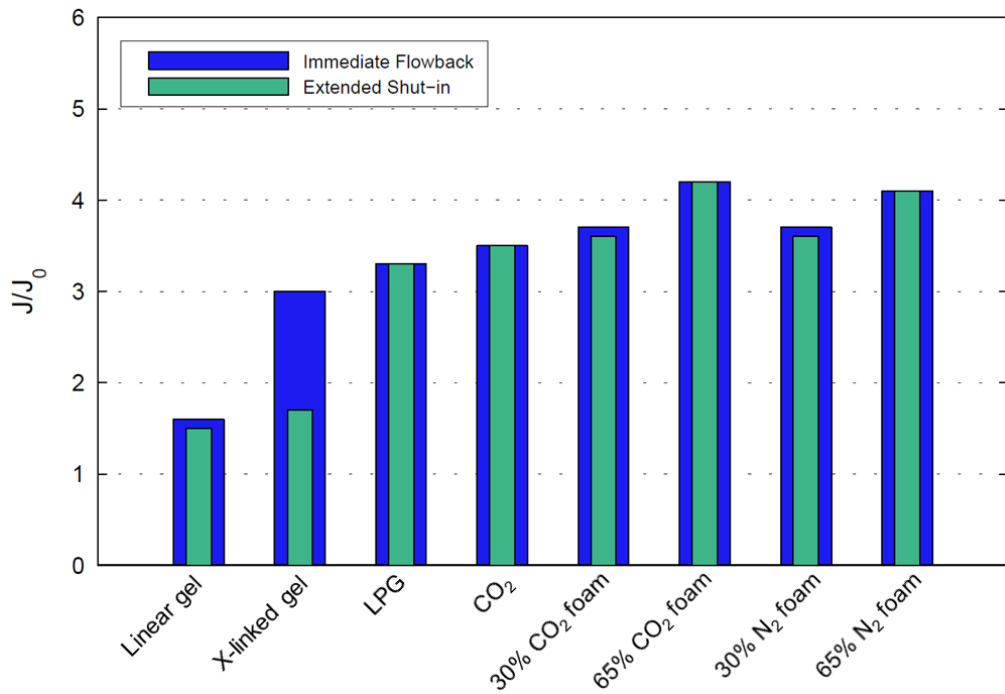


Figure 8.10: Fracture productivity of the various fluid candidates for the immediate flowback and extended shut-in cases.

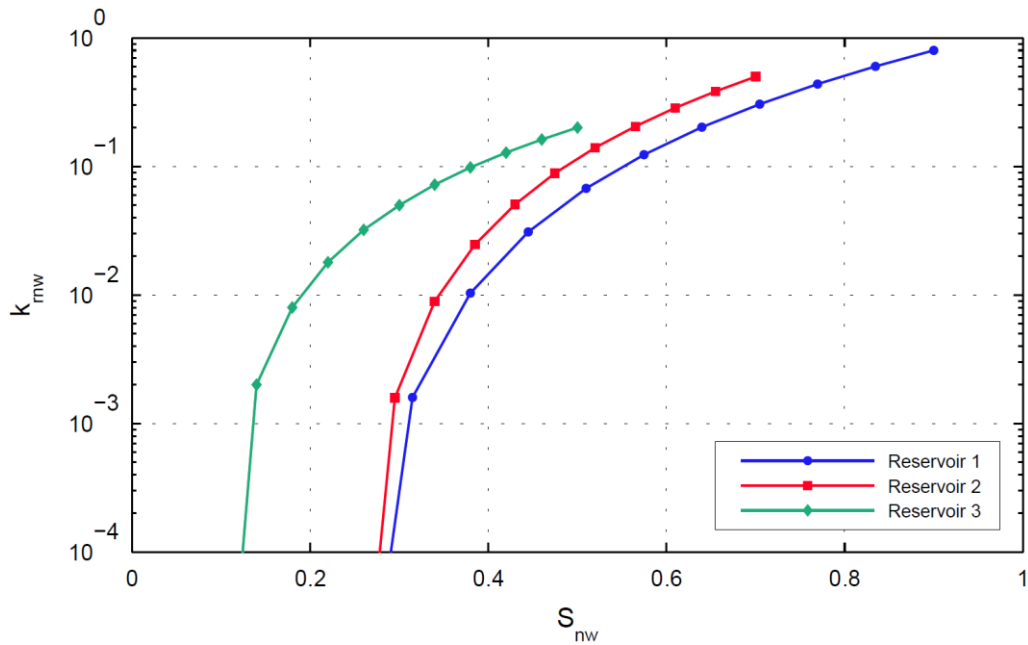


Figure 8.11: Relative permeability curves that are representative of (1) dry gas reservoir, (2) intermediate reservoir, and (3) strongly water-wet reservoir.

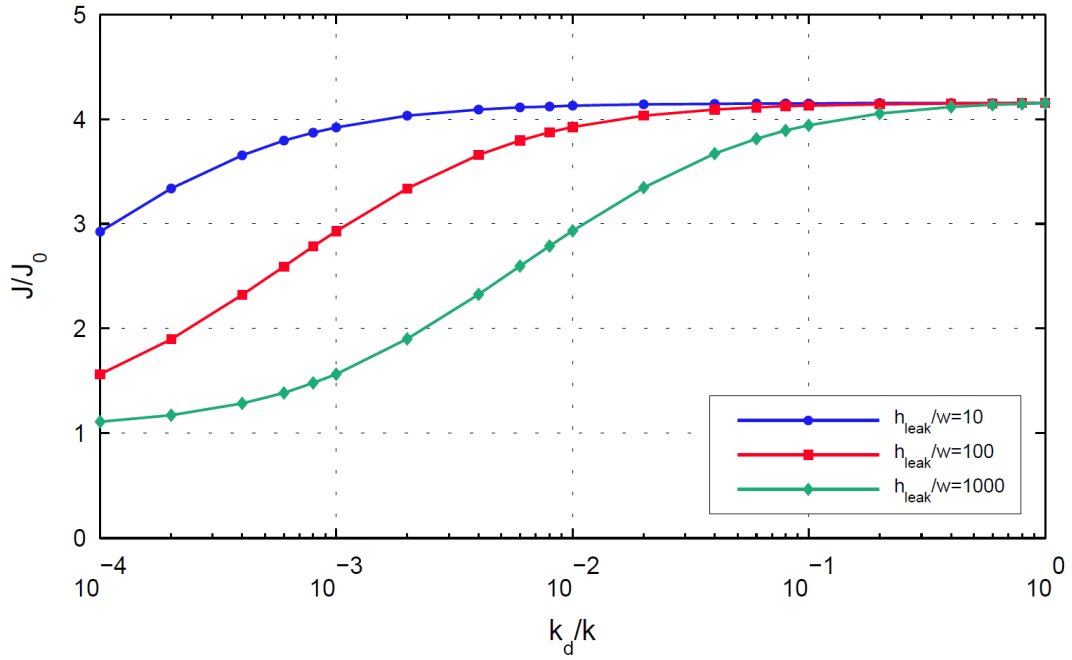


Figure 8.12: Impact of invaded zone permeability on productivity ($L_f/L_{drained}=1$ and $F_{cd}=0.6$).

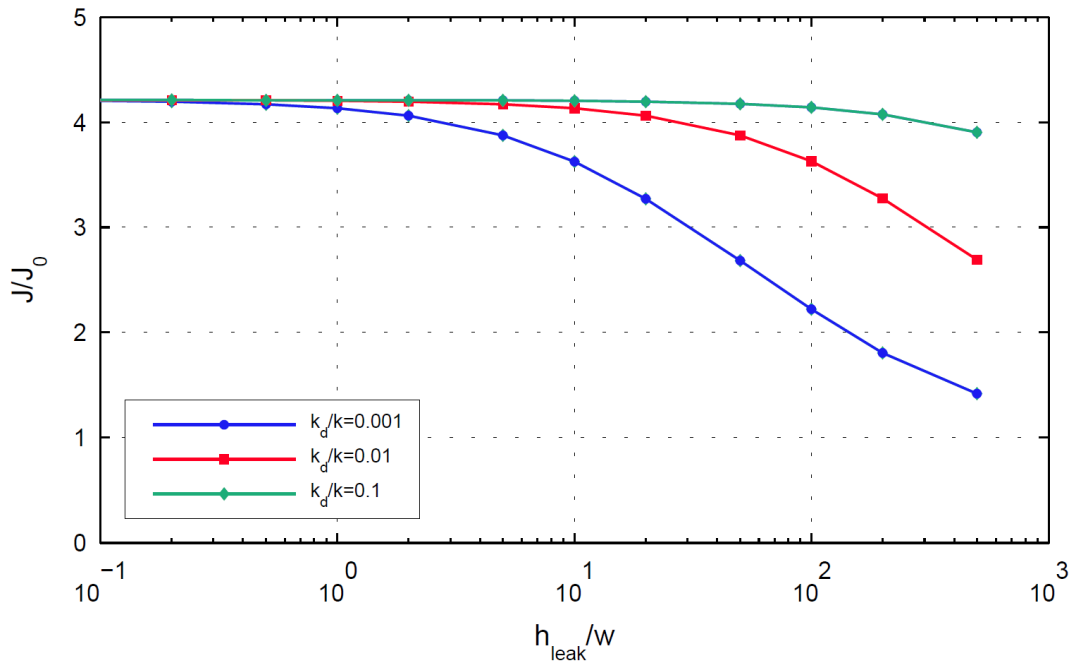


Figure 8.13: Impact of invaded zone length on productivity ($L_f/L_{drained}=1$ and $F_{cd}=0.6$).

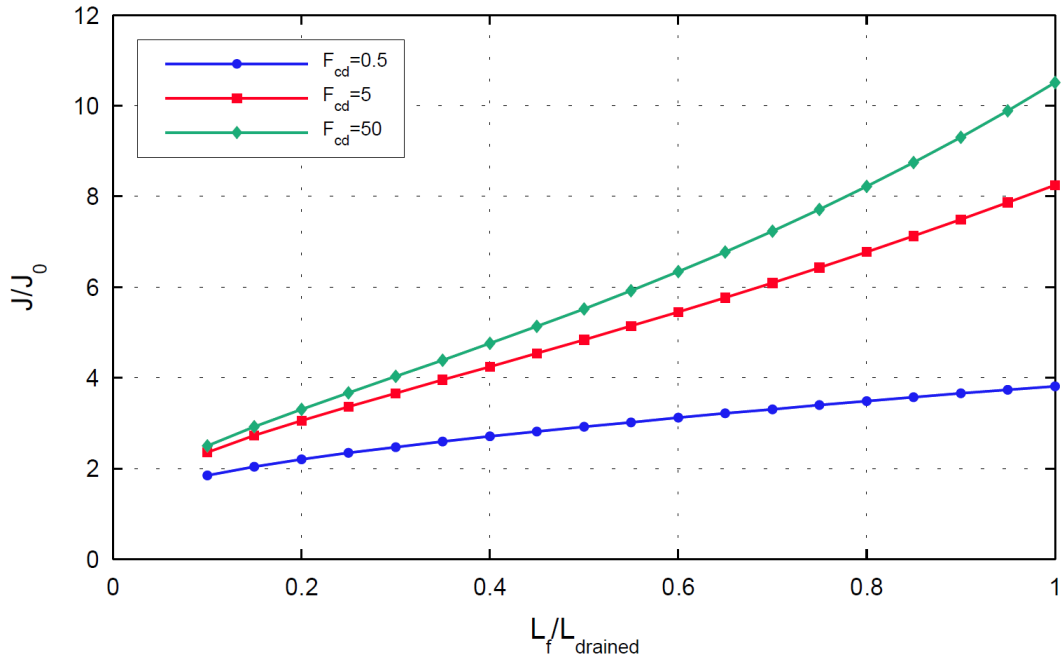


Figure 8.14: Impact of fracture length on productivity ($k_d/k=0.01$ and $h_{leak}/w=20$).

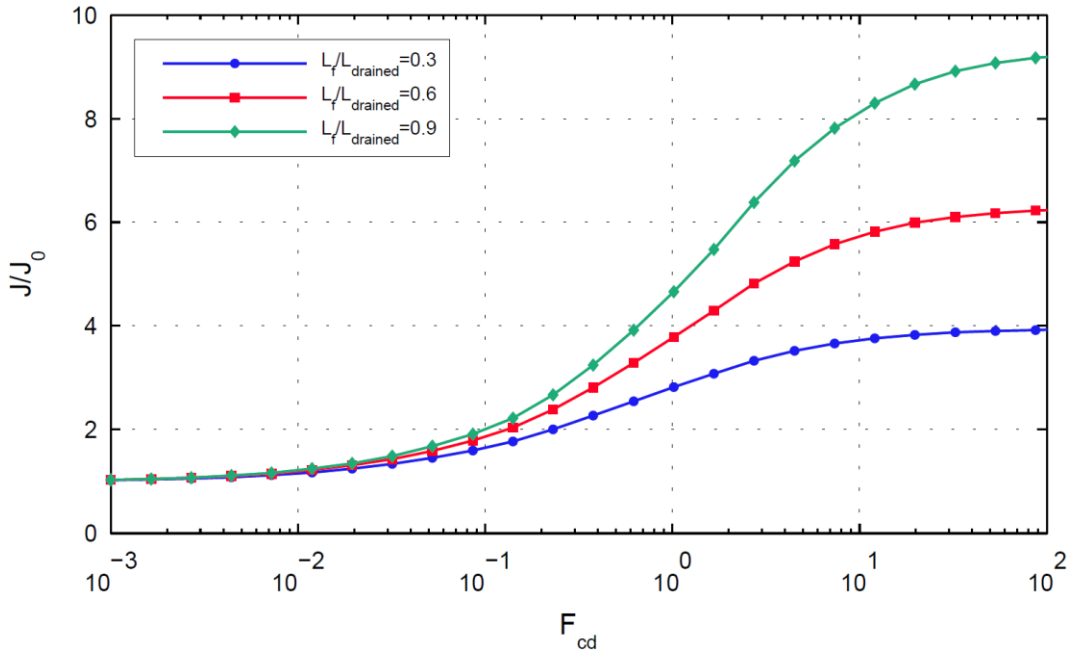


Figure 8.15: Impact of fracture conductivity on productivity for different fracture lengths ($k_d/k=0.005$ and $h_{leak}/w=20$).

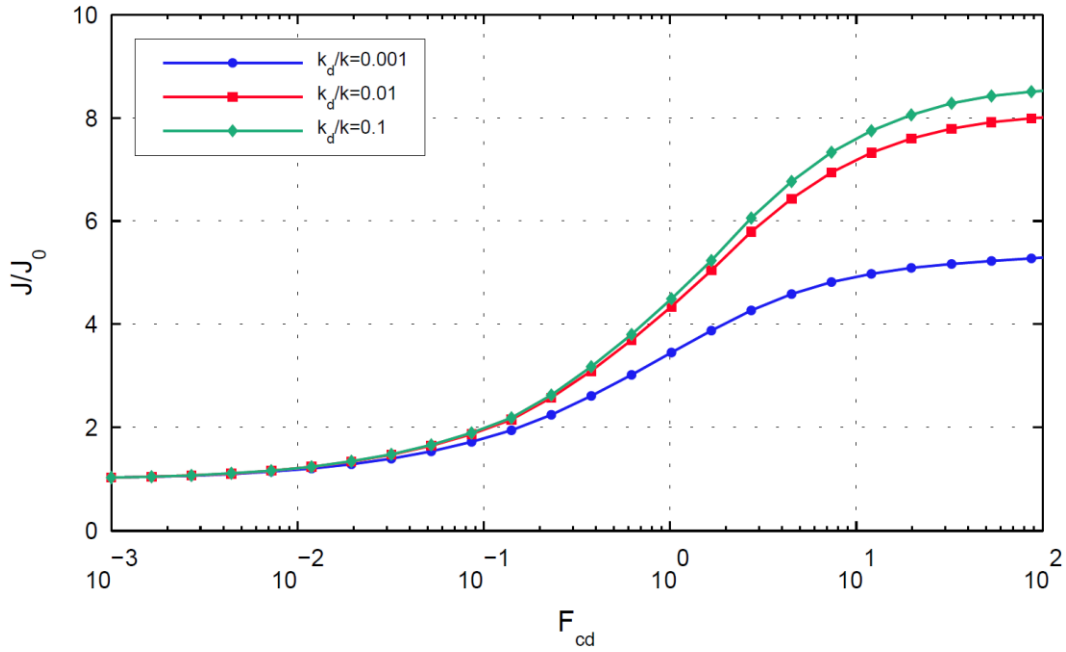


Figure 8.16: Impact of fracture conductivity on productivity for different permeabilities in an undamaged reservoir ($L_f/L_{drained}=0.8$ and $h_{leak}/w=50$).

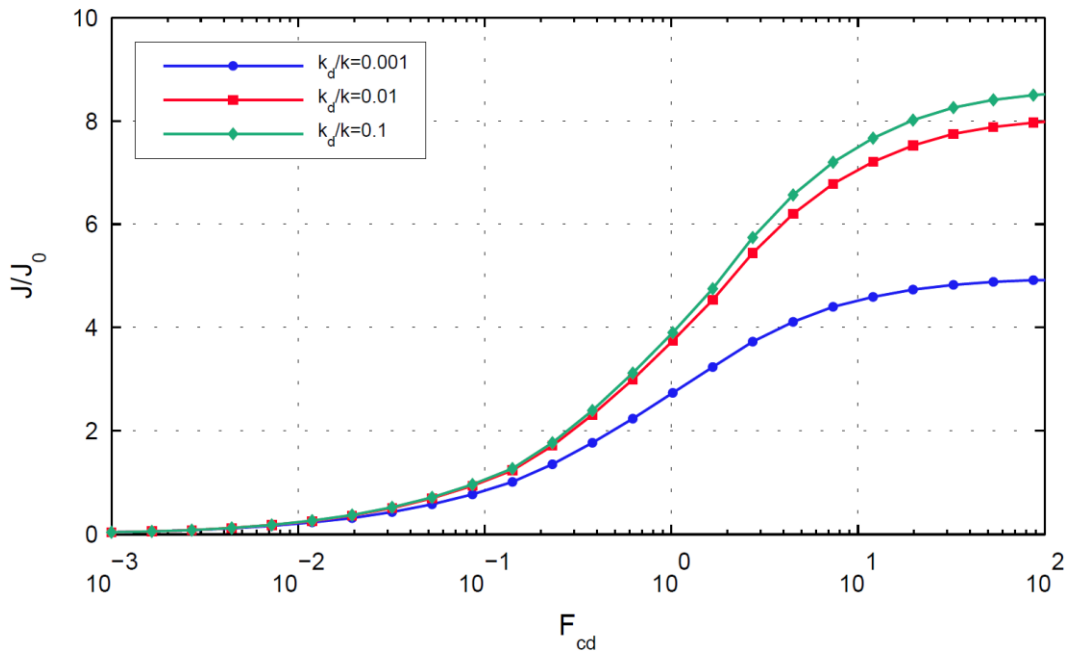


Figure 8.17: Impact of fracture conductivity on productivity for different permeabilities in a damaged reservoir ($L_f/L_{drained}=0.8$, $h_{leak}/w=50$, $k_s/k=0.001$, and $r_s/r_w=3$).

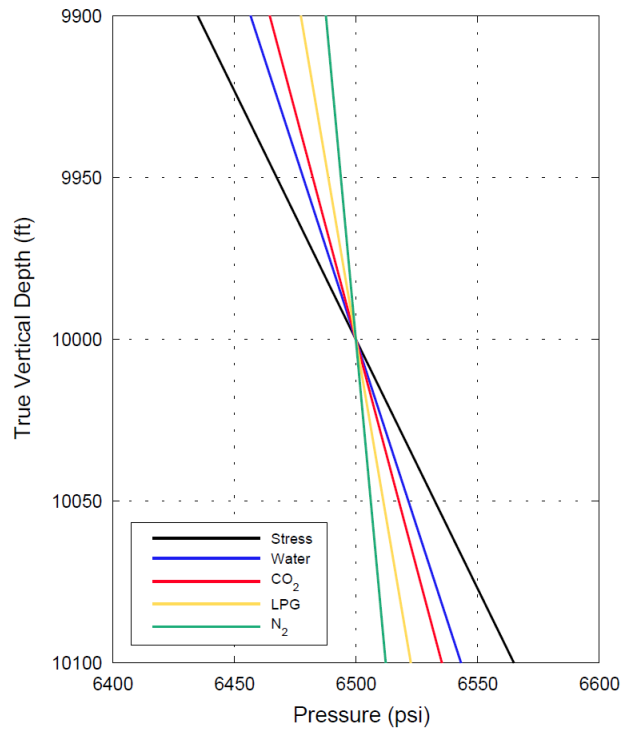


Figure 8.18: Impact of fluid density on fracture propagation. Lighter fluids are more prone to vertical migration because of the increasing contrast between the stress gradient (0.65 psi/ft here) and the fluid gradient (0.433, 0.354, 0.222, and 0.125 psi/ft for water, CO₂, LPG and N₂, respectively) in a given layer.

NOMENCLATURE

C_w	= leakoff coefficient, ft/ $\sqrt{\text{min}}$
E	= Young's modulus, psi
F_{cd}	= fracture conductivity
h_f	= fracture height, ft
h_{leak}	= invaded zone length, ft
h_{pay}	= pay zone height, ft
J	= productivity index, BPD/psi
J_0	= productivity index for unfractured, undamaged well, BPD/psi
k	= reservoir permeability, mD
k_d	= damaged zone permeability (effective permeability of the producing phase i.e. oil/gas)
k_{rnw}	= relative permeability of non-wetting phase
k_{rnw0}	= endpoint relative permeability of non-wetting phase
k_s	= permeability of (mechanical) damage around the wellbore, mD
$L_{drained}$	= drainage radius, ft
L_f	= fracture half-length, ft
n	= Corey exponent in relative permeability curve
r_s	= mechanical skin radius, ft
r_w	= wellbore radius, ft
S_{nwr}	= residual non-wetting phase saturation
S_w	= wetting phase saturation
S_{wr}	= residual wetting phase saturation
w	= fracture width, ft
ν	= Poisson's ratio

REFERENCES

- Friehauf, K.E. 2009. Simulation and Design of Energized Hydraulic Fractures. Ph.D. Dissertation, The University of Texas at Austin, Austin, Texas (August 2009).
- Friehauf, K.E. and Sharma, M.M. 2009. A New Compositional Model for Hydraulic Fracturing With Energized Fluids. *SPE Prod & Oper* **24**(4): 562-572. SPE 115750-PA.
- Friehauf, K.E., Suri, A., and Sharma, M.M. 2010. A Simple and Accurate Model for Well Productivity for Hydraulically Fractured Wells. *SPE Prod & Oper* **25**(4): 453-460. SPE 119264-PA.
- GasFrac Energy Services, 2013. Documentation available at <http://www.gasfrac.com/safer.html>.
- Harris, P.C. 1985. Dynamic Fluid-Loss Characteristics of Nitrogen Foam Fracturing Fluids. *J. Pet Tech* **37**(11): 1847-1852. SPE 11065-PA.
- Harris, P.C. 1987. Dynamic Fluid-Loss Characteristics of CO₂-Foam Fracturing Fluids. *SPE Prod Eng* **2**(2): 89-94. SPE 13180-PA.
- Reidenbach, V.G., Harris, P.C., Lee, Y.N, and Lord, D.L. 1986. Rheological Study of Foam Fracturing Fluids using Nitrogen and Carbon Dioxide. *SPE Prod Eng* **1**(1): 31-41. SPE 12026-PA.
- Ribeiro, L.H. and Sharma, M.M 2013a. A New 3D Compositional Model for Hydraulic Fracturing with Energized Fluids. *SPE Prod & Oper* **28**(3): 259-267. SPE 159812-PA.
- Ribeiro, L.H. and Sharma, M.M 2013b. A Three-Dimensional Compositional Model for Hydraulic Fracturing with Energized Fluids. Paper ARMA 13-409 presented at the 47th U.S. Rock Mechanics/Geomechanics Symposium, San Francisco, California, 23-26 June 2013.
- Watts, R. 2013. A Day in the Life of a Barrel of Water. Transcript of the presentation made at the 4th Annual AIPG Symposium, Canton, Ohio. 10 April.

Chapter 9: Conclusions and Recommendations

9.1 SUMMARY

The use of gases and foams has experienced a significant resurgence in popularity with the development of unconventional reservoirs. Nevertheless, current practices in energized treatments remain rudimentary in comparison to other fracturing fluid technologies. None of the available 3D fracturing models for incompressible water-based fluids have been able to capture the thermal and compositional effects that are important in energized fluids. In these models, the constitutive equations assume single-phase, single-component, incompressible fluid flow; therefore, they do not accurately capture the unique behavior of these fluids.

The primary objective of this work was to improve the design of energized fracturing treatments using a fully compositional 3D fracturing model (Ribeiro and Sharma 2013a, 2013b, and 2013c). The main tasks accomplished in this dissertation may be further broken down as follows:

1. We formulated a well-posed mathematical problem that governs the propagation of a 3D planar fracture initiated by an energized fluid.
2. We developed the first compositional 3D fracturing simulator. Notably, the simulator captures the thermal and compositional changes occurring in the fracturing fluid.
3. We implemented a fractured well productivity model to assess the performance of the fracturing treatment.

4. We provided design recommendations for different types of reservoirs in lieu of a costly field trial-and-error approach.
5. We identified reservoir parameters that are critical for fluid selection.
6. We emphasized the need for supporting laboratory and field testing to complement our modeling study.

9.2 CONCLUSIONS

9.2.1 Capabilities of the Fracturing Simulator

The combination of the fracture, productivity, and wellbore models presented in this dissertation forms a standalone modeling tool to design and optimize energized treatments. The main differences between this model and a traditional 3D planar model are comparable to the differences between a compositional reservoir model and a black oil reservoir model. The proposed simulator includes the following capabilities:

1. The model allows for multi-phase, multi-component, compressible fluid flow both in the fracture and in the wellbore.
2. The model predicts variations in temperature, pressure, and fluid composition.
3. The fracture can propagate across multiple layers, where height growth is controlled by the vertical distribution of the minimum horizontal stress.
4. The model is suitable for any well configuration: vertical, deviated, or horizontal.
5. The fracture model is connected to a productivity model, which is similar to the model developed by Friehauf, Suri, and Sharma (2010). The model accounts for:

- (i) two-phase fluid flow, (ii) damage in the invaded zone, (iii) finite fracture conductivity, (iv) mechanical skin, and (v) changes in fluid composition.
6. The model is suitable for many different applications ranging from hydraulic fracturing to long-term injections for enhanced oil recovery, well clean-up, or carbon sequestration purposes.

9.2.2 Design Recommendations

Although fluid selection should be evaluated on a case-by-case basis, several design recommendations can be made based upon the analysis of the results presented in this dissertation:

1. If the fluid-induced damage is acceptable, water-based fluids constitute a simple and attractive solution. This is the case when the drawdown pressure is sufficient to recover the damaging fluid.
2. When water blocking severely impedes gas flow, the use of energized fluids improves clean-up and well productivity.
3. Reductions in relative permeability to gas (oil) by less than a factor of ten do not affect hydrocarbon production; therefore, low-quality foams often allow enough gas to invade the formation to limit the water blocking effect.
4. In depleted reservoirs, recovering any of the water lost to the formation is challenging because the drawdown pressure is limited. Alternatively, energized fluids experience a significant fluid expansion that improves fluid clean-up.
5. In under-saturated rocks, any water lost to the rock matrix remains trapped, thereby lowering the relative permeability to gas. When energized fluids are used,

an extended shut-in can improve fluid clean-up by placing an additional amount of gas into the formation.

6. Non-aqueous fluids such as LPG and CO₂ are preferred in reservoirs that are prone to excessive fines migration and clay swelling. High-quality foams reduce the amount of water in contact with clays, although they do not eliminate clay swelling.
7. Fluids with higher solubility in the liquid phase have an increased ability to reduce damage in the invaded zone. Adding a component such as methanol increases the solubility of CO₂ in the liquid phase and alleviates fine migration and clay swelling in some sandstone reservoirs.
8. High-quality foams favor the propagation of short and wide fractures of high fracture conductivities, while low-quality foams promote the propagation of elongated fractures.
9. In many reservoirs, comingled fluids (30 to 50% quality) are optimum because they not only create long fractures with satisfactory proppant placement, but they also reduce the fluid-induced damage enough to ensure good flowback performance.
10. An extended shut-in is detrimental when damaging fluids are used because more liquid invades the rock formation. However, some of the proppant may be recovered when the fracturing fluid is flowed back immediately. If this is the case, it is important to slowly bring the well back to production by carefully ramping-up the production rate.

9.2.3 Unique Properties of Energized Fluids

The additional complexity of the compositional model enables us to model the unique properties of energized fluids; therefore, an accurate fluid characterization that is consistent with experimental data is critical for evaluating fluid performance. In this study, we highlighted the impact of the following fluid properties:

1. *Density*: Under typical fracturing conditions, CO₂, LPG, and N₂ expand by more than 15% inside the fracture as the reservoir heats the fluid.
2. *Solubility*: Under typical fracturing conditions, the mass fraction of CO₂ in water is between 5% and 10%. The addition of methanol increases CO₂ solubility to more than 20% on a mass basis.
3. *Rheology*: Foams offer a wide range of viscosities without using excessive amounts of gelling agents and additives. At high shear rates, high-quality foams are dramatically more viscous than the base-fluid while low-quality foams have a viscosity similar to the base-fluid.
4. *Filter-cake*: Foams provide superior fluid-loss control without using excessive amounts of gelling agents. The filter-cake is supplemented by the presence of gas bubbles that reduce liquid-flow into the porous medium.
5. *Liquid leak-off*: Our experimental work showed that low-quality foams were effective at reducing liquid leak-off (by at least a factor of three), and high-quality foams further reduced liquid invasion by a factor of two.
6. *Gas leak-off*: We demonstrated that the gas phase leaks off into the reservoir. The ability of the gas to invade the reservoir has a critical effect on fracture design and well productivity.

Essentially, energized fluids offer properties similar to any water-based fluids in terms of fracture creation, proppant transport, and fracture conductivity, while also offering the advantage of limited fluid-induced damage as compared to water-based fluids. Nevertheless, the use of energized fluids typically requires larger capital expenditures, so it would only make sense to use these fluids when the profits associated with increased production outweigh the additional expenditures. The following safety and economic considerations play important roles in fluid selection:

1. *Safety hazards:* The use of gases requires additional safety measures because of their compressibility. High-pressure storage units are required, with numerous instruments to prevent and monitor potential leaks. This is also true when using LPG because of its flammability and volatility.
2. *Operational considerations:* The use of gases such as N₂ and LPG may require pumping equipment with more horsepower because of the limited weight of the fluid column inside the wellbore. When using foams, care should be taken to avoid the formation of extremely-high-viscosity foams, which would halt pumping operations.
3. *Cost and availability:* In certain areas, the use of large quantities of gas is prohibitive because of the costs associated with the deployment of many trucks and pressurized storage units. Notably, this is the case in remote areas where there are no nearby gas power plants or pipelines.

9.3 RECOMMENDATIONS FOR FUTURE WORK

9.3.1 Usability of the Simulator

The recommendations presented in this section are intended to improve the current version of the simulator, without proposing fundamentally different capabilities. These improvements would, instead, make the simulator more user-friendly, by improving its accuracy, speed, and usability on the field.

1. *Field validation*: Although we worked in close collaboration with major gas providers, we did not have the opportunity to calibrate the model against field data. The calibration and field validation of the model is one of the key areas of improvement for this work, and we recommend history-matching the rate and net-pressure response of several treatments in the future. A comparison with micro-seismic data would benefit this work, as it would give us reasonable confidence that the essential physics of the problem have been captured.
2. *Computation speed and accuracy*: Over the past decade, there have been significant developments in re-meshing techniques and adaptive schemes for moving boundary problems. Notably, the video game industry has developed fast and flexible unstructured meshing schemes that could be applicable to fracturing. In addition, new solvers and interpolation schemes could be implemented to improve current gridding capabilities, reduce computation time, and improve numerical stability.
3. *Numerical accuracy*: Oscillations are frequent when solving convection-dominated equations. To dampen oscillations, one of the most popular approaches is to use *upwind* discretization schemes. In upwind schemes, the spatial

differences are skewed in the upwind direction, i.e. the direction from which the flow originates, so that the numerical scheme “follows” the transport of the quantity of interest. More advanced discretization schemes, such as *multi-level* and *Lax Wendroff* schemes, could improve the accuracy of the numerical solution (Morton and Mayers 1995, Chapter 4).

4. *Near-wellbore friction loss*: As discussed in Section 5.3, the current treatment of the near-wellbore friction drop in deviated and horizontal wells is limited. A comprehensive study on the effect of fracture re-orientation, turning, and twisting would be beneficial, particularly for history-matching net pressure data.
5. *Front advancement*: Propagation speed is controlled by the maximum front displacement, which is a numerical parameter that is not estimated from experimental data. Thus, its impact on the propagation process is not desirable. We recommend investigating better ways to control front advancement, such as monitoring the velocity of the fluid front near the fracture tip (Linkov 2011).
6. *Fluid description*: As discussed in Chapter 7, we used empirical correlations to estimate phase density and component solubility in order to reduce computation time. However, several discrepancies occurred at low-to-moderate pressures, as shown in Section 7.1. A more accurate representation of the fluid behavior would better capture the essential physics of the problem.
7. *User interface*: To improve the implementation of the simulator in the field, users could upload well logs to extract the stress distribution and the mechanical properties of the reservoir layers. Also, the interface could display the results in real time to allow rate and pressure adjustments during the fracturing treatment.

9.3.2 Key Areas of Improvement

The following recommendations would constitute major improvements to the current model:

1. *Flowback and productivity model*: The reservoir is represented by a superposition of individual planes; therefore, there is no cross-flow, and gravity effects are not accounted for inside the reservoir. These assumptions are too simplistic to evaluate a gravity-driven liquid unloading process (Agrawal and Sharma 2013). A major improvement would be to link the fracture model to a fully compositional reservoir model.
2. *Multi-fracture propagation (without stress interferences)*: When multiple fractures are initiated simultaneously (either from different layers in a vertical well, or from different clusters in a horizontal well), they do not grow independently. Even if the stress interferences between fractures are not accounted for, one fracture (or more) dominates the surrounding fractures, as it receives more fluid. The objective would be to determine the fraction of the total flow rate entering each set of perforations.
3. *Multi-fracture propagation (with stress interferences)*: When multiple fractures are initiated, the growth of a given fracture generates a local stress change perturbing the growth of the surrounding fractures. This effect, often referred to as *stress shadow*, results from mechanical interactions between nearby fractures. A reservoir geomechanics model would be required to solve the elasticity problem in the portion of the reservoir containing the fractures. An alternative would be to use an analytical expression similar to the one first proposed by Sneddon (1946).

4. *Curving fracture propagation with an arbitrary direction:* The first challenge is to propagate a curved fracture following a known direction of propagation. As the fracture turns, additional stresses are generated, which makes the problem highly anisotropic and non-symmetric. The second challenge is to determine the path the fracture follows. The direction of fracture propagation depends on the local stress orientation, which may be altered by mechanical interactions between fractures and poroelastic stresses (Roussel 2011).
5. *Pressure-dependent leak-off:* In naturally-fractured reservoirs, Carter's leak-off model may not offer a realistic representation of fluid leak-off. In these reservoirs, leak-off may be dominated by discrete natural fractures that act as local sink terms. Using an averaged leak-off coefficient for the entire fracture surface is not representative of this behavior.
6. *Thermal stresses:* As the fluid leaks-off into the reservoir, it typically cools down the rock formation surrounding the well. The subsequent change in temperature causes the rock to contract, thereby altering the stresses both in the region of reduced temperature and in the surrounding rock. The thermoelastic stresses can be obtained from an analytical formula (Perkins and Gonzalez 1984).
7. *Poroelastic stresses:* Fluid leak-off modifies pore pressure, and hence the stress state of the rock. Lubinski (1954) showed that, for a non-deformable pore structure, the poroelastic stresses can be evaluated analytically using a linear coefficient of pore pressure expansion. This correction could easily be incorporated into the simulator.

8. *Heterogeneity*: In the current model, each reservoir layer is homogenous with constant mechanical properties, and the stress distribution is identical for each horizontal section of the reservoir. A possible improvement would be to incorporate a more realistic representation of the reservoir and to propose a model that would be suitable to account for reservoir heterogeneity.

9.3.3 Fluid Characterization

An accurate fluid characterization is critical to ensure that the simulations are realistic; therefore, we recommend the following experimental studies:

1. *Leak-off*: The only published data on multi-phase leak-off were presented by Harris (1985, 1987), Penny *et al.* (1985), and Ribeiro and Sharma (2012). These data are too limited to estimate multi-phase leak-off in many reservoirs, primarily because the data were obtained with rock samples of permeabilities higher than 0.1 mD. We recommend measuring the multi-phase leak-off of foams under a wider range of reservoir conditions. The experimental setup described by Ribeiro and Sharma (2012) may be a starting point for the study.
2. *Slurry rheology*: The rheology of foams and gelled CO₂ and LPG fluid formulations is poorly documented. Specifically, the effect of proppant concentration on rheology is poorly understood. Additional experimental studies are thus required to properly characterize the rheology and proppant transport capabilities of common energized fluids.
3. *Interactions with reservoir fluids*: In this dissertation, the fluid leaking-off displaces the reservoir fluids in a 1D piston-like manner. In reality, leak-off is a complicated process, in which the fracturing fluid is displacing one or two

hydrocarbon mixtures. The interactions between the fluid leaking-off and the reservoir fluids are not fully understood. For instance, CO₂ can swell the oil phase and reduce its mobility, thereby affecting flowback and the subsequent hydrocarbon production. An experimental study on the impact of fluid invasion on the regain permeability to gas (oil) would improve our understanding of the flowback performance.

The work presented in this dissertation introduced the first version of a new, fully compositional, 3D fracturing simulator. We expect many improvements to the simulator in the future, as this field of study is emerging in the industry. As water supply becomes constrained in many areas, reducing the water footprint and the environmental impact is of paramount concern. We hope that this work will contribute to a more efficient implementation of energized treatments in the field, not only to reduce water usage, but also to improve oil and gas production.

REFERENCES

- Agrawal, S. and Sharma, M.M 2013. Impact of Liquid Loading in Hydraulic Fractures on Well Productivity. Paper SPE 163837 presented at the SPE Hydraulic Fracturing Technology Conference, The Woodlands, Texas, 4-6 February.
- Friehauf, K.E., Suri, A., and Sharma, M.M. 2010. A Simple and Accurate Model for Well Productivity for Hydraulically Fractured Wells. *SPE Prod & Oper* **25**(4): 453-460. SPE 119264-PA.
- Harris, P.C. 1985. Dynamic Fluid-Loss Characteristics of Nitrogen Foam Fracturing Fluids. *J. Pet Tech* **37**(11): 1847-1852. SPE 11065-PA.
- Harris, P.C. 1987. Dynamic Fluid-Loss Characteristics of CO₂-Foam Fracturing Fluids. *SPE Prod Eng* **2**(2): 89-94. SPE 13180-PA.
- Linkov, A.M. 2011. On Efficient Simulation of Hydraulic Fracturing in terms of particle Velocity. *Int. J. Eng. Sci.* **52**: 77-88.
- Lubinski, A. 1954. The Theory of Elasticity for Porous Bodies Displaying a Strong Pore Structure. *Proc. 2nd U.S. Congress of Appl. Mech.*: 247-256.
- Morton, K.W. and Mayers D.F. 1995, *Numerical Solution of Partial Differential Equations* (Chapter 4), Cambridge University Press, New York City, New York.
- Penny, G.S., Conway, M.W, and Lee, W. 1985. Control and Modeling of Fluid Leakoff During Hydraulic Fracturing. *J. Pet Tech* **37**(6): 1071-1081. SPE 12486-PA.
- Perkins, T.K. and Gonzalez, J.A. 1984. Changes in Earth Stresses Around a Wellbore Caused by Radially Symmetrical Pressure and Temperature Gradients. *SPE J.* **24**(2): 129-140. SPE 10080-PA.
- Ribeiro, L.H. and Sharma, M.M.. 2012. Multi-Phase Fluid-Loss Properties and Return Permeability of Energized Fracturing Fluids. *SPE Prod & Oper* **27**(3): 265-277. SPE 139622-PA.
- Ribeiro, L.H. and Sharma, M.M 2013a. Fluid Selection for Energized Fracture Treatments. Paper SPE 163867 presented at the SPE Hydraulic Fracturing Technology Conference, The Woodlands, Texas, 4-6 February.
- Ribeiro, L.H. and Sharma, M.M 2013b. A Three-Dimensional Compositional Model for Hydraulic Fracturing with Energized Fluids. Paper ARMA 13-409 presented at the 47th U.S. Rock Mechanics/Geomechanics Symposium, San Francisco, California, 23-26 June 2013.
- Ribeiro, L.H. and Sharma, M.M 2013c. A New 3D Compositional Model for Hydraulic Fracturing with Energized Fluids. *SPE Prod & Oper* **28**(3): 259-267. SPE 159812-PA.

Roussel, N.P. 2011. Stress Reorientation in Low Permeability Reservoirs. Ph.D. Dissertation, The University of Texas at Austin, Austin, Texas (August 2011).

Sneddon, I.N 1946. The Distribution of Stress in the Neighbourhood of a Crack in an Elastic Solid. *Proc Roy Soc Lond, Series A* **187**: 229-260.

References

- Abel, J.C. 1981. Application of Nitrogen Fracturing in the Ohio Shale. Paper SPE 10378 presented at the SPE Eastern Regional Meeting, Columbus, Ohio, 4-6 November.
- Abou-Sayed, A.S, Sinha, K.P., and Clifton, R.J 1984. Evaluation of the Influence of *In-Situ* Reservoir Conditions on the Geometry of Hydraulic Fractures Using a 3-D Simulator: Part 1–Technical Approach, Paper SPE/DOE/GRI 12877, Unconventional Gas Recovery Symposium, Pittsburg, Pennsylvania, 13-15 May.
- Adachi, J.I, Siebrits, E., Peirce, A., and Desroches, J. 2007. Computer Simulation of Hydraulic Fractures, *Int. J. Rock Mech. and Min. Sci. & Geomech.* **44**: 739-757.
- Advani, S. and Lee, J. 1982. Finite Element Model Simulations Associated with Hydraulic Fracturing. *SPE J.* **22**(2): 209-219. SPE 8914-PA.
- Agrawal, S. and Sharma, M.M 2013. Impact of Liquid Loading in Hydraulic Fractures on Well Productivity. Paper SPE 163837 presented at the SPE Hydraulic Fracturing Technology Conference, The Woodlands, Texas, 4-6 February.
- Alekseenko, O.P., Potapenko, D.I., Cherny, S.G., Esipov, D.V., Kuranakov, D.S., and Lapin, V.N. 2013. 3D Modeling of Fracture Initiation From Perforated Non-cemented Wellbore. *SPE J.* (to be published). SPE 151585-PA.
- Barree, R.D. and Winterfeld, P.H. 1998. Effects of Shear Planes and Interfacial Slippage on Fracture Growth and Treating Pressures. Paper SPE 48926 presented at the SPE Annual Technical Conference and Exhibition, New Orleans, Louisiana, 27-30 September.
- Becker, E.B., Carey, G.F., and Oden, J.T. 1981, *Finite Elements: An Introduction*, Volume 1, Prentice-Hall, Inc., Englewood Cliffs, NJ.
- Beggs, D.H. and Brill, J.P. 1973. A Study of Two-Phase Flow in Inclined Pipes. *J. Pet Tech* **25**(5): 607-617. SPE 4007-PA.
- Bleakley, W.B. 1980. Mitchell Energy Foam Fracs Tight Gas Zones. *Pet. Eng. Intern.* December 1980: 24-28.
- Brooks, R.H. and Corey, A.T. 1966. Properties of Porous Media Affecting Fluid Flow. *J. Irrigation and Drainage Div., Proc. ASCE* **92**: 61-88.
- Bui, H. 1977. An Integral Equations Method for Solving the Problem of a Plane Crack of Arbitrary Shape. *J. Mech. Phys. Solids* **25**: 29-39.
- Burke, L.H., Nevison, G.W., and Peters W.E. 2011. Improved Unconventional Gas Recovery With Energized Fracturing Fluids: Montney Example. Paper SPE 149344 presented at the SPE Eastern Regional Meeting, Columbus, Ohio, 17-19 August.

- Carslaw, H.S. and Jaeger, J.C. 1959, *Conduction of Heat in Solids*, 2nd edition, Clarendon Press, Oxford, UK.
- Carter, R.D. 1957. Derivation of the general equation for estimating the extent of the fractured area, Appendix to *Optimum Fluid Characteristics for Fracture Extension*, by Howard, G.C. and Fast, C.R., *Drilling and Production Practices*, API: 261-270.
- Chesapeake, water usage website, 2012. Available at <http://www.hydraulicfracturing.com/Water-Usage/Pages/Information.aspx>.
- Cleary, M.P., Kawadas, M., and Lam, K.Y. 1983. Development of a Fully Three-Dimensional Simulator for Analysis and Design of Hydraulic Fracturing. Paper SPE 11631 presented at the Symposium on Low-Permeability Gas Reservoirs, Denver, Colorado, 14-16 March.
- Clifton, R.J. and Abou-Sayed, A.S. 1981. A Variational Approach to the Prediction of the Three-Dimensional Geometry of Hydraulic Fractures. Paper SPE 9879 presented at the SPE/DOE Low Permeability Gas Reservoirs Symposium, Denver, Colorado, 27-29 May.
- Crump, J. and Conway, M. 1988. Effects of Perforation-Entry Friction on Bottomhole Treating Analysis. *J. Pet Tech* **40**(8): 1041-1048. SPE 15474-PA.
- Dahi-Taleghani, A. and Olson, J.E. 2011. Numerical Modeling of Multistranded-Hydraulic-Fracture Propagation: Accounting for the Interaction Between Induced and Natural Fractures. *SPE J.* **16**(3): 575-581. SPE 124884-PA.
- Dantas, T.N., Santanna, V.C., Neto, A.A. and Moura M.C. 2005. Hydraulic Gel Fracturing. *J. Dispersion Sci. Technol.* **26**: 1-4.
- de Pater, C.J. and Beugelsdijk, L.J.L. 2005. Experiments and Numerical Simulation of Hydraulic Fracturing in Naturally Fractured Rock. Paper ARMA 05-780 presented at The 40th U.S. Symposium on Rock Mechanics (USRMS), Anchorage, Alaska, 25-29 June.
- Denn, M.M. 1980, *Process Fluid Mechanics*, Prentice Hall, Englewood Cliffs, New Jersey.
- Economides, M. and Nolte, K.G. 2000, *Reservoir Stimulation, Third Edition*, John Wiley and Sons, New York City, New York.
- Freeman, E.R., Abel, J.C., Kim, C.M., and Heinrich, C. 1983. A Stimulation Technique Using Only Nitrogen. *J. Pet Tech* **35**(12): 2165-2174. SPE 10129-PA.
- Friehauf, K.E. 2009. Simulation and Design of Energized Hydraulic Fractures. Ph.D. Dissertation, The University of Texas at Austin, Austin, Texas (August 2009).
- Friehauf, K.E. and Sharma, M.M. 2009. A New Compositional Model for Hydraulic Fracturing With Energized Fluids. *SPE Prod & Opera* **24**(4): 562-572. SPE 115750-PA.
- Friehauf, K.E., Suri, A., and Sharma, M.M. 2010. A Simple and Accurate Model for Well Productivity for Hydraulically Fractured Wells. *SPE Prod & Oper* **25**(4): 453-460. SPE 119264-PA.

- Gabris S. and Taylor J., 1986. The Utility of CO₂ as an Energizing Component for Fracturing Fluids. *SPE Prod Eng* **1**(5): 351-358. SPE 13794-PA.
- Gadde P. B., Liu Y., Norman J., Bonnecaze, R. and Sharma, M. M. 2004. Modeling Proppant Settling in Water-Fracs. Paper SPE 89875 presented at the SPE Annual Technical Conference and Exhibition, Houston, Texas, 26-29 September.
- GasFrac Energy Services, 2013. Documentation available at <http://www.gasfrac.com/safer.html>.
- Geertsma, J., and de Klerk, F. 1969. A Rapid Method of Predicting Width and Extent of Hydraulically Induced Fractures. *J. Pet Tech* **21**(12): 1571-1581. SPE 2458-PA.
- Gidley, J.L., Holditch, S.A., Nierode, D.E., and Veatch, R.W. Jr. 1989. *Recent Advances in Hydraulic Fracturing*. Monograph Series **12**, SPE, Richardson, Texas.
- Goodman, J.B and Krase, N.W. 1931. Solubility of Nitrogen in Water at High Pressures and Temperatures. *Ind. Eng. Chem*, **23**: 401-404
- Gottschling, J.C., Royce, T.N., and Shuck, L.Z. 1985. Nitrogen Gas and Sand: A New Technique for Stimulation of Devonian Shale. *J. Pet Tech* **37**(5): 901-907. SPE 12313-PA.
- Granado, L.E., Garritano R., Loreface, R., and Ceccarelli, R.L. 2013. Revitalizing Mature Gas Field Using Energized Fracturing Technology In South Italy. Paper SPE 164649 presented at the SPE North Africa Technical Conference and Exhibition, Cairo, Egypt, 15-17 April.
- Groenenboom, J., van Dam, D.B. and de Pater, C.J 2001. Time-Lapse Ultrasonic Measurements of Laboratory Hydraulic-Fracture Growth: Tip Behavior and Width Profile. *SPE J.* **6**(1): 14-24. SPE 68882-PA.
- Grundman, S.R. 1983. Foam Stimulation. *J. Pet Tech* **35**(3): 597-602. SPE 9754-PA.
- Gu, H. 1987. A Study of Propagation of Hydraulically Induced Fractures, Ph.D. Dissertation, The University of Texas at Austin, Austin, Texas (December 1987).
- Gupta, D.V.S. 2011. Unconventional Fracturing Fluids: What, Where and Why. Technical Workshops for the Hydraulic Fracturing Study, U.S. E.P.A., presented at Arlington, Virginia, February 2011.
- Gupta, D.V.S. and Bobier, D.M. 1998. The History and Success of Liquid CO₂ and CO₂/N₂ Fracturing System. Paper SPE 40016 presented at the SPE Gas Technology Symposium, Calgary, Canada, 15–18 March.
- Harris, P.C. 1985. Dynamic Fluid-Loss Characteristics of Nitrogen Foam Fracturing Fluids. *J. Pet Tech* **37**(11): 1847-1852. SPE 11065-PA.
- Harris, P.C. 1987. Dynamic Fluid-Loss Characteristics of CO₂-Foam Fracturing Fluids. *SPE Prod Eng* **2**(2): 89-94. SPE 13180-PA.

- Harris, P.C. 1992. Application of Foam Fluids To Minimize Damage During Fracturing. Paper SPE 22394 presented at the International Meeting on Petroleum Engineering, Beijing, China, 24-27 March.
- Harris, P.C., Klebenow, D.E., and Kundert, D.P. 1991. Constant-Internal-Phase Design Improves Stimulation Results. *SPE Prod Eng* **6**(1): 15-19. SPE 17532-PA
- Hasan, A. and Kabir, S. 1994. Aspects of heat Transfer During Two-Phase Flow in Wellbores. *SPE Prod & Fac* **9**(1): 12-16. SPE 22948-PA.
- Hasan, A. and Kabir, S. 2002, *Fluid Flow and Heat Transfer in Wellbores*, Society of Petroleum Engineers, 2002.
- Hasan, A. and Kabir, S. 2012. Wellbore Heat-Transfer Modeling and Applications. *J. Pet Sci. & Eng.* **86**: 127-136.
- Hossain M.M., Rahman M.K. and Rahman, S.S. 2002. A Shear Dilation Stimulation Model for Production Enhancement From Naturally Fractured Reservoirs. *SPE J.* **7**(2): 183-195. SPE 78355-PA.
- Hurst, R.E. 1972. Use of Liquified Gases as Fracture Fluids for Dry Gas Reservoirs. Paper SPE 4116 presented at the Fall Meeting of the Society of Petroleum Engineers of AIME, San Antonio, Texas, 8-11 October.
- Hutchins, R.D. and Miller, M.J. 2005. A Circulating-Foam Loop for Evaluating Foam at Conditions of Use. *SPE Prod & Fac* **20**(4): 286-294. SPE 80242-PA.
- Jones, R.H. and Hirth, J.P. 2001. Effects on Mixed-Mode I/III Loading on Environment-Induced Cracking. *J. Corrosion* **57**(1).
- Jonoud, S., Wennberg, O.P. Casini, G., and Larsen, J.A. 2013. Capturing the Effect of Fracture Heterogeneity on Multiphase Flow During Fluid Injection. *SPE RE & E* **16**(2): 194-208. SPE 147834-PA.
- Kassir, M.K. and Sih, G.C. 1966. Three-Dimensional Stress Distribution Around an Elliptical Crack Under Arbitrary Loadings. *ASME J. Appl. Mech.* **33**: 601-611.
- Khade, K. and Shah, S. 2004. New Rheological Correlations for Guar Foam Fluids. *SPE Prod & Fac* **19**(2): 77-85. SPE 88032-PA.
- Khristianovich, S.A. and Zheltov, Y.P 1955. Formation of Vertical Fractures by means of Highly Viscous Liquid. *Proc. SPE 4th World Pet congress* **2**: 579-586. Rome, Italy. WPC 6132.
- King, G.E. 1985. Foam and Nitrified Fluid Treatments-Stimulation Techniques and More. Paper SPE 14477 based on a speech presented as a Distinguished Lecture during the 1985-1986 season.
- King, G.E. 2010. Thirty Years of Gas Shale Fracturing: What Have We Learned? Paper SPE 133456 presented at the SPE Annual Technical Conference and Exhibition, Florence, Italy, 19-22 September.

- Kossecka, E. 1971. Defects as Surface Distribution of Double Forces. *Arch. Mech.* **23**: 481-494.
- Kovscek, A. and Radke, C. 1994. *Foams: Fundamentals and Applications in the Petroleum Industry*, Schramm, L., Editor, American Chemical Society, Washington D.C.
- LAPACK, Linear Algebra PACKage, information available at www.netlib.org/lapack/.
- Lestz, R.S., Wilson, L., Taylor, R.S., Funkhouser, G.P., Watkins, H., and Attaway, D. 2007. Liquid Petroleum Gas Fracturing Fluids for Unconventional Gas Reservoirs. *J Cdn. Pet Tech* **46**(12): 68-72.
- Leverett, M.C. 1940. Capillary Behavior in Porous Solids. *Trans. AIME* **142**(1): 152-169. SPE 941152-G.
- Lillies, A.T. and King S.R. 1982. Sand Fracturing with Liquid Carbon Dioxide. Paper SPE 11341 presented at the SPE Production Technology Symposium, Hobbs, New Mexico, 8-9 November.
- Linkov, A.M. 2011. On Efficient Simulation of Hydraulic Fracturing in terms of particle Velocity. *Int. Journ. Eng. Sci.* **52**: 77-88.
- Liu, Y. 2006. Settling and Hydrodynamic Retardation of Proppants in Hydraulic Fractures, Ph.D. Dissertation. The University of Texas at Austin, Austin, Texas (May 2006).
- Lubinski, A. 1954. The Theory of Elasticity for Porous Bodies Displaying a Strong Pore Structure. *Proc. 2nd U.S. Congress of Appl. Mech.*: 247-256.
- Mahadevan, J. and Sharma, M.M. 2005. Factors Affecting Cleanup of Water Blocks: A Laboratory Investigation. *SPE J.* **10**(3): 238-246. SPE 103229-PA.
- Mastrojannis, E.N., Keer, L.M., and Mura, T. 1979. Stress Intensity Factor for a Plane Crack under Normal Pressure. *Int. Journ. Fracture* **15**: 247-258.
- Mazza, R. 2001. Liquid-Free CO₂/Sand Stimulations: An Overlooked Technology – Production Update. Paper SPE 72383 presented at the SPE Eastern Regional Meeting, Canton, Ohio, 17-19 October.
- McClain, C. 1963, *Fluid Flow in Pipes*, The Industrial press, New York City, New York.
- McGowen, J.M and Vitthal, S. 1996a. Fracturing-Fluid Leakoff Under Dynamic Conditions Part 1: Development of a realistic Laboratory testing Procedure. Paper SPE 36492 presented at the 1996 Annual Technical Conference held in Denver, Colorado, 6-9 October.
- McGowen, J.M and Vitthal, S. 1996b. Fracturing-Fluid Leakoff Under Dynamic Conditions Part 2: Effect of Shear Rate, Permeability and Pressure. Paper SPE 36493 presented at the 1996 Annual Technical Conference held in Denver, Colorado, 6-9 October.
- Meyer, B.R. 1989. Heat Transfer in Hydraulic Fracturing. *SPE Prod Eng* **4**: 423-429. SPE 17041-PA.

- Morton, K.W. and Mayers D.F. 1995, *Numerical Solution of Partial Differential Equations* (Chapter 4), Cambridge University Press, New York City, New York.
- Mukherjee, H. and Economides, M.J. 1991. A Parametric Comparison of Horizontal and Vertical Well Performance, *SPE Form Eval* **6**(2): 209-216. SPE 18303-PA.
- Nicot, J.P. and Scanlon, B.R. 2012. Water Use for Shale-Gas Production in Texas, U.S. *Environ. Sci. Technol.* **46**: 3580-3586.
- Nordgren, R.P. 1972. Propagation of a Vertical Hydraulic Fracture. *SPE J.* **12**(4): 306-314. SPE 3009-PA.
- Olson, J.E. 2004. Predicting Fracture Swarms – the Influence of Subcritical Crack Growth and the Crack-Tip Process on Joint Spacing in Rocks. In *The Initiation, Propagation, and Arrest of Joints and Other Fractures*, Geol soc London Special publication **231**: 73-87.
- Ouyang, S. 1994. Propagation of Hydraulically Induced Fractures with Proppant Transport, Ph.D. Dissertation. The University of Texas at Austin, Austin, Texas (December 1987).
- PacWest FracDB, Product Overview. Available at www.pacwestcp.com/research/fracdb
- Palmer, I.D. and Carroll, H.B. Jr 1983. Three-Dimensional Hydraulic Fracture Propagation in the Presence of Stress Variations. *SPE J.* **23**: 870-878. SPE 10849-PA.
- Parekh, B. and Sharma, M.M. 2004. Cleanup of Water Blocks in Depleted Low-Permeability Reservoirs. Paper SPE 89837 presented at the SPE Annual Technical Conference and Exhibition, Houston, Texas, 26–29 September.
- Penny, G.S. and Conway, M.W. 1989. *Recent Advances in Hydraulic Fracturing*. Monograph Series, SPE, Richardson, Texas **1**: 147-176.
- Penny, G.S., Conway, M.W, and Lee, W. 1985. Control and Modeling of Fluid Leakoff During Hydraulic Fracturing. *J. Pet Tech* **37**(6): 1071-1081. SPE 12486-PA.
- Perkins, T.K and Kern, L.R. 1961. Widths of Hydraulic Fractures, *J. Pet Tech* **13**(9): 937-949. SPE 89-PA.
- Perkins, T.K. and Gonzalez, J.A. 1984. Changes in Earth Stresses Around a Wellbore Caused by Radially Symmetrical Pressure and Temperature Gradients. *SPE J.* **24**(2): 129-140. SPE 10080-PA.
- Pierce, A.P and Siebrits, E. 2001. The Scaled Flexibility Matrix Method for the Efficient Solution of Boundary Value Problems in 2D and 3D Layered Elastic Media. *Comp. Meth. Appl. Mech. Eng.* **190**(46): 5935-5956.
- Prats, M. 1961. Effect of Vertical Fractures on Reservoir Behavior – Incompressible Fluid Case. *SPE J.* **1**(2): 105-117. SPE 1575-G.
- Ramey, H.J. 1962. Wellbore Heat Transmission. *J. Pet Tech* **14**(4): 427-435. *Trans. AIME* 225. SPE 96-PA.

- Reidenbach, V.G., Harris, P.C., Lee, Y.N, and Lord, D.L. 1986. Rheological Study of Foam Fracturing Fluids using Nitrogen and Carbon Dioxide. *SPE Prod Eng* **1**(1): 31-41. SPE 12026-PA.
- Renka, R.J. 1981. Triangulation and bivariate interpolation for irregularly distributed data points. Ph.D. Dissertation, The University of Texas at Austin, Austin, Texas (December 1981).
- Ribeiro, L.H. and Sharma, M.M. 2012. Multi-Phase Fluid-Loss Properties and Return Permeability of Energized Fracturing Fluids. *SPE Prod & Oper* **27**(3): 265-277. SPE 139622-PA.
- Ribeiro, L.H. 2012. Multi-Phase Fluid-Loss Properties and Return Permeability of Energized Fracturing Fluids. Master's Report, The University of Texas at Austin, Austin, Texas (May 2012).
- Ribeiro, L.H. and Sharma, M.M 2013a. Fluid Selection for Energized Fracture Treatments. Paper SPE 163867 presented at the SPE Hydraulic Fracturing Technology Conference, The Woodlands, Texas, 4-6 February.
- Ribeiro, L.H. and Sharma, M.M 2013b. A Three-Dimensional Compositional Model for Hydraulic Fracturing with Energized Fluids. Paper ARMA 13-409 presented at the 47th U.S. Rock Mechanics/Geomechanics Symposium, San Francisco, California, 23-26 June 2013.
- Ribeiro, L.H. and Sharma, M.M 2013c. A New 3D Compositional Model for Hydraulic Fracturing with Energized Fluids. *SPE Prod & Oper* **28**(3): 259-267. SPE 159812-PA.
- Roussel, N.P. 2011. Stress Reorientation in Low Permeability Reservoirs. Ph.D. Dissertation, The University of Texas at Austin, Austin, Texas (August 2011).
- Rumpf, B., Nicolaisen, H., and Maurer, G. 1994. Solubility of Carbon Dioxide in Aqueous Solutions of Sodium Chloride: Experimental Results and Correlation. *J. Solution Chem.* **23**(3): 431-448.
- Rungamornrat, J., Wheeler, M.F., and Mear M.E. 2005. Coupling of Fracture/Non-Newtonian Flow for Simulating Non-planar Evolution of Hydraulic Fractures. SPE Paper 96968 presented at the SPE Annual Technical Conference and Exhibition, Dallas, Texas, 9-12 October.
- Saddington, A.W. and Krase, N.W. 1934. Vapor-Liquid Equilibria in the System Nitrogen-Water. *J. Amer. Chem. Soc.* **56**: 353-361
- Sandler, S.I. 2006, *Chemical, Biochemical, & Engineering Thermodynamics, Fourth Edition*, John Wiley and Sons, New York City, New York.
- Settari, A. and Cleary, M.P. 1984. Three-Dimensional Simulation of Hydraulic Fracturing. *J. Pet Tech* **36**(7): 1177-1190. SPE 10504-PA.
- Simonson, E.R., Abou-Sayed, A.S., and Clifton, R.J. 1978. Containment of Massive Hydraulic Fractures. *SPE J.* **18**(1): 27-32. SPE 6089-PA.

- Sinal, M.L. and Lancaster, G. 1987. Liquid CO₂ Fracturing: Advantages and Limitations. *J Cdn. Pet Tech* **26**(5): 26-30.
- Smith, C.F. 1973. Gas Well Fracturing Using Gelled Non-Aqueous Fluids. Paper SPE 4678 presented at the Fall Meeting of the Society of Petroleum Engineers of AIME, Las Vegas, Nevada, 1-3 October 1973.
- Sneddon, I.N. 1946. The Distribution of Stress in the Neighbourhood of a Crack in an Elastic Solid. *P Roy Soc Lond, Series A* **187**: 229-260.
- Sneddon, I.N. and Elliott, H.A. 1946. The Opening of a Griffith Crack Under Internal Pressure. *Quart Appl. Math* **4**: 262-267.
- Sonnenberg, S.A. 2010. Core Analysis and Unconventional Reservoirs, available online at <http://www.tight-oil-shale-plays.com/media/downloads/inline/steve-sonnenberg-colorado-school-of-mines.1295453329.pdf>
- Spence, D.A. and Sharp, P.W. 1985. Self-Similar Solution for Elastohydrodynamic Cavity Flow. *P Roy Soc Lond, Series A* **400**: 289-313.
- Standing, M.B. and Katz, D.L. 1942. Density of Natural Gases. *Trans. AIME* **146**(1): 140-149. SPE 942140-G.
- Suri, A. and Sharma, M.M. 2007. A Model for Water Injection in Frac-Packed Wells. Paper SPE 110084 presented at the 2007 SPE Annual Technical Conference and Exhibition held in Anaheim, California. 11-14 November.
- Taylor, R.S., Lestz, R.S., Bennion, D.B., Funkhouser, G.P., and Geddes, I.R. 2005. Rheological Evaluations of COMiscible Hydrocarbon Fracturing Fluids. Paper 2005-023 presented at the Canadian International Petroleum Conference, held in Calgary, Alberta, June 7-9.
- Taylor, R.S., Lestz, R.S., Wilson, L., Funkhouser, G.P., Watkins, H., and Attaway, D. 2006. Liquid Petroleum Gas Fracturing Fluids for Unconventional Gas Reservoirs. Paper 2006-169 presented at the Canadian International Petroleum Conference, Calgary, Canada, June 13-15.
- Tudor, E.H., Nevison, G.W., Allen, S., Pike, B. 2009. 100% Gelled LPG Fracturing Process: An Alternative to Conventional Water-Based Fracturing Techniques. Paper SPE 124495 presented at the SPE Eastern Regional Meeting, Charleston, West Virginia, 23-25 September.
- Tudor, R., Vozniak, C., Peters, W., and Banks, M.-L. 1994. Technical Advances In Liquid CO₂ Fracturing. Paper 94-36 presented at the Annual Technical Meeting, Calgary, Canada, June 12-15.
- U.S. Energy Information Administration 2011. Annual Energy Outlook 2011 with projections to 2035. DOE/EIA-0383.
- U.S. Energy Information Administration 2013. Annual Energy Outlook, Early Release 2013. DOE/EIA-0383ER.

- Valkó, P. and Economides, M.J. 1992. Volume Equalized Constitutive Equations for Foamed Polymer Solutions. *J. Rheol.* **36**(6): 1033-1055.
- Valkó, P. and Economides, M.J. 1995, *Hydraulic Fracture Mechanics, First Edition*, John Wiley and Sons, New York City, New York.
- Valkó, P. and Economides, M.J. 1997. Foam-Proppant Transport. *SPE Prod & Fac* **12**(4): 244-249. SPE 27897-PA.
- Van Dam, D.B. and de Pater C.J. 2001. Roughness of Hydraulic Fractures: Importance of In-Situ Stress and Tip Processes. *SPE J.* **6**(1): 4-13. SPE 68775-PA.
- Van Dam, D.B., Papanastasiou, P., and de Pater C.J. 2002. Impact of Rock Plasticity on Hydraulic Fracture Propagation and Closure. *SPE Prod & Fac* **17**(3): 149-159. SPE 78812-PA.
- Virk, P.S. 1975. Drag Reduction Fundamentals, *AIChE J.* **21**(4): 625-656.
- Ward, V.L. 1986. N₂ and CO₂ in the Oil Field: Stimulation and Completion Applications. *SPE Prod Eng* **1**(4): 275-278. SPE 12594-PA.
- Warpinski, N.R. and Teufel, L.W. 1987. Influence of Geologic Discontinuities on Hydraulic Fracture Propagation, *J. Pet. Tech.* **39**(2): 209-220. SPE 13224-PA.
- Watts, R. 2013. A Day in the Life of a Barrel of Water. Transcript of the presentation made at the 4th Annual AIPG Symposium, Canton, Ohio, 10-12 April.
- Weaver, J. 1977. Three-Dimensional Crack Analysis. *Int. J. Solids Structures* **13**: 321-330.
- Wendorff, C.L. and Ainley, B.R., 1981. Massive Hydraulic Fracturing of High-Temperature Wells with Stable Frac Foams. Paper SPE 10257 presented at the Fall Technical Conference and Exhibition, San Antonio, Texas, 5-7 October.
- Weng, X. 1992. Incorporation of 2D Fluid Flow Into a Pseudo-3D Hydraulic Fracturing Simulator. *SPE Prod Eng.*, **7**(4): 331-337. SPE 21849-PA.
- Xia, J, Jdecke, M, Prez-Salado Kamps, I, and Maurer, G. 2004. Solubility of CO₂ in (CH₃OH + H₂O). *J. Chem. Eng. Data* **49**(6): 1756-1759.
- Yew, C.H. 1997, *Mechanics of Hydraulic Fracturing*, Gulf Publishing Company, Houston, Texas.
- Zhang, X., Jeffrey, R.G. and Thiercelin, M. 2007. Deflection and propagation of fluid-driven fractures at frictional bedding interfaces: A numerical investigation, *J. Structural Geol.* **29**: 396-410.

The format used for the references is recommended by The Society of Petroleum Engineers (2013).

Vita

Lionel Hervé Noël Ribeiro was born in Bron, France. He attended the “Aux Lazaristes” prep school in Lyon, France, before joining l’Ecole des Mines de Nancy (School of Mines) in 2006. He received a Bachelor of Science degree and a “Diplôme d’Ingénieur” from that school. In 2008, he enrolled at the University of Texas in the department of Petroleum Engineering, where he has worked under the supervision of Dr. Mukul M. Sharma for the completion of his Master’s and Ph.D. degrees.

Permanent e-mail address: lionelhibeiro@gmail.com

This dissertation was typed by the author.